

CRANFIELD UNIVERSITY

Gonçalo Nuno Rodrigues Pardal

Joining of steel to aluminium and stainless steel to titanium for
engineering applications

SCHOOL OF AEROSPACE, TRANSPORT AND
MANUFACTURING
Welding Engineering and Laser Processing Centre

PhD
Academic Year: 2015 - 2016

Supervisor: Dr. Ganguly Supriyo and Prof. Stewart Williams
May 2016

CRANFIELD UNIVERSITY

SCHOOL OF AEROSPACE, TRANSPORT AND
MANUFACTURING
Welding Engineering and Laser Processing Centre

PhD

Academic Year 2015 - 2016

Gonçalo Nuno Rodrigues Pardal

Joining of steel to aluminium and stainless steel to titanium for
engineering applications

Supervisor: Dr. Ganguly Supriyo and Prof. Stewart Williams
May 2016

© Cranfield University 2016. All rights reserved. No part of this
publication may be reproduced without the written permission of the
copyright owner.

List of publications:

Meco, S. et al. (2012) 'Overlap conduction laser welding of aluminium to steel', The International Journal of Advanced Manufacturing Technology, 67(1-4), pp. 647–654. Available at: 10.1007/s00170-012-4512-6 (Accessed: 20 January 2014).

Pardal, G. et al. (2014) 'Dissimilar metal laser spot joining of steel to aluminium in conduction mode', The International Journal of Advanced Manufacturing Technology, 73(1-4), pp. 365–373. Available at: 10.1007/s00170-014-5802-y (Accessed: 5 December 2014).

Meco, S. et al. (2015) 'Application of laser in seam welding of dissimilar steel to aluminium joints for thick structural components', Optics and Lasers in Engineering, 67 Elsevier, pp. 22–30.

Pardal, G. et al. (2016) 'Dissimilar metal joining of stainless steel and titanium using copper as transition metal', The International Journal of Advanced Manufacturing Technology

International conferences

"Dissimilar metal joining of stainless steel and titanium using copper as transition metal" – EUROMAT 2013 – September 2013

ABSTRACT

Dissimilar welding has been subject of several investigations due to its potential importance in various industrial fields such as transportation, energy generation and management. Dissimilar welding can increase the design efficiency, by the use of complementary alloys with different properties, cost cutting and light weighting structures. The use of different materials within a component or structure to best suit a particular task, requirement or increase its life and performance has always been an ambition of several designers and engineers.

This project investigated the joining steel and aluminium for the automotive industry and also stainless steel and titanium to be applied in the civil nuclear energy generation industry. These dissimilar metallic combinations are metallurgically incompatible and the formation of brittle intermetallic phases (IMC) need to be controlled or eliminated.

To join steel to Al, laser spot welding process was selected, to avoid the bulk melting of steel and Al at the joint interface that enhance the formation of brittle IMC. This part of the work was focused in controlling the joining process to control the IMC formation of galvanized and uncoated steel to Al and verify if it was possible to have a sound and reliable joint in the presence of an IMC layer.

In the second part of this study, stainless steel to titanium joining, a different approach was taken with the application of weld metal engineering to modify or eliminate the IMC formation. Several metals were evaluated as potential interlayers to use and laser welding with a Ni interlayer was evaluated with moderate success, due to the modified IMC with improved mechanical properties and the good compatibility between Ni and the stainless steel. A further improvement was achieved when Cu was brazed between stainless steel and Ti using CMT (Cold Metal Transfer) a low heat input MIG process. The final attempt was to use a different interlayer that was 3D printed and deposited in several layers. This interlayer was composed Cu and Nb that were selected as candidates to avoid the IMC formation between the stainless steel and Ti. With this approach it was possible to build an IMC free component and possibly improve and avoid IMC formation in several other dissimilar metallic combinations.

Keywords:

Welding, Laser, GMAW, GTAW, Copper, Niobium

ACKNOWLEDGEMENTS

I would like to thank my supervisors Dr. Supriyo Ganguly and Professor Stewart Williams, for all the support and guidance during this project. I would also like to thank the remainder of the team from the welding engineering and laser processing centre, with a special mention to my colleagues and the lab technicians. Without their help and support some of the work would not be possible or it would not be so enjoyable. I would also like to thank my sponsors the LATEST 2 grant for the Al and Fe and AWE for the freedom to try different approaches to solve this issue of dissimilar metallic joining.

I would like to thank all my family, specially my parents that always believed in me and made me pursuit an academic path.

And finally I would like to thank my soulmate, Sonia Meco, with whom I shared these later years of my life. She has been a great girlfriend and now a wonderful wife, helping me along the way in this quest that has been our PhD.

TABLE OF CONTENTS

ABSTRACT	iii
ACKNOWLEDGEMENTS.....	v
LIST OF FIGURES.....	ix
LIST OF TABLES	xvi
LIST OF ABBREVIATIONS.....	xix
1 INTRODUCTION.....	1
1.1 Aim.....	5
1.1.1 Objectives	5
2 Literature review.....	7
2.1 Dissimilar joining types	7
2.1.1 Type 1 – Metallurgically compatible dissimilar metal joining	7
2.1.2 Type 2 – Metallurgically incompatible dissimilar metal joining.....	10
2.1.3 Type 3 – Dissimilar material joining.....	11
2.2 Type 2 dissimilar welding challenge (Intermediate phases or intermetallic compounds)	13
2.3 Strategies to mitigate the IMC formation.....	18
2.3.1 Physical control - Joining process control	18
2.3.2 Metallurgical control (weld metal engineering)	27
2.4 Dissimilar metallic combinations studied.....	32
2.4.1 Fe-Al dissimilar joining	32
2.4.2 Steel to aluminium spot joining.....	37
2.4.3 – Stainless steel to Ti dissimilar joining.....	40
2.5 Welding Processes	48
2.5.1 Laser light.....	48
2.5.2 Laser welding	51
2.5.3 Gas tungsten arc welding - GTAW	54
2.5.4 Gas metal arc welding - GMAW	57
2.5.5 CMT – Cold Metal Transfer	60
2.6 Summary of literature review	62
2.7 Knowledge gaps identified	63
3 Steel and Aluminium spot welding.....	65
3.1 Chapter introduction.....	65
3.2 Low carbon steel and aluminium spot welding.....	67
3.2.1 Introduction	67
3.2.2 Conduction mode laser spot welding.....	67
3.2.3 Material and experimental setup	69
3.2.4 Experimental parameter (system and fundamental).....	70
3.2.5 Results and discussion.....	72
3.2.6 Conclusions.....	82

3.3 Galvanized steel and aluminium spot welding	84
3.3.1 Introduction	84
3.3.2 Experimental procedure	85
3.3.3 Results and discussion.....	87
3.3.4 Conclusions.....	94
3.4 Chapter Conclusions.....	96
4 Stainless steel and Titanium welding	97
4.1 Chapter introduction.....	97
4.2 Keyhole laser welding of stainless steel to Ti with and without Ni as an interlayer	100
4.2.1 Introduction	100
4.2.2 Experimental procedure	102
4.2.3 Results and discussion.....	107
4.2.4 Conclusions.....	124
4.3 CMT Cu deposition	126
4.3.1 Introduction	126
4.3.2 Experimental procedure	129
4.3.3 Results and discussion.....	134
4.3.4 Conclusions.....	157
4.4 Chapter conclusions	158
5 Compatible metal selection and additive manufacturing	159
5.1 Introduction	159
5.1.1 Joining process selection	165
5.2 Experimental procedure.....	167
5.3 Results and discussion	171
5.4 Chapter conclusions	187
6 Conclusions.....	189
7 Future work	191
7.1 Fe-Al spot welding	191
7.2 Ti to stainless steel	191
REFERENCES.....	193
APPENDICES	203
Appendix A – Experimental tables from chapter 5	203
Appendix B – Research papers generated during the period of this research.....	206

LIST OF FIGURES

Figure 1 – SLC final prototype and the distribution of each metal by weight (SLC Consortium, 2008).	2
Figure 2 – Ag (silver) – Au (gold) phase diagram (ASM - International, 1992) ...	8
Figure 3 – Fe-Cu phase diagram (ASM - International, 1992).....	9
Figure 4 – Al –Ti phase diagram (ASM - International, 1992).....	10
Figure 5 – Al-Ni phase diagram (ASM - International, 1992).....	14
Figure 6 – Al-Fe and Fe-Ti phase diagrams (ASM - International, 1992).	15
Figure 7 – Rotational friction welding a) (Forward Precision Equipment Ltd, 2011) and linear Friction welding b) (Threadgill, 2008).....	19
Figure 8 – Friction stir welding process (Wiki, 2014).	21
Figure 9 – Experimental setup a) and double shoulder FSW tool b) (Fazel-Najafabadi et al., 2011).....	21
Figure 10 – Joints made using 700 rpm rotation speed a) and with 1100 rpm b) (longitudinal section) and transversal sections (c) (Fazel-Najafabadi et al., 2011).	22
Figure 11 – Optical a) and SEM b) imaging at the bimetallic vortices region (Fazel-Najafabadi et al., 2011).	23
Figure 12 – Lap shear test results for the FSW welded specimens (Fazel-Najafabadi et al., 2011).....	23
Figure 13 – Tensile shear test result for the Fe-Ti FSW specimen (Liao et al., 2010).	24
Figure 14 – Diffusion bonding chamber (Vacuum Furnace Engineering Limited, 2011).	25
Figure 15 - Width of the IM compounds formed in the reaction zone (Poddar, 2009).	26
Figure 16 – Shear strength, tensile strength and breaking strength evolution with applied temperature of the joints made between stainless steel and Ti (Poddar, 2009).....	26
Figure 17 – Bead morphology, top surface a), root surface b) and cross section c).	28
Figure 18 – Ti to stainless steel electron beam weld bead morphology.	29
Figure 19 – Possible IMC phases present on the weld a) and correspondent weld harness profile b).....	30

Figure 20 – Fe-Al phase diagram (Okamoto, 2010).	32
Figure 21 – Optical micrograph of IMC layer between Fe and molten Al at 800 °C with immersion time of 30 s a) and 30 min b). SEM of the IMC layer identifying the Fe ₂ Al ₅ and FeAl ₃ phases (15 min immersion time) c).	33
Figure 22 – Cross sectional macro section for a voestalpine brazed joint.	36
Figure 23 – Optical micrographs of the transverse section through the dissimilar Al - Fe spot weld produced using tool rotational speed of 3000 rpm and plunge rate of 1 mm/s and dwell time of 4s: Pin penetration depths into Fe of 0.4 mm a) 0.85 b).	38
Figure 24 – Top view of dissimilar welding between Al6061 and steel a) corresponding macroscopic appearance of the cross section welded zone b) photographs showing the tool geometry c).	39
Figure 25 – Schematic diagram of the orbital translation path used and tool geometry a). Typical cross sections of welds with translation speeds of 60 b) and 600 m/min c).	40
Figure 26 – Vickers hardness plot from the stainless steel Ni interface a), Ni Ti interface b) and joint mechanical properties vs joint temperature c) (Kundu and Chatterjee, 2008b).	42
Figure 27 – Hardness distribution for the Fe-Ti joint bonded at 850 °C for 90 min (Elrefaey and Tillmann, 2009).	43
Figure 28 – Autogenous Fe-Ti weld cross section SEM micrograph a), higher magnification of zone I b) and potential IMC phases c) (Wang et al., 2012).	44
Figure 29 – Micro hardness distribution profiles for the Ti-Fe and Ti-Cu-Fe joints (Wang et al., 2012).	44
Figure 30 – Weld bead morphology, electron beam a) and pulsed laser b) (Tomashchuk et al., 2011).	45
Figure 31 – Stress strain curve for samples joined between stainless steel and Ti at 900 °C for 10 min with different interlayers (V, V-Cr, V-Cr-Ni) (Lee et al., 2010)	47
Figure 32 – Laser schematic representation (Paul et al., 2013).	49
Figure 33 – a) Electron configuration for spontaneous emission. b) Electron configuration on a population inversion and with stimulated emission (Paul et al., 2013).	49
Figure 34 – Laser active fibre components and corresponding refraction index profile (Buchfink, 2007).	50
Figure 35 – Solid state laser system (Buchfink, 2007).	51

Figure 36 – Conduction, transition and keyhole modes on S355 steel plates (Assuncao et al., 2012).....	54
Figure 37 – GTAW welding process schematics.	55
Figure 38 – Influence of the polarity on the weld bead profile (American Welding Society, 1991).....	56
Figure 39 – GMAW welding process schematics (Hayden corp., 2014).....	58
Figure 40 – GMAW short circuiting transfer mode arcing phases (American Welding Society, 1991).....	59
Figure 41 – Different CMT phases, a) arc ignition b) short circuit phase c) inversion of wire feed direction d) arc re-ignition	60
Figure 42 – Schematic representation of conduction mode laser spot welding for each set of experiments.....	68
Figure 43 - Clamping system with laser beam schematic representation.....	68
Figure 44 – Tensile shear test specimen dimension.	70
Figure 45 – Conduction mode laser spot welding macro section.	72
Figure 46 – Intermetallic measurement example a) and plot of the IMC layer thickness for each of the five micrographs done across the weld interface b).	73
Figure 47 – IPG YLR 8000 laser energy distribution for a defocused position.	74
Figure 48 – Evolution of the IMC layer thickness with the specific point energy a) and selected Cu backing bar micrographs b).	76
Figure 49 – Optical micro section of IMC layer.....	77
Figure 50 – EDS of the intermetallic layer (left), Elemental distribution (right)..	77
Figure 51 – Micro hardness pattern representation.....	78
Figure 52 – Hardness values in a vertical traverse across the weld interface ..	79
Figure 53 - Lap Shear strength behaviour vs. specific point energy a), shear strength vs. IMC layer thickness b).....	80
Figure 54 – Shear strength – displacement graph for selected samples.....	82
Figure 55 – Graded Al micrograph a), SEM/EDS image b) and corresponding acquisition areas.....	86
Figure 56 – Macrographs from samples 1 a) and sample 4 b)	88
Figure 57 – IMC layer thickness and its variability low carbon steel vs galvanized steel (sample 7 vs sample 8).....	88

Figure 58 – Micrographs from the samples joined with uncoated steel (a, b and c) and Zn coated steel (d, e and f).....	89
Figure 59 – SEM micrograph taken from the centre of the IMC layer and corresponding spectrum positions.....	90
Figure 60 – SEM-EDS analysis made at the edge of the spot weld.	91
Figure 61 – Shear load results for both Al alloys vs the specific point energy. .	93
Figure 62 – Load results for Fe-Al joints produced with galvanized and uncoated steel and 6111 Al.....	94
Figure 63 – Fe-Ti phase diagram (ASM - International, 1992).	97
Figure 64 – Fe-Ni a) and Ni-Ti b) phase diagrams (ASM - International, 1992).	101
Figure 65 – Autogenous laser welding of Ti and stainless steel experimental setup.....	103
Figure 66 – Schematic representation from the autogenous laser welding from stainless steel to Ti.....	104
Figure 67 – Schematic representation of the experimental setup for butt weld configuration a) and the actual experimental setup b).....	105
Figure 68 – Ti to Ni and Ni to stainless steel joining a) and different weld pool compositions between Ti and Ni using the laser scanned diagonally at the interface b).....	106
Figure 69 – Micrographs with evident cracking from direct overlap samples between stainless steel and Ti. Sample 1 shows micro cracking a), while samples 2 and 8 show macroscopic cracking b) and c).....	108
Figure 70 – Loss of weld profile due to high brittleness and cracking occurred during welding, cutting and handling of the sample.	109
Figure 71 – EDS mapping (Fe and Ti) to evaluate the mixing ratio uniformity inside the weld profile. Sample 1 a), sample 2 b) and sample 8 c).....	110
Figure 72 – Mixing ratios achieved during direct joining of Ti and stainless steel in overlap configuration over layered into the Fe-Ti phase diagram.	111
Figure 73 – Thick Ni interlayer sample on stainless steel to titanium welding keyhole laser welding.	112
Figure 74 – Optical micrograph from sample created with two weld seams and an interlayer of Ni.	113
Figure 75 – Back scattered electron image a) for the Ti–Ni interface and corresponding Ti b) and Ni c) distributions at the weld pools.....	113

Figure 76 – Back scattered electron image for the Ni-Fe interface a) and corresponding Fe b) and Ni c) distributions at the weld pools.	114
Figure 77 – 900 ° C isothermal of the Fe-Cr-Ni ternary phase diagram.....	115
Figure 78 – Ni-Ti phase diagram.....	116
Figure 79 – Metallographic samples extracted for further investigation.....	116
Figure 80 – Atomic composition for a horizontal line across the weld bead. Sample C a), sample D b) and sample E c).....	119
Figure 81 – Hardness profiles for samples C a), D b) and E c).	121
Figure 82 – Cu-Fe binary phase diagram (ASM - International, 1992).....	127
Figure 83 – Qualitative assessment for the welding process applicability on Cu and Cu alloys.....	128
Figure 84 – Schematics from the welding-brazing technique	130
Figure 85 – CMT Cu deposition experimental setup.	131
Figure 86 – Samples preparation for metallographic analysis (two) and the sample for mechanical tests.	131
Figure 87 – Tensile test setup used for CMT Cu welded samples.	132
Figure 88 – Welding wire positioning during the welding-brazing experiments	133
Figure 89 – Ultimate tensile strength vs heat input of welded samples with different welding wire distances to the stainless steel plate.....	135
Figure 90 – Selected sample macrographs I – 0.5 mm, II – 0.85 mm III – 1.20 mm, a, b, and c increasing heat input.....	136
Figure 91 – Stress strain curves for the selected samples	137
Figure 92 – Hardness mapping and corresponding optical macrographs for samples: CMT 2 a), CMT 4 b) and CMT 5 c).....	138
Figure 93 – Cu deposited weld bead macrograph and distinctive areas a). Backscattered SEM image b). EDS mapping showing the main elements present on the sample c).	140
Figure 94 – SEM and EDS mapping for the stainless steel Cu interface layer. SEM image a), Composite EDS mapping b), Cu c), Fe d), Cr e) and Ti f) EDS mapping.	141
Figure 95 – Stainless steel Cu SEM backscattered image and phases investigated.	142

Figure 96 – SEM and EDS mapping for the Cu Ti interface layer. SEM image a), Composite EDS mapping b), Ti c), Cu d), Si e) and Fe f) EDS mapping.	145
Figure 97 – Cu Ti interface layer SEM backscattered image and phases investigated.	146
Figure 98 – Cu-Ti phase diagram with the corresponding IMC phases indicated by an orange line.	147
Figure 99 – Si-Ti phase diagram and the representation of phase C (ASM - International, 1992).	148
Figure 100 – Cu-Fe-Ti phase diagram isothermal section at 849 °C with phase D plotted a) (Raghavan, 2002) and Cu-Ti phase diagram with phase E plotted b) (ASM - International, 1992).	149
Figure 101 – Cu-Fe-Ti phase diagram at 849 °C. Phase F – red, phase G – green and phase H – blue (Raghavan, 2002).	150
Figure 102 – Cu Ti interface layer vicinity SEM backscattered image and phase investigated.	151
Figure 103 – SEM and EDS mapping for the scattered IM compounds close to stainless steel. a) SEM image, b) Composite EDS mapping, c) Cu, d) Fe, e) Si and f) Ti EDS mapping.	152
Figure 104 – Scattered IMC's close to stainless steel SEM backscattered image and phases investigated.	153
Figure 105 – SEM and EDS mapping for the scattered IM compounds close to Ti. a) SEM image, b) Composite EDS mapping, c) Cu, d) Si, e) Ti and f) Fe EDS mapping.	155
Figure 106 – Scattered IMC's close to Ti SEM backscattered image and phases investigated.	156
Figure 107 – IM phase formation for different elements (Fe – green, Ti – blue) (Ferro and Saccone, 2007).	160
Figure 108 – Diagram showing the IMC formation for various elements (blue square elements are the compatible metals selected)(Ferro and Saccone, 2007).	163
Figure 109 – Schematic representation for the dilution of metal B into metal A.	166
Figure 110 – AM experimental setup.	168
Figure 111 – Metal deposition strategy a) distance and angles used when feeding the wires b).	169
Figure 112 – Schematic representation for final steps on the inserts manufacturing process.	171

Figure 113 – Composite macro from sample AM1 a), AM2 b) and detailed macrostructure of sample AM2 interface between Nb and Cu c).....	172
Figure 114 - Composite macrograph from specimen AM2 SEM/EDS analysis a) and graphic with elemental atomic composition across AM4 specimen b).	173
Figure 115 – Composite macro from samples AM3 a) and AM4 b).....	174
Figure 116 – Composite macrograph from AM4 SEM/EDS analysis a) and graphic with elemental atomic composition across AM4 specimen b).....	176
Figure 117– Composite macro from sample AM5 a) and AM6 b).....	177
Figure 118 - Composite macrograph from sample AM5 SEM/EDS analysis a) and graphic with elemental atomic composition across AM5 specimen b).	178
Figure 119 – Nb-Cu interface SEM micrograph a) and corresponding EDS mapping b).....	179
Figure 120 – Cu-Nb phase diagram (ASM - International, 1992).	179
Figure 121 –SEM and EDS mapping for the Cu-Fe interface. a) SEM image, b) Composite EDS mapping, c) Cu, d) Fe, e) Cr and f) Si EDS mapping. ...	181
Figure 122 – Cu-Fe interface SEM micrograph and corresponding identifiable phases.....	182
Figure 123 – Fe-Cu Cu-Cr and Cu-Ni phase diagrams	184
Figure 124 – Sample AM5 hardness mapping indents a) and corresponding hardness map b).....	185

LIST OF TABLES

Table 1 – Selected Fe and Cu thermal and physical properties (Gale and Totemeier, 2003).	9
Table 2 – Fe-Al and Ti-Fe IM compounds and correspondent micro harnesses Fe-Ti (ASM - International, 1992; Thomy and Moller, 2013; Tomashchuk et al., 2011).....	16
Table 3 – Thermal and physical properties for Fe, Al and Ti.....	16
Table 4 – IMC’s present at the joint interfaces for different joining temperatures (Kundu and Chatterjee, 2008b).	41
Table 5 – Advantages and disadvantages for GTAW process.	55
Table 6 – Advantages and disadvantages for GMAW process.	58
Table 7 – Al and Fe physical properties (Gale and Totemeier, 2003).	65
Table 8 – Chemical composition (%wt) for DC04 steel and 6111-T4 aluminium alloy	69
Table 9 – Mechanical properties of the weld members	69
Table 10 – System parameters used for conduction mode laser spot welding.	71
Table 11 – Fundamental energy parameters used for conduction mode laser spot welding.....	71
Table 12 – IMC layer thickness and corresponding standard deviation.	74
Table 13 – EDS semi-quantitative analysis results for Fe and Al at the joint interface.....	78
Table 14 – Zn coating chemical composition (wt.%).	85
Table 15 – Galvanized steel chemical composition (wt.%).	85
Table 16 – 6016 and 4045 Al alloys nominal composition (wt %).	86
Table 17 – Experimental welding parameters (system and fundamental) to evaluate the influence of using a different Al alloy for dissimilar spot welding of steel to aluminium.....	87
Table 18 - Experimental welding parameters (system and fundamental) to characterise the influence of Zn in the IMC layer.....	87
Table 19 – At % of spectrums analysed in Figure 59.	91
Table 20 – Atomic percentage for the analysed spectrums at Figure 60.....	92
Table 21 – Fe and Ti physical properties (Gale and Totemeier, 2003).	98

Table 22 – Selected stainless steel and Ti alloy compositions	102
Table 23 – Autogenous stainless steel to Ti experimental data.....	104
Table 24 – Welding parameters for thick Ni interlayer evaluation.....	107
Table 25 – Fe and Ti mixing ratios inside the weld pool and penetration depth for the lower plate in laser overlap keyhole welding of Ti and stainless steel.	109
Table 26 – Weld pool composition at the stainless steel Ni and Ti – Ni interfaces.	114
Table 27 – Ti-Ni micrographs and selected samples hardness maps for the Ni- Ti diagonal weld.....	118
Table 28 – Comparison between the surface melting distribution, the average atomic percentage and identification of the correspondent IMC phase. ..	120
Table 29 – SEM images from samples C, D and E interfaces between the parent metals and weld pool and corresponding analysed phases.	122
Table 30 – Spectrums and possible IMC phases formed at the Ni and Ti interfaces (at%) shown in Table 29.	123
Table 31 – Melting point and Vickers hardness values for Cu, Fe, Ni and Ti .	127
Table 32 – Selected welding wire mechanical properties and melting point...	129
Table 33 – Parent materials atomic composition (%wt).....	130
Table 34 – CMT welding-brazing parameters for the welding-brazing experiments.....	134
Table 35 – Elemental composition in weight percentage from the phases identified on the stainless steel Cu interface layer.....	143
Table 36 – Elemental composition in weight percentage from the phases identified on the Cu Ti interface layer.	146
Table 37 – Elemental composition in weight percentage from the phase identified on the Cu Ti interface layer vicinity.....	151
Table 38 – Elemental composition in weight percentage from the phases identified in Figure 104.	153
Table 39 – Elemental composition in weight percentage from the phases identified in Figure 106.	156
Table 40 – Melting temperature the selected compatible metals (Gale and Totemeier, 2003).	161
Table 41 – Melting temperature for no IMC selected metals.	162

Table 42 – Physical and mechanical properties and prices of selected metals (Gale and Totemeier, 2003).....	164
Table 43 – AM used alloys chemical composition in weight percentage.	167
Table 44 – Ti and Nb thermal properties (Gale and Totemeier, 2003).	175
Table 45 – EDS quantitative analysis from phases identified on Figure 119 a).	180
Table 46 – EDS semi-quantitative analysis (Wt%) from phases identified on Figure 122.	183
Table 47 – Hardness values for the alloys used at samples AM5 and AM6...	185
Table 48 – AM feasibility experiments deposition parameters.	203
Table 49 – AM Ti diffusion experiments deposition parameters.	204
Table 50 – AM final experiments deposition parameters.....	204

LIST OF ABBREVIATIONS

3D	Three Dimensions
AC	Alternate Current
Ag	Silver
Al	Aluminium
AM	Additive Manufacturing
Au	Gold
CMT	Cold Metal Transfer
CO ₂	Carbon dioxide
CTWD	Contact Tip to Work Distance
CW	Continuous Wave
DC	Direct Current
DCEN	Direct current electrode negative
DCEP	Direct current electrode positive
EDS	Energy Dispersive Spectroscopy
E _{sp}	Specific point energy
Fe	Iron
FEG-SEM	Field emission gun – scanning electron microscopy
FSW	Friction Stir Welding
GMAW	Gas Metal Arc Welding
GTAW	Gas Tungsten Arc Welding
HAZ	Heat Affected Zone
IMC	Intermetallic compound
IR	Infra-Red
(L)	Length
Mg	Magnesium
Ni	Nickel
PD	Power density
RSW	Resistance spot welding
SEM	Scanning Electron Microscopy
Si	Silicon
SLC	Super Light Car

(T)	Thickness
Ta	Tantalum
Ti	Titanium
t_i	Interaction time
UK	United Kingdom
V	Vanadium
(W)	Width
Zn	Zinc

1 INTRODUCTION

Dissimilar metal welding is a research field for the future structure design and evolution due to enabling the creation of low mass and tailored structures. The advantage of these structures is the combination of the best properties of the different metals.

This project focuses in two particular dissimilar metallic combinations, thin plate aluminium (Al) to steel (Fe) spot joining for automotive applications and stainless steel to titanium (Ti) butt joining for the nuclear industry. These two dissimilar metallic combinations are difficult to joint due to the metallurgical incompatibility i.e. due to the formation brittle intermetallic compounds (IMC) formed during the joining process. These IMC appear due to lack of solid solubility between the investigated metallic combinations and also due to their different physical properties. IMC formation and growth has been described in literature, but an efficient way of producing reliable and resilient joints made by a fusion welding processes has eluded the researchers.

The development of new techniques for welding dissimilar metals is subject of high relevance in the automotive sector. According to a recent white paper (H.M. Government, 2009) the carbon emission target for UK's domestic transportation sector is 130 g/km by 2012 and is likely to be further restricted to 95 g/km by 2020. The automotive manufacturers, therefore, are focussed on re-visiting the vehicle design to incorporate lighter metals and alloys as a structural member of automotive frames and components. As a result, a significant research effort has now been put into finding the joining solution between the different structural materials. One example of this research is the European project SuperLIGHT-CAR that was aimed to reduce the weight of a C segment vehicle by 30%. From this project a concept car (Figure 1) was developed with the use of dissimilar metals to achieve the targeted 30% weight reduction (SLC Consortium, 2008).

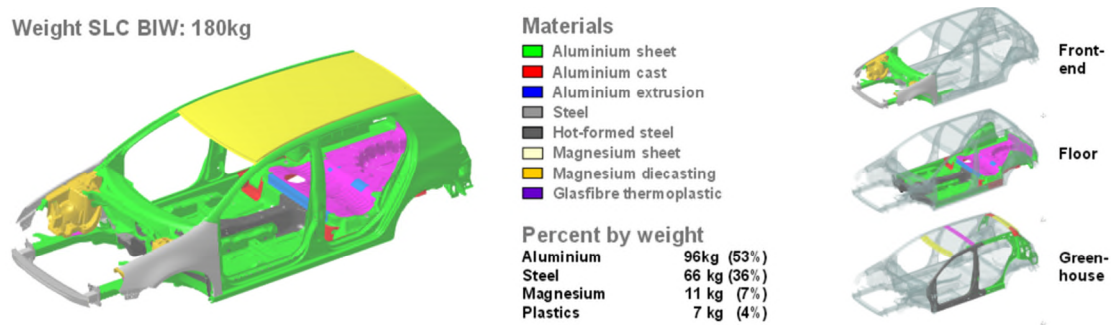


Figure 1 – SLC final prototype and the distribution of each metal by weight (SLC Consortium, 2008).

Figure 1 demonstrates that to obtain the required 30% reduction in weight, this concept car integrated several different alloys in its structure. However the main obstacle for the wide application of dissimilar structures like the SLC prototype is the joining of these dissimilar alloys which are often metallurgically incompatible.

One focus of this thesis is the Al-Fe dissimilar metallic combination that needs to be addressed to achieve the final goal of 30% weight reduction of the SLC project where these two alloys compose 90% of the weight of the prototype. In figure 1 the Al-Fe dissimilar combination can be verified at the floor section and the front end of the proposed final prototype. Where the necessity of a reliable Fe-Al dissimilar combination is necessary to join the transmission tunnel made of steel to the remainder of the prototype floor made of Al and the wheel arch made of steel and the front pillar made of Al.

The second part of this thesis was focused on the research of joining stainless steel to titanium. This dissimilar metallic combination has application in the civil nuclear industry. In particular in the process of recycling or reprocessing of used nuclear fuel, where the used nuclear fuel is boiled in nitric acid inside an electrolytic dissolver reactor. Due to the higher corrosion resistance, Ti was selected to be the main metal used for the construction of the reactor, whilst the other components of the reprocessing plant are made of stainless steel (Dey et al., 2009).

This shows the necessity of finding a solution for this dissimilar metallic combination that is reliable and can be used to facilitate the fabrication of these reprocessing plants.

These dissimilar applications were researched in this thesis by using a laser spot welding in conduction mode for the Fe-Al dissimilar combination and the use of different interlayers for the Fe-Ti dissimilar combination.

The laser spot welding in conduction mode was selected due to its similarity with RSW (Resistance Spot Welding) used traditionally during the automotive manufacturing. This process enables the control of the IMC formation and growth by having the steel on the solid state and the Al brazing the steel. The laser spot welding in conduction mode uses the different melting points and thermal conductivities of the parent metals to achieve the selective melting of Al. This innovative joining process linked with the fundamental metal interaction parameters and the IMC analysis generates a clear view where are the limitations of using a joining process control approach for a fusion joining process. This approach can decrease and control the IMC formation and growth, however even avoiding the bulk melting of the steel and Al is not sufficient to avoid the diffusion/reaction of both metals and the decrease of the mechanical properties of the joined samples.

In the second part of the work due to the similar physical properties of the parent metals, the introduction of other metals as interlayers was necessary.

The first metal selected for this part of the work was Ni, this metal is compatible with Fe and shows some compatibility towards Ti. This was demonstrated by a weld without cracks between Ni and Fe, but the IMC and crack formation was not avoided with Ti. The second metal selected was Cu due to the same reasons referenced before for Ni and the addition of a lower melting point and higher ductility. In this section Cu was brazed in a gap between Fe and Ti. These joints were crack free and could be mechanically tested obtaining a maximum strength of 200 MPa that is 21 % of the Ti-6Al-4V.

The final section of this work used an innovative way to select the metals to be used as interlayers. The hypothesis postulated at this section was if there was one metal or metals that could be used and would not generate any IMC with the parent metals (Fe, Ti) and between each other. At the end of this analysis the metallic combination to be used as interlayer was Ti-Nb-Cu and Fe. This interlayer was manufactured as an intermediate component using a 3D printing technology termed WAAM. This revealed that a systematic approach in interlayer selection can be used to generate a structure that does not have any IMC present.

This approach can possibly be used to solve other dissimilar metallic combination where the formation of IM is present.

1.1 Aim

The aim of this project is to understand the formation and development of IMC phases for the Fe-Al and stainless steel-Ti dissimilar combinations, characterize them, verify their importance in decreasing the weld mechanical properties and act to avoid or eliminate their formation.

1.1.1 Objectives

- Fe-Al
 - Investigate how the different physical properties of Fe-Al can be used to achieve dissimilar laser spot joining.
 - Understand the relation between the process parameters and galvanized steel coating interact with the IMC and mechanical properties of the laser spot joint.
- Fe-Ti
 - Investigate how different interlayers can be used to decrease or prevent the IMC formation.
 - Understand how different joining processes can be used to mitigate the IMC formation (laser, MIG and TIG).

2 Literature review

2.1 Dissimilar joining types

Dissimilar welding and joining is defined when the two materials to be joined are of different nature, their chemical and or physical properties are not the same. These joints can be divided in three different categories that describe the different degrees of complexity present in the joints:

- Metallurgically compatible dissimilar metal joining – Type I
- Metallurgically incompatible dissimilar metal joining – Type II
- Dissimilar material joining – Type III.

These different types of dissimilar joining are described below;

2.1.1 Type 1 – Metallurgically compatible dissimilar metal joining

Type I joining is characterized either by joining metals which are the same, but the crystallographic structure is different or in which the main metal constituent is common but the alloying elements are different (e.g. joining of different Al alloys). Alternatively Type I can also be the joining of two different metals which are metallurgically compatible, do not make any IMC phases in equilibrium conditions. These metallurgical compatible metals can be divided into two further categories, soluble and insoluble systems. Silver and gold are an example of a soluble type 1 dissimilar metallic combination (Figure 2).

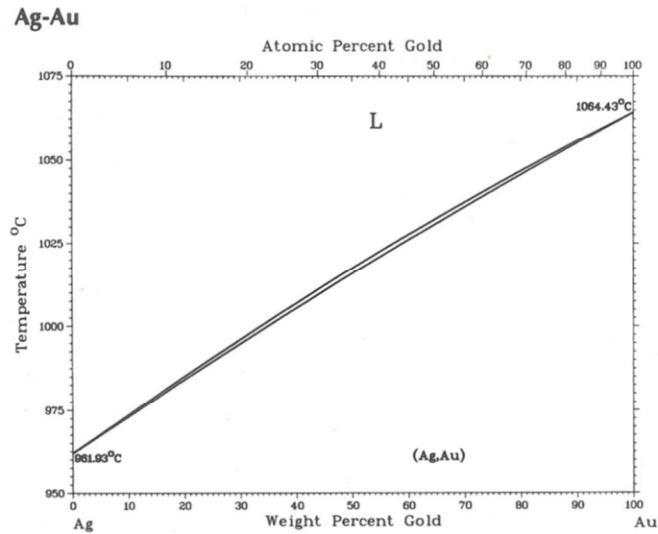


Figure 2 – Ag (silver) – Au (gold) phase diagram (ASM - International, 1992)

Figure 2, the Ag-Au phase diagram shows which phases are present in equilibrium conditions for any concentration of the two metals, the Ag-Au system does not form any intermediate brittle phases in equilibrium conditions for any weight percentage and it also forms solid solutions in all ranges of self-dilutions. This happens when two metals are very close in the periodic table and their crystal structure is similar. Both Ag and Au have a face centred cubic crystal structure and both elements are placed in the eleventh column of the Periodic table.

Iron and copper is an example of a system that is type I, but is insoluble, these metals do not form any intermediate phases, but they do not present a solid solution over all ranges of self-dilutions. They have two small solid solution regions and show a large region where the two phases co-exist with similar properties, as can be observed in the phase diagram in Figure 3.

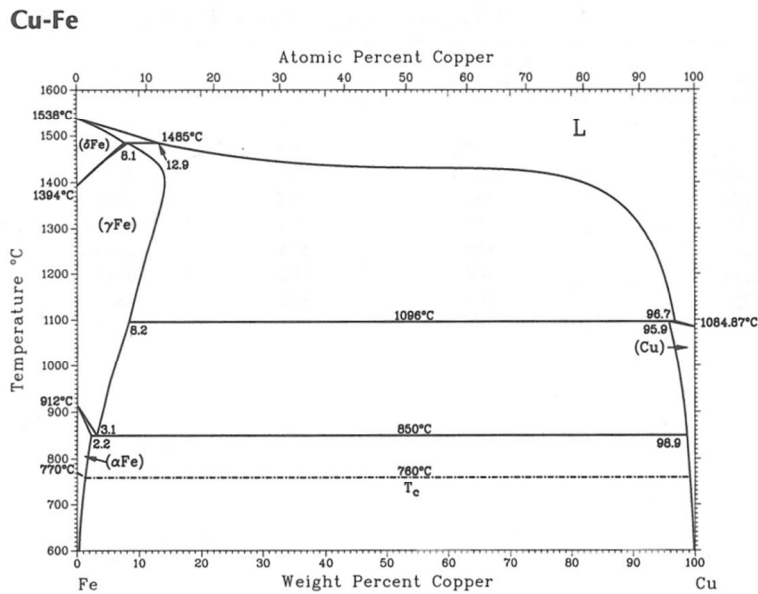


Figure 3 – Fe-Cu phase diagram (ASM - International, 1992).

The previously mentioned dissimilar metallic combinations do not show the presence of any brittle intermediate phases. Nevertheless as the thermal and physical properties of the participating metals are different, cold cracking, galvanic corrosion, and other incompatibilities can be originated in a joint created by such dissimilar systems. Table 1 shows the different physical properties between Fe and Cu.

Table 1 – Selected Fe and Cu thermal and physical properties (Gale and Totemeier, 2003).

Property	Fe	Cu
Melting point (°C)	1538.0	1084.6
Boiling point (°C)	2861.0	2562.0
Thermal conductivity (W/(m.K))	80.4	398.0
Thermal expansion (µm/(m.K) @ 25° C)	11.8	16.5

The incompatibilities between these metals are observed by (Yao et al., 2009) with their work about CO₂ laser welding between Cu and steel. In this work two different joints with higher and lower intermixing ratios were produced. The joint

with higher intermixing failed at the joint interface whilst the joint with lower intermixing ratio showed higher ductility and tensile strength with a ductile failure location present at the Cu part of the joint. The presence of intermediate phases was not detected, but the incompatibility between the two metals needed to be addressed by limiting the intermixing in the joint.

2.1.2 Type 2 – Metallurgically incompatible dissimilar metal joining

Dissimilar metal joining of Type II corresponds to joining of two metals which are metallurgically incompatible and therefore form several intermediate phases over a broad range of composition ratio. Examples of joining of Type II are Fe to Al, Fe to Ti, Al to Ti, etc. The metallurgical incompatibility between these metals can be verified by the intermediate phases present on their corresponding phase diagrams (Figure 4).

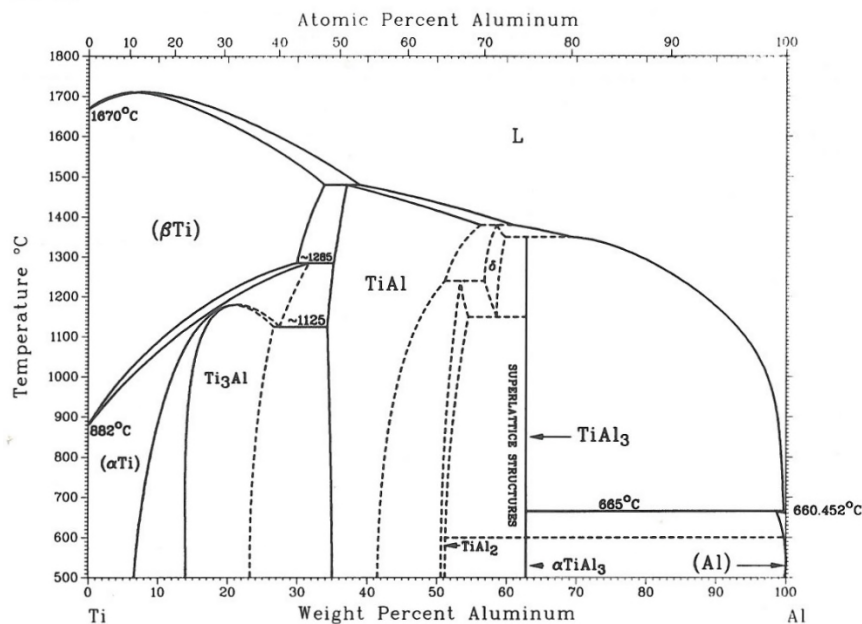


Figure 4 – Al –Ti phase diagram (ASM - International, 1992).

From Figure 4 it is possible to identify four intermediate phases at room temperature (Ti₃Al, TiAl, TiAl₂ and TiAl₃) that are formed at equilibrium conditions between Ti and Al.

The main issue with the intermediate phases formed is the brittle nature of these compounds. This brittle nature causes a reduction of the mechanical properties and enhances the crack formation within these joints. Phase diagrams are determined in equilibrium conditions, however welding processes are transient. This enables the formation of IM phases different from the phases shown in the phase diagram. Besides the intermediate or intermetallic phase formation the same dissimilar physical and thermal properties identified for type 1 dissimilar joining are also applied to this type of dissimilar joining.

2.1.3 Type 3 – Dissimilar material joining

This type of dissimilar welding does not restrict itself to metallic systems, and so welding and brazing techniques are less applicable. This type of joining is necessary when trying to join dissimilar materials, e.g. composite material to a metal (carbon fibre reinforced polymer to Ti), glass to metal, plastics to metal, etc.

(Tamrin et al., 2013) have a review paper on laser welding for dissimilar materials where different lasers and joining techniques are evaluated. The main conclusions of this work are that the optimum experimental parameters cannot be transferred or adapted from a material to another, and so the predictability of the results is the main issue when joining dissimilar materials. There is also a lack of understanding of the problem with the selection of the best joining parameters based on the ultimate tensile strength without a deeper investigation of other fundamental tests as fatigue life and corrosion. There is also lack of results studying the minimum bond area to have a successful joint.

To avoid the extreme dissimilarities presented in this type of joining, fusion welding processes are usually avoided and mechanical joining with rivets and bolts has been used, but the added weight can be disadvantage.

Glues were also used, but there are also limitations in their applicability for higher working temperatures. Weaving techniques have also been tested by (Möller et al., 2010), and Ultrasonic joining by (Wagner et al., 2013) to join

carbon fibre reinforced polymer to Al. Inductive spot welding was also studied (Mitschang et al., 2013) to join carbon fibre reinforced polymers to several metals. These studies resulted in strengths comparable to those of adhesive bonding.

2.2 Type 2 dissimilar welding challenge (Intermediate phases or intermetallic compounds)

The main focus of this work was the study and understanding of type 2 dissimilar joining. The dissimilar metallic combinations studied in this project were steel to aluminium and stainless steel to titanium.

As referred previously, the main challenges of Type 2 dissimilar welding are the intermediate phase formation or intermetallic compounds (IMC) and the dissimilar thermal and physical properties of these metals. IMC phases are defined by (Linnert, 1995) as phases that can form in solid alloys which can have structures that are crystallographically different from the matrix of the solvent metal. These phases can be bounded by electron sharing or by covalent bonding. The IM compounds have completely different properties from the parent metals that originated them, being usually brittle and poor conductors of electricity.

Intermetallics can be of invariant composition and are described as stoichiometric phases or intermetallic compounds. On the contrary if they are solid phases with a variable composition they are described as non-stoichiometric compounds or intermetallic phases. Figure 5 shows the Al-Ni phase diagram where Al_3Ni is a stoichiometric compound or intermetallic compound and Al_3Ni_2 is a non-stoichiometric compound or intermetallic phase.

Al-Ni

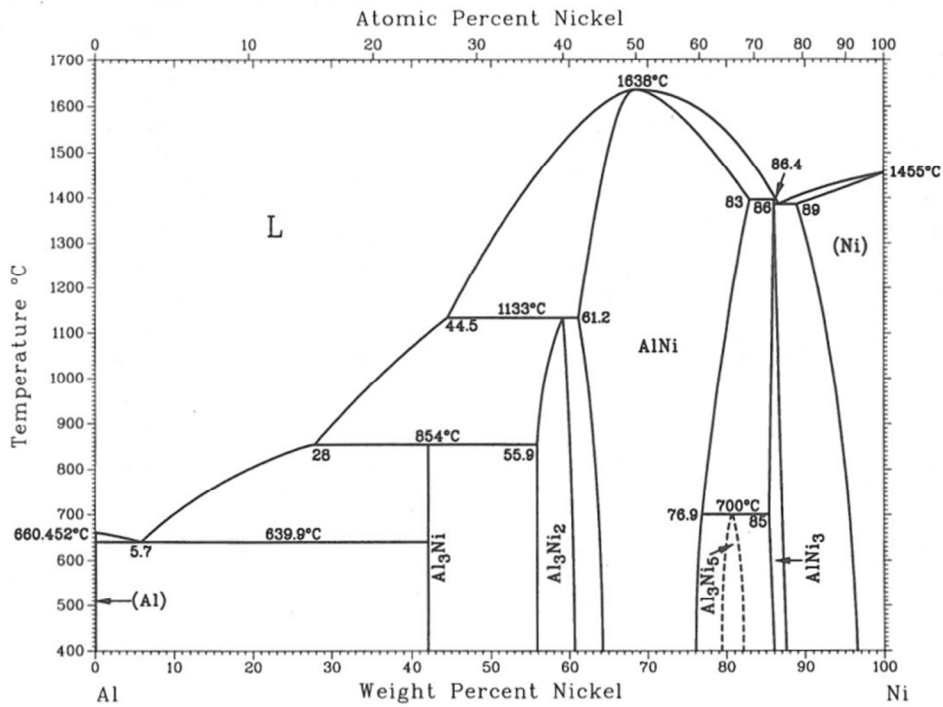
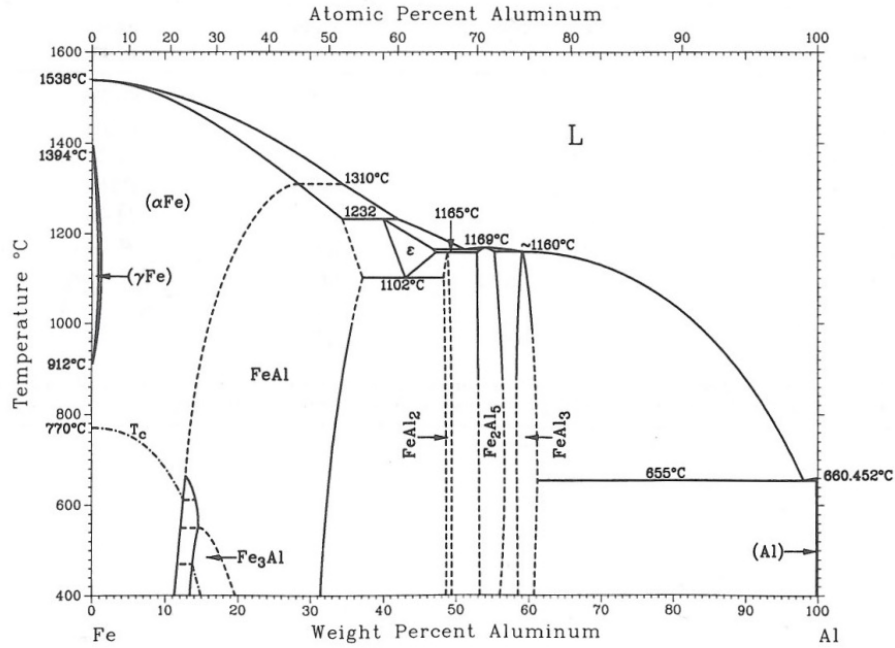


Figure 5 – Al-Ni phase diagram (ASM - International, 1992).

In this review of dissimilar metallic systems from this point on there will be no distinction between intermetallic phases and intermetallic compounds and they will be designated as intermetallic compounds (IMC).

The chemical and physical properties of an IMC are dependent on temperature, pressure, electronegativity, atomic radii and electron configurations. The phase diagrams for the selected metal combinations (Fe-Al and Fe-Ti) are shown in Figure 6.

Al-Fe



Fe-Ti

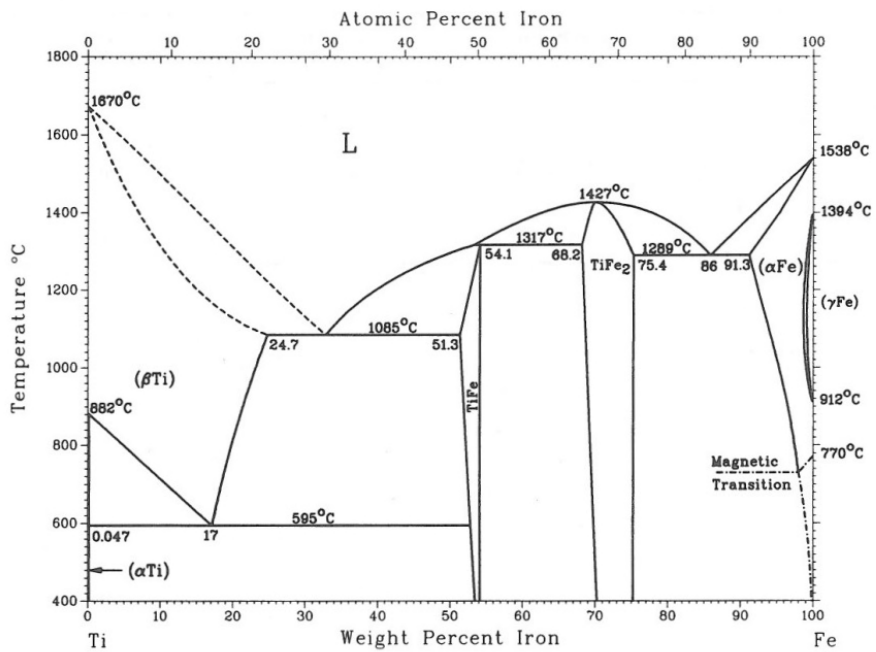


Figure 6 – Al-Fe and Fe-Ti phase diagrams (ASM - International, 1992).

In equilibrium conditions and at room temperature, there are five different Fe-Al IMC compounds whilst only 2 IM compounds for the Fe-Ti combination. The

hardnesses of the previously mentioned IM compounds are presented on Table 2.

Table 2 – Fe-Al and Ti-Fe IM compounds and correspondent micro hardnesses Fe-Ti (ASM - International, 1992; Thomy and Moller, 2013; Tomashchuk et al., 2011).

IMC	Micro Hardness (HV)
Fe₃Al	250-350
FeAl	400-1050
FeAl₂	1000-1050
Fe₂Al₅	1000-1100
FeAl₃	820-980
TiFe	600
TiFe₂	>1000

With the exception of Fe₃Al that has a slightly lower micro hardness, all the remaining equilibrium IM compounds that are formed by these two metallic combination studied have a very high micro hardness and so are brittle in nature.

As mentioned before, the complexity of joining type 2 dissimilar metals is enhanced by the different thermal and physical properties e.g. melting point, thermal conductivity etc. from the participating alloys. Table 3 shows the dissimilar thermal and physical properties for Fe, Al and Ti.

Table 3 – Thermal and physical properties for Fe, Al and Ti

Property	Fe	Al	Ti
Melting point	1538.0	660.3	1668.0
Thermal conductivity (W/(m.K))	80.4	247.0	11.4
Coefficient of Thermal expansion (µm/(m.K) @ 25° C	11.8	23.1	8.6

These dissimilar physical properties will result in non-uniform thermal distributions, weld pools, crack formation under cooling due to mismatch of thermal expansion coefficients and generation of internal residual stresses.

The combination of these two characteristics (IMC formation and dissimilar thermal and physical properties) for type 2 dissimilar welding makes this a particularly challenging subject.

To avoid the poor mechanical properties and to form a robust joint, defects of type 2 dissimilar joints and in particular Al-Fe and Fe-Ti dissimilar combinations, it is necessary to understand the IMC formation and avoid their growth and propagation.

2.3 Strategies to mitigate the IMC formation

As mentioned before the IMC formation is determined by chemical (electronegativity, atomic radii, electron configuration) and physical properties (melting point, coefficient of thermal expansion, etc.) of the parent metals to be joined. Therefore two main strategies can be applied to mitigate or eliminate the IMC formation. These two strategies are based on physical control (welding/joining process parameters) or chemical control (insert different metals to change the weld pool composition) of the joining process.

As the IMC formation is diffusion dependent, by selecting and controlling the joining process energy input researchers can interact with the time and temperature cycles and decrease the IMC formation and its growth. However the same goal can be obtained by using different intermediate metals that can change, inhibit or block the formation and growth of the IM compounds, by blocking or changing the rate of diffusion. A third option combines these two approaches by using a low heat input joining process and the use of other metals to achieve the same goal of decreasing or eliminating the IMC formation.

2.3.1 Physical control - Joining process control

This strategy has been used by several researchers (Dey et al., 2009; Fazel-Najafabadi et al., 2011; Liao et al., 2010; Meshram et al., 2007; Poddar, 2009) and focuses in controlling the thermal cycle applied during the joining process (these works are going to be described in greater detail further ahead in this section). The joining thermal cycle can be divided in two areas, the overall heat (energy) flow and the reaction time imposed to the participating metals or alloys.

The first group of joining processes that can be considered on the low heat input processes are the solid state processes (friction welding, friction stir welding, explosion welding, ultrasonic welding etc.). In these welding processes the alloys being welded do not achieve the melting point and are just plasticized. In this way it is possible to decrease the reaction rate and control the IMC formation.

Friction welding can be classified as rotational or linear, in rotational friction welding one of the parts to be welded is fixed and the other is rotated. Pressure is applied and the bonding is obtained and there is the formation of flash as the two parts plasticise to create the bonding. Linear friction welding uses oscillation instead of rotation to produce the welds.

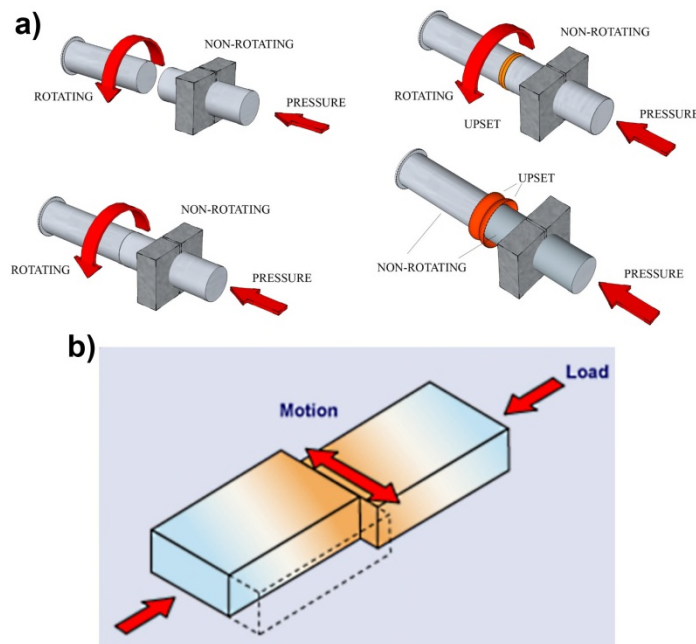


Figure 7 – Rotational friction welding a) (Forward Precision Equipment Ltd, 2011) **and linear Friction welding b)** (Threadgill, 2008).

The advantages of this joining method are the low heat input and temperatures (solid state welding) and the relatively faster welding times (seconds).

The mechanical properties of several dissimilar metal combinations using friction welding as joining process were studied by Meshram et al. 2007. During this study a low heat input process was used (rotational friction welding) and two different burn lengths of 3 mm and 5 mm were used to infer how this value interacts for several dissimilar metal combinations. Burn length is the length of the two bars lost during the joining process and this relates to the amount of interaction between the two metallic bars. The dissimilar metal combinations used were Cu-Ti, Fe-Ti, Fe-Cu, Cu-Ni, Fe-Ni and they can be related with the dissimilar joining types defined in section 2. From type 1 dissimilar welding are

Fe-Cu, Cu-Ni without IMC formation, and type 2 Fe-Ni with one (FeNi_3) IMC, Cu-Ti with (CuTi_2 , CuTi , Cu_4Ti_3 , Cu_3Ti_2 and βTiCu_4), Fe-Ti with (FeTi and Fe_2Ti) IMC phases at room temperature and in equilibrium conditions. The soluble Type 1 and Type 2 (Cu-Ni and Fe-Ni) dissimilar metal combinations were favoured for the longer interaction time due to a better homogeneity of the joint, but the fracture location for the Cu-Ni combination was located on the Cu adjacent to the interface, whilst it is outside the weld for the Fe-Ni system. For the type II dissimilar welds with major IMC formation and no solubility, the increase in interaction time reduced the mechanical properties of the joint due to the increase in the IM compounds (CuTi_3 and Fe_2Ti). Fe-Cu dissimilar combination also showed worsening mechanical properties with the increase in interaction time, due to the immiscibility of the metals, but not by the presence of new IMC phases.

(Dey et al., 2009) used friction welding to weld 304L stainless steel and Titanium grade 1. Two rods of Ti and stainless steel with 18 and 14 mm diameter respectively and 100 mm length were used. The stainless steel rod was made to rotate and the Ti rod was kept stationary. Each welded rod was hollowed out to have pipes with 3 mm of thickness for tensile tests, to perform bend tests strips of 8mm were cut by EDM from the previously mentioned pipes. Four tests were carried out with two different pressures (100 and 200 MPa) and burn-off lengths (1 and 2 mm). A post heat treatment was applied to each sample on vacuum chamber at a temperature of 600 °C and holding times of 0, 15 and 30 minutes with heating rate of 20 K/min and were cooled afterwards to 400 °C and purged in an argon chamber to room temperature. The sample with friction pressure of 100 MPa and 1 mm of burn-off length obtained the best results with 400 MPa of tensile strength and a fracture location on the Ti, avoiding the interfacial failure. All the samples with higher pressure and higher burn-off length resulted into higher temperature, heat input and thermal cycle inducing the IMC formation and the reduction of mechanical properties. The bent ductility tests were improved to a maximum of 5 degrees with the post weld heat treatment of 15 min.

A similar welding process used to weld dissimilar metals is friction stir welding (FSW); this process can also be classified as a solid state joining process. In this process a tool is plunged on the metals to be joined, it stirs the metal, until it plasticises and the metal flows from the advancing to the retreating side and the bonding is achieved.

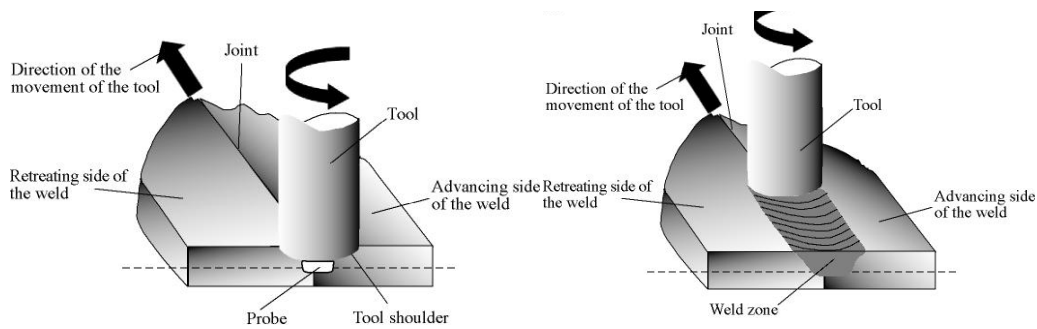


Figure 8 – Friction stir welding process (Wiki, 2014).

(Fazel-Najafabadi et al., 2011) used friction stir welding to join commercially pure Ti and 304 stainless steel alloy. In this research 50 x 100 x 4 mm thick plates were used with a 10 mm overlap of 2 mm thickness. A double shoulder and pin tool was used (Figure 9) with the first, second shoulders and pin diameters of 16, 7 and 2.5 mm respectively.

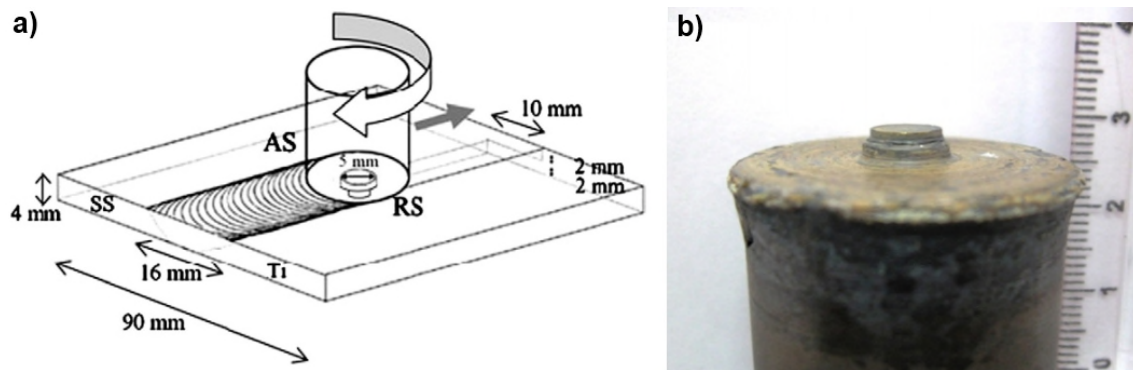


Figure 9 – Experimental setup a) and double shoulder FSW tool b) (Fazel-Najafabadi et al., 2011).

The double shoulder tool was made of H13 steel and the pin of tungsten carbide. Using the tool rotation speed of 1100 rpm and advancing speed of 50

mm/min was possible to produce an active upward flow of titanium, enabling a mechanical interlock between the two participating metals (Figure 10).

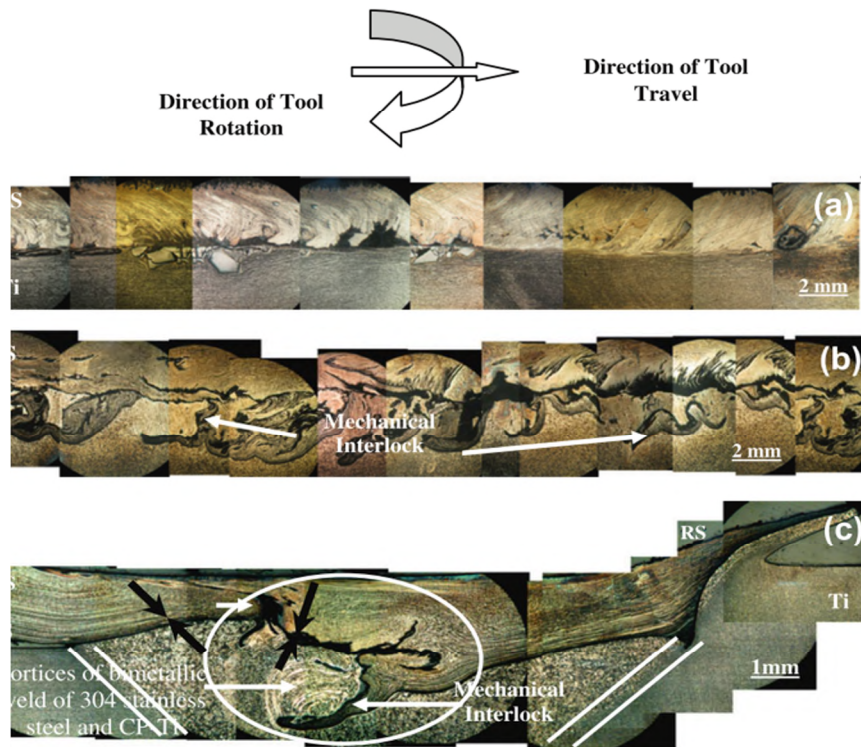


Figure 10 – Joints made using 700 rpm rotation speed a) and with 1100 rpm b) (longitudinal section) and transversal sections (c) (Fazel-Najafabadi et al., 2011).

Detailed microstructure of the welds revealed different zones, the stir zone, composed of the top 304 stainless steel and the bottom Ti vortices, the mechanical interlock features, a thin section from the stir zone and the CP Ti, the thermomechanical affected zones at the bottom the weld and the sides of the stainless steel and the heat affected zone surrounding the thermal mechanical heat affected zones. At the bottom of the stir zone, a region of bimetallic vortices was observed. This zone is separated from the CP Ti by a continuous IMC layer of FeTi (Figure 11).

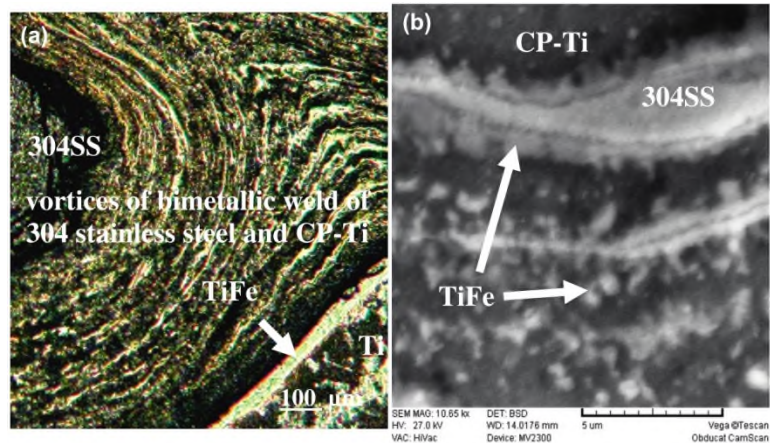


Figure 11 – Optical a) and SEM b) imaging at the bimetallic vortices region (Fazel-Najafabadi et al., 2011).

On the mechanical lap shear tests, the welds failed from the IMC layer with a flat surface for welds produced with 700 rpms and also from the TiFe IMC but with a wavy surface due to the bimetallic vortices for samples produced with 1100 rpms.

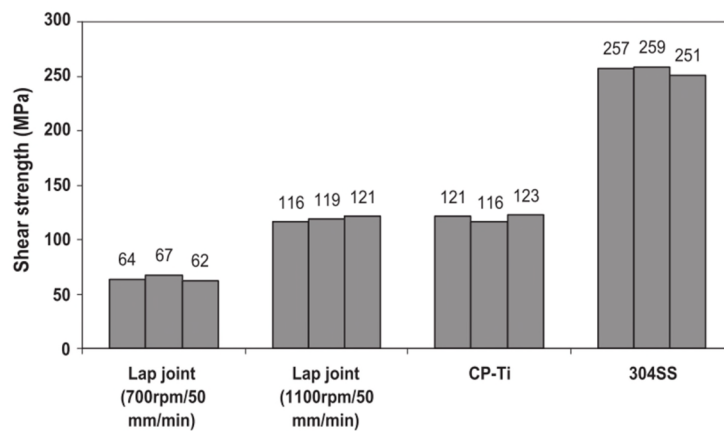


Figure 12 – Lap shear test results for the FSW welded specimens (Fazel-Najafabadi et al., 2011).

(Liao et al., 2010) also used FSW to join Ti and Fe, the approach taken was slightly different using the Ti as the upper plate of the lap joint. The dimension for the Ti plate was 300x100x2 mm and the dimensions for the steel plate were 300x100x6 mm. For the FSW process a WC-Co tool was fabricated with a concave shoulder with 15 mm diameter, a cylinder pin of 2 mm in length and 6

mm in diameter. The tool rotation speed was kept at 300 rpm and the advancing speed was 75 mm/min. After metallurgical analysis the mixing of Ti and steel at the interface is apparent (macro intermixing zones). With a closer TEM analysis scattered FeTi and Fe₂Ti were found on the micro intermixing zones and away from them. In the micro intermixing zones FeTi and βTi were found. These findings point to an interface temperature of at least 595 °C during welding, due to the lower temperature present on the Fe-Ti phase diagram for this phase formation being 595 °C. The tensile shear tests showed a shear strength value higher than 178 MPa, high ductility and plasticity with the failure located at the Ti base plate (Figure 13).

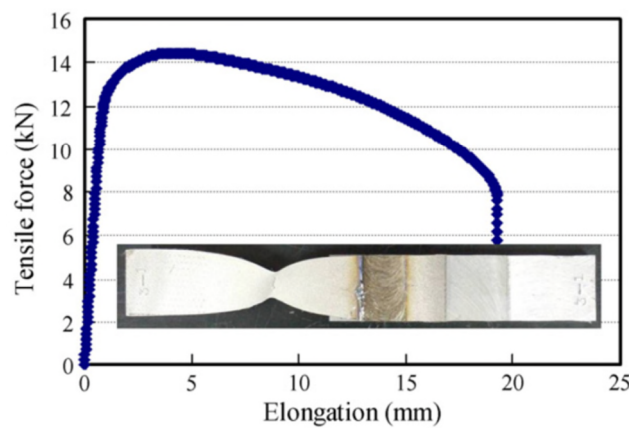


Figure 13 – Tensile shear test result for the Fe-Ti FSW specimen (Liao et al., 2010).

Using friction and friction stir welding and controlling the diffusion and heat input between the participating alloys it was not possible to avoid the IMC formation. Due to the inherent high hardness of these IMC's the failure of the specimens is located in these places.

An important review paper worth mentioning about FSW on dissimilar metal joining is (Murr, 2010) where 25 different dissimilar metallic systems were joined using this welding technique.

Another low heat input joining process was used with some success was direct diffusion bonding. In this joining process pressure and temperature are applied

to a specimen for a long period of time. The temperature is lower than the melting point of the two parent materials, achieving a controlled diffusion at the joint interface and so reducing and controlling the IMC formation.



Figure 14 – Diffusion bonding chamber (Vacuum Furnace Engineering Limited, 2011).

The main disadvantages of diffusion bonding are the use of chambers (Figure 14) that can limit the size of the components to be joined and the necessity of using expensive and complicated tooling when the components have non-uniform shapes. The time necessary to achieve a successful bonding is another drawback for this joining process.

(Poddar, 2009) used diffusion bonding to join commercially pure Ti and precipitation hardening stainless steel. The goal of this work was to verify the IMC formation and growth with the temperature used for the diffusion bonding and the mechanical properties of the joint. Each material was machined to obtain 15 mm diameter rods of 30 mm length. A 3.5 MPa pressure was applied for diffusion bonding experiments at temperatures of 800, 850, 900, 950 and 1000 °C. The temperatures were applied for a period of one hour and at a vacuum of 4 to 6 x10⁻³ Pa. The heating rate selected was 0.24 °C/h and a cooling rate of 0.1 °C/h. The interface of the diffusion bonds was defect free and no discontinuities were formed. During metallographic examination IMC layers were identified, these IMC layers were present for all the range of temperatures applied. Figure 15 shows the identified reaction layers and the size of each against the temperatures used.

Bonding temperature (°C)	Width of the reaction products in the diffusion zone (μm)				
800	$\lambda + \text{FeTi} \sim 1.3$				$\beta\text{-Ti} \sim 15.3$
850	$\lambda + \text{FeTi} \sim 1.9$				$\beta\text{-Ti} \sim 17.2$
900	$\lambda + \alpha\text{-Fe} \sim 7.4$	$\lambda + \chi \sim 1.1$	$\lambda + \text{FeTi} \sim 1.6$	-	$\beta\text{-Ti} \sim 40.5$
950	$\lambda + \alpha\text{-Fe} \sim 15.1$	$\lambda + \chi \sim 1.2$	$\lambda + \text{FeTi} \sim 1.4$	$\text{FeTi} + \beta\text{-Ti} \sim 1.1$	$\beta\text{-Ti} \sim 61.1$
1000	$\lambda + \alpha\text{-Fe} \sim 40.1$	$\lambda + \chi \sim 2.1$	$\lambda + \text{FeTi} \sim 2.2$	$\text{FeTi} + \beta\text{-Ti} \sim 2.3$	$\beta\text{-Ti} \sim 118.3$

Figure 15 - Width of the IM compounds formed in the reaction zone (Poddar, 2009).

With the increase on processing temperature the nature and thickness of the IMC formed varied, with an increase of IMC formed as the temperature increases. As this is a diffusion controlled process as the temperature increases, the energy and the diffusion is enhanced and so the mixing of the parent materials is enhanced. With the enhancement of the mixing ratios the amount of IM compounds formed also increases.

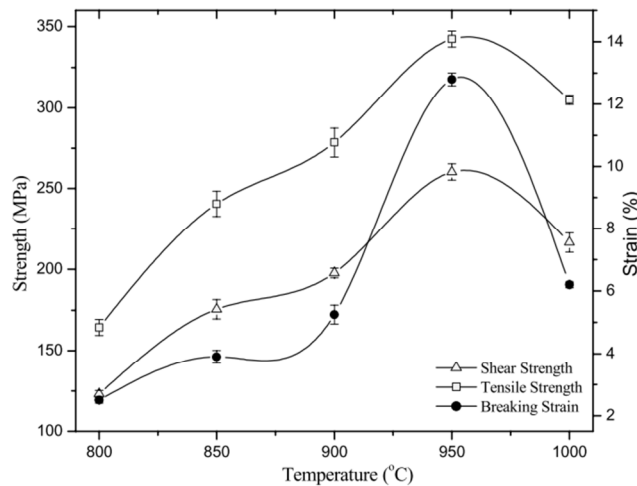


Figure 16 – Shear strength, tensile strength and breaking strength evolution with applied temperature of the joints made between stainless steel and Ti (Poddar, 2009).

The mechanical properties described by the plot in Figure 16 are in agreement with the IMC growth path shown in Figure 15.

The IMC thickness increases with the temperature, however the mechanical properties also increase until it reaches a maximum at 950 °C. At lower

temperatures, the joint is still benefiting from an increase in the atomic diffusion to increase the mechanical properties, whilst the increase in IMC thickness is still insignificant. However for temperatures higher than 950 °C the IMC thickness is the dominant factor, initiating a downward trend in the tensile properties of the weld.

A final low heat input joining process was studied by (Kahraman et al., 2005) explosion welding where the interaction time is very low. This reduces the diffusion between the parent metals. In this work (Kahraman et al., 2005) shows that it is possible to join Ti to stainless steel and the mechanical properties of the joint were higher than each of the parent metals. A bended sample with 180 degrees of bending angle was possible to obtain and no IMC were detected at the interface.

2.3.2 Metallurgical control (weld metal engineering)

A second approach to type II dissimilar metal welding is changing the melt pool composition to influence or to block diffusion to control IMC formation.

By shifting the weld pool composition away from the two elements that are metallurgically incompatible, the IMC formation can be prevented. This different composition translates in different IMC phases formed (softer) or in the complete elimination of the IMC. The shifting of the weld pool composition is usually achieved either by changing the welding wire composition (where applicable) or by introducing interlayers.

One example of that translates to a hybrid approach using different welding wires to change the weld pool composition and consequently the IMC formation is presented by (Dong et al., 2012) in dissimilar joining of Al to galvanized steel using Al-Si, Al-Cu, Al-Si-Cu and Zn-Al welding wires. Overlap GTAW joints were produced using the same welding parameters for every wire. The joints were made by melting the welding wires and the top Al plate at the Al-steel interface and so wetting the steel, without promoting its melting and reducing the reaction. For these joining conditions the Al-Si wires (5% wt and 12% wt Si)

presented the best tensile strength with 134 and 136 MPa respectively whilst the Zn based welding wire presented the worst results with 63 MPa (despite its lower melting point). The intermediate phases present at the wire-steel interface were also different, with a continuous 2 μm layer composed of 64% Al, 18% Fe, and 17% Si (at %) with the Al12Si wire and a 10 μm Zn rich discontinuous layer with a composition of 69 %Al, 22% Fe, 4%Zn and 4%O (at %) for the Zn15Al welding wire.

A similar work using filler wires to improve the mechanical properties of a joint between stainless steel and Titanium to produce different IMCs was reported by (Gao et al., 2012). Fe-Ti IM compounds are common when welding Fe and Ti as shown before, but Gao et al changed the usual IMC's present in this dissimilar weld by introducing an Mg filler wire. The wire used was an AZ31B Mg alloy and the joints were made by brazing this wire between two 2 mm thick AISI 304L and Ti-6Al-4V plates with a 0.4 mm gap. The heat to melt the wire was provided by a 7kW laser focused on the top of the plates, the laser power was varied between 1.6 and 3.5 kW. Figure 17 shows the joint morphology for this type of brazed joint.

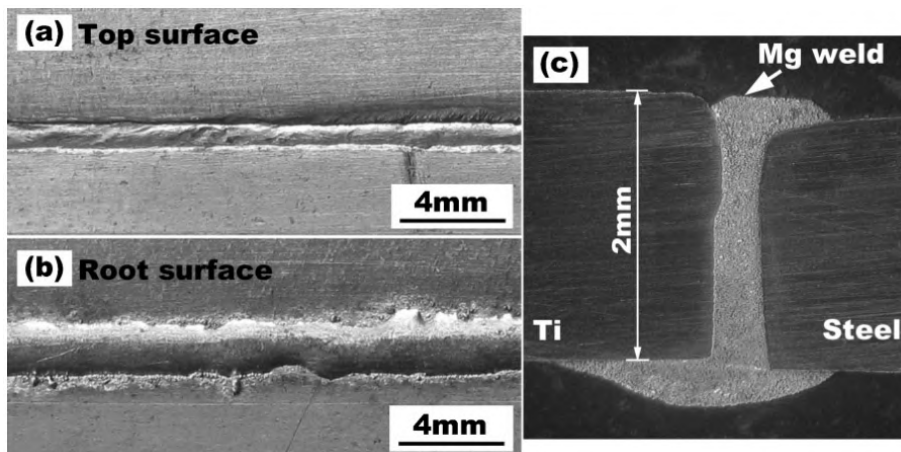


Figure 17 – Bead morphology, top surface a), root surface b) and cross section c).

Whilst intermediate phases are present at the Ti weld interface no intermediate phases seem to be present on the stainless steel weld interface. The IMC's

detected were also different from the Fe-Ti IMC's, as they were mainly composed of Al and Mg with the stoichiometry of $Mg_{17}Al_{12}$. The IMC formation at the Ti interface can be explained due to the lower thermal conductivity of Ti and consequently higher interaction times at high temperature and higher diffusion rates, in addition the presence of higher levels of Al present on the Ti alloy. A maximum tensile strength of 221 MPa was achieved.

Weld metal engineering can also be achieved by using interlayers with different thicknesses, depending on the welding process to be used and the amount of participation of these elements on the weld pool composition. Thicker interlayers can be used not only to change the weld pool composition, but also to create a barrier to prevent the migration of the parent metal atoms.

(Wang et al., 2010) used electron beam welding and a 1 mm thick Cu interlayer to make crack free welds between stainless steel and Ti. As the electron beam is a very narrow beam it was necessary to perform a dual pass weld, being the first 0.3 mm away from the Ti and inside the Cu layer and the second on the interface between the Cu and the stainless steel. The weld bead morphology is shown in Figure 18 and the melting of the parent metal is evident.

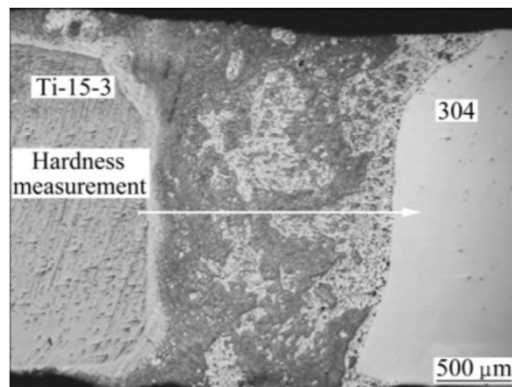


Figure 18 – Ti to stainless steel electron beam weld bead morphology.

Several IM compounds or phases were detected on the weld bead with particular incidence on the Ti and stainless steel interfaces. IM compounds present on weld centre were a solid solution between Cu and $TiFe_2$ that improve the relative softness attributed to the Cu solid solution. The two IMC

layers close to the parent metals are responsible for the low joint mechanical properties. The location of the mechanical tests fracture is the Cu-Ti intermetallic layer, proving that this layer is the weakest point of the weld interface. The IMC composition and joint hardness profile are presented in Figure 19.

a)

Weld near titanium alloy										Weld center		Weld near steel	
I			II				III						
A	B	C	D	E	F	G	H	I	K	M	N	O	P
Cu(ss)	Cu ₄ Ti ₃ or CuTi	Fe _{0.5} Cu _{0.5} Ti	TiFe	Fe _{0.5} Cu _{0.5} Ti	Cu ₄ Ti ₃ or CuTi	Cu ₂ Ti	Ti(ss)+ Ti ₂ Cu	Cu ₄ Ti ₃ or CuTi	TiFe ₂	Cu(ss)	Fe(ss)	TiFe ₂	Cu(ss)

ss—Solid solution.

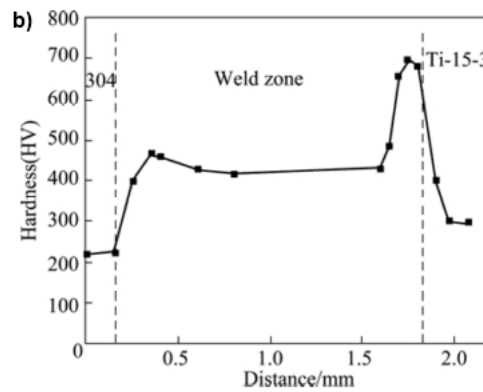


Figure 19 – Possible IMC phases present on the weld a) and correspondent weld harness profile b).

The maximum joint's strength was 224 MPa with an elongation of 3.6%.

As another example of a hybrid approach is the study by (Ashfaq et al., 2011) where rotational friction welding is applied with the use of several interlayers. The goal of this study is to join 304 stainless steel and Ti using several interlayers to avoid once again the IMC formation. This hybrid approach is a continuation of the research showed in the previous section with the same authors using solely the joining process control (Dey et al., 2009). The interlayers selected were commercially pure Ni, Ta and V these interlayers were used individually or in combinations (Ni-Ta, Ni-Va). The optimum joining parameters established in the previous work by the same authors were not

suitable for this work, indicating a different behaviour after insertion of the interlayers. Welds formed using single interlayer showed a maximum bend angle of 5° , while with the use of a double interlayer (Ta/Ni and V/Ni) the ductility of the samples increased, achieving a bend angle of approximately 40° . This difference was related to the presence of brittle Ni-Ti IM compounds on the joints made with a single Ni interlayer and the direct contact of Fe and Ti in the joints made with Ta and V. In contrast the joints produced with the double layers, the introduction of V and Ta avoided the formation of Fe-Ti IMC's and also the direct contact between Ti and Fe. These results demonstrate that by controlling the joint metallurgy, higher mechanical properties can be achieved for the Fe-Ti dissimilar joint.

2.4 Dissimilar metallic combinations studied

The goal of this work is to understand the underpinning mechanism as to how the following dissimilar alloying combinations could be joined:

- Steel to aluminium spot joining for the automotive industry
- Stainless steel to Ti for the energy generation industry.

In the next two sections a review focused on the most recent studies and knowledge acquired for these dissimilar metallic combinations is made.

2.4.1 Fe-Al dissimilar joining

The driving force to join Fe to Al for the automotive industry is the reduction in the mass of new vehicles and subsequently the CO₂ emissions. Therefore, in recent years a lot of research focus has been given towards welding steel to aluminium for application by the automotive industry.

This particular dissimilar combination can be classified as a type II dissimilar welding (metallurgically incompatible dissimilar metal joining). This incompatibility is clearly illustrated by the Al-Fe phase diagram (Figure 20) the IMC phases present and the previously mentioned dissimilar thermal and physical properties (Table 3).

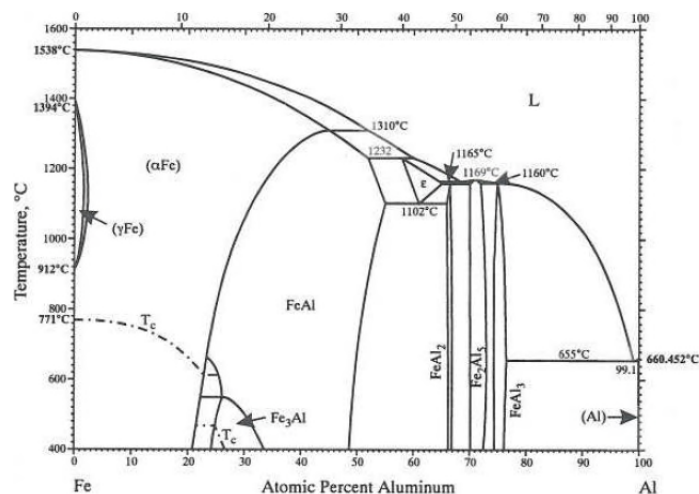


Figure 20 – Fe-Al phase diagram (Okamoto, 2010).

Al and Fe are metallurgically incompatible in equilibrium conditions while Al has some solubility in Fe (12 %at), Fe has virtually no solid solubility on aluminium. This translates in the possible formation of several intermetallic (IMC) phases (FeAl_2 , Fe_2Al_5 and FeAl_3) during welding. Welding is not an equilibrium process due to the rapid heating and cooling cycle, however the phase diagram can be used as a guideline for the stoichiometry of IMC that are formed between these two metallic materials. To better understand the nature of the IMC phases present in this dissimilar joint combination the studies by (Agudo et al., 2007; Bouche et al., 1998) are fundamental. The study from Bouche et al. consisted of immersion tests between a solid steel bar in a liquid aluminium bath with immersion times between 30 s and 30 min. The aluminium bath was maintained between the temperatures of 700 and 900 °C. During these experiments a two phase IMC layer was formed between the Fe and Al (Figure 21).

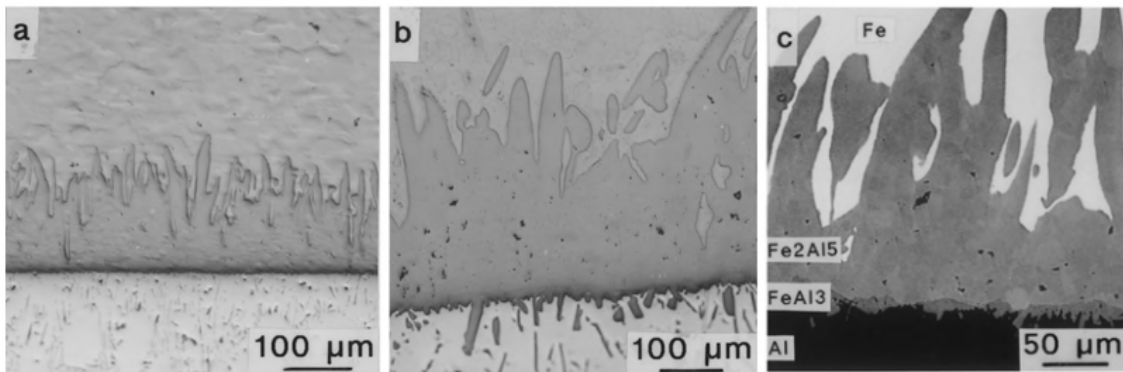


Figure 21 – Optical micrograph of IMC layer between Fe and molten Al at 800 °C with immersion time of 30 s a) and 30 min b). SEM of the IMC layer identifying the Fe_2Al_5 and FeAl_3 phases (15 min immersion time) c).

The two phases were identified as the Al rich phases present in the equilibrium phase diagram Fe_2Al_5 and FeAl_3 . It is also shown that the growth of these phases is controlled by the diffusion between the two metals. The absence of the other phases present at the equilibrium conditions is justified due to their very low growth rates. These results show that even in non-equilibrium conditions, the phases present in the IMC layer are in good agreement with the phase diagram. However welding and joining conditions have even lower

interaction times. This question was studied by Agudo et al. when they investigated the IMC formation in the steel-Al alloy fusion welds. In this study CMT (Cold metal transfer) was used to join Al and galvanized steel using a 99.8 Al welding wire. The IMC's were characterized by TEM (transmission electron microscopy). Results from TEM analysis agree with the work by Agudo et al. with an IMC layer composed by Al rich IMC's. The IMC layer present had 2.3 μm thickness and was composed of trapezoidal nearly equiaxial grains of Fe_2Al_5 and elliptical grains FeAl_3 . These results indicate once again that the Al rich phases present in the Fe-Al phase diagram are in good agreement with the IMC layer developed during welding.

To control the IMC formation researchers have been using the previously mentioned strategies for IMC control:

- 2.3.1 - Joining process control
- 2.3.2 - Weld metal engineering

For the Joining process control, several studies were made with solid state welding (explosion welding, magnetic pressure welding, friction welding and spot welding).

Magnetic pressure welding is similar to explosion welding, but the force that enables the flyer plate to contact the parent plate is an electromagnetic force instead of an explosive force. In this welding process the flyer plate has a strong acceleration against the parent plate with collision speeds between 300 and 400 m/s. This reduces the contact time between the two plates and thus the welding and diffusion time between the two metals, avoiding the IMC formation. Due to the low interaction time, (Lee et al., 2007) used this joining process in a lap joint configuration, and verified the similar wave patterns present on explosion welding with a continuous IMC layer on interface between the low carbon steel and A6111 Al alloy. This layer had higher hardness than the two parent metal and is composed of fine Al crystals grains and Al-Fe IMC's. Despite the IMC formation, the failure of the welded specimens was located at the steel metal

and not at the interface. This can be related with the relative small dimension of this IMC layer.

Friction stir welding is another solid state process that was researched to obtain reliable Fe-Al joints. (Tanaka et al., 2009) researched the possibility of direct joining between mild steel and A7075-T6 Al alloy using FSW. These welds were made in butt configuration with a tool with shoulder diameter of 12 mm, probe diameter 4 mm and probe length of 2.9mm. Each plate was 3 mm thick and the tool was setup to rotate between 400 to 1200 rpm and with an advancing speed of 100 mm/min. The presence of IM compounds was detected at the interface with a maximum thickness of 0.34 μm . The maximum strength of the samples was 333 MPa and the sample fracture location was at the interface. These results demonstrate that even for lower process temperatures than the melting point and for low interaction times between these two metals it is not possible to prevent the IMC formation and consequently the loss of joint integrity.

Weld metal engineering can also be used to prevent the IMC formation by changing the weld pool composition. This process was used by (Jácome et al., 2009; Murakami et al., 2003) where Si wires were used to change the melt pool composition and reduce the IMC formation. Murakami et al. used overlap welding of Al (A1050) to Fe 2 mm thick and used DC (direct current) pulsed GMAW (Gas metal arc welding) brazing with Al-12.0%Si fluxed cored wire. The main parameters varied in this work were the torch positioning, the welding speed whilst the wire feed speed was kept constant at 4 m/min. The best results were achieved when the failure location is in the Al heat affected zone (HAZ), where no cracks were visible at the joint. The best result was obtained with an IMC thickness of 2.5 μm and the ultimate tensile strength was of 80 MPa, when the IMC thickness increases from 2.5 μm , the fracture location is verified at the joint interface. Jácome et al. used a particular butt welding configuration with a voestalpine welding geometry. This geometry consists in using a wedged steel plate against a straight Al plate and brazing the aluminium alloyed wire at the joint interface (Figure 22). This joint configuration increases the contact area between the steel and Al filler wires.

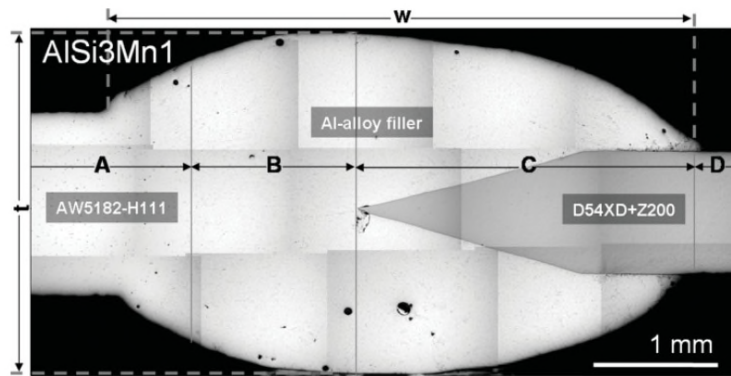


Figure 22 – Cross sectional macro section for a voestalpine brazed joint.

Four different welding wires with different Si content were used, Al 99.5, AlSi5, AlMn1 and AlSi3Mn1. The IMC layer formation could not be avoided, but the use of AlSi5 wire could limit it to around 2.0 μm . This IMC layer was composed of θ -AlFeSi, η -AlFe₂, α_c -AlFeSi. The best result was obtained by the AlSi3Mn1 wire with 304 MPa and an elongation of 21% with an IML with 2.2 μm .

Other metals and metallic alloy have been tested to vary the weld pool composition and the consequent IMC formation. (Mathieu et al., 2007) used a zinc based filler wire to weld aluminium and steel. He used laser to melt the filler wire and wet the steel-aluminium interface on a partial overlap configuration. This particular filler wire was selected due to its low melting point and compatibility towards Al. This process was characterized as a welding-brazing process due to the brazing of the steel by the Zn based filler wire and the welding between the Zn based wire and the Al plate. The failure causes for the joint were not only attributed to the IMC phases formed (especially for samples with IMC layers lower than 10 μm), but also on the bead shape and geometry (concavity, wetting, etc.).

Other techniques used to alter the weld pool composition are to coat one of the parent metals or the use of interlayers. These interlayers and coatings are usually thin, μm scale for the coatings and from μm to mm scale for the interlayers and are placed at the joint interface, where the melt pool is formed. This approach was used by (Sasabe et al., 2009) when he used advanced hot-dip aluminized steel sheet that consists of low carbon steel with a Al-Si coated

layer. Between the Al-Si layer and the Fe a 2 μm IMC layer of $\text{Fe}_2\text{Al}_8\text{Si}$ was formed. The brazing wire used was Al-2.7Mg. The failure location for this weld was in the Al heat affected zone as opposed to the interface for non-aluminized steel. This was related to the lower levels of IMC formation, particularly to two zones without IMC formation.

Fe-Al welding or brazing is a Type II dissimilar weld with the formation of IMC compounds and to control their formation, there is the necessity of controlling the thermal cycle of the weld, the weld pool composition or both of them simultaneously.

2.4.2 Steel to aluminium spot joining

Resistance Spot Welding (RSW) is one of the most commonly used joining processes on automotive industry, each car has 2000 to 3000 spot welds (Alu matter, 2014). The main advantages of this process are: low costs (<0.05€ per weld), rapid process (<1 s per weld), easily automated, no weld consumables and no added mass to the vehicle. With the high penetration of resistance spot welding in this market, a great effort have been given to see the application of dissimilar spot welding joints (made with different joining processes) to prevent radical changes of the processes currently in use by the automotive industry.

RSW uses the Joule's law to generate heat at the interface and produce the weld joint; this concept is very difficult to apply at Al joints. This is due to the high electrical and thermal conductivity of Al where it is necessary to apply high current levels to have a reliable joint. To overcome this problem (Qiu et al., 2009) used a steel cover plate to generate the heat at the Al plate. Overlap welds between Al5052 and cold rolled steel with a cold rolled steel cover plate were investigated. The welding time was fixed at 0.2s, with welding current varying from 6 to 12 kA and an electrode force of 1715 N. With these parameters, a maximum IMC layer of 7 μm was verified and the IMC present were Fe_2Al_5 and FeAl_3 . The IM compounds were identified as detrimental to the joint mechanical properties, with maximum resistance of 5 kN for a weld nugget of around 9 mm of diameter. (Oikawa et al., 1999) pursued a different route to

dissimilar RSW, they used insert plates instead of cover plates. These plates were a composite made using hot rolling of Al on a steel plate, effectively cladding the Al on the steel. These inserts were then welded using RSW and compared with RSW of direct steel to Al and similar steel and Al welds. The results showed that the welds made with insert metals would perform better than the conventional steel to Al welds, despite the higher IMC formation.

Due to the IMC formation and loss of integrity of the Fe-Al spot joints, other joining processes different from the classic RSW were tested. Friction stir spot welding (FSSW) was one of these processes. This process was selected once again due to its solid state welding characteristics when compared with traditional RSW. (Liyanage et al., 2009) verified the possibility of using RSW using a tool with pin to join Al6111 alloy to Zn coated low carbon steel. An overlap welding with Al on top of Fe was made by plunging the tool on the Al alloy without any relative movement to perform a spot weld. The tool was plunged through the Al plate and plunged on the Fe plate, generating a mechanical interlock between the two plates (Figure 23).

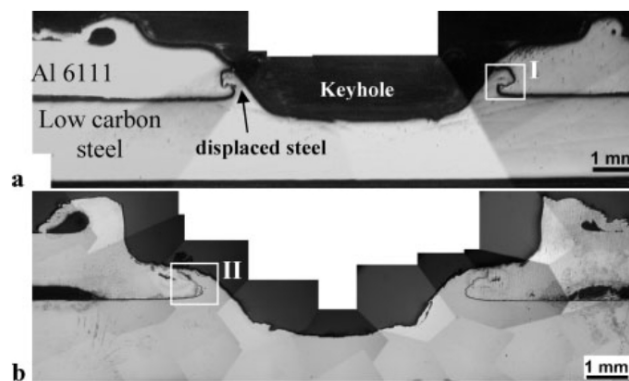


Figure 23 – Optical micrographs of the transverse section through the dissimilar Al - Fe spot weld produced using tool rotational speed of 3000 rpm and plunge rate of 1 mm/s and dwell time of 4s: Pin penetration depths into Fe of 0.4 mm a) 0.85 b).

The presence of IM compounds and the crack formation close to the mechanical interlock features was verified. The mechanical properties of the weld were similar to Al 6111 resistance spot welds, 2.0 kN for 0.4 mm

penetration on the lower plate (Al) and 3.6 kN for 0.85 mm penetration sample. The presence of cracks close to the mechanical interlock area could affect the fatigue life of the samples. (Uematsu et al., 2011) used a similar approach to perform FSSW, but the penetration of the tool was limited to the Al, relying on the heat conduction to make the joint (Figure 24 a) & b)). This tool had no probe and it had a 0.5 mm scroll groove (Figure 24 c)). The metals used were low carbon steel and A6061 – T6 Al alloy. The joining parameters were penetration on the aluminium plate 1 mm, rotational speed of 3000 rpm, holding time of 5s and plunge rate of 10 mm/min.

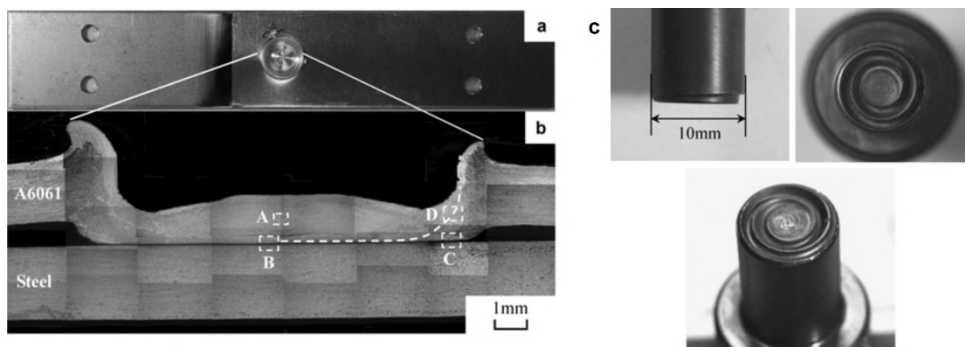


Figure 24 – Top view of dissimilar welding between Al6061 and steel a) corresponding macroscopic appearance of the cross section welded zone b) photographs showing the tool geometry c).

The results showed a non-uniform adhesion along the weld nugget, with tensile shear strength of 52 MPa averaged over the total nugget area. If the results are averaged over the effective nugget size (area of aluminium that adhered on the steel after fracture) the results increase to 151 MPa.

(Chen et al., 2012) used a slightly different approach to FSSW, by introducing abrasion circle friction stir spot welding. In this approach, instead of no movement between the tool and the plates, a circular path is implemented on the tool to increase the contact area between the plates and thereby increase the joined area without the need of increasing the tool diameter. Al 6111-T4 alloy and DC04 steel with 1mm thickness were used, the tool had a 11 mm shoulder with a scroll profile an tapered 3 mm diameter probe with 1 mm length

(Figure 25). The path translation speed was varied between 60-2000 mm/min that translated in weld times of 0.5-18 s and the rotation speed was kept at 800 rpm and plunge depth of 0.1 mm.

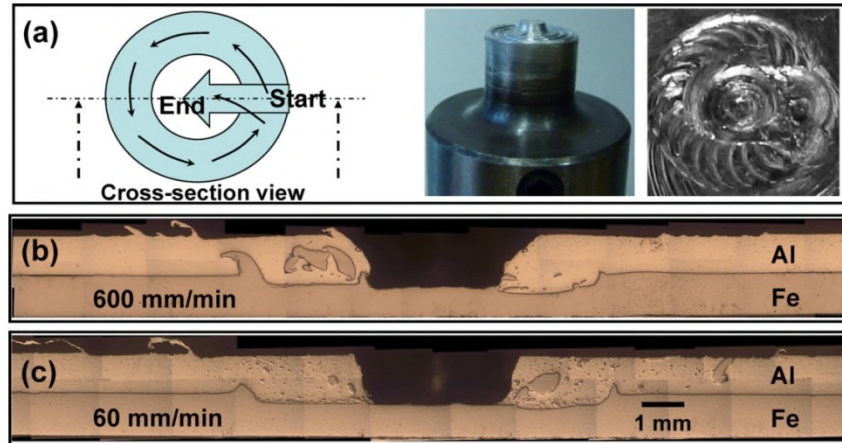


Figure 25 – Schematic diagram of the orbital translation path used and tool geometry a). Typical cross sections of welds with translation speeds of 60 b) and 600 m/min c)

The results obtained showed that samples had a higher contact area when compared with stationary probe welds; a wider processing window was also obtained with good results presented for samples with weld times of 0.5 s. No IM compounds were detected on the joint interface due to the low heat input introduced by this weld.

2.4.3 – Stainless steel to Ti dissimilar joining

The same strategies shown in the previous sections were used by the researchers for this type of dissimilar welding. Autogenous dissimilar friction welding (Dey et al., 2009), FSW (Fazel-Najafabadi et al., 2011), explosion welding (Kahraman et al., 2005) and diffusion bonding (Kundu and Chatterjee, 2008a; Poddar, 2009) were experimented for solid state welding and heat input restrictions.

Also the metallurgical control of the weld pool by wires and interlayers was extensively investigated to minimize or change the IMC formation on Fe to Ti joining. The use of a single, double or hybrid layers to minimize, block or

change the IMC formation was studied by several researchers. Several metals were researched as candidates for a single interlayer: Cu, Ni, V, Ta and even Al.

(He et al., 1999) and (Kundu and Chatterjee, 2008b) studied the joining of Ti and stainless steel using Ni as an interlayer. Both studies revealed an optimum temperature of 850 °C for the process and reported the formation of several IMC phases. (He et al., 1999) studied the possibility of joining Ti-6Al-4V to an 18Cr10Ni stainless steel web. He used a 30 µm Ni layer as interlayer and varied the bond temperature between 750 and 910 °C and the bond specific stress between 3 and 20 MPa. He reported the formation of different layers of Ti-Ni IMC on the Ti-Ni interface (TiNi₃, Ti₂Ni and TiNi) for the samples welded at higher temperatures whilst a single thick NiTi layer was formed for samples joined at lower temperatures. Similar findings are reported by (Kundu and Chatterjee, 2008b), but the Ni-Ti IM compounds changed to Fe-Ti and ternary phased IMC's for samples with higher temperatures (Table 4).

Table 4 – IMC's present at the joint interfaces for different joining temperatures
(Kundu and Chatterjee, 2008b).

Processing temperature (°C)	Width of the reaction products in the diffusion zone (µm)					
	Ti-Ni interface			Ni-SS interface		
800	Ti ₂ Ni ~ 2.9	TiNi ~ 7.9	TiNi ₃ ~ 4.7	-	-	-
850	Ti ₂ Ni ~ 5.9	TiNi ~ 14.1	TiNi ₃ ~ 6.1	-	-	-
900	-	-	-	λ+χ+α-Fe ~ 11.4	λ+FeTi ~ 1.7	λ+FeTi+β-Ti ~ 7.4
950	-	-	-	λ+χ+α-Fe ~ 15.8	λ+FeTi ~ 2.1	λ+FeTi+β-Ti ~ 8.8

This shows that at 900 °C the Ti atoms can migrate through the Ni interlayer and generate IMC's at the Ni - stainless steel interface.

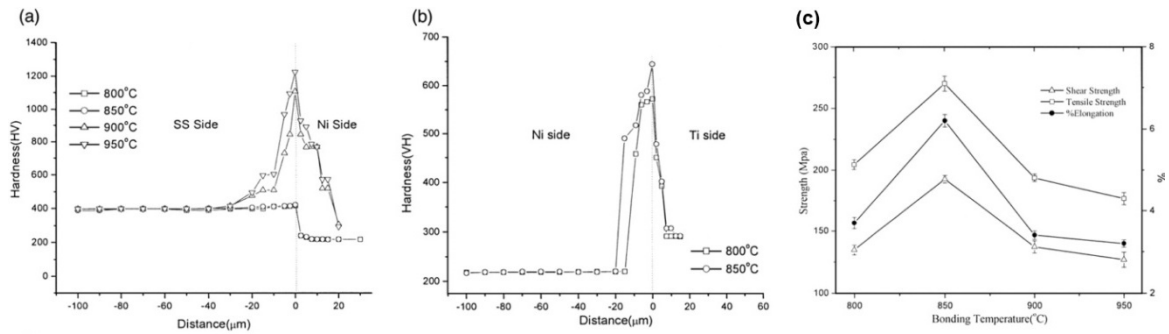


Figure 26 – Vickers hardness plot from the stainless steel Ni interface a), Ni Ti interface b) and joint mechanical properties vs joint temperature c) (Kundu and Chatterjee, 2008b).

These results show that depending of the interface thermal cycle the IM compounds formation and growth are affected (with or without the use of interlayers).

Another metal that have been researched as a candidate for interlayer to improve the Ti-Fe joint is Cu.

Solid state diffusion bonding was used by (Elrefaey and Tillmann, 2009) to join Ti and low carbon steel. An alloy composed of Cu-12Mn-2Ni with 100 μm was applied between the CP Ti and the low carbon steel. The joining conditions were 3 MPa at temperatures of 800 and 850 °C for holding times from 30 to 180 min. Sample prepared at 800 °C were not joined and broke during metallographic preparation, whilst samples prepared at 850 °C showed some resistance. Several IM compounds were detected at the joint interface, but the intermediate phases had been changed to other phases instead of the Fe-Ti IM compounds. This demonstrates that a Cu interlayer in these joining conditions is capable of avoiding the inter diffusion between Fe and Ti. Figure 27 shows that the change in the IMC phases is positive due to their lower hardness when compared with the traditional Fe-Ti IMC's (+/- 1000 HV).

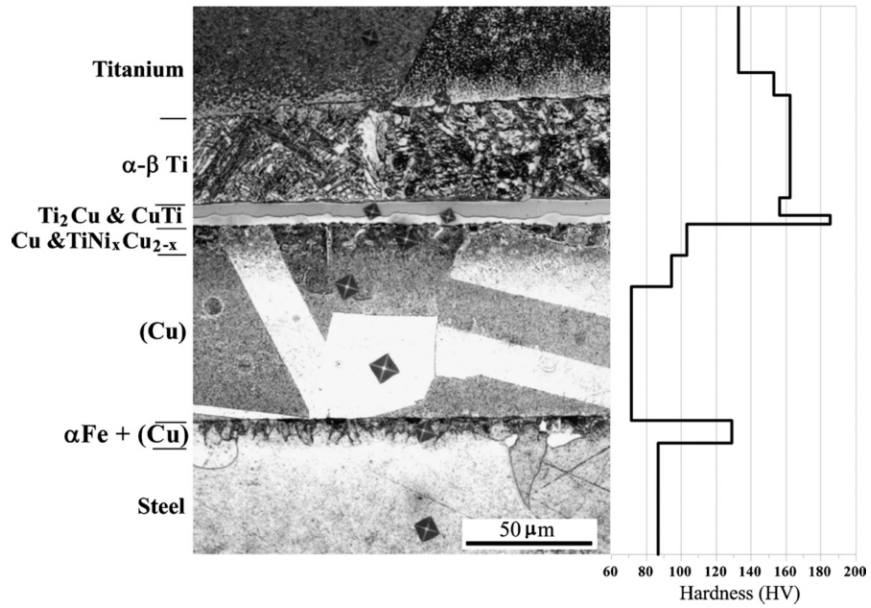
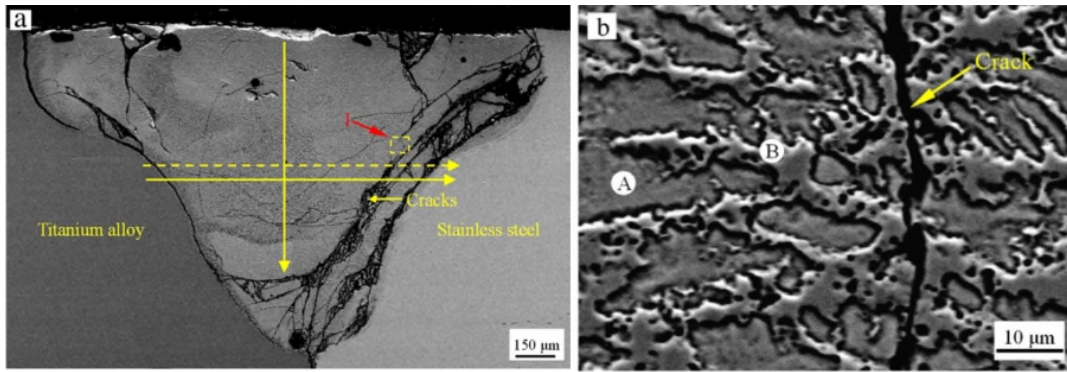


Figure 27 – Hardness distribution for the Fe-Ti joint bonded at 850 °C for 90 min
(Elrefaey and Tillmann, 2009).

This joint interface corresponds to the sample with higher mechanical properties (105.2 MPa of shear stress), but the fracture location is at the Ti-Cu IMC phases showing that the formation of more ductile and soft IMC phases, they are still the limiting factor in achieving a very high joint strength.

A direct comparison between stainless steel (18Cr9Ni) and Ti (Ti6Al2Mo2V2Zr) alloys with and without Cu interlayers was investigated by (Wang et al., 2012). The autogenous weld between stainless steel and Ti using electron beam welding showed immediate cracking during welding and it failed whilst handling the sample. Figure 28 shows the crack formation on the weld bead and also the brittle Fe-Ti IMC's formed during the weld.



C

	Ti	Al	Fe	Cr	Ni	Potential phase
A	33	4	38	20	5	TiFe ₂ +TiCr ₂
B	43	6	31	9	11	TiFe

Figure 28 – Autogenous Fe-Ti weld cross section SEM micrograph a), higher magnification of zone I b) and potential IMC phases c) (Wang et al., 2012).

On the contrary the weld performed with a Cu interlayer of 1 mm thickness had no cracks formed and the hardness profile was lower than that of the direct Fe-Ti weld sample (Figure 29).

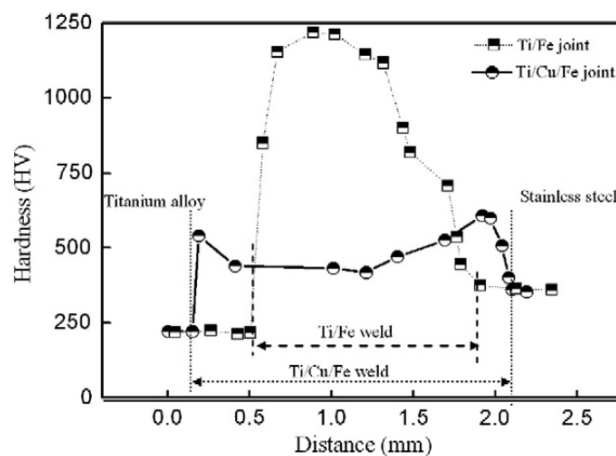


Figure 29 – Micro hardness distribution profiles for the Ti-Fe and Ti-Cu-Fe joints (Wang et al., 2012).

The maximum tensile strength obtained was 310 MPa for the joint with the Cu interlayer.

(Tomashchuk et al., 2011) also used electron beam welding with a Cu interlayer, however this study also compares this process with pulsed laser

welding to obtain a sound joint. Pure Cu interlayer with thickness of 500 μm was inserted between 2 mm thick AISI 316L and Ti-6Al-4V plates. The welds were made to have a restricted melting of Ti and so the electron and laser beams were focused on the Cu-Fe interfaces. Figure 30 shows the joint morphology for both welding processes.

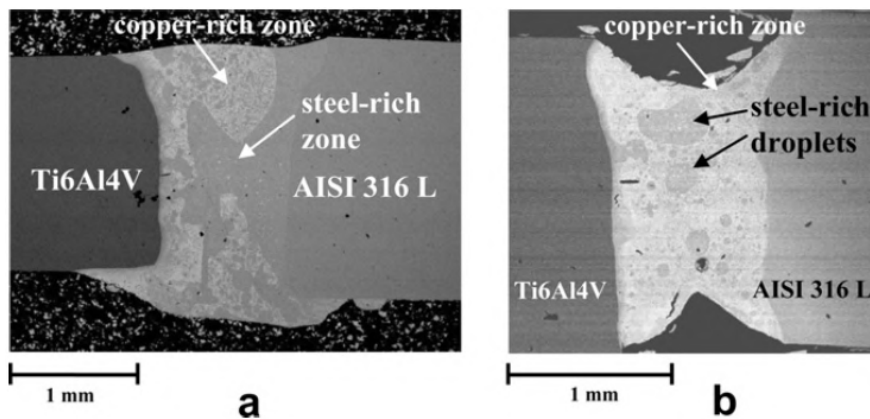


Figure 30 – Weld bead morphology, electron beam a) and pulsed laser b)

(Tomashchuk et al., 2011).

No defects were observed with either of the welding processes; however differences are detected on the bead morphology. Electron beam welding has a high cooling gradient and slow melt convection this is shown by the high inhomogeneity present at the weld, with a clear steel rich area inside Cu interlayer, whilst the dynamic nature of pulsed laser welding resulted in a more intense mixture. There is also a reduction on the formation of the brittle Fe-Ti and Fe-Cr IMC phases, but is not possible to have a complete removal of these IMC phases.

On the pursuit of defect and IMC free welds (Wang et al., 2013) introduced a different approach to the studies mentioned beforehand. In their research they introduced an interlayer based on the element metallurgical compatibility and produced a hybrid interlayer composed of two different layers. The metals selected for this hybrid interlayer were V and Cu. This hybrid layer was manufactured using two different commercially pure sheets of Cu and V of 0.7 mm thickness. Each weld was composed of 2 passes, the first pass on the Cu

layer and the second on the vanadium layer. These metals were selected due to their mutual metallurgical compatibility and their compatibility with the parent metals. Two attempts of welding the hybrid interlayer were made, the first with a lower heat input and a second with a higher heat input. The first attempt resulted on an uneven melting of the layers and the second resulted into a cracked weld. The cracks present on attempt made with higher heat input were due to several IMC phases (TiFe , TiCu_2 , etc) present on the weld bead due to high mixing of the parent metals. The weld performed with lower heat input did not present any crack formation, but had an unmelted zone on the vanadium interlayer that initiated the crack propagation on the sample mechanically tested. The sample presented a maximum tensile strength of 288 MPa.

A second approach was made by creating a different interlayer that was made out of V and Cu powders instead of V and Cu foils. This new interlayer was composed of pure vanadium layer and a second one of mixed vanadium and Cu with a density of 97% of the theoretical maximum. This second interlayer was developed to avoid the lack of fusion defects present on the previous interlayer when welded with a lower heat input. As result no lack of fusion was verified and was possible to create a crack free weld. The sample was almost IMC free with the exception of $\sigma\text{-FeV}$ IMC. The final tensile strength of the sample welded with this new hybrid layer created from the mixture of V and Cu powders was of 395 MPa.

(Lee et al., 2010) also used a metallurgical compatibility method to discover possible interlayers to use for a possible joint between stainless steel and Ti. The joining processes selected for this work was diffusion bonding due to its carefully controlled thermal cycles and its solid state joining process that decreases the interaction between the participating alloys. The first layer attempt was a V layer, but brittle IMC's of V-Fe and V-Cr-Fe were formed. The next interlayer proposed was composed of V and Cr but brittle sigma IMC phases were also discovered. The third interlayer developed was composed of Ni-Cr-V, this interlayer prevented the IMC formation with results on the

mechanical properties of the joint, Figure 31 shows the mechanical properties for the different joints made with different interlayers.

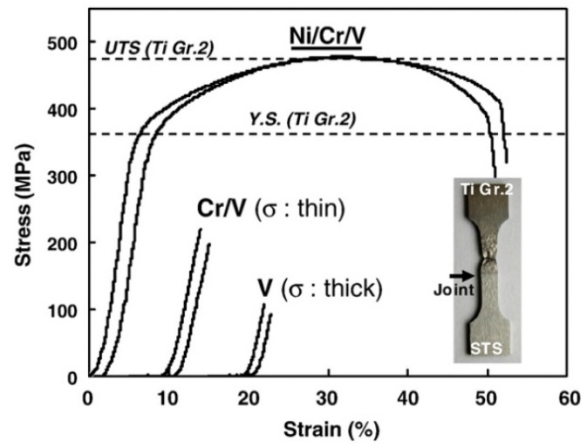


Figure 31 – Stress strain curve for samples joined between stainless steel and Ti at 900 °C for 10 min with different interlayers (V, V-Cr, V-Cr-Ni) (Lee et al., 2010) .

Figure 31 shows the presence of an elastic and plastic regime for the sample welded with three layered interlayer that is characteristic of a ductile joint.

2.5 Welding Processes

This section of the literature review serves to introduce and give an overview of the welding and joining processes used during this work.

2.5.1 Laser light

Laser is an acronym for light amplification by stimulation emission of radiation. This term was first used Gordon Gould in 1959 on a conference paper entitled “The LASER, Light Amplification by Stimulated Emission Radiation”. The first functional laser was used one year afterwards by Theodore H. Maiman at the Hughes research Laboratories on Malibu California. This was a ruby laser and was a pulsed laser on the 694nm wavelength (Buchfink, 2007). In the same year the first continuous wave laser was operated by Aly Javan, William R. Bennet and Donald Herriott and worked in the infra-red spectrum.

At the second half of the 20th century and at the beginning of the 21st century, the laser power energy and reliability increased considerably whilst its costs reduced. This increased the applicability of lasers in several industrial fields as cutting, welding heat treating etc.

The light that is produced by a laser source can be classified as monochromatic, coherent and directional. It is monochromatic due to the narrow electromagnetic spectrum of the beam; it is coherent because all the photons produced are in phase and directional due to the travel direction of the produced photons.

The basic components of a laser system are:

- Laser pumping energy
- Active medium
- Mirrors (Fully and partially reflective)
- Laser beam

All of these components are represented in Figure 32.

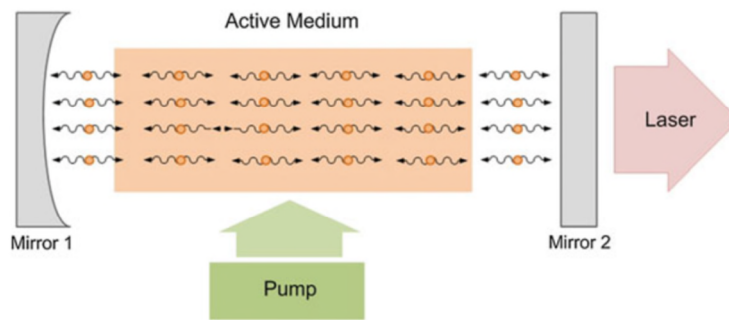


Figure 32 – Laser schematic representation (Paul et al., 2013).

The process starts with the generation of energy on the pumping system. The pumping energy can be generated either by optical, electrical or chemical energy. This energy is partially absorbed by the active medium and other part is lost by heat that needs to be extracted from the system. The energy that is absorbed by the active medium excites the electrons of the active medium atoms to achieve a population inversion. With the population inversion (more electrons on the excited level than on the unexcited level) the light emitted is not of random nature anymore and have previously referred properties of laser light (monochromatic, coherent and directional) (Figure 33).

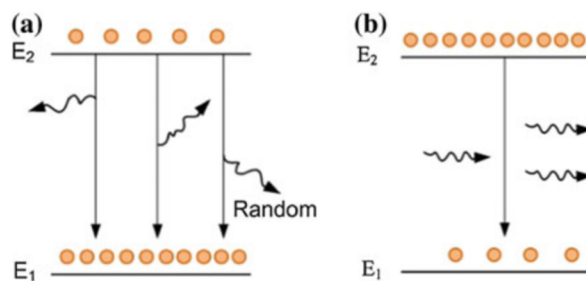


Figure 33 – a) Electron configuration for spontaneous emission. b) Electron configuration on a population inversion and with stimulated emission (Paul et al., 2013).

The active medium can be a solid, liquid or a gas, but it needs to produce a specific electromagnetic radiation wavelength when the atoms return from the excited state.

The light produced by the active medium is generated inside an optical cavity that has two different mirrors on their extremities, one is 100% reflective to the laser light whilst the other is partially reflecting mirror which is the end point of the laser light in the optical cavity. Inside the optical cavity the photons produced by the active medium excite new electrons on the active medium amplifying the light source.

The laser light can be generated in a continuous mode, continuous wave (CW laser), or as a number of finite bursts of energy or pulses (Pulsed laser).

The laser used during this work is a solid state fibre laser. In fibre lasers the laser is generated inside a laser active fibre. As fibres have a very high surface to volume ratio the cooling system is less complicated than in rods and other types of solid state laser. The mirrors can be integrated inside the fibre and all the light is enclosed inside the laser active fibre. The laser active fibre has an active core, a pump cladding and an outer cladding (Figure 34). These fibres are known as double clad quartz fibres and each zone on these fibres has a different refractive coefficient and it is lower than the index of the zone inside.

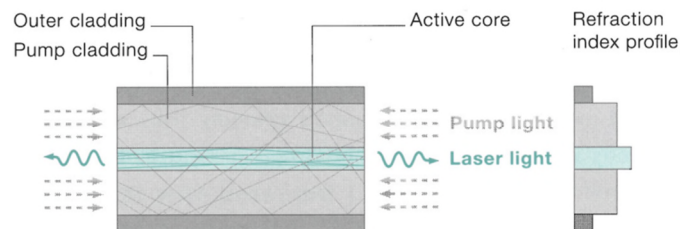


Figure 34 – Laser active fibre components and corresponding refractive index profile (Buchfink, 2007).

The light is pumped on the outer region of the cladding and excites the inner core of the fibre and the laser light is produced.

The laser light produced by fibre lasers is on the near infrared spectrum and so silica fibres can be used to deliver the beam to the focusing optics and deliver the beam to the work piece.

2.5.2 Laser welding

After the laser beam comes out of the delivery fibre, the laser light needs to be collimated, and focused. For welding and cutting and other applications it is necessary to focus or defocus the laser beam, either to increase or decrease its intensity. This is done by the means of optical lenses that will shape the laser beam.

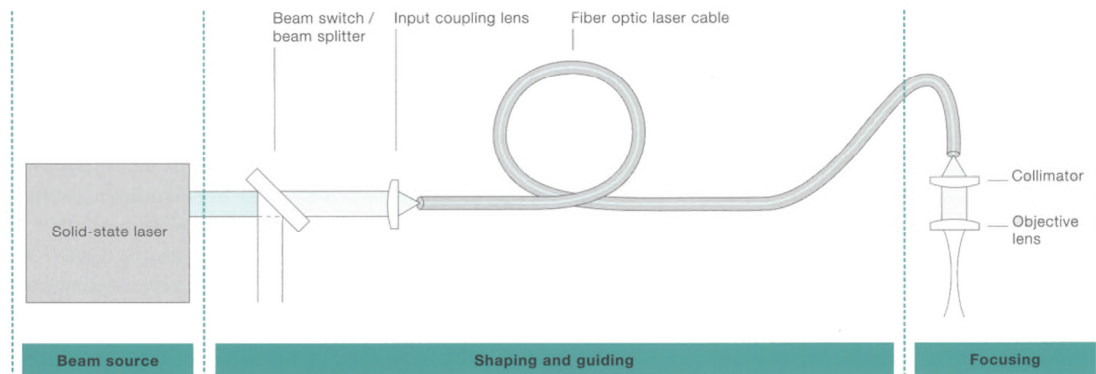


Figure 35 – Solid state laser system (Buchfink, 2007).

The laser used during this study was an IPG 8kW continuous wave laser. The way the laser interacts with the material can be described with two different perspectives:

- System parameters, these are the parameters that are available to the laser user (power, travel speed and spot diameter). These parameters dismiss the interaction between the laser and the material and how the energy is transferred to the workpiece.
- Fundamental material interaction parameters, this perspective tries to verify how the material is influenced by the laser light and takes into account the interactions between the laser and the material, by deriving meaningful physical parameters.

- **System parameters:**

The system parameters are defined by the laser system and do not take in account the interaction between the laser and material. These parameters are Laser power, spot size and welding speed. The laser power is measured in watts and it is the power measured at the exit of the laser by a power meter. The spot size is beam's diameter (for a circular beam) at a certain distance from the optics system. For the same system this value can vary by changing the focusing lens or by changing the distance between the optics and the material. This value is usually measured by a beam profiler; this equipment can give not only the beam size but also the spatial beam distribution. The travel speed is the speed at which the spot is irradiated on the work piece (moving beam).

- **Fundamental material interaction parameters:**

The fundamental material interaction parameters are derived from the system parameters; however these parameters translate how the material interacts with the laser beam. The first parameter is the power density (PD), this parameter is the power divided by the spot diameter and it averages the laser power over the area of the laser spot the units are kW/cm².

$$PD = \frac{Power}{Spot\ area} \quad (1)$$

The next parameter to be defined is the interaction time (t_i). This parameter is the time that an infinitesimally small area on the surface of the material is irradiated by the laser beam. The t_i has two different formulations for pulsed or continuous wave welding. For continuous welding it is the spot diameter divided by the travel speed or the welding speed.

$$t_i = \frac{spot\ diameter}{travel\ speed} \quad (2)$$

For the pulsed laser welding it is defined as the irradiation time, due to the stationary state of the beam and its finite duration in time. The units for either formulation of the interaction time are seconds (s).

$$t_i = \text{irradiation time} \quad (3)$$

The last parameter to be defined is the specific point energy (E_{sp}) and it is the level of energy experienced by the material and the units for expressing E_{sp} are Joules (J)

$$E_{sp} = PD \cdot t_i \cdot \text{spot diameter} \quad (4)$$

When the laser beam is irradiated at the material and interacts with it, the size or shape of the originated melt pool is dependant of several factors: material melting temperature, vapour pressure, reflectivity to the laser wavelength etc... The shape of the weld pool can be classified in three different modes and these modes can be differentiated using the fundamental material interaction parameters.

The three different modes are conduction, transition and keyhole.

The difference between conduction and key-hole is very evident on a weld profile; the key-hole weld has a very high aspect ratio while the conduction mode as a small aspect ratio. This is due to the different process conditions and fundamental material interaction parameters used during the welding phase.

The conduction mode is a process usually characterized by lower power densities and longer interaction times, this leads to defect free welds but lower penetrations and productivity. The keyhole mode uses higher power densities and lower interaction times; this process has enough energy to vaporize the metal and open a key-hole. This leads to welds with more defects as porosities, undercuts compared with conduction mode (Figure 36).

Beam Diameter = 1.18 mm and $t_i = 20$ ms

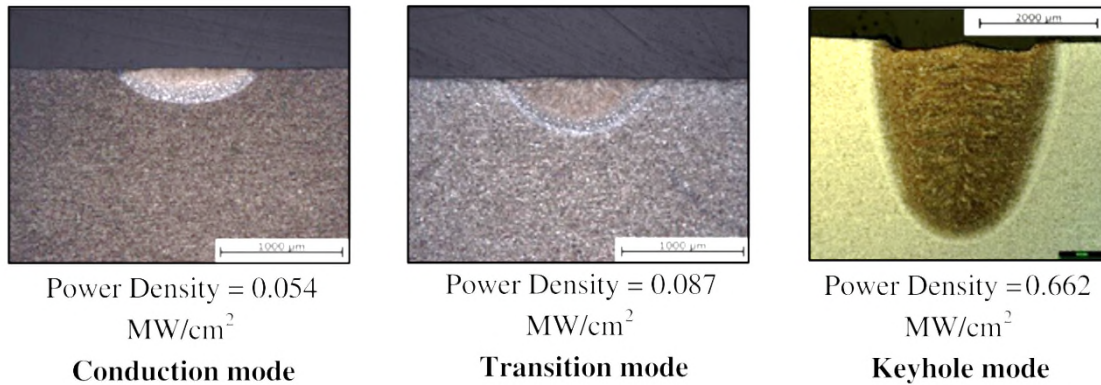


Figure 36 – Conduction, transition and keyhole modes on S355 steel plates

(Assuncao et al., 2012).

The transition mode has characteristics of both processes mentioned beforehand, it has an higher aspect ratio than welds produced in conduction mode and starts to have the defects present on key-hole mode, but the power density and the interaction time are not enough to open a key-hole.

2.5.3 Gas tungsten arc welding - GTAW

GTAW (Gas Tungsten Arc welding) was developed in the middle of the XX century, due to the low capability of the common welding processes to shield nonferrous metals as Al or Mg. With the 2nd world war there was a greater necessity for building aircraft using these lighter nonferrous alloys. Using tungsten electrodes and direct current arc power with the electrode negative, a stable, efficient heat source was produced to make excellent welds (American Welding Society, 1991). With further understanding of how the polarity had influence on the welding results a steep development of this welding process was initiated.

GTAW uses a non-consumable tungsten electrode to initiate a welding arc in a protective inert gas atmosphere (Argon, Helium). The electric arc task is to provide the heat to generate the melt pool and, when necessary, melt the added welding wire (Santos and Quintino, 1997). Consumable welding wire is fed to the welding process manually or by an automated machine, but the welding arc

is always made between the tungsten electrode and the substrate. Once the welding arc and the weld pool are stable, the torch is moved along the joint to melt and produce the weld (Figure 37).

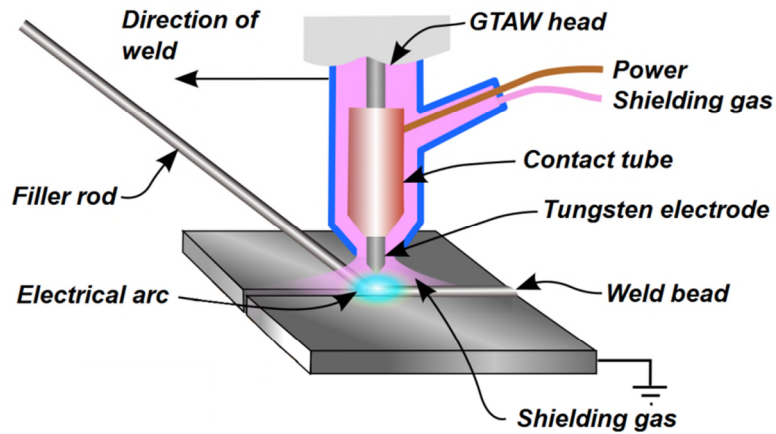


Figure 37 – GTAW welding process schematics.

On Table 5 are presented the main advantages and disadvantages of this welding process.

Table 5 – Advantages and disadvantages for GTAW process.

Advantages	Disadvantages
Generally defect free welds	Deposition rates lower than the rates possible with electrode arc processes
Spatter free	It is more expensive to weld thicker substrates, above 10 mm
Heat source and filler metals can be controlled independently	More difficult to weld manually, as the operator needs to add the filler metal.
Can be used autogenously	
Can be used to weld almost any metal, including dissimilar metal joints	

Several welding modes can be selected for GTAW welding:

- Direct current
- Alternating current

- **Direct current (DC)**

In DC mode, the electrode can be connected either to the negative or positive terminal (polarity) of the power source. When the electrode is connected to the negative pole (straight polarity - DCEN), the electrons flow from the electrode to the work piece. In this configuration 70% of the energy is generated at the substrate and 30% is generated at the electrode. This mode leads to deeper penetration than reverse polarity. With reverse polarity (DCEP) mode the energy generation is inverted and 30% of the generated energy is concentrated at the work piece whilst 70% is on the electrode. This leads to lower penetration and wider weld pools (Figure 38). This mode also produces a cleaning effect that releases the refractory oxide layer that prevents the wetting of the weld metal. This effect is more noticeable on Al and Mg alloys.

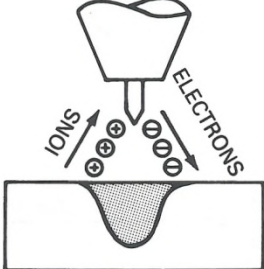
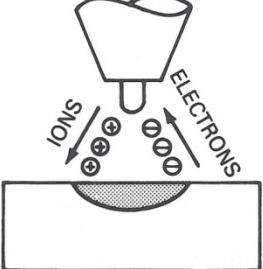
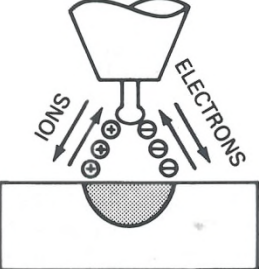
CURRENT TYPE	DCEN	DCEP	AC (BALANCED)
ELECTRODE POLARITY	NEGATIVE	POSITIVE	
ELECTRON AND ION FLOW			
PENETRATION CHARACTERISTICS			
OXIDE CLEANING ACTION	NO	YES	YES-ONCE EVERY HALF CYCLE
HEAT BALANCE IN THE ARC (APPROX.)	70% AT WORK END 30% AT ELECTRODE END	30% AT WORK END 70% AT ELECTRODE END	50% AT WORK END 50% AT ELECTRODE END
PENETRATION	DEEP; NARROW	SHALLOW: WIDE	MEDIUM
ELECTRODE CAPACITY	EXCELLENT e.g., 1/8 in. (3.2 mm) 400 A	POOR e.g., 1/4 in. (6.4 mm) 120 A	GOOD e.g., 1/8 in. (3.2 mm) 225 A

Figure 38 – Influence of the polarity on the weld bead profile (American Welding Society, 1991).

- **Alternate current (AC)**

In AC mode the polarity of the current alternates from straight polarity to reverse polarity and combines the two phases mentioned previously. It combines the

deeper welding penetration of direct current and the cleaning effect from the reverse polarity. During this mode the current needs to be zero during some time to enable the polarity inversion. During this time the electric arc is extinguished and it needs to be reignited afterwards. This is easy when the electrode becomes negative it immediately supplies thermionic electrons and the arc is reignited. However when the electrode is positive the weld pool cannot provide electrons until the voltage is raised and the cold-cathode emission is initiated. Without this voltage increase the arc becomes unstable. This difference in the polarity modes leads to an unbalanced current between the DCEN and DCEP phases. The modern power supplies use electronic wave balancing to provide balanced current waveforms and distribute evenly the heat generation between the electrode and the work piece (Figure 38).

2.5.4 Gas metal arc welding - GMAW

GMAW (Gas Metal Arc Welding) was also invented at the beginning of 20th century, 1920. In 1948 the first commercially available system was introduced and was considered to be a high current density bare metal electrode using an inert gas shielding. As GTAW, this welding process was also used to weld Al. The development of operation regimes at lower current densities, the use of active gases and the application to different metals made GMAW one of the most industrial used welding processes.

GMAW is a welding process that uses an electric arc between a consumable electrode and a workpiece to generate heat to form a weld pool and transfer the metal from the electrode to the workpiece. This process is shielded with either an inert or active gas and the electrode is continuously fed and consumed during the welding process (Figure 39).

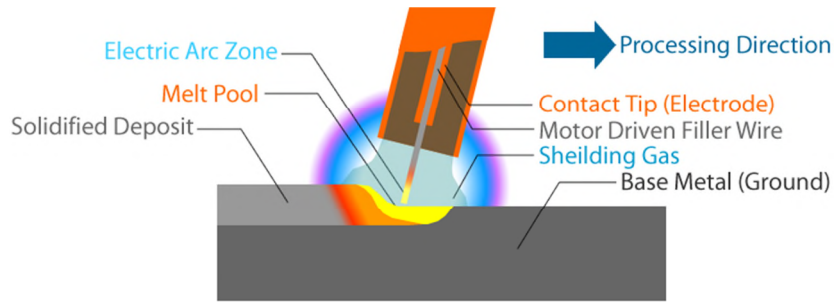


Figure 39 – GMAW welding process schematics (Hayden corp., 2014).

In Table 6 the main advantages and disadvantages of GMAW welding process are presented.

Table 6 – Advantages and disadvantages for GMAW process.

Advantages	Disadvantages
Higher productivity when compared with Shielded Metal Arc Welding (SMAW) and GTAW.	The arc must be protected against draughts
Minimal post welding cleaning when compared with SMAW	Equipment higher complexity when compared with SMAW
Easily automated	Spatter formation

GMAW has different transfer modes that can be achieved depending on the type of metals and goal for a particular welding procedure. These modes are designated as metal transfer mechanisms and relate the manner in which the molten electrode metal is deposited in the work piece.

- Short circuiting transfer
- Globular transfer
- Spray transfer

- **Short circuiting transfer**

This transfer mode happens when using low current levels and electrodes of small diameter. This transfer mode does not happen across the welding arc, the transfer of metal only occurs when the wire is in contact with the weld pool.

There are several electrical stages during a short circuiting transfer cycle. The electrode starts to melt and the weld pool is formed, due to the forward motion of the electrode it contacts with the weld pool. At this moment the short circuit happens and the current increases, increasing the electrode temperature and a detachment of the electrode metal is obtained. This metal is then added to the molten pool metal and a new arc is ignited between the electrode and the work piece. This arc is enough to maintain the molten pool on the liquid state. A new short circuit is formed and a new cycle is initiated (Figure 40).

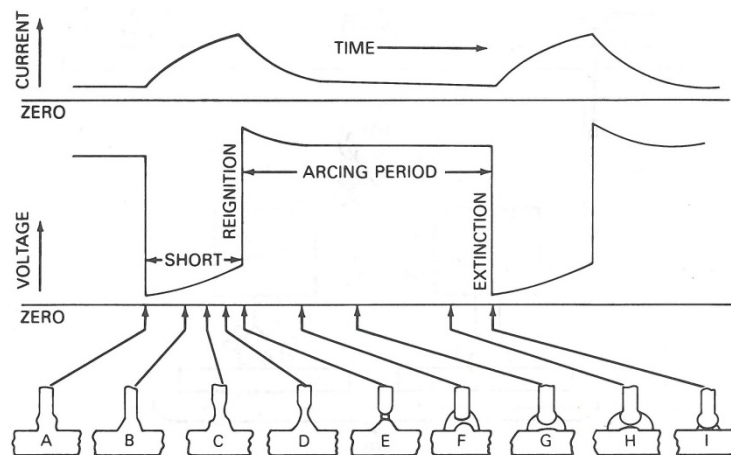


Figure 40 – GMAW short circuiting transfer mode arcing phases (American Welding Society, 1991).

Due to the low current and heat input this mode is used for welding thin substrates and root passes.

- **Globular transfer**

Globular transfer is characterized by an electrode droplet detachment with bigger radius than the electrodes diameter. This transfer happens for relatively low currents using reverse polarity, regardless of the shielding gas used. However for carbon dioxide and helium atmospheres, this transfer mode can be used with usable levels of current. With average currents slightly higher than short circuiting transfer it is possible to have globular transfer. However for low arc lengths (low voltage), the high dimension droplet can short circuit and

generate spatter. The arc needs to be long enough to permit the droplet detachment without short circuiting.

- **Spray transfer**

Spray transfer mode occurs generally on Ar rich shielding atmospheres and is characterized by a spatter free metal transfer. This mode is used in reverse current mode and for currents higher than the transition current, for lower currents the globular transfer mode is obtained. The droplets formed are of small dimensions, the transfer frequency is high and they are accelerated by the arc forces. The smaller dimensions of the droplets prevent the short circuit formation. This welding transfer mode is difficult to apply on thin substrates due to the high heat input and the distortions and the high arc forces can also cut through the substrate.

2.5.5 CMT – Cold Metal Transfer

CMT is a variant from GMAW process, with lower heat input that is used to weld thin substrates and so has high application at the automotive industry.

This process is a GMAW process that uses the short circuiting metal transfer mode, as explained before. The main difference introduced by CMT is the additional control of the welding wire on the droplet detachment during the welding process (Figure 41).

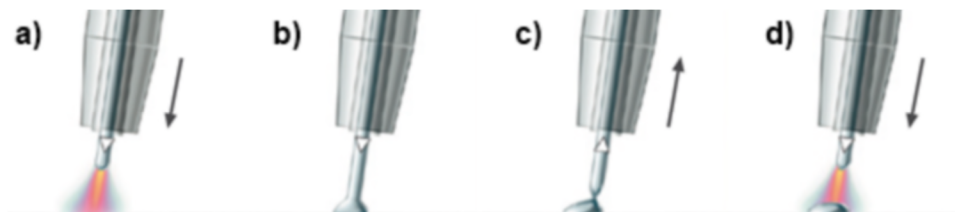


Figure 41 – Different CMT phases, a) arc ignition b) short circuit phase c) inversion of wire feed direction d) arc re-ignition

GMAW in short circuiting transfer mode rely on the surface tension to detach the droplet from the welding wire to the weld pool. This occurs in the short circuit phase of the process where the voltage drops close to zero and the

current increases, increasing the heat input to the workpiece. CMT does not need to increase the current on the short circuit phase due to the retraction movement of the welding wire and so it can avoid the current increase at the short circuit phase, decreasing the heat input transferred to the work piece.

2.6 Summary of literature review

This literature review shows that there is a great deal of research made in the field of dissimilar metallic joining, in particular for the two dissimilar metallic combinations that are important for this work, Fe-Al and Fe to Ti.

These dissimilar alloys can be categorized as Type 2 dissimilar metallic alloys, because there is the formation of intermediate phases between these metallic combinations and so the traditional joining process and metallurgical control can be used to minimize or reduce the IMC formation. Both of these IMC mitigation techniques were used in both of these dissimilar metallic combinations, with several joining processes and intermediate metal tested to reduce the IMC formation.

For the Fe-Al spot welding several research was done using RSW due to its current application in the automotive industry and FSSW due to its low heat input. This reveals a trend towards the use of process control towards the Fe-Al dissimilar welding instead of a metallurgical control. This can be justified due to the higher dissimilar physical properties (melting point and thermal conductivity) of Fe and Al when compared with Fe-Ti.

In the joining of Fe to Ti, both of the IMC mitigation techniques were used, with great results shown by using explosion welding by (Kahraman et al., 2005) achieving a IMC free joint between Fe and Ti. For the metallurgical control of the weld pool several single and multiple interlayers were used (Cu, Ni, V, Ta and Al), with the formation of IM compounds and associated lower mechanical properties. The exception being the work done by (Lee et al., 2010) where it is used a Ni/Cr/V hybrid interlayer to join Ti Gr2 to stainless steel, obtaining a final UTS equivalent to the UTS of Ti Gr2.

2.7 Knowledge gaps identified

The points shown below are the gaps in knowledge found in the literature review.

- The joining process control approach for spot welding of Fe to Al is generally based in traditional RSW or solid state FSSW. There is the lack of research on different fusion joining techniques to spot weld Fe to Al.
- All the results shown in the literature review use the system parameters and so a higher level of analysis should be done by using the fundamental material interaction parameters to fully understand the IMC formation and growth.
- There is almost no systematic approach in the selection of possible interlayers to be used in dissimilar metallic combination. The strategy used is to choose a metal and join it with several joining techniques and verify if it is possible to reduce or eliminate the IMC formation between the parent metals.

3 Steel and Aluminium spot welding

3.1 Chapter introduction

In the literature review, Fe-Al welding is classified as type II dissimilar welding, and this can be verified by the IMC formation detected in the Fe-Al phase diagram (Figure 20).

From the phase diagram, five different IMC phases can be observed at equilibrium: Fe_3Al , FeAl , FeAl_2 , Fe_2Al_5 and FeAl_3 . These IMC have to be avoided or minimized due to the high values of hardness consequently the detrimental value induced in the joined specimens.

To join these two alloys, the approach selected was not only physical control of the welding process referenced in chapter 1.4.1 but also an attempt of using Zinc in the galvanized steel as metallurgical control (1.4.2).

The first part of this chapter is dedicated to welding process control to explore the different physical properties of these Al and Fe (Table 7)

Table 7 – Al and Fe physical properties (Gale and Totemeier, 2003).

Physical Property	Al	Fe
Melting Point (°C)	660.3	1536.0
Thermal conductivity [W/(m.K)] at 25 °C	247.0	80.4
Thermal expansion [$\mu\text{m}/(\text{m.K})$] at 25 °C	23.1	11.8

Aluminium has a lower melting point and a higher thermal conductivity than Fe and so in this part of the research laser welding in conduction mode was used to control the thermal field applied to these metals. Both metals were placed in an overlap configuration with the steel on top and the aluminium in the bottom and the heat was conducted through the steel and melted the aluminium. The control in the thermal field achieved by laser conduction welding is enough to avoid the simultaneous melting of both metals at the interface, steel remained

solid whilst the Al was molten. This decreased the diffusion/reaction of these metals and so decreasing the IMC formation.

The second part of this chapter was dedicated to study the influence of the Zn present in the galvanized steel and verify if it can act as a barrier or has an interlayer and possibly change the IMC nature and composition.

3.2 Low carbon steel and aluminium spot welding

3.2.1 Introduction

As mentioned in the literature review, Fe-Al dissimilar welding has been actively researched by the automotive industry to reduce the weight of future automotive vehicles. As spot welding is already an established joining method for the automotive industry laser spot joining in conduction mode was selected as the joining method for this research.

This joining method uses lower power densities when compared with laser key hole to generate a thermal gradient that will melt the Al maintaining the Fe in solid state. This would decrease the reaction rate between the participating metals and will enable a better control in the IMC formation.

Non galvanized low carbon steel was selected due to its application in the automotive industry and also to establish a base line of Fe and Al joining. Subsequently, an experimental trial between galvanized steel and aluminium was made and compared with the results obtained in this chapter.

3.2.2 Conduction mode laser spot welding

In this study, uncoated steel (DC04) was welded to an Al alloy (6111 Al alloy) in an overlapping configuration with steel on the top. Two different backing bars were used (copper and aluminium) to vary the heat extraction coefficient and thermal profiles during welding.

The power density of the laser spot was controlled so that the impinged energy was transferred through the steel plate to the aluminium resulting in melting of Al and wetting of the steel surface (which remains in solid state). The melting of aluminium and wetting of steel surface enables the joint formation (Figure 42). This is possible due to the dissimilar melting points, 652°C and 1535°C of the metals used, Al and Fe respectively, and the higher thermal conductivity of Al which guaranties the directionality in the heat extraction and helps in raising the temperature at the steel aluminium interface.

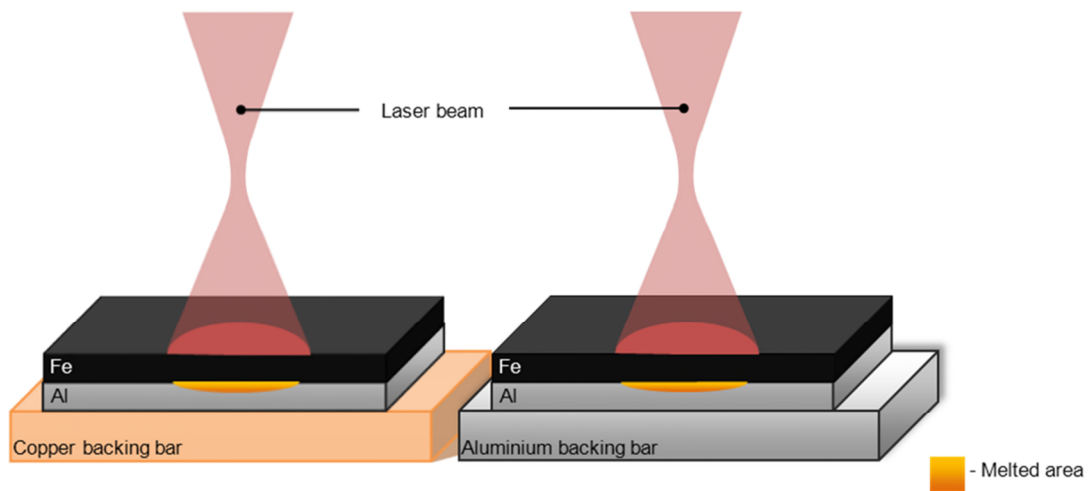


Figure 42 – Schematic representation of conduction mode laser spot welding for each set of experiments.

To achieve the required melting of Al at the interface, special care needs to be taken to ensure proper interfacial contact. A clamping system with a metallic ring around the spot weld was developed with two clamps exerting pressure to avoid any gap between the plates (Figure 43). This was developed to ensure consistent contact between the plates necessary for repeatability and reproducibility of the process.

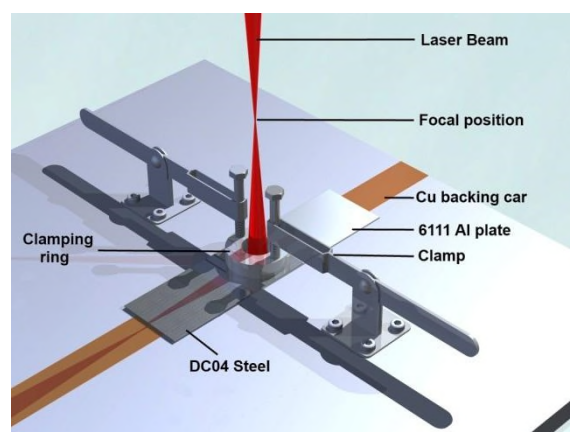


Figure 43 - Clamping system with laser beam schematic representation

A gap between the two plates would prevent the heat conduction from the steel to the aluminium and would result in a rise of temperature in the steel plate and consequently the melting of this plate. In thin sheet dissimilar welding, the formation of a keyhole is undesirable as it would result in melting of the steel substrate material and result in uncontrolled mixing and consequent reaction of Fe and Al. To achieve the conduction mode the laser beam was defocused to have a lower power density. This laser welding process differs from regular laser welding due to the solid-liquid interface generated by the melting of the Al substrate whilst the steel remained in solid state.

3.2.3 Material and experimental setup

The material used was 1 mm thick DC04 steel and 1 mm thick 6111-T4 aluminium alloy. Chemical compositions and mechanical properties of the two alloys are given in Table 8 and Table 9 respectively.

Table 8 – Chemical composition (%wt) for DC04 steel and 6111-T4 aluminium alloy

Material	C	Mn	P	S	Al	Fe	Mg	Si	Cu
DC04	0.08	0.4	0.03	0.03	-	Bal.	-	-	-
6111-T4	-	-	-	-	Bal.	0.25	0.8	0.7	0.7

Table 9 – Mechanical properties of the weld members

Material	Yield strength [MPa]	Tensile Strength [MPa]	Elongation [%]
DC04	210	270 – 350	----
6111-T4	165	295	26

Plates cut into 105 x 45 mm rectangular section were used in the experiments. The aluminium plates were finished immediately before welding, time from finishing to welding was restricted to below 10 min to avoid reoxidation and both plates were cleaned with acetone. In order to make specimens for mechanical

testing the plates were positioned with an overlap of 35 mm to comply with the (BS EN ISO 14273, 2001) standard (Figure 44).

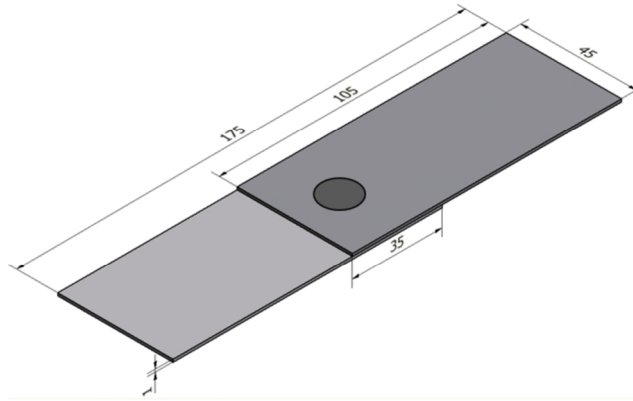


Figure 44 – Tensile shear test specimen dimension.

The welds were made using an 8 kW fibre laser (IPG YLR 8000) with an optical lens of 500 mm focal length. The laser beam was used in out of focus position and was defocused to obtain a 13 mm diameter beam with a Gaussian distribution of energy. Two different, Cu and Al, backing bars were used in these experiments. The aluminium backing bar was water cooled to facilitate the heat extraction. To produce the spot welds, the laser beam was irradiated on the steel surface without any movement (the laser is stationary with respect to the substrate). Metallographic examination of the welds was carried out by cutting and mounting the weld cross section and then an appropriate polishing and grinding technique was used to reveal the metallographic details near the weld centre. After polishing the samples were etched with 2% Nital (steel) and Keller's reagent (Al). The samples were observed under an optical microscope for microstructural and weld profile analysis and then analysed by energy dispersive spectroscopy (EDS) in a FEG-SEM (Field Emission Gun – Scanning Electron Microscopy) to estimate the stoichiometry of the IMC formed. Finally shear strength of the joints was determined by tensile shear tests using an INSTRON 5500R universal tensile testing machine.

3.2.4 Experimental parameter (system and fundamental)

The system parameters used during the experiments are presented in Table 10.

Table 10 – System parameters used for conduction mode laser spot welding

Spot size [mm]	Irradiation time [s]	Power [kW]
13	3	3.00
13	3	3.35
13	3	3.50
13	3	3.65
13	3	3.80

To understand the laser-metal interaction, three fundamental parameters which determine the energy transferred to the material during the application of laser were studied, power density (PD), interaction time (t_i) and specific point energy (E_{sp}) (Assuncao et al., 2012). These parameters were defined in the literature review. The values for the fundamental energy parameters used during the experiments were calculated from the system parameters and are presented in Table 11.

Table 11 – Fundamental energy parameters used for conduction mode laser spot welding

Power density [MW/cm²]	Interaction time [s]	Specific point energy [kJ]
2.26 E-3	3.0	9.00
2.52 E-3	3.0	10.05
2.64 E-3	3.0	10.50
2.75 E-3	3.0	10.95
2.86 E-3	3.0	11.40

The interaction time was kept constant and to a maximum of 3 s to maintain the process economically viable, as large interaction times are not recommended for spot welding operations.

3.2.5 Results and discussion

The macrostructures of the welds revealed that an appropriate thermal gradient could be established which allowed melting of the Al along the joint interface. There was some evidence of steel melting at the top surface, under the area which is directly irradiated by the laser, which was necessary to create the thermal gradient required. It is clear from the macrograph (Figure 45) that the two different alloys were not mixed in the molten state. The heat from the top surface was, therefore, conducted to the interface which resulted in a transient thermal field that allowed the aluminium to melt and wet the steel surface, while the steel itself remained in the solid state.



Figure 45 – Conduction mode laser spot welding macro section.

To have an accurate measurement of the IMC layer thickness formed by the Fe-Al reaction five micrographs were taken along the IMC layer (Figure 46 a). In each micrograph 20 IMC layer thickness measurements were taken where each measurement was separated by 10 μm . The mean of the measurements for each micrograph was calculated and the maximum value for the five inspected micrographs was considered as the maximum of the IMC layer thickness and reported (Figure 46).

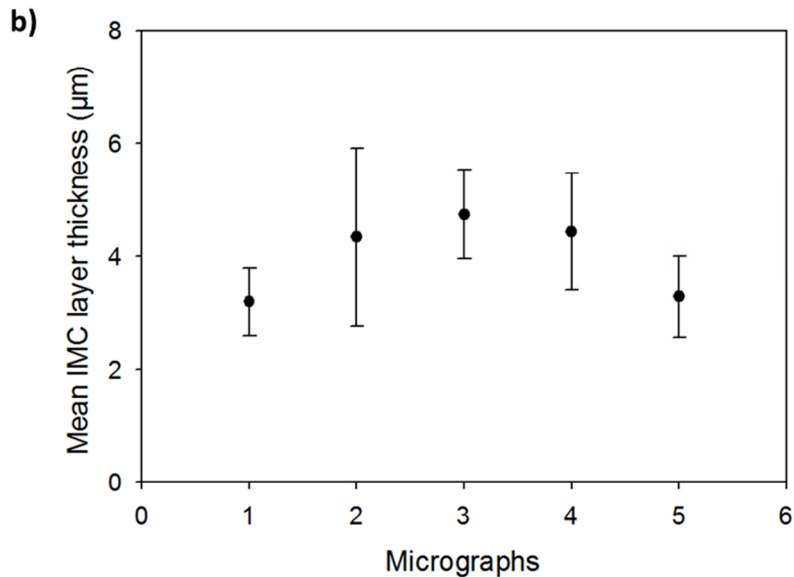
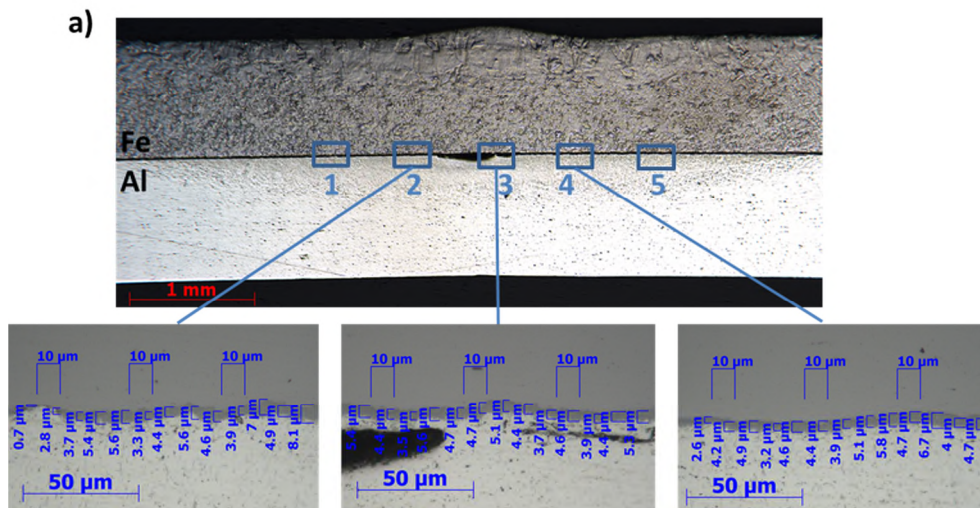


Figure 46 – Intermetallic measurement example a) and plot of the IMC layer thickness for each of the five micrographs done across the weld interface b).

Micrograph 3 was selected as the maximum for the IMC layer thickness for this particular sample. Table 12 show the IMC layer maximum thickness for each sample and the associated standard deviation.

Table 12 – IMC layer thickness and corresponding standard deviation.

Sample	Backing bar	Power density [MW/cm ²]	Interaction time [s]	Specific point energy [kJ]	IMC layer thickness (μm)	Standard deviation (μm)
1	Cu	2.52 E-3	3.0	10.05	4.64	1.06
2	Cu	2.64 E-3	3.0	10.50	4.75	0.79
3	Cu	2.75 E-3	3.0	10.95	7.59	1.26
4	Cu	2.86 E-3	3.0	11.40	20.21	3.79
5	Al	2.26 E-3	3.0	9.00	32.36	2.66
6	Al	2.52 E-3	3.0	10.05	35.16	1.21

The formation of IMC is a diffusion/reaction controlled process and therefore dependent on the time and temperature of the weld pool or in other words the thermal profile of the spot.

As discussed the spot welds were made in laser conduction mode where the energy within the laser spot was controlled by holding the specimens in a defocused position. In the defocused condition the energy shows a Gaussian distribution, whilst on the focal position the beam has a top hat energy distribution. Figure 47 (Assuncao and Williams, 2013) shows the energy distribution (Gaussian distribution) of a laser beam with a power distribution of 1000 W for a focal lens of 250 mm in defocus position.

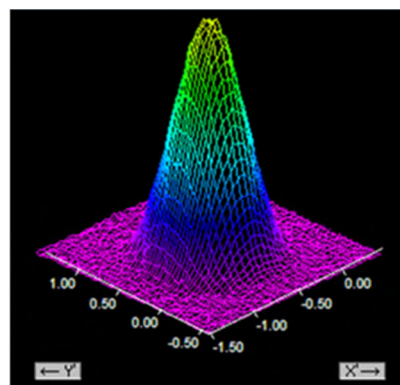


Figure 47 – IPG YLR 8000 laser energy distribution for a defocused position.

This translates in a temperature distribution which has a maximum near the centre while substantially less towards the edge of the spot. This will also result in a faster cooling rate near the edge of the weld pool as compared to the centre of the weld. The pattern of intermetallic compound formation followed the weld thermal profile across the melt pool. On the extreme edges of the spot, the intermetallic layer had a lower thickness and it was fragmented in appearance (due to the lower intensities on the extremities of the spot, Gaussian profile, and the non-constant cooling conditions from the edge of the spot into the parent metals). On the central part of the spot, where the temperature was higher, the intermetallic layer was thicker and continuous in nature.

In Figure 48 the maximum IMC layer thickness as function of specific point energy was plotted for both the Cu and Al backing bars. The corresponding micrographs for the welds made with a copper backing bar, along with the specific point energy were shown in Figure 48.

Irrespective of the backing bar, IMC layer thickness increased, as the laser specific point energy was increased. However, it can be observed that as the aluminium backing bar had a lower thermal conductivity the heat extraction was slower which resulted in a lower cooling rate. The resulting thermal profile of the spot welds from the aluminium backing bar caused the formation of a thicker intermetallic layer even at a lower energy level when compared to the copper backing bar at a higher energy level as shown in Figure 48 a for example. At a comparable value of E_{sp} , 10.05 kJ, the IMC layer thickness of the sample welded with an aluminium backing bar was 35 μ m whilst the sample welded with a Cu bar is 5 μ m.

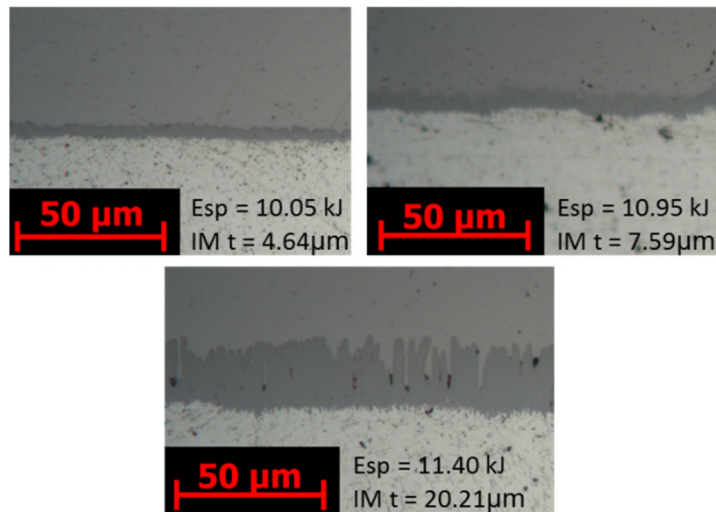
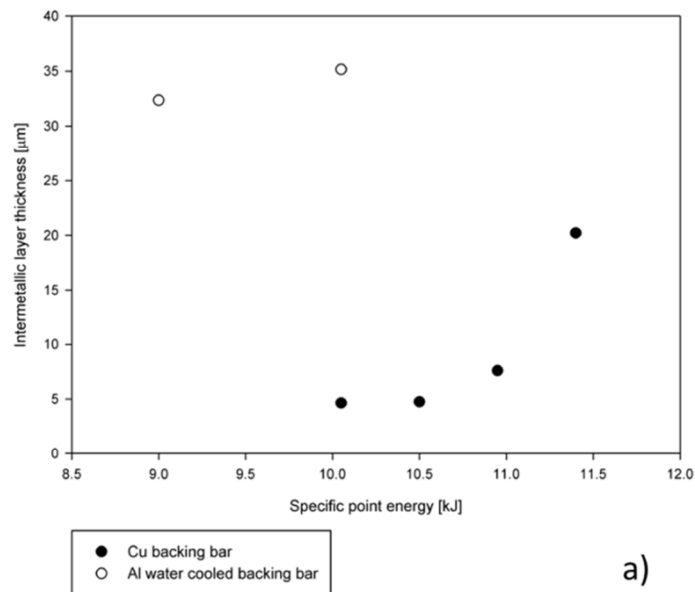


Figure 48 – Evolution of the IMC layer thickness with the specific point energy a) and selected Cu backing bar micrographs b).

The IMC layer thickness for the copper backing bar exhibited an exponential growth with increase in E_{sp} , revealing that this parameter has an important role on the formation and growth of the IMC layer.

On the optical micrograph after etching two different intermetallic layers can be observed, as shown in Figure 49. A thinner layer (represented by IMC-1) was present closer to the aluminium side and a thicker layer (represented by IMC-2)

was present closer to the steel side. The contrast in their appearance in optical microscopy can be attributed to the difference in stoichiometry between the two layers.

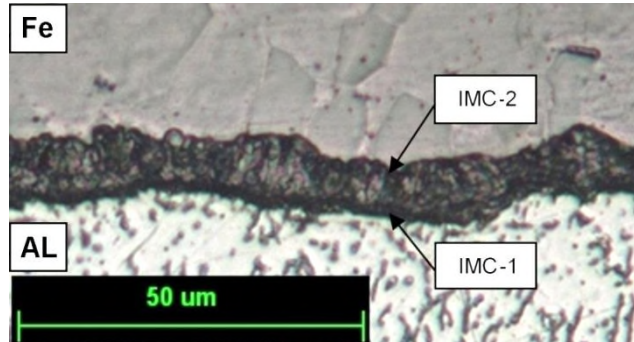


Figure 49 – Optical micro section of IMC layer

From EDS analysis it is possible to determine the atomic proportion of Fe and Al in the IMC layers. It was found that the intermetallic compound was principally formed by Fe and Al. By the elemental map it is possible to identify three different areas near the fusion zone of the weld. Area A (green) and C (red) are the two parent materials Fe and Al respectively whilst area B is the IMC layer that is originated from the diffusion between Fe and Al.

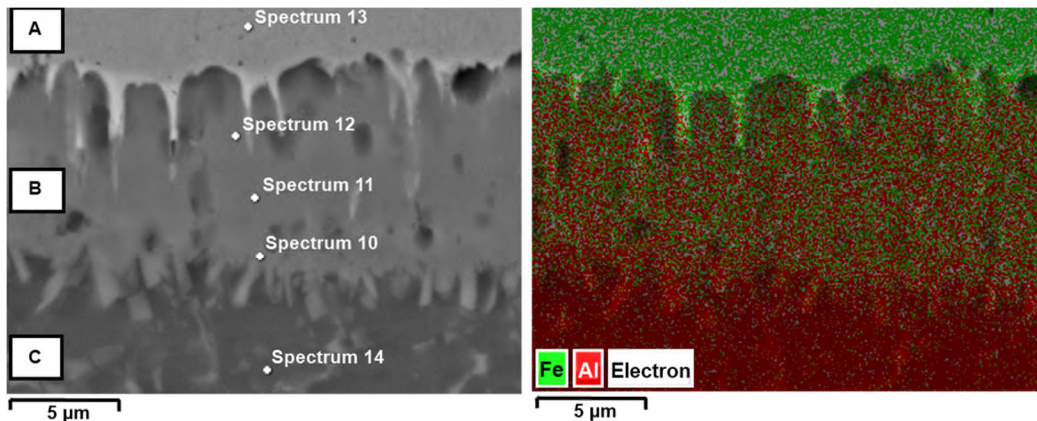


Figure 50 – EDS of the intermetallic layer (left), Elemental distribution (right).

The EDS analysis (Table 13) indicated that the stoichiometry of the thinner layer IMC-1 (Figure 50) as FeAl_3 and IMC-2 as Fe_2Al_5 .

Table 13 – EDS semi-quantitative analysis results for Fe and Al at the joint interface.

Spectrum	Fe [%wt]	Al [%wt]	IMC
10	39.66	60.34	FeAl ₃
11	45.57	54.43	Fe ₂ Al ₅
12	46.47	53.53	Fe ₂ Al ₅
13	100	0	Fe
14	4.19	95.81	Al

These observations are in agreement with previous research by Qiu et al (Agudo et al., 2007; Bouche et al., 1998; Qiu et al., 2009) and in accordance with the diffusion mechanisms that rule the IMC formation; in that the Al richer phase (FeAl₃) is closer to the Al side whilst the phase richer in Fe (Fe₂Al₅) is closer to the Fe side of the weld.

To evaluate the hardness of the samples and in particular the hardness of the IMC layer, a micro hardness testing was carried out. A vertical line of indentations was made across the centre of the weld with the spacing between indentations of 0.1 mm, as shown on Figure 51. The indentations load used was 25 g with load application duration of 10 s.

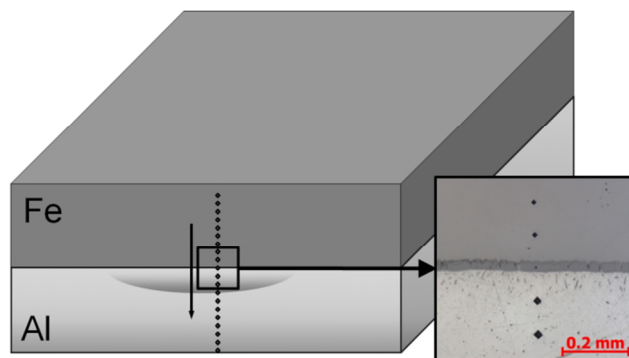


Figure 51 – Micro hardness pattern representation.

A low value of hardness was observed on Fe and Al, when compared with the maximum hardness value of 968 HV near the centre of the IMC layer. The hardness of the IMC layer was 4.5 times the hardness of the welded steel, and around 14.5 times the hardness of the aluminium therefore, it is more brittle

when compared to the matrix structure (Figure 52). Al-Fe IMC are also known to be inherently brittle (Kobayashi and Yakou, 2002).

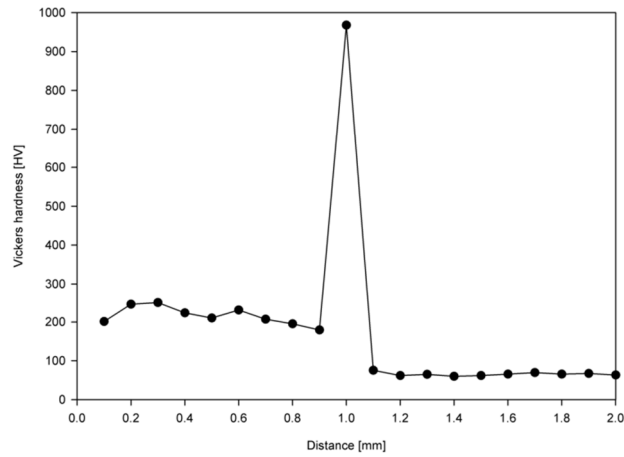


Figure 52 – Hardness values in a vertical traverse across the weld interface

The lap shear test performed to the experimental samples revealed that, for the welds made using an aluminium backing bar the lap shear strength decreased as the E_{sp} increased (Figure 53 a). The level of IMC formation was also higher for welds made using the aluminium backing bar when compared to welds produced with the copper backing bar (Figure 53 b), even when the energy levels were lower. This can be related to the different thermal cycle experienced by the two sets of welds. As the aluminium backing bar has a lower thermal conductivity, the energy was kept in the weld for longer and consequently the temperature at the interface was higher for a longer time, resulting in a thicker IMC layer that negatively affected the strength of the welded structure.

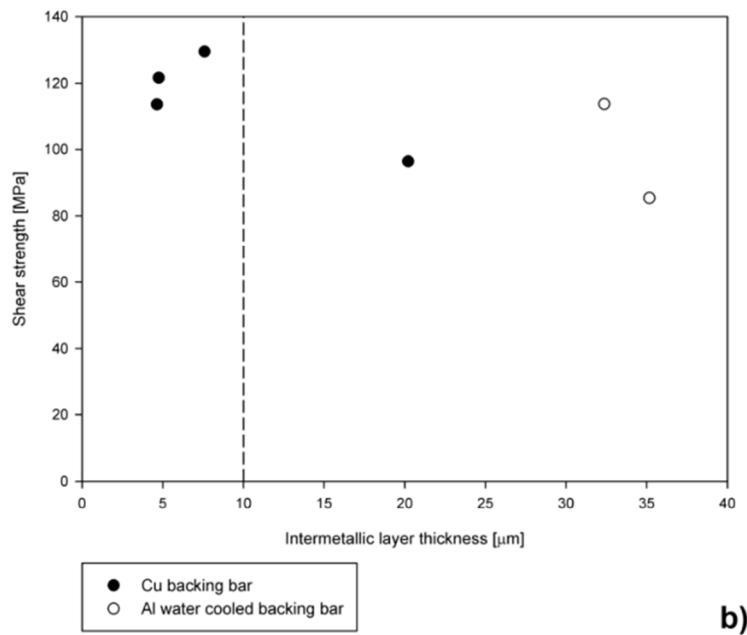
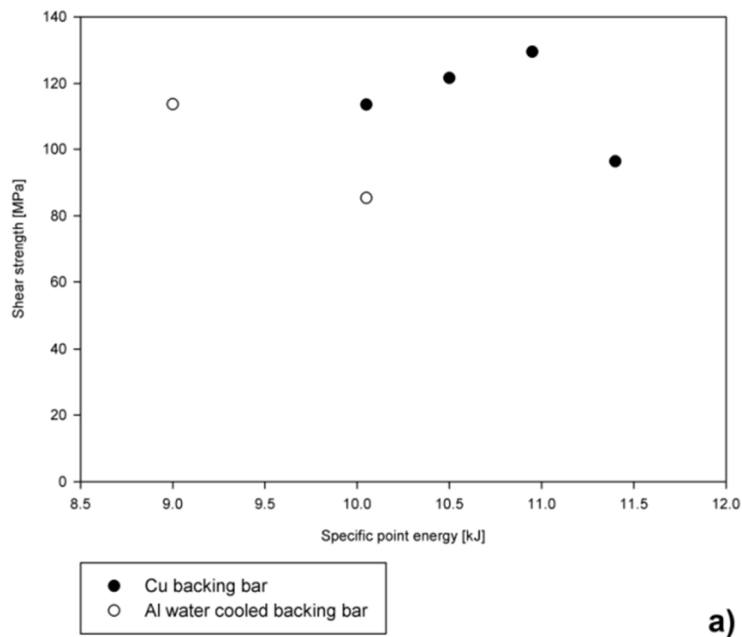


Figure 53 - Lap Shear strength behaviour vs. specific point energy a), shear strength vs. IMC layer thickness b).

As the copper backing bar has a higher thermal conductivity, the energy was transferred more quickly and therefore, the thermal cycle was shorter, reducing the overall growth of the IMC layer, even for welds with higher energy levels. From Figure 53 a) it can be seen that there is an increase in the shear strength

with an increase of the applied energy, but after 11kJ the trend reversed. The maximum shear stress value of around 130MPa was observed when the IMC layer thickness was close to 10 μm (Figure 53 b) which has been reported as a benchmark value for the mechanical properties of a dissimilar weld between aluminium and steel (Sepold and Kreimeyer, 2003). This condition seems to produce the best combination of diffusion and bonding strength relative to the interface brittleness introduced by the IMC layer. The two IMC layer thicknesses for the samples with 10 and 10.5 kJ are very similar, as shown in Figure 53, this is due the applied energy being used to melt more aluminium and increase the wetting/bonding area. For lower energy levels, the energy is enough to create a bonding and increase the melting of the Al, but there is not enough energy to increase the IMC thickness. This can be substantiated from the increase in shear strength for the sample made with 10.5 kJ of applied energy without a big increase of the IMC layer thickness.

In Figure 54 shear strength is plotted against cross-head displacement, this also shows evidence of plastic deformation until fracture that translates into the toughness of the welded sample. For specimens with IMC layer thicknesses greater than 10 μm not only was the shear strength lowered, but also the plastic deformation was reduced (Figure 54).

The effect of the thicker IMC is not only to lower the shear strength of the weld, but also to lower its deformability. This can be correlated to the high hardness and brittle nature of the IMC compounds which facilitates crack propagation, resulting in lowering the failure energy (toughness) of the welded joint.

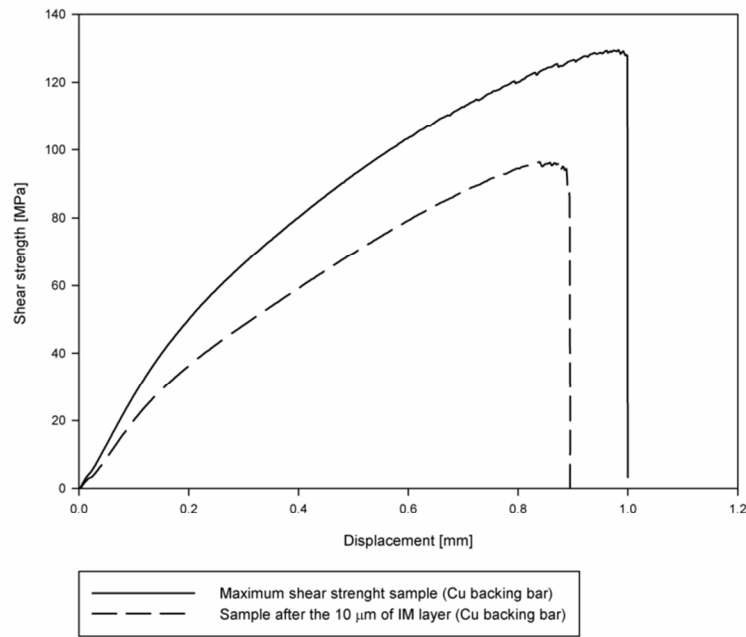


Figure 54 – Shear strength – displacement graph for selected samples.

To obtain the best mechanical properties it is necessary to balance the energy input with the formation of the IMC layer. With lower energy levels a thinner IMC layer formed, but there isn't enough energy to make an effective bond between the two materials over a large weld area. In contrast, when the energy level is significantly higher diffusion of aluminium into iron is much faster and the IMC layer is thick, resulting in a lowering of the mechanical properties of the joint. Thus in the presented work a higher energy level with a very fast heat extraction resulted in an improved joint strength.

3.2.6 Conclusions

It is possible join DC04 to 6111-T4 aluminium in using laser spot welding in conduction mode. However the interfacial failure cannot be avoided. It was possible to melt the aluminium and prevent the bulk melting of the steel. This enabled a liquid-solid interface region and reduced the inter-diffusion of both materials and subsequently a control of the IMC layer thickness. Nevertheless, despite exploring a range of conditions an IMC reaction layer was always found

at the interface between Al and steel, which was determined to be composed mainly of Fe_2Al_5 and FeAl_3 IM compounds. This IMC layer has an exponential growth with the increase of the specific point energy.

With the same backing bar, the IMC layer thickness could be controlled by controlling the fundamental energy parameters. Due to the high level of hardness of the IMC layer (968 HV), failure of the joints was always located in the interfacial region with a maximum tensile shear strength of 130 MPa for an IMC layer thickness close to 10 μm , when joined using a copper backing bar.

The application of different, Al and Cu, backing bars revealed that IMC formation and growth is a function of the transient thermal cycle. Samples produced with identical energy level of 10 kJ showed 757% increase in IMC layer thickness. This also adversely affected the mechanical strength of the samples produced using the Al backing bar.

3.3 Galvanized steel and aluminium spot welding

3.3.1 Introduction

After confirming that it is possible to use laser in conduction mode to make dissimilar spot welds between Fe and Al for the automotive industry, it is necessary to evaluate how the Zn present on galvanized steel would influence this joining process. Verify how the Zn interacts with the participating alloys composition.

Galvanized steel is used in the automotive industry to improve the corrosion resistance of steel. This is done by introducing a thin layer (typically lower than 100 μ m) of Zn on the exposed steel surface. Zn can protect Fe from oxidation in two different ways: barrier protection and galvanic protection. Zn has the effect of a protective barrier, because it makes an impermeable barrier to humidity, avoiding the oxidation of steel. The galvanic protection happens when the galvanized steel is scratched and the Fe substrate is exposed. This initiates a cathodic reaction provided by the Zn coating that protects the Fe from corrosion by the sacrificial corrosion of the Zn adjacent to the exposed steel. As Zn is more electronegative (more reactive) than steel it will corrode before Fe and so preventing Fe corrosion (Marder, 2000).

The process of galvanization can be made in several ways (hot-dip galvanizing, electro galvanizing, Zinc spraying, etc), however the most common and popular way is continuous hot-dip galvanizing process. In this method a hot rolled steel strip is uncoiled, continuously fed through a cleaner and annealing furnace and then dipped into a molten Zn bath. Afterwards the coated Zn thickness is controlled and left to solidify to obtain a traditional galvanized, galfan or galvalume coating or it can be thermally treated to obtain a galvanneal coating (Zn-Fe alloy) (Marder, 2000). The difference between the galvanized, galfan and galvalume is the amount of Al introduced into the coating with <1 wt%, 5 wt% and 55 wt% respectively.

For this project a DX56+Z steel with a galvanized Zn coating was chosen. Its composition is shown in Table 14.

Table 14 – Zn coating chemical composition (wt.%).

Material	Zn	Fe	Al	Pb	Sb
Zn coating	Bal	2.75	0.47	0.01	<0.01

The main goal of the work shown in this section is to verify how Zn present in the galvanized steel changes the IMC behaviour (formation, growth, composition) and how it improves or deteriorates the joint mechanical properties.

3.3.2 Experimental procedure

The experimental procedure is similar to that presented in subchapter 3.2.3 with the following exceptions:

- The use of a different steel alloy, instead of the DC04 used in the chapter 2.2. For these experiments the alloy selected was DX56 + Z, galvanized steel with a chemical composition that can be verified in Table 14 and Table 15.

Table 15 – Galvanized steel chemical composition (wt.%).

Material	C	Mn	Ti	S	N	Al	Fe	Pb	Sb	Zn
DX56	0.02	0.15	0.055	0.01	0.004	0.05	Bal.	-	-	-

- The study was limited to one backing bar, after the results presented on the previous section, the importance of higher cooling rates in the IMC formation was verified and only the Cu backing bar was selected.
- Due to the Zn coating the steel samples surface was not ground, to avoid the Zn removal.
- Graphite coating was applied to the Zn surface to avoid the higher reflectivity present and consequently lower absorption coefficient to laser light when compared to uncoated steel.

For this particular study, the evaluation of a graded aluminium alloy was also conducted to verify if it is more suitable for laser applications. This alloy is composed of a core with AA6016 alloy and two exterior layers of AA4045 Al alloy. This alloy is produced using continuous casting technique, the layer thickness and main components compositions was evaluated using SEM/EDS technique (Figure 55).

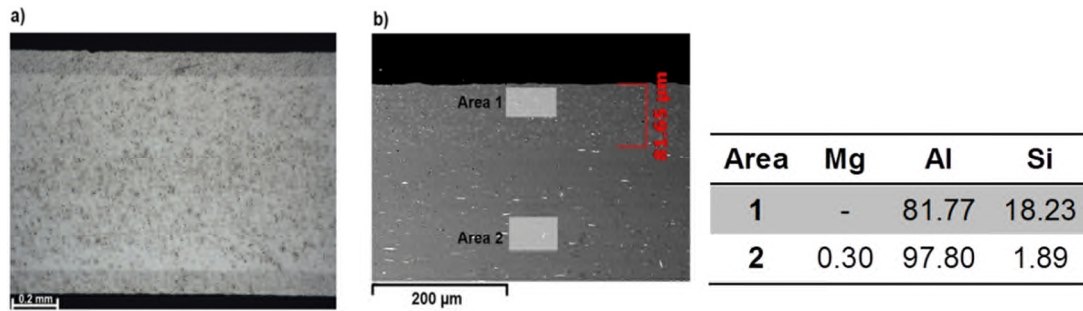


Figure 55 – Graded Al micrograph a), SEM/EDS image b) and corresponding acquisition areas.

In Figure 55 b) it is possible to identify that the AA4045 layer thickness is around 80 µm and the main components are in agreement with an outside layer of 4 series Al and a core of 6 series Al. A more detailed composition of the two alloys used is shown in Table 16.

Table 16 – 6016 and 4045 Al alloys nominal composition (wt %).

Alloy	Al	Si	Fe	Cu	Ti	Zn	Mg	Mn	Cr
4045	Bal	9-11	<0.8	<0.3	<0.2	<0.1	<0.05	<0.05	-
6016	Bal.	1-1.5	<0.5	<0.2	<0.15	<0.2	0.25-0.60	<0.2	<0.1

The welding parameters and material combinations experimentally relevant for this section of the thesis are shown in

Table 17 and Table 18.

Samples 7 and 8 were laser spot joined to evaluate how the Zn content influences the IMC layer formation. Sample 7 was welded using an uncoated steel on top of AA6111 aluminium alloy. These samples were repeated 4 times and they had a different sample size (50 mm x 50 mm). Both samples were

coated with graphite to prevent a different coupling coefficient from the laser with the Zn coated and the uncoated steel.

Table 17 – Experimental welding parameters (system and fundamental) to evaluate the influence of using a different Al alloy for dissimilar spot welding of steel to aluminium.

Sample	System parameters			Fundamental laser parameters			Material
	Spot diameter [mm]	Power [kW]	Irradiation time [s]	Power density [MW/cm ²]	Interaction time [s]	Energy [kJ]	Al alloy
1	13	3.0	3	2.3E-3	3.00	9.0	AA6111
2	13	3.2	3	2.4E-3	3.00	9.6	AA6111
3	13	3.5	3	2.6E-3	3.00	10.5	AA6111
4	13	3.0	3	2.3E-3	3.00	9.0	AA6016+4045
5	13	3.2	3	2.4E-3	3.00	9.6	AA6016+4045
6	13	3.5	3	2.6E-3	3.00	10.5	AA6016+4045

Table 18 - Experimental welding parameters (system and fundamental) to characterise the influence of Zn in the IMC layer.

Sample	System parameters			Fundamental laser parameters			Material
	Spot diameter [mm]	Power [kW]	Irradiation time [s]	Power density [MW/cm ²]	Interaction time [s]	Energy [kJ]	Al alloy
7 (non galvanized)	13	3.1	3	2.4E-3	3.00	9.3	AA6111
8 (Galvanized)	13	3.1	3	2.4E-3	3.00	9.3	AA6111

3.3.3 Results and discussion

The macrographs from the welded samples present similar weld morphology when compared with the experiments from the previous chapter.

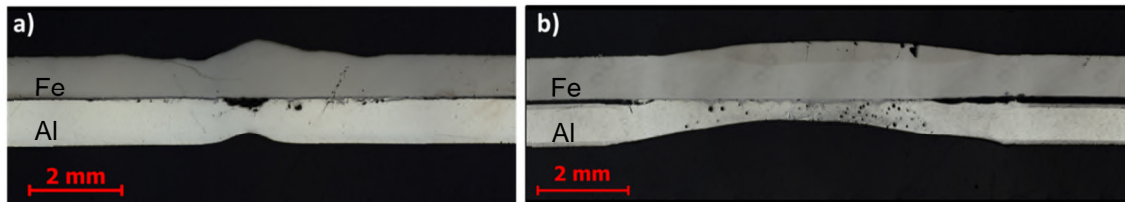


Figure 56 – Macrographs from samples 1 a) and sample 4 b)

Porosity and a central defect were observed in all samples produced with this joining technique. This arises from the thermal input inserted in the Al (higher temperatures at the central region and lower in the edges), discussed in the previous sub chapter. Higher levels of porosity can be observed in sample b).

The presence of Zn resulted in a more complex intermetallic compound formation, instead of the uniform IMC observed in the previous chapter; the IMC formation is higher and more irregular. This can be verified in Figure 57.

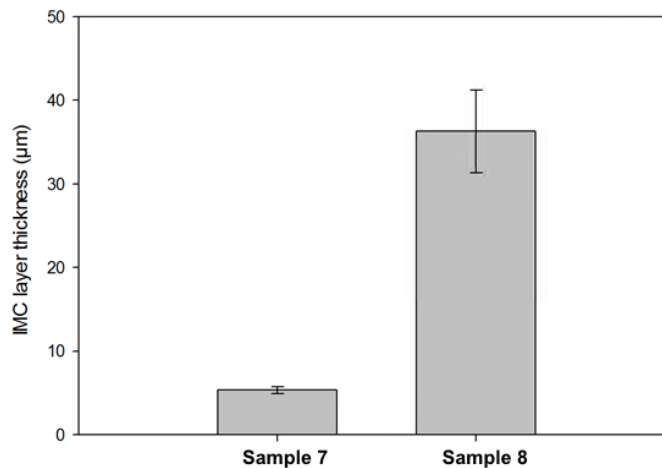


Figure 57 – IMC layer thickness and its variability low carbon steel vs galvanized steel (sample 7 vs sample 8).

Figure 57 shows higher IMC formation and growth for samples made with galvanized steel, with the uncoated sample showing an IMC layer smaller than 10 µm and a low standard deviation when compared with the Zn coated sample. However the sample joined with the galvanized steel shows an average IMC layer higher than 30 µm and a standard deviation of several micrometres. This can be justified by a larger stir movement of the weld pool of samples welded

between galvanized steel and Al. Figure 58 shows the micrographs taken for the interface of uncoated steel vs galvanized steel samples.

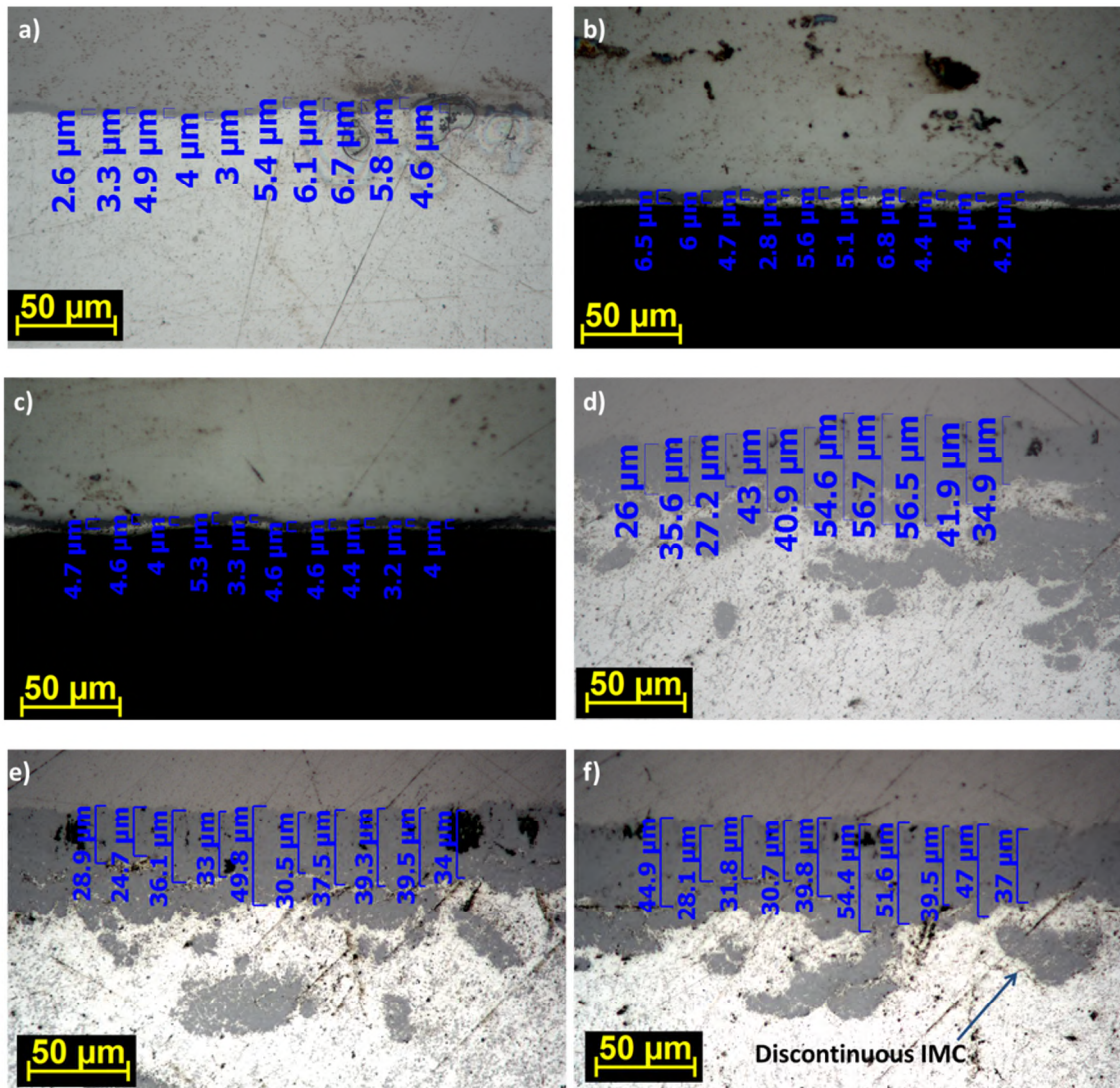


Figure 58 – Micrographs from the samples joined with uncoated steel (a, b and c) and Zn coated steel (d, e and f).

When examined in greater detail, the samples joined with the galvanized steel have a thicker IMC layer, but also the presence of discontinuous IM compounds inside the Al alloy. These discontinuous IM compounds are not present in the samples joined with uncoated steel and they were not accounted for in the IMC layer thickness measurements, because they are isolated from the main IMC layer.

Galvanized steel samples do not possess the same trend verified for the non-galvanized steel, of having a thicker IMC layer in the central region and thinner IMC layer at the edges. This is observable at Figure 58 d, e and f with the thicker IMC layer being present at Figure 58 d, which was taken closer to the samples edge.

SEM-EDS analysis was also carried out to verify the nature of the IMC layer and the islands originated in the presence of Zn samples.

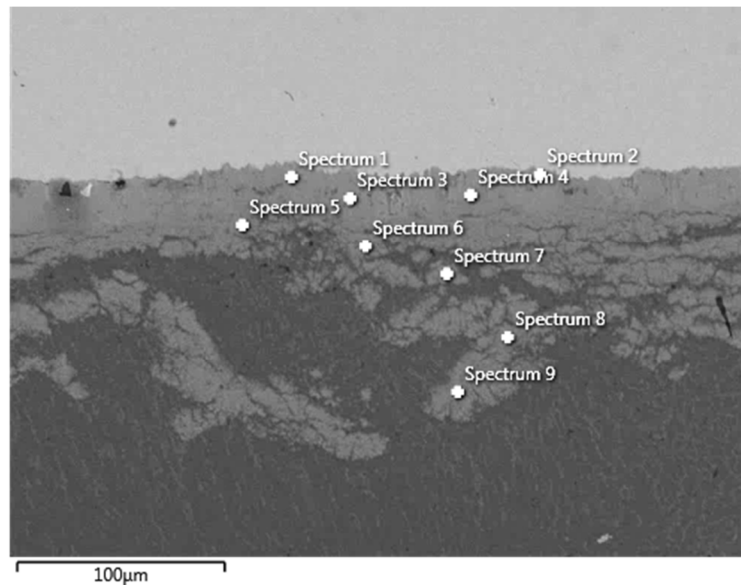


Figure 59 – SEM micrograph taken from the centre of the IMC layer and corresponding spectrum positions.

This EDS analysis was made in the section where the IMC layer was well developed and presented discontinuous IM compounds. The highest level of Zn was detected at spectrum 2 that is closer to the Fe side, with a maximum value of 3.66 % at. As the values of Zn are minimal for all of the spectrums taken, the IMC's were evaluated against the Fe-Al phase diagram and only Fe and Al at% were taken into account.

Table 19 – At % of spectrums analysed in Figure 59.

Spec Label	Spec. 1	Spec. 2	Spec. 3	Spec. 4	Spec. 5	Spec. 6	Spec. 7	Spec. 8	Spec. 9
Al	69.32	68.92	70.10	71.91	77.77	80.57	83.17	78.56	79.41
Fe	30.68	31.08	29.90	28.09	22.23	19.43	16.83	21.44	20.59

Spectrum 1 to 4 can be classified as Fe_2Al_5 , and spectrum 5 to 9 can be classified as FeAl_3 . The resulting IMC layer has the same composition of the samples produced between uncoated steel and Al. The discontinuous IMC (spectrum 8 and 9) have a composition very similar to the FeAl_3 intermetallic phase and can be identified as such.

From these spectrums, the presence of Zn was negligible at the weld centre, this may be justified due to the lower melting (419.13 °C) and boiling (907 °C) temperatures of Zn when compared with Al melting point (660.38 °C). There is the possibility of having vaporized the Zn content at the interface of the sample, justifying the low values of Zn at the IMC layer and also to a certain degree, the porosity present at the sample central region.

The Zn presence was also investigated at the edges of the spot weld (Figure 60).

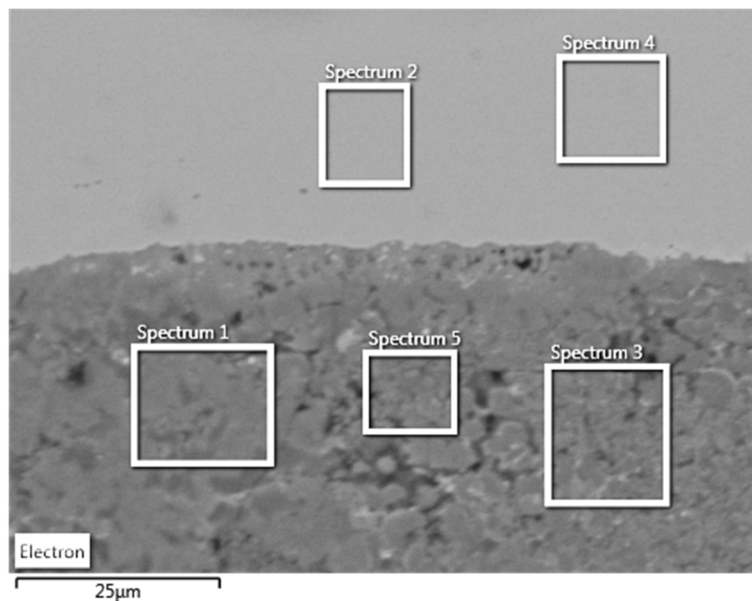


Figure 60 – SEM-EDS analysis made at the edge of the spot weld.

Five rectangular areas were investigated at the Al-Fe interface and the atomic percentage of each element is shown in Table 20.

Table 20 – Atomic percentage for the analysed spectrums at Figure 60.

Spectrum Label	Spec. 1	Spec. 2	Spec. 3	Spec. 4	Spec. 5
Al	75.01	0.68	73.66	0.67	72.37
Fe	13.04	99.32	7.70	99.33	9.28
Zn	11.95	0.00	18.64	0.00	18.35

The Zn content was not detected at the Fe (Spectrum 2 and 4), but Zn was detected close to the Al-Fe interface, and inside the Al alloy. This shows diffusion between the Zn and the Al at the edges of the spot weld. This presence of Zn can be attributed as mentioned before to the lower temperatures and thermal cycles experienced at the weld edges. The presence of Zn shows that the maximum temperatures experienced in this region of the sample were lower to the Zn boiling temperature (907 °C).

The Zn presence at the edges of a weld brazing joint was also reported by (Cao et al., 2013) when using CMT to braze galvanized steel to Al. CMT welding process can also be modelled by a Gaussian energy profile, which will induce a similar Zn distribution inside the weld pool. On the contrary, the IMC detected at the centre of the weld pool by (Cao et al., 2013) were Fe₃Al and FeAl₃ that were different from the ones identified during this work.

To verify if there is any advantage in using the graded aluminium in spite of the Al6111 alloy, shear load tests were made for both Al alloys and the results are shown in Figure 61.

Shear load results for the samples joined with graded aluminium are lower when compared with the aluminium used in the previous set of experiments AA 6111. The relative lower levels of standard deviation of the samples joined with the graded Al (Figure 61) are due to some failure of the joints when handled that made impossible to test them reducing the number of samples to extract

data. This can be justified with the higher defects detected at the joining interface (several porosities).

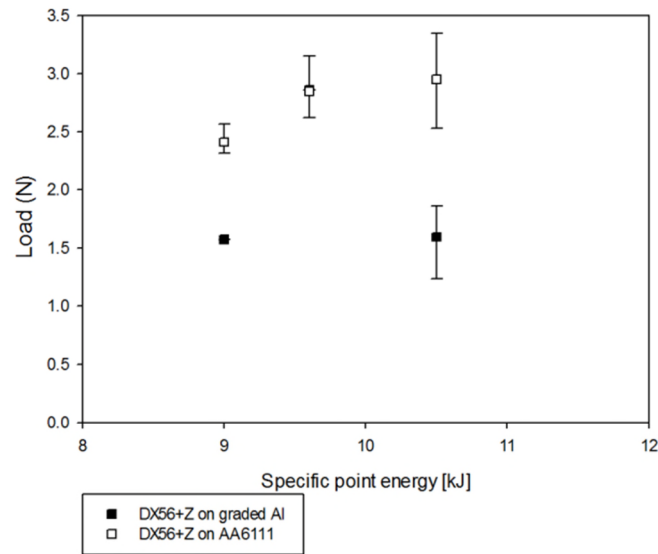


Figure 61 – Shear load results for both Al alloys vs the specific point energy.

To verify if there is any advantage of using galvanized steel to join Fe and Al, the samples produced in section 3.2 and this chapter were compared (Figure 62). These results depict if the addition of Zn at the interface increases the mechanical properties of the joint or if reduces it.

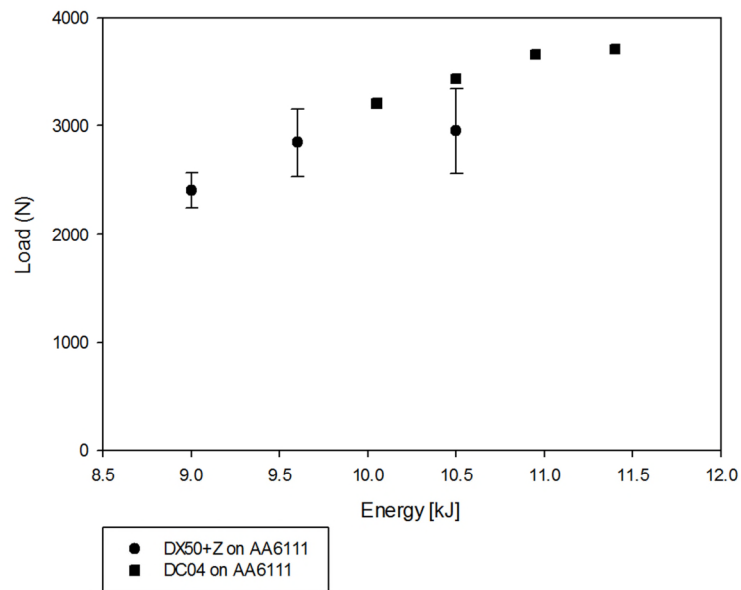


Figure 62 – Load results for Fe-Al joints produced with galvanized and uncoated steel and 6111 Al.

It is observable at Figure 62 that in both cases the shear load increases with the increase of the energy. Samples made between the galvanized steel and the Al alloy had slightly lower mechanical properties when compared with uncoated steel. The lower energy levels at which the galvanized steel samples could be made were due to the use of graphite to increase the coupling coefficient between the laser and the substrate. The Zn acted as a reflective layer that prevented the coupling between the laser light and the sample. For the experiments made in the previous chapter between DC04 (uncoated steel) and Al there was no necessity of introducing the graphite to increase the coupling coefficient and this contributed to higher levels of energy to obtain joined samples.

3.3.4 Conclusions

The presence of Zn was not detected at the centre of the IMC layer, where the joining temperatures are higher. Nevertheless, the IMC layer formation was changed by the presence of Zn with thicker IMC layers and the formation of discontinuous IM compounds. This was justified due to the introduction of a higher stir of the weld pool possibly induced by the Zn vaporization.

The IMC chemical composition was not changed in the presence of Zn. Two layers of Fe_2Al_5 and FeAl_3 were identified for welds between steel (galvanized and uncoated) and Al.

The use of the graded Al (AA4045 + AA6016) alloy was not beneficial for this joining technique, with the samples joined with this aluminium alloy having lower mechanical properties when compared with the previously used 6111Al alloy. This can be related with the higher levels of porosity shown by samples welded with this aluminium.

The mechanical properties of the dissimilar spot joining of galvanized steel and Al. vs uncoated steel and Al. are slightly lower. This is a consequence of the higher levels of the same IMC present at samples made with galvanized steel and also higher levels of porosity detected in the samples.

3.4 Chapter Conclusions

Laser spot welding in conduction mode is a joining process that can be used to join Fe to Al. However the welding range is limited, with an exponential increase in the IMC layer thickness when the specific point energy is increased. This demonstrates that the IMC generation is related with the time temperature profile of the welding process and it is impossible to avoid the IMC formation using the joining process control when using a fusion welding process.

The IMC layer is composed of two different IM compounds, Fe_2Al_5 closer to the steel and FeAl_3 closer to the Al. These compounds showed a maximum hardness of 935 HV that reduced the mechanical properties of the joints. All of the joints obtained had an interfacial failure located where the IMC layer is located, proving that its presence was the dominant factor for the reduced mechanical properties of the joints.

Galvanized steel was also tested, due to its high application in the automotive industry. The presence of the Zn coating at the interface and its low vaporization point, introduced a higher level of stirring of the weld pool. This generates higher levels of IM layers and some defects at the interface. Despite the addition of Zn its presence is not detected at the centre of the weld pool, where the temperatures are higher and the IM compounds present still are Fe_2Al_5 and FeAl_3 . The higher levels of IMC formation are translated to slightly lower mechanical properties of the joints when compared with the joints made with uncoated steel.

In summary laser spot welding in conduction mode can be used to join galvanized and uncoated steel to Al for automotive applications. However the mechanical properties of the joints are lower than those of non-dissimilar welds of Fe and Al. This is due to IMC formation that can be controlled by this welding process but not totally avoided.

4 Stainless steel and Titanium welding

4.1 Chapter introduction

In the literature review Fe and Ti dissimilar joining are classified as a type II dissimilar welding. This is due to the inexistence of solid solubility and the formation of IM compounds (Figure 63) and the dissimilar thermal and physical properties (Table 21).

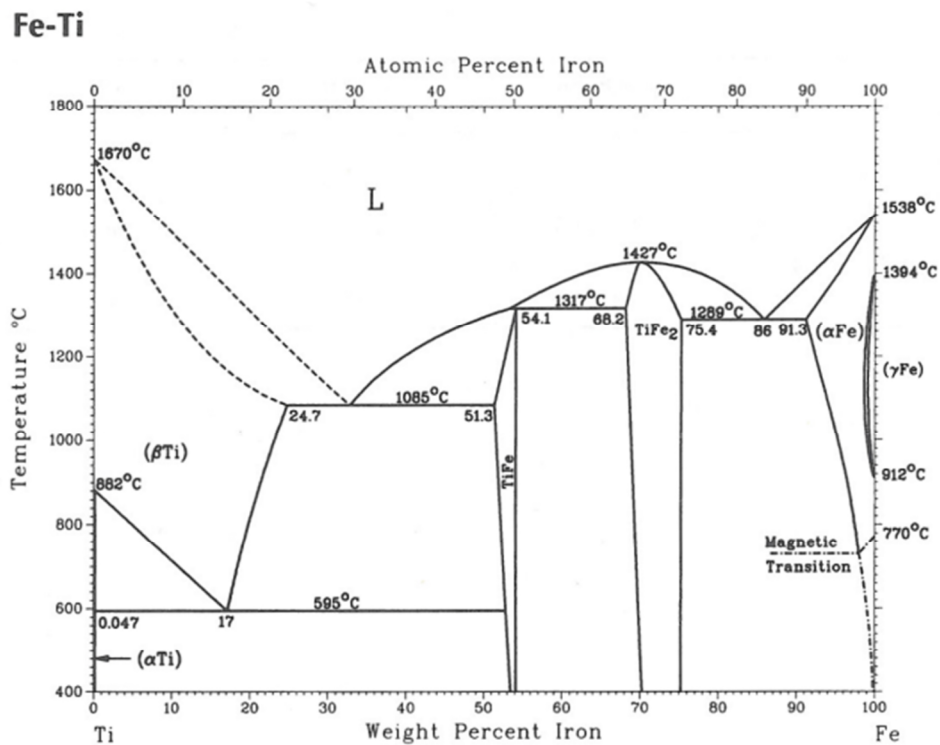


Figure 63 – Fe-Ti phase diagram (ASM - International, 1992).

From the Fe-Ti phase diagram it is possible to identify two equilibrium IMC phases TiFe and TiFe₂. As mentioned in the literature review these phases need to be avoided due to their brittle behaviour (TiFe with 600 HV and TiFe₂ > 1000 HV).

Table 21 shows the different thermal and physical properties of Fe and Ti. It is verifiable that the melting points and the thermal conductivities of these two metals are too similar to try and achieve selective melting of any of the alloys.

Table 21 – Fe and Ti physical properties (Gale and Totemeier, 2003).

Physical property	Fe	Ti
Melting point (°C)	1538	1668
Thermal conductivity [W/(m.K)] at 25 °C	80.4	21.9
Thermal expansion [$\mu\text{m}/(\text{m.K})$ 25 °C	11.8	8.6

As the physical properties (melting point and thermal conductivity) for the Fe-Ti combination are too similar, it will not be possible to do a selective melting of one of the metals using an overlap configuration and a butt joint needs to be considered.

Without the possibility of using the physical properties of the metals as an advantage, the reaction level between the two metals is going to increase and thus the IMC formation.

However, as an initial benchmark overlap autogenous keyhole laser welding was investigated, to establish if there was any weld pool composition range where it was possible to have a satisfactory weld, despite the IMC phases present at the Fe-Ti phase diagram.

After this initial benchmark, due to the similar physical properties between the two parent metals and the welding processes available for our investigation, the second IMC control strategy referenced in chapter 2.3.2 (metallurgical control) is going to be pursued. The metallurgical control of the weld pool by wires and interlayers was extensively investigated to minimise or change the IMC formation on Fe to Ti joining. The use of a single, double or hybrid layers composed of a single, double or multiple metals to minimize block or change the IMC formation was studied by several researchers (Ashfaq et al., 2011; Gao et al., 2012; Tomashchuk et al., 2011; Wang et al., 2013, 2012, 2010).

Two single interlayers were applied to understand how the weld pool composition changes with the introduction of a third metal.

The selected single interlayers were Ni and Cu, and laser welding and CMT welding were used respectively. The final part of this chapter is an investigation in using hybrid interlayers to prevent the IMC formation. The metals used in the hybrid interlayer were carefully chosen to prevent any reaction with the parent metals. And the application of this hybrid interlayer was done by WAAM (Wire Plus Arc Additive Manufacturing) (Kazanas et al., 2012). This process is a 3D printing process that uses welding equipment to build a structure layer by layer using a welding arc process. Using this process is possible to manufacture tailored interlayered component in any shape to be applied to the final component or structure.

4.2 Keyhole laser welding of stainless steel to Ti with and without Ni as an interlayer

4.2.1 Introduction

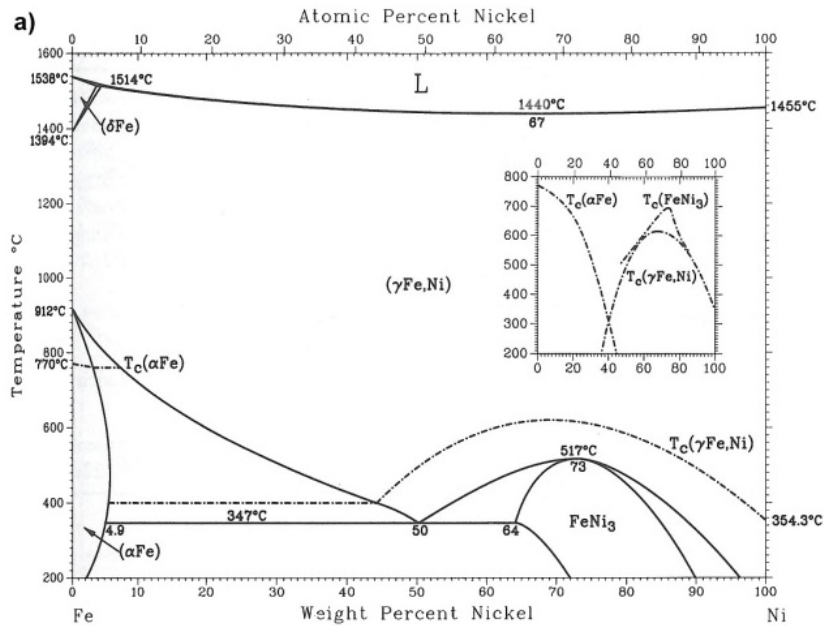
To fully assess the degree of incompatibility between stainless steel and Ti and the necessity of acting at the weld pool metallurgy and composition, it is necessary to investigate autogenous welding of these metals. This investigation will verify if there is any dilution ratio between the two parent metals where a mechanical sound joint is obtainable. To evaluate the possibility of direct welding of Ti and stainless steel, overlap keyhole mode laser welding was selected. Overlap laser keyhole welding was selected due to the following characteristics:

- Energy control – Laser welding enables a better control in the energy used during welding when compared with Arc welding processes. A broad spectrum of mixing ratios between the two parent metals will be achievable by changing the penetration depth at the lower plate in the overlap configuration.
- High mixing ability – Keyhole mode is formed by vaporization of the parent metals. This vaporization induces a high stirring effect in the weld pool and enables an even distributed weld pool composition (Steen and Mazumder, 2010).

If the presence of IMC phases and or cracks on the welding beads could not be avoided by changing the mixing ratio of the parent metals, the use of interlayers and other materials needs to be investigated.

The first metal selected as a candidate interlayer was nickel. Nickel has melting point close to the parent metals (1455 °C) and has a good compatibility with stainless steel (Figure 64), being one of the main alloying elements present on AISI 316L stainless steel (10 Wt%) and also shows a solid solubility of 5 Wt% with Ti.

Fe-Ni



Ni-Ti

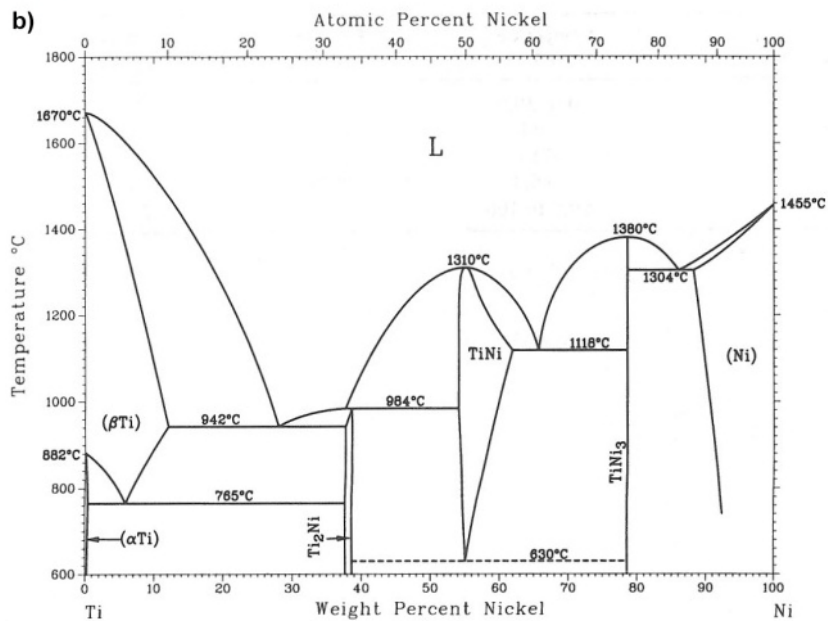


Figure 64 – Fe-Ni a) and Ni-Ti b) phase diagrams (ASM - International, 1992).

The compatibility of Fe and Ni is expressed by the Fe-Ni phase diagram, with only one IMC phase present, FeNi₃. A lower solid solubility between Ni and Ti is verified in the Ni-Ti phase diagram, with the presence of several IMC phases (Ti₂Ni, TiNi and TiNi₃). Nevertheless TiNi IMC has acceptable mechanical

properties; it is used as shape memory alloy and is more commonly referred as Nitinol (Otsuka and Ren, 2005). It is also observable a terminal solid solution between Ti and Ni for alloys or melt pool compositions with high concentrations of Ni (close to 100 %wt Ni). The goals for this experiment are to verify if the use of thick Ni interlayer with two separate laser welds (Ni-Fe and Ni-Ti interfaces) in a butt joint configuration could generate a defect and IMC free joint, by avoiding direct mixing between Fe and Ti. Or if by changing the laser beam distribution, ratio of energy incident in the interlayer and parent metal, is possible to avoid or eliminate IMC and crack formation and generate a defect free weld between Ti and stainless steel.

4.2.2 Experimental procedure

4.2.2.1 Autogenous laser overlap dissimilar welding

To address the possibility of direct laser welding of Ti to stainless steel two alloys used by the aerospace and energy generation industries were selected, AMS 4911L (Ti-6Al-4V) and AISI 316L (Table 22).

Table 22 – Selected stainless steel and Ti alloy compositions

Material	C	Si	Mn	P	S	Cr	Ni	Mo	N	Fe	Pb	Al	Cu	V	O
AISI 316L	0.020	0.45	1.73	0.032	0.01	17.2	10.0	2.07	0.054	Bal	-	-	-	-	-
AMS 4911L	0.08	-	-	-	-	-	-	-	0.5	0.3	-	5.5 - 6.75	-	3.5- 4.5	0.2

Stainless steel plates with dimensions 150x100x2 mm (LxWxT) and Ti plates with dimensions 150x100x1.7 mm were used in full overlap configuration. The weld seams produced were 130 mm length. Each plate was manually ground with SiC paper, finished and finally cleaned with acetone prior to each experiment. Figure 65 depicts the experimental setup for this set of experiments.

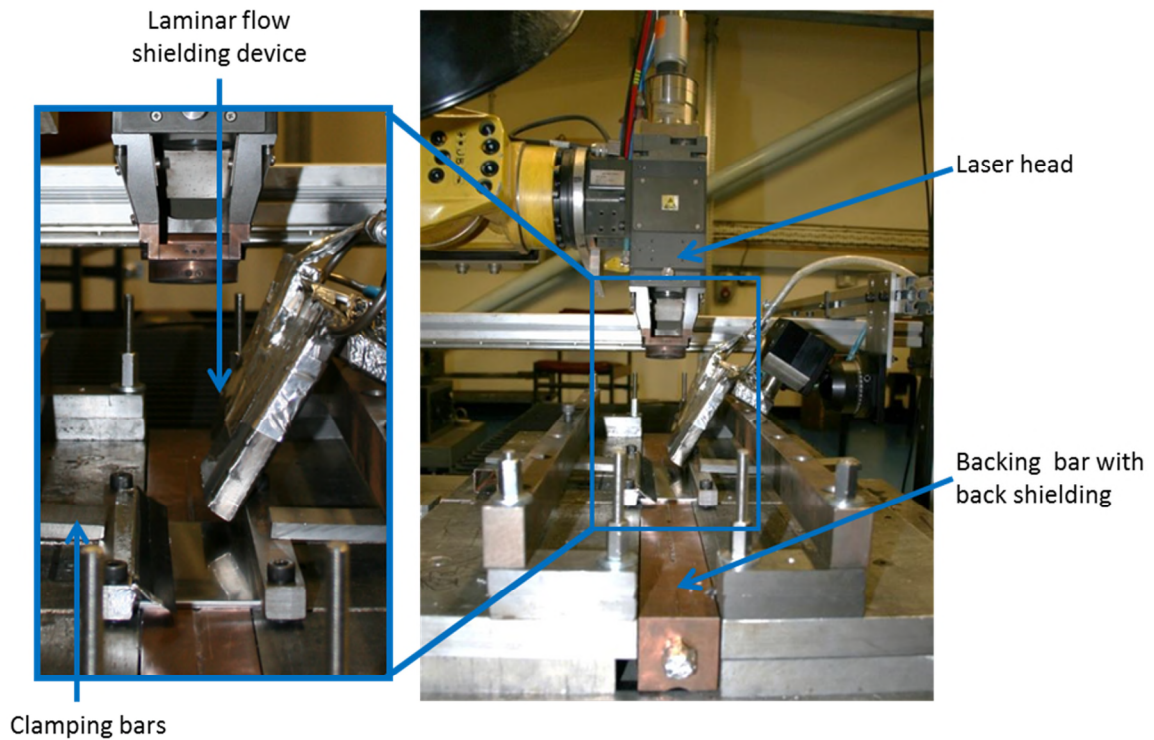


Figure 65 – Autogenous laser welding of Ti and stainless steel experimental setup.

The clamping system was composed of a Cu backing bar inserted into an Al base plate. Titanium is a reactive metal and it reacts with oxygen at temperatures above 400 °C. This generates the necessity of not only shielding the weld pool with argon, but also the already solidified metal after the melt pool, that remains at temperatures above the previously mentioned 400 °C. A laminar shielding device was used to shield the complete weld seam during welding. To prevent any oxidation of the welded joints, the laser was maintained 30 mm behind the beginning of the laminar shielding device. This enables a pre shielding effect as well as a post shielding effect and so reducing the oxidation levels during welding. The laser beam and the laminar shielding device were kept stationary whilst the plates were displaced at constant speed to create the welded joint. The root of the weld was also shielded using a drilled Cu backing bar with a low flow of Argon shielding. Two clamping bars were used against the top plate to exert pressure between the two plates and enable the overlap joint to form.

As mentioned before the laser beam was used in keyhole mode, so the beam was used at its focal position with a diameter of 0.6mm, using the 250 mm focusing lenses. To obtain several weld pool compositions the plates were alternated from top to bottom and the laser interaction parameters were also changed (Figure 66).

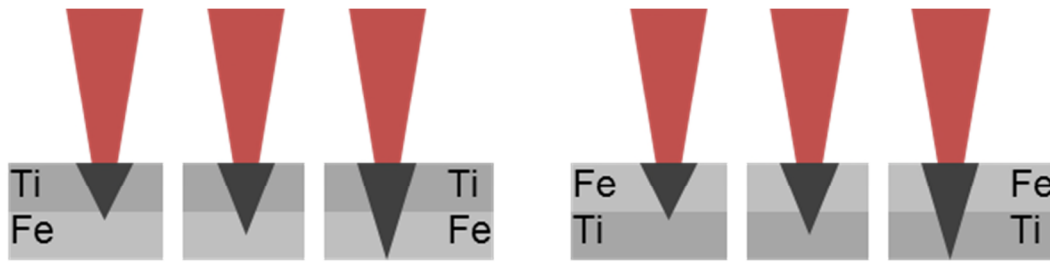


Figure 66 – Schematic representation from the autogenous laser welding from stainless steel to Ti.

The relevant experimental parameters are shown in Table 23.

Table 23 – Autogenous stainless steel to Ti experimental data.

Sample	Plate configuration (Top – bottom)	System parameters			Fundamental laser interaction parameters		
		Spot diameter (mm)	Power (kW)	Travel speed (cm/min)	Power density (kw/cm ²)	Interaction time (s)	Specific point energy (J)
1	Ti-Fe	0.6	1.0	100	353.68	0.036	36.0
2			1.3		459.78		46.8
3			1.5		530.52		54.0
4			1.8		636.62		64.8
5	Fe-Ti		1.3		459.78		46.8
6			1.5		530.52		54.0
7			1.8		636.62		64.8
8			2.0		707.36		72.0

4.2.2.2 - Butt dissimilar laser welding using a thick Ni interlayer

For the Ni interlayer based experiments laser was also used in keyhole mode, but the joint was positioned in butt configuration. With this configuration it is

easy to change the laser distribution between the interlayer and the parent metals to obtain different weld pool compositions. This configuration also enables to have two separated weld pools and evaluate the interaction between the Ni interlayer and each of the parent metals. The experimental setup used to test the Ni interlayer is similar to the direct joining of stainless steel and Ti (described previously). The laser beam and the laminar flow shielding device are stationary and the laser beam is also located 30 mm from the beginning of the laminar shielding device. However this experiment is done in butt configuration and it was necessary to introduce pressure bars and positioners to enhance the contact between the parent metals and the interlayers and also ensure the positioning between laser beam and the interfaces to be joined (Figure 67 a).

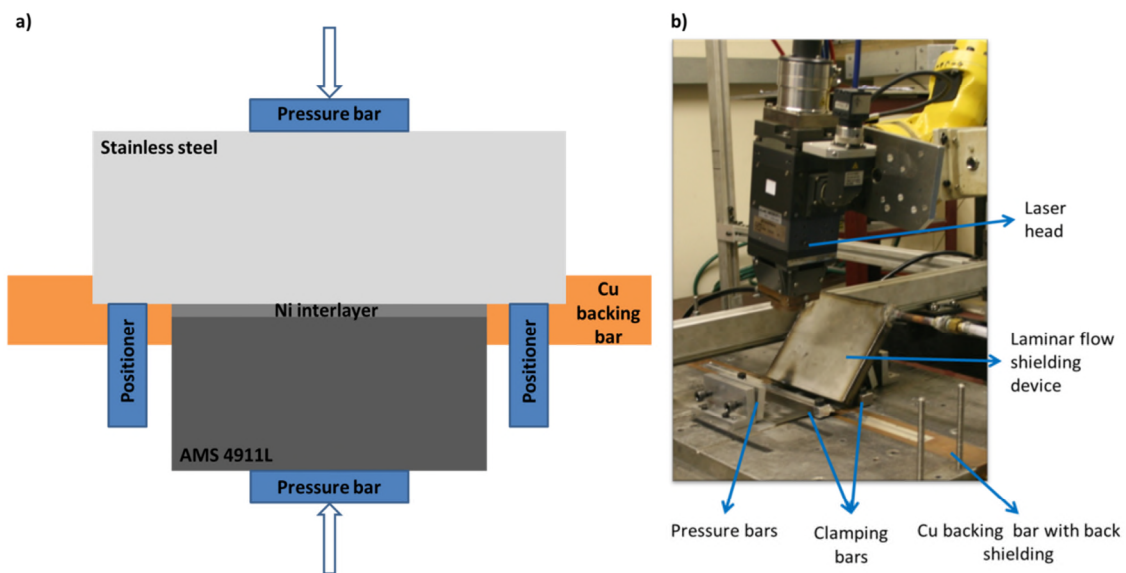


Figure 67 – Schematic representation of the experimental setup for butt weld configuration a) and the actual experimental setup b).

Stainless steel plates with dimensions 150x100x2 mm (LxWxT) and Ti plates with dimensions 100x100x1.7 mm (LxWxT) were used and the alloys used were the same as in the previous experiments (AISI 316L and AMS 4911L). The plates were positioned in the butt configuration with the Ni interlayer between them.

The first weld sample 9 from Table 24 was made using a Nickel interlayers with 100x3x2 mm (LxWxT) that was positioned between the two parent metals and two weld seams were made leaving a solid barrier of Ni in the centre of the interlayer to avoid the diffusion between the parent metals Figure 68 a).

A second weld was made subsequently sample 10 Table 24 (Figure 68 b) to identify the most suitable mixing ratio between Ti and Ni. This sample consisted in a single weld between the Ni interlayer and the Ti. In this case the beam was scanned diagonally over the interface between Ti and Ni to create different beam distributions and consequently different weld pool compositions (Figure 68 b).

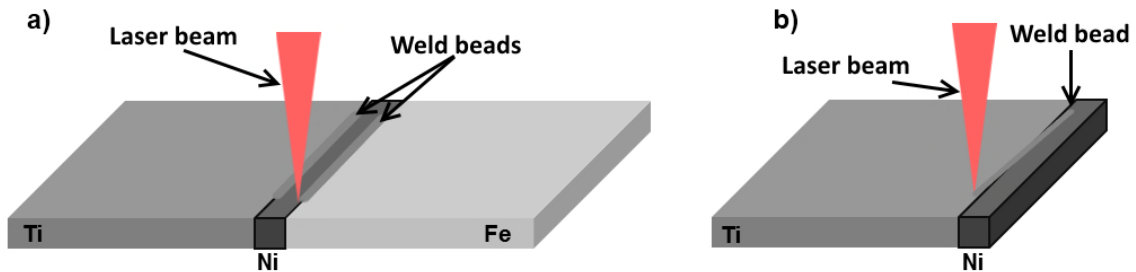


Figure 68 – Ti to Ni and Ni to stainless steel joining a) and different weld pool compositions between Ti and Ni using the laser scanned diagonally at the interface b).

The welding parameters for the experiments depicted in the previous figure are shown in Table 24.

Table 24 – Welding parameters for thick Ni interlayer evaluation.

Sample	Interface	Spot diameter (mm)	Power (kW)	Travel speed (m/min)	Power density (kw/cm²)	Interaction time (s)	Specific point energy (J)
9	Ti – Ni	0.6	1.2	1.0	424.41	0.036	43.2
	Ni – Fe	0.6	1.2	1.0	424.41	0.036	43.2
10	Ti -Ni	0.6	1.1	1.0	389.05	0.036	39.6

After the welding experiments metallographic specimens were prepared by cutting and mounting the samples in conductive resin. The samples were ground using silicon carbide paper and polished using diamond paste and colloidal silicon suspension mixed with oxalic acid. They were analysed by optical microscopy and by scanning electron microscopy and electron dispersive spectroscopy (SEM/EDS). Hardness mapping of the specimens was also carried out using a ZWICK Vickers micro hardness machine. The Harness tests were made following the EN6507-1 ISO standard (BS EN ISO 6507 - 1, 2005) and with the following parameters HV 0.1 / 10.

4.2.3 Results and discussion

4.2.3.1 Autogenous laser overlap dissimilar welding

Overlap direct welding of Ti and stainless steel revealed that the direct welding of these two metals was not possible. Applying keyhole welding and enabling the different mixing ratios between the two metals was not enough to prevent the crack formation and the joints brittleness. This is demonstrated by the presence of micro and macro cracks shown in Figure 69.

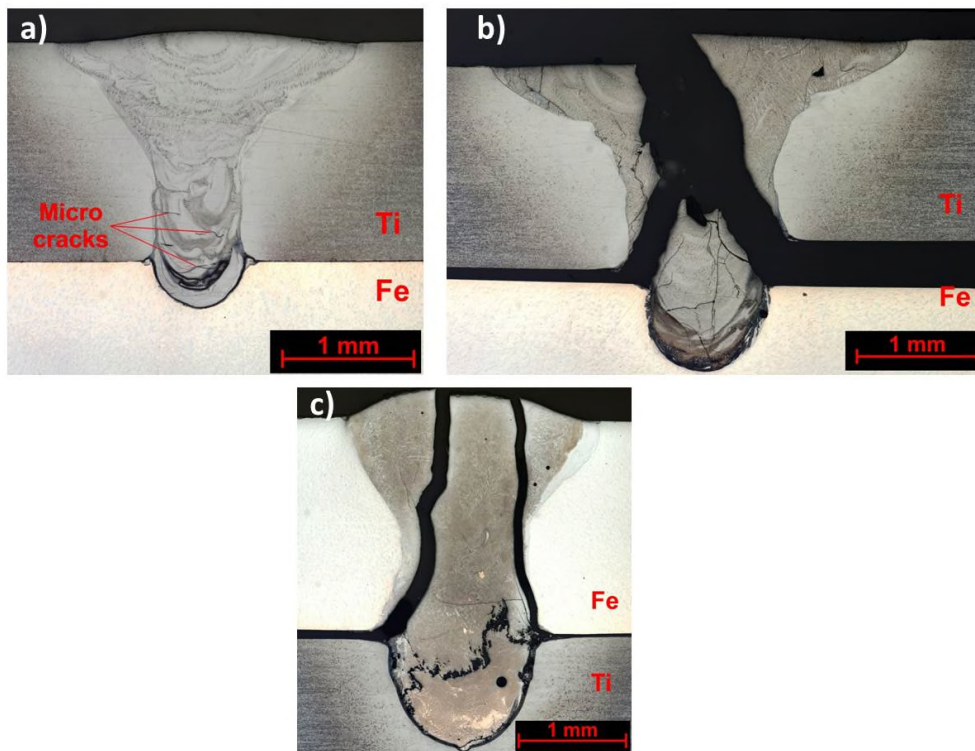


Figure 69 – Micrographs with evident cracking from direct overlap samples between stainless steel and Ti. Sample 1 shows micro cracking a), while samples 2 and 8 show macroscopic cracking b) and c).

To understand the mixing ratios between Fe and Ti for all the welded specimens, SEM analysis was carried out. The atomic percentage of Ti and Fe was analysed inside the weld profile (Table 25).

The only specimen without cracks was specimen 5 (table 25), however the mixing ratio between the two metals was very low which impairs the mechanical properties due to low dilution.

Table 25 – Fe and Ti mixing ratios inside the weld pool and penetration depth for the lower plate in laser overlap keyhole welding of Ti and stainless steel.

Sample	Ti (%at)	Fe (%at)	Lower plate penetration depth (mm)	Lower plate penetration depth (%)	Lower plate
1	89.38	10.62	0.33	16.50	Fe
2	80.08	19.92	0.72	36.00	Fe
3	74.09	25.91	0.93	46.50	Fe
4	68.65	31.35	1.31	65.50	Fe
5	2.87	97.13	0.07	4.12	Ti
6	20.30	79.70	0.52	30.59	Ti
7	38.32	61.68	0.84	49.41	Ti
8	28.99	71.01	1.00	58.82	Ti

As expected the table shows that with the increase in the penetration depth at the lower plate there is also an increase of the distribution of Fe or Ti inside the weld pool composition. However this cannot be applied to samples 7 and 8, this can be explained by the loss of a considerable part of the weld during cutting and polishing phases (Figure 70) leaving just a small area close to the lower plate (Ti) to make the EDS analysis.

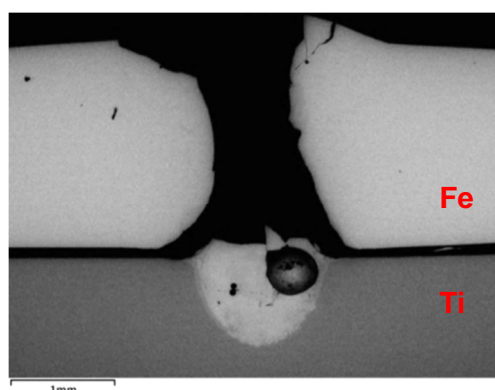


Figure 70 – Loss of weld profile due to high brittleness and cracking occurred during welding, cutting and handling of the sample.

To further investigate if the mixing ratio was constant through the depth of the weld bead, EDS mapping was also carried out for samples one, three and eight (Figure 71).

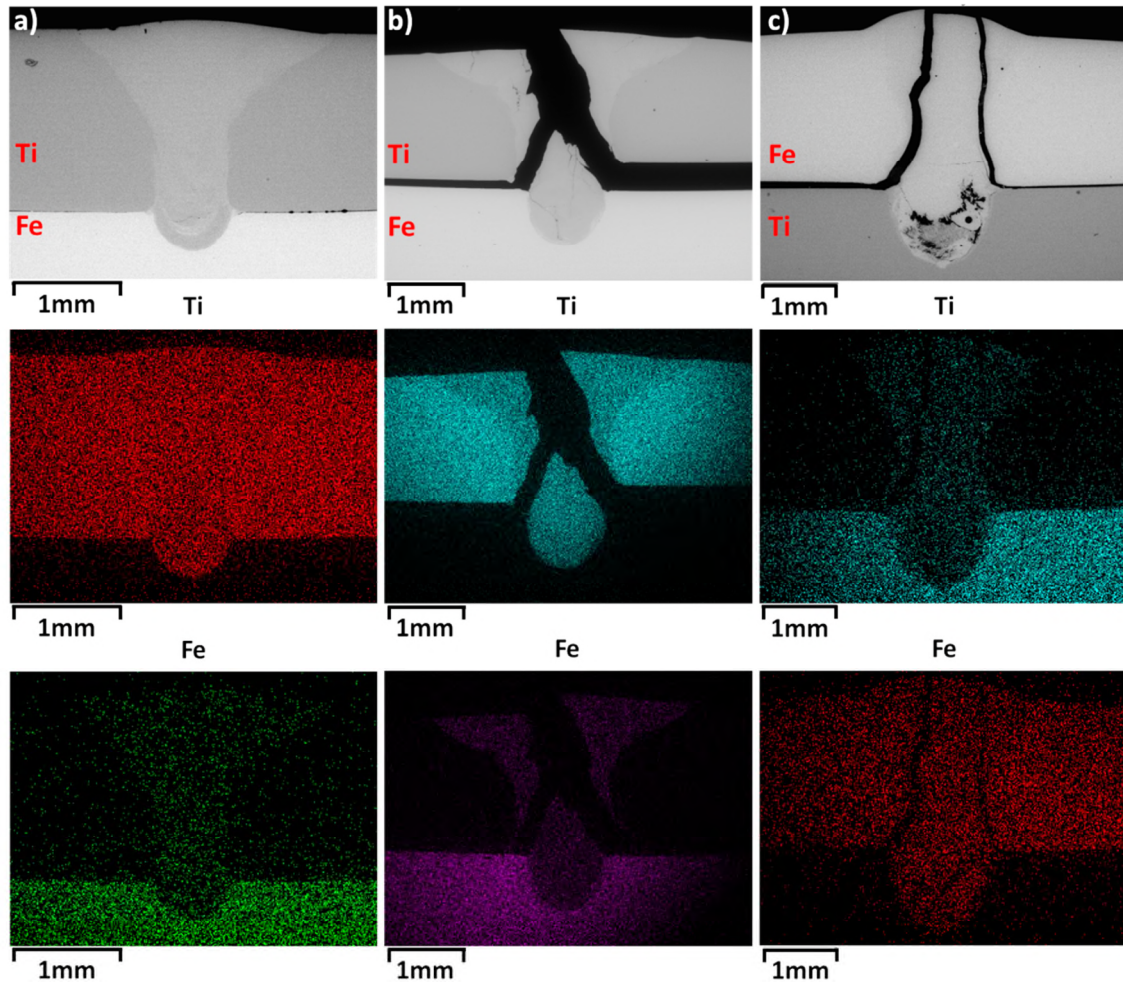


Figure 71 – EDS mapping (Fe and Ti) to evaluate the mixing ratio uniformity inside the weld profile. Sample 1 a), sample 2 b) and sample 8 c).

These EDS mapping results show that there is no concentration gradient either of Ti or Fe through the weld bead after welding. This is due to the relative low travel speed that these welds were made and also due to the high stirring levels of keyhole laser welding.

these two metals and their alloys. It was necessary to introduce a new metal to bridge the different dissimilar mechanical and metallurgical properties.

4.2.3.2 - Butt dissimilar laser welding using a thick Ni interlayer

Ni was chosen as a candidate metal to mitigate the dissimilarities between Fe and Ti. The first set of experiments consisted in having a thick interlayer of Ni between the stainless steel and Ti. Two separated welds were made, by using once again the laser in keyhole mode. These two welds were made at the Ni stainless steel and Ni Ti interfaces and care was taken to avoid any connection between the two weld seams (Figure 73).

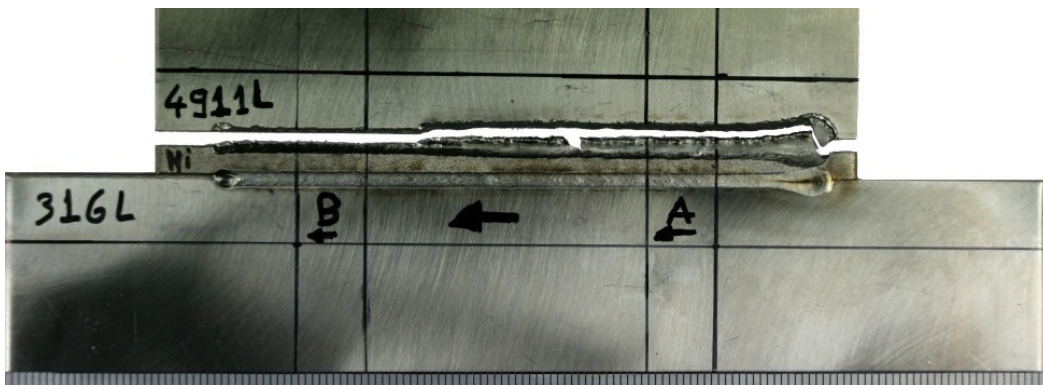


Figure 73 – Thick Ni interlayer sample on stainless steel to titanium welding keyhole laser welding.

The separation of the two weld seams is important to prevent any diffusion between Ti and stainless steel enabling the possibility to evaluate the compatibility of the selected interlayer towards each of the parent metals (Fe and Ti).

The weld seam at the Ni-Ti interface presents a crack along the weld bead, this indicates a high brittle behaviour present between Ti and Ni. In the opposite spectrum is the stainless steel – Ni weld seam that does not present any crack and major superficial defect. This was expected due to Ni higher metallurgical solid solubility towards Fe than Ti. To further investigate the difference between these two welds the sample was sectioned and the side A of the sample (Figure

73) was observed under the optical microscope. Figure 74 shows the samples macro section.

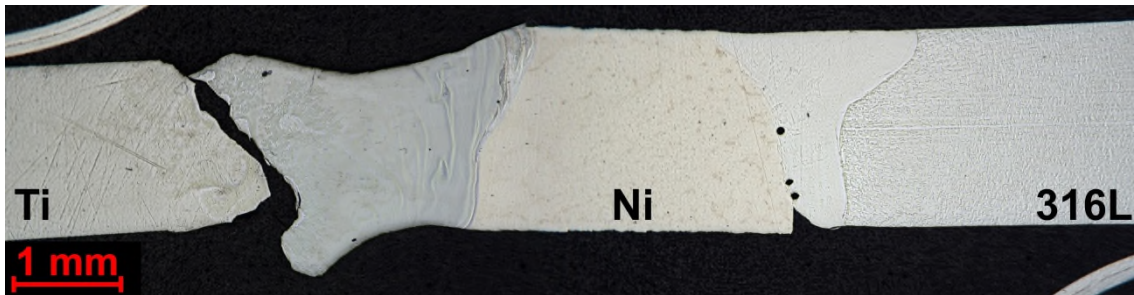


Figure 74 – Optical micrograph from sample created with two weld seams and an interlayer of Ni.

At the stainless steel Ni interface no internal crack could be detected, but a lack of fusion is observed. In contrast the Ni Ti weld, at the interface shows good wetting and mixing, but it has a macroscopic crack is present. To identify the possible presence of IM compounds in this sample both welds were characterised by SEM/EDS analysis (Figure 75 and 77).

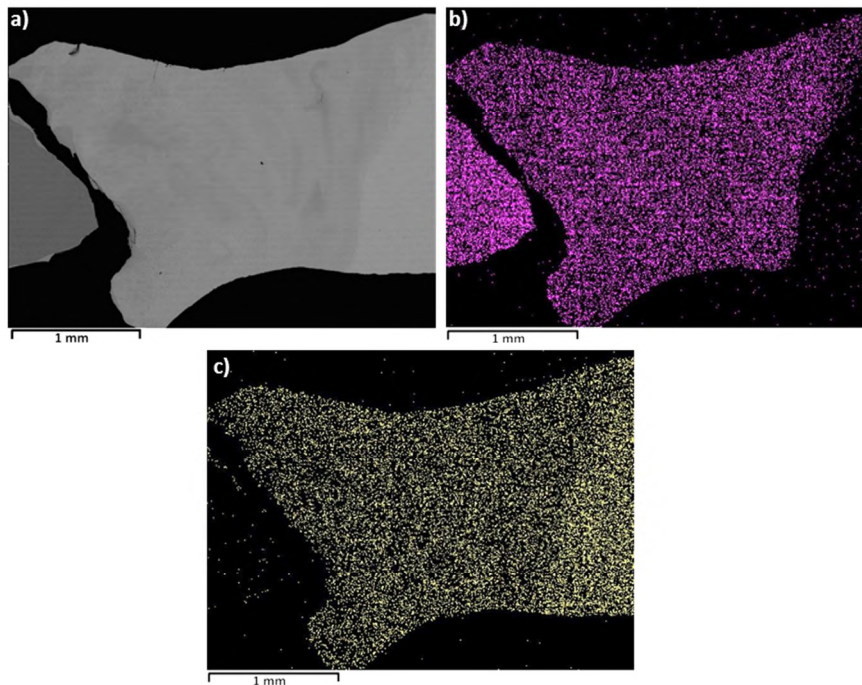


Figure 75 – Back scattered electron image a) for the Ti–Ni interface and corresponding Ti b) and Ni c) distributions at the weld pools.

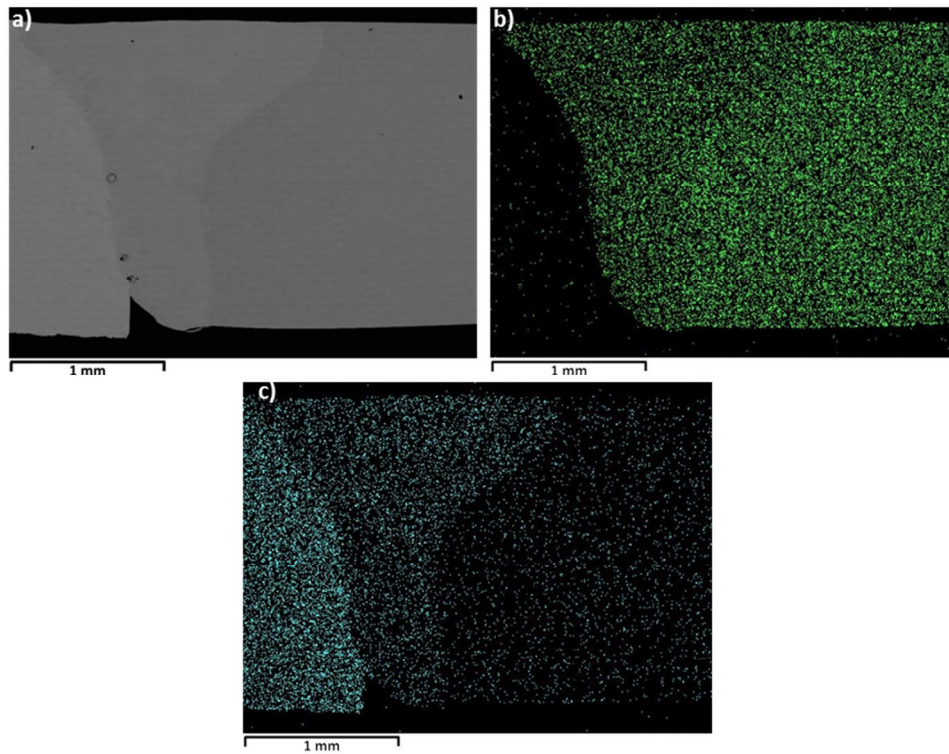


Figure 76 – Back scattered electron image for the Ni-Fe interface a) and corresponding Fe b) and Ni c) distributions at the weld pools.

From the weld pool mapping it is again observable a good stirring of the weld pool, without concentration gradients in either the vertical or horizontal directions.

The correspondent weld pool compositions are shown in Table 26.

Table 26 – Weld pool composition at the stainless steel Ni and Ti – Ni interfaces.

Material	Cr (%at)	Fe (%at)	Ni (%at)	Ti (%at)
Fe-Ni interface weld	13.03	49.18	37.78	-
Ti-Ni interface	-	-	57.41	42.59

At the Fe-Ni interface, the weld pool composition needs to be evaluated against a ternary phase diagram (Figure 77) (ASM - International, 2012; Raynor and Rivlin, 1988) due to the high levels of chromium present in the weld pool that were introduced by the stainless steel (Fe). The weld pool composition is inside the all austenitic phase that dominates the Fe-Cr-Ni phase at 900° C. This

process can also be described as an addition of Nickel content into the 316L stainless steel, as one major alloying elements of stainless steel is Ni. The addition of Ni in stainless steel has the advantage of adding corrosion resistance at high temperatures (Reardon, 2011).

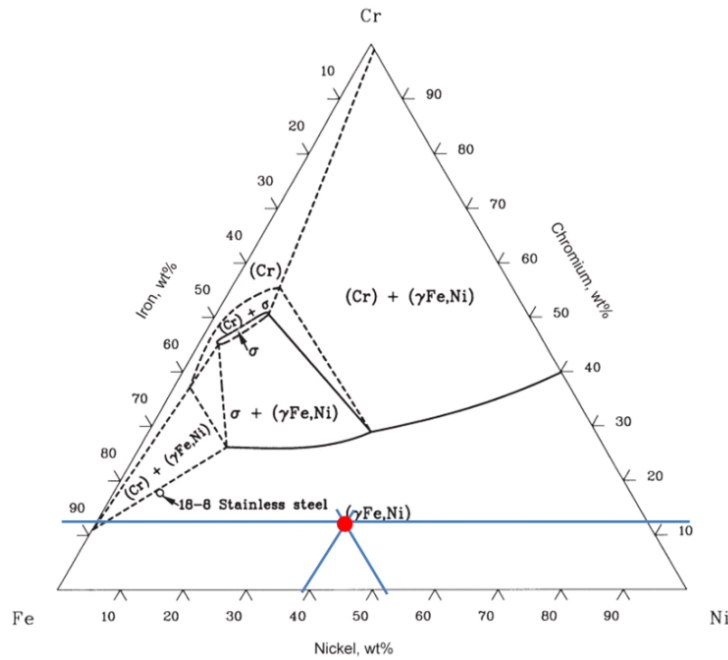


Figure 77 – 900 °C isothermal of the Fe-Cr-Ni ternary phase diagram.

However, at the Ni-Ti interface, brittle IMC compounds have developed, this is evidenced by the macroscopic crack present in the referred weld pool. This weld pool composition shown in Table 26 is between NiTi and TiNi₃ phases, confirming the brittle IMC formation.

By using two different welds it is possible to avoid the formation of the brittle Ti-Fe phases; however different brittle Ni-Ti phases are present.

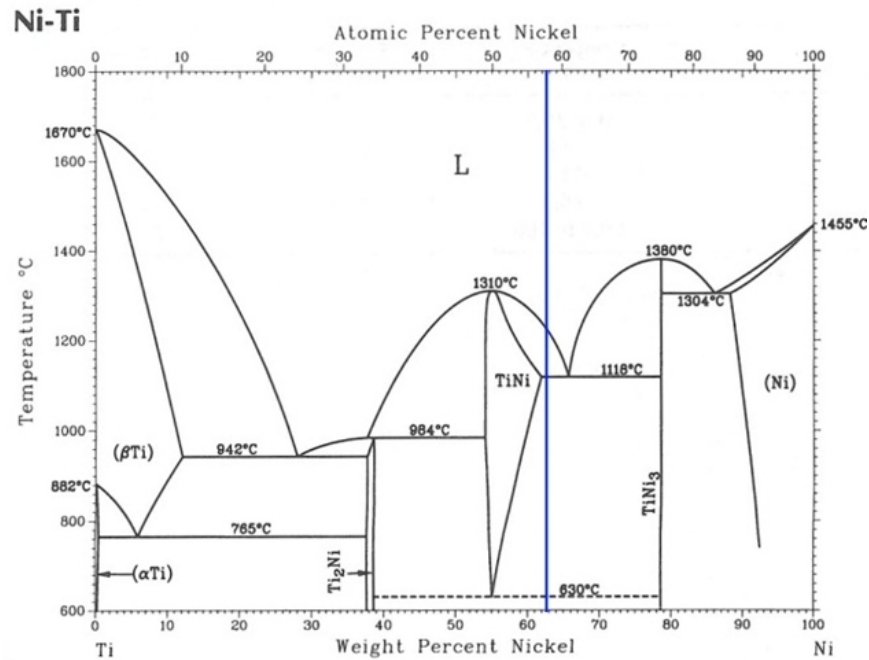


Figure 78 – Ni-Ti phase diagram.

The presence of brittle IMC's on the Ni-Ti interlayer showed the necessity to assess if by changing the weld pool composition between these two metals would enable an IMC free weld pool. As referred in the experimental procedure, a diagonal weld across the Ti-Ni interface was made. The laser was scanned across the Ni-Ti interface, starting 100% on Ti and finishing 100% on the Ni side. This diagonal scanning from the laser beam across the two metals originated several different weld pool composition and mixtures. Several metallographic samples were extracted along the weld seam (Figure 79).

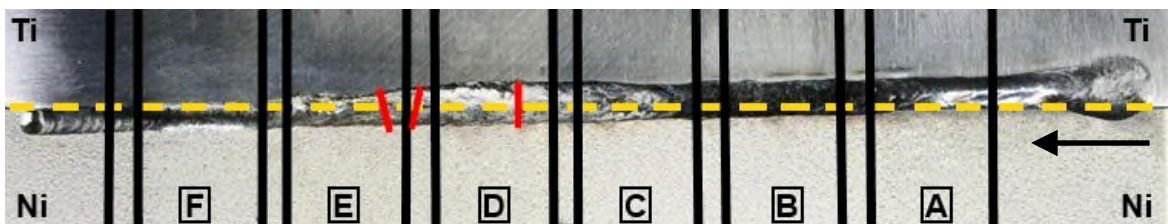


Figure 79 – Metallographic samples extracted for further investigation.

In Figure 79 the dashed yellow line represents the interface between the two participating alloys before the welding process, and the red lines represent superficial crack location. The double vertical black lines represent where the

samples were cut and observed under the microscope. The black arrow shows the laser scanning direction.

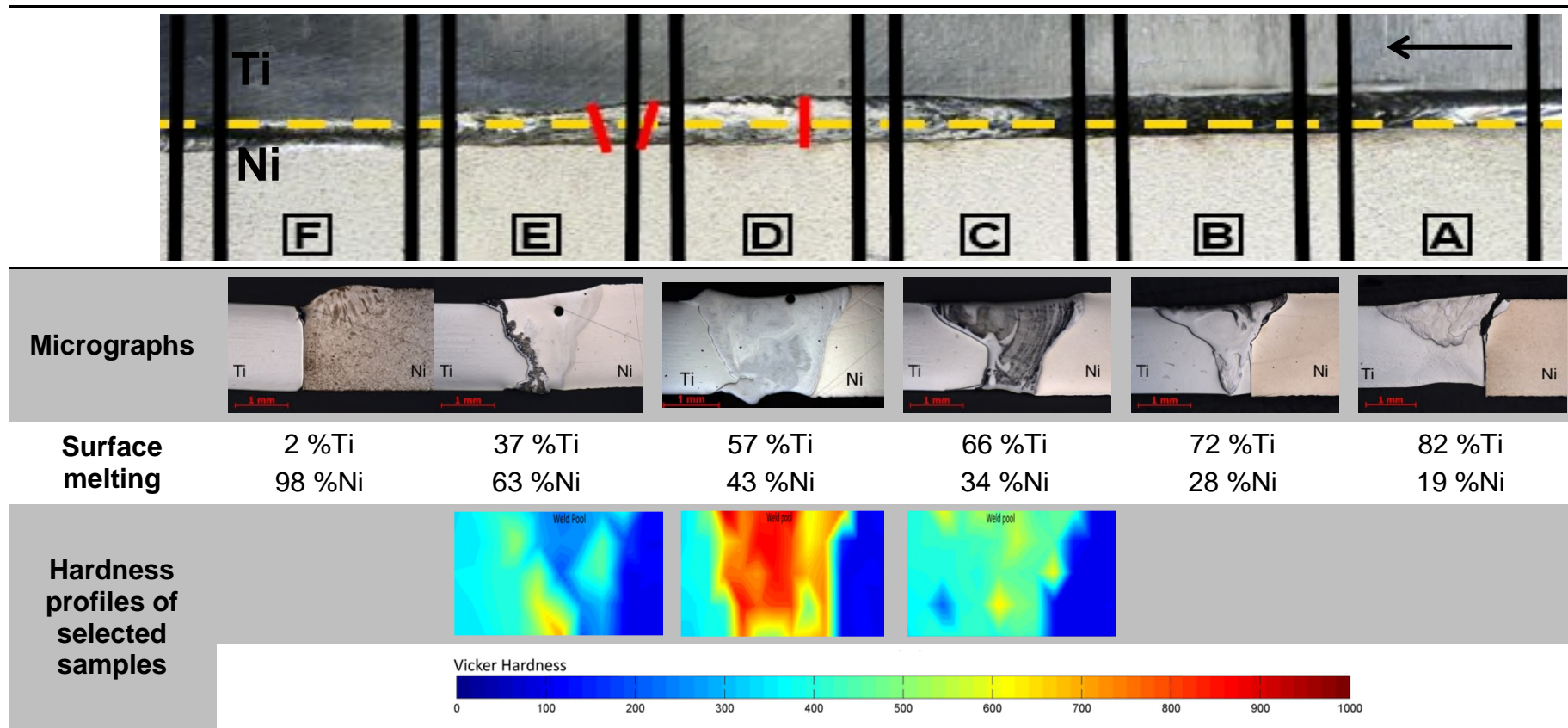
Table 27 shows the micrographs for samples A to F and the corresponding surface melting in relation to the material interface (how the surface melting is distributed in relation to Ni and Ti). In this table, the hardness profile of the selected samples is also shown; however a greater detail of these maps is shown in Figure 81.

Samples A, B and F were not analysed further due to weld location in relation to the joint, the wetting of the metals is not enough to generate an acceptable weld.

Samples C, D and E were analysed under the SEM and chemical composition of several spectrums along a horizontal line were measured. The chemical composition was plotted in graphs that are presented in Figure 80.

In each of the graphs, the vertical dashed lines represent the location of the parent metals in relation to the horizontal line where the EDS spectrums were extracted. Analysing Table 27 and Figure 80, there is a more uniform mixing in samples C and D, while sample E has a segregation of the IMC formed towards the Ti side. This can be related with the energy distribution, towards the Ni side, that increases the Ni content in the weld pool. In the three observed samples, the Ni content in the weld pool increases with the increasing of the energy distribution towards the Ni metal. This reveals the high directionality and the high precision in which the laser energy distribution can be controlled when compared with the arc welding processes.

Table 27 – Ti-Ni micrographs and selected samples hardness maps for the Ni-Ti diagonal weld.



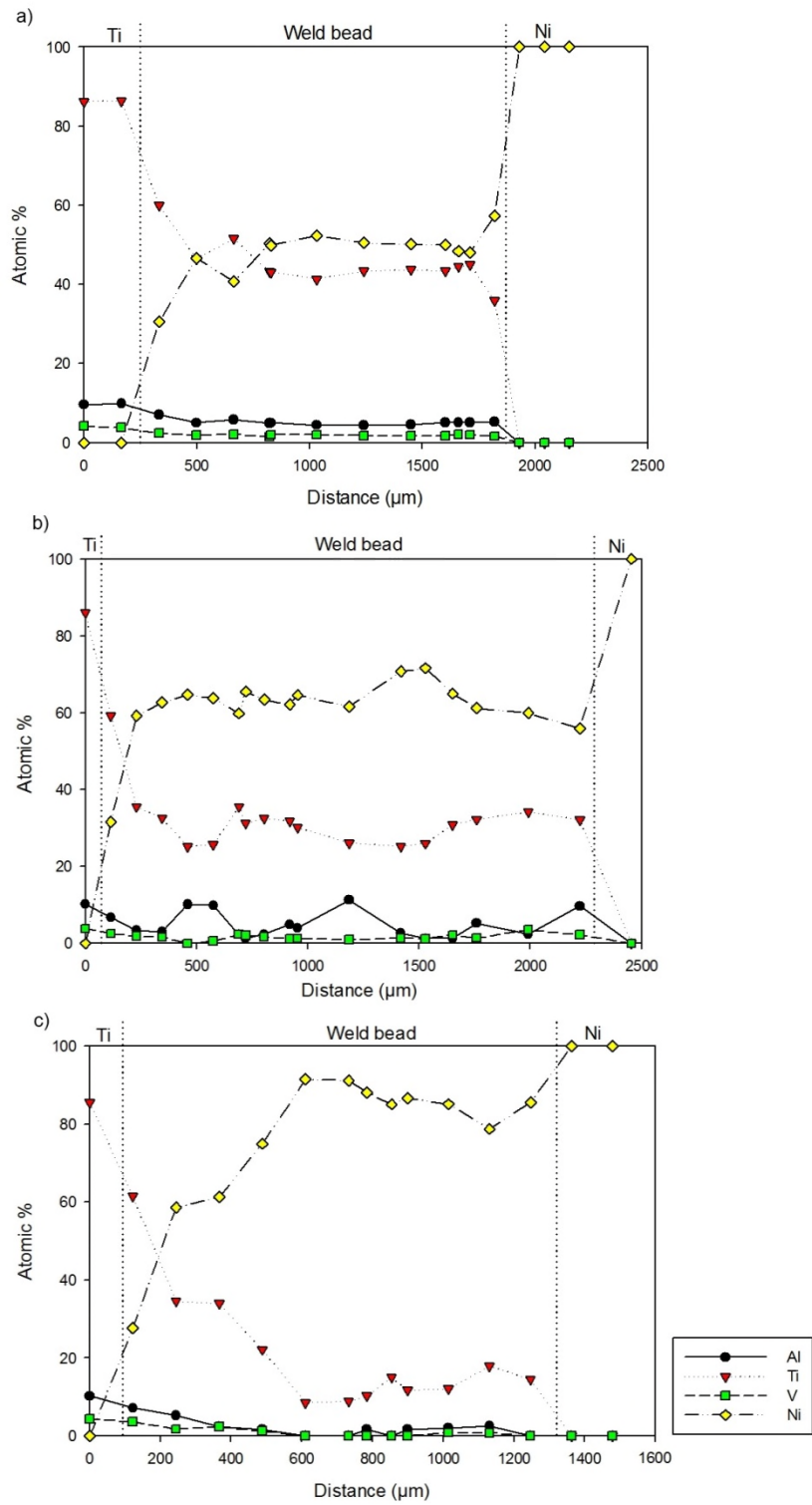


Figure 80 – Atomic composition for a horizontal line across the weld bead. Sample C a), sample D b) and sample E c).

Verifying each of the stable regions of the weld pool composition, of each of the samples shown, it is possible to evaluate the IMC composition for the bulk of the weld pool (Table 28).

Table 28 – Comparison between the surface melting distribution, the average atomic percentage and identification of the correspondent IMC phase.

Sample	Surface melting distribution (%)		Average atomic percentage in stable region (at %)		Possible IMC phase
	Ti	Ni	Ti	Ni	
C	66	34	46.5	53.5	NiTi+ Ti Ni₃
D	57	43	32.8	67.2	NiTi+ Ti Ni₃
E	37	63	12.6	87.4	Ti Ni₃+Ni

Table 28 shows that the surface melting distribution it is not a good indicator of the atomic percentage in the weld pool, with a higher concentration of Ni in the weld pool when compared with the surface distribution. This can be related with the weld pool shape and also the dissimilar thermal properties of the welded metals generating an asymmetric weld pool. The weld pool shape seems to favour the melting of Ni in the depth direction, due to its higher thermal conductivity and lower melting point when compared with Ti. The same aspect can be verified in the work by (Chatterjee et al., 2006) where CO₂ laser welding between Ti and Ni was achieved. However this work only analysed one energy distribution and so only one weld pool composition was achieved for the bulk of the weld pool.

The different atomic percentages observed at the constant areas of the weld pool, show that the surface melting closer to 50% of energy distribution (sample D) is the sample with higher values of the TiNi₃ IMC. However the remainder two samples have a higher percentage of NiTi and Ni and so the hardness levels should be lower. To evaluate the hardness distribution and variation in each sample, contour maps of the Vickers micro hardness were plotted (Figure 81).

These maps reveal a good agreement with the IMC's found on the bulk of the weld pool, showing the higher hardness for sample D, that has higher percentage of NiTi₃. This is the phase with the higher hardness in the Ni-Ti phase diagram with a determined value of 1000 HV (Thoma, 1986). Sample C has an intermediate hardness, but it is well distributed throughout the weld pool. However sample E has higher levels of hardness close to the Ti – weld pool interface. This is related to the segregation of the IMC to this zone of the weld pool. Welding processes are not done in equilibrium; the interaction time is measured in millisecond which inevitably reduces the time for diffusion.

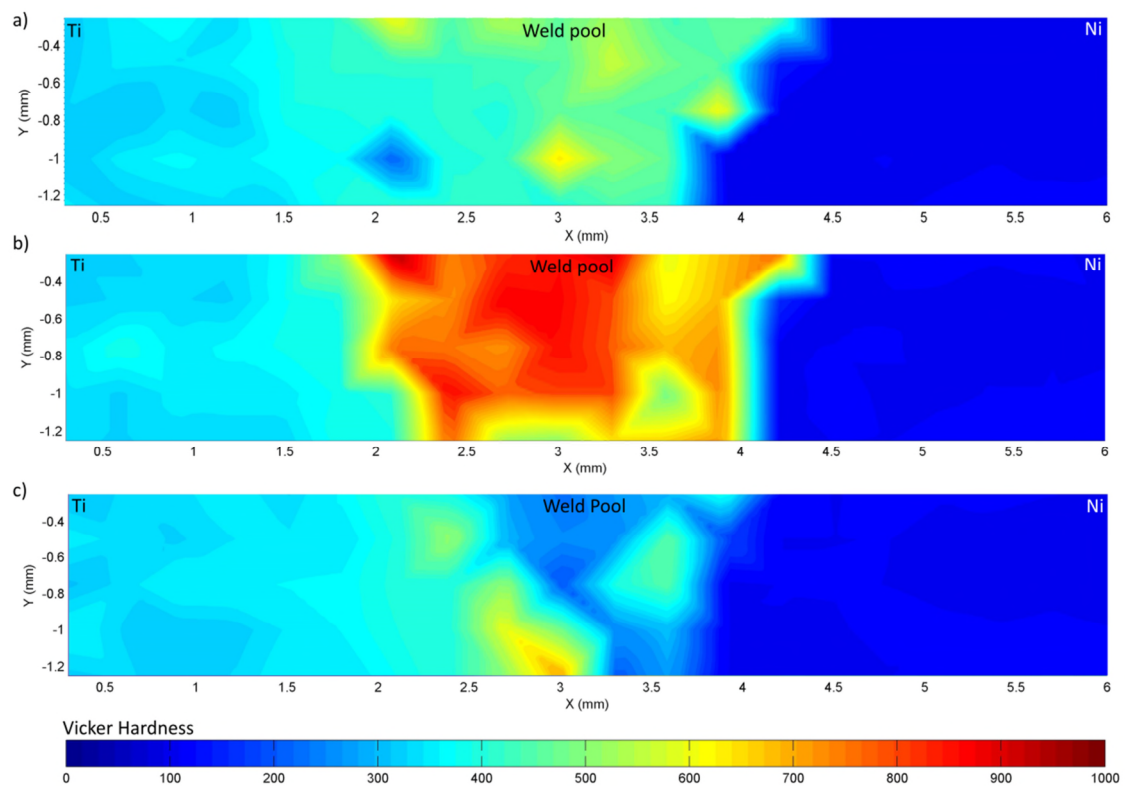
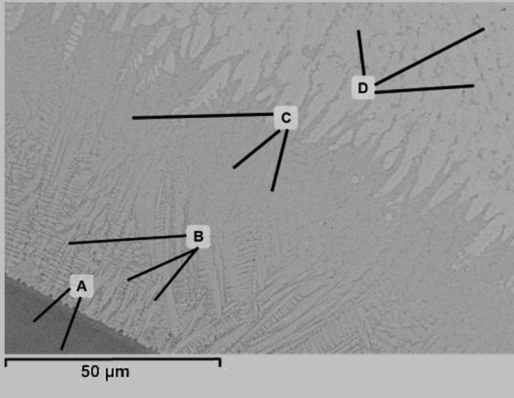
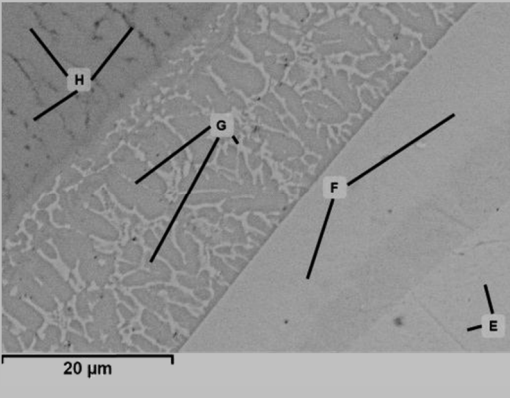
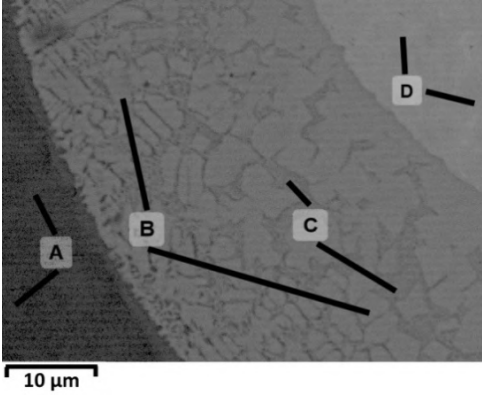
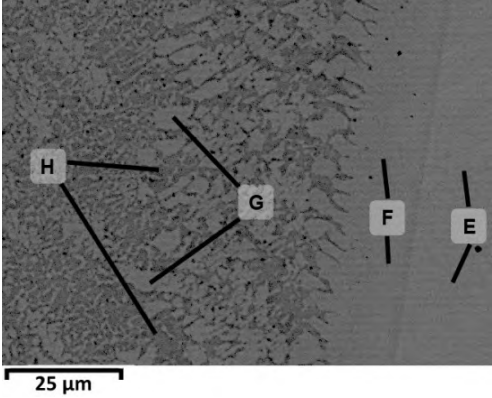
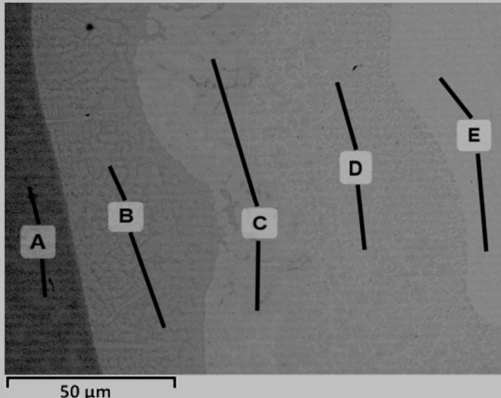



Figure 81 – Hardness profiles for samples C a), D b) and E c).

This aspect combined with the laser energy distribution at the interface can prevent the formation of truly homogeneous weld pool composition in the horizontal direction for sample D. The hardness values for sample C and E are in agreement with the values found in (Kundu and Chatterjee, 2008b) for similar IMC compounds, however sample D has a considerable higher weld pool hardness.

To verify the possible IM compounds formed at the interface of these samples a more detailed EDS analysis was carried out at the Ti and Ni -weld pool interfaces (Table 29).

Table 29 – SEM images from samples C, D and E interfaces between the parent metals and weld pool and corresponding analysed phases.

Sample	Ti-weld pool interface	Ni-weld pool interface
C		
D		
E		

At higher magnifications, it was possible to identify several layers formed at the parent metals-weld pool interfaces. Each of the layers and possible phases were analysed and the correspondent values are shown in Table 30.

Table 30 – Spectrums and possible IMC phases formed at the Ni and Ti interfaces (at%) shown in Table 29.

Sample	Phase	Al	Ti	V	Ni	Phase/IMC
C	A	10.12	86.40	3.48	0.00	Ti
	B	7.85	61.66	3.44	27.04	Ti+Ti ₂ Ni
	C	7.53	59.26	3.16	30.04	Ti ₂ Ni+NiTi
	D	5.08	43.96	1.70	49.26	Ti ₂ Ni+NiTi
	E	0.00	0.00	0.00	100.00	Ni
	F	1.91	17.04	0.88	80.18	Ni+TiNi ₃
	G	1.91	36.53	1.94	59.65	NiTi+TiNi ₃
	H	5.28	43.80	2.00	48.92	NiTi+TiNi ₃
D	A	9.50	78.02	3.20	9.27	Ti+Ti ₂ Ni
	B	7.34	61.67	2.23	28.75	Ti+Ti ₂ Ni
	C	8.20	62.65	3.09	26.06	Ti+Ti ₂ Ni
	D	6.23	47.95	1.80	44.03	Ti ₂ Ni+TiNi
	E	0.69	7.05	0.32	91.94	TiNi ₃ +Ni
	F	2.93	18.60	0.65	77.82	TiNi ₃ +Ni
	G	2.63	24.33	0.67	72.38	TiNi ₃
	H	4.68	28.53	1.61	65.18	NiTi+TiNi ₃
E	A	9.95	76.76	2.87	10.43	Ti+Ti ₂ Ni
	B	7.39	59.76	2.22	30.62	Ti ₂ Ni
	C	5.85	46.10	1.86	46.19	TiNi
	D	5.95	40.02	1.60	52.43	TiNi+TiNi ₃
	E	3.44	25.15	0.98	70.44	TiNi+TiNi ₃

From these results it is observable that the weld pool composition needs to go from 100 % Ni to 100% Ti, for this reason several IMC phases are formed during the welding process. Different heat distributions and profiles resulted in different IMC distribution on the bulk of the weld pool and also at the weld pool

– parent metals interface. The possible IM compounds are the same in every sample analysed, but the distribution among the weld bead and interfaces is changed. Weld pools with considerable lower hardness are possible to achieve when the bulk of the weld pool has NiTi IMC or a solid solution of Ni and TiNi₃. However the formation of layers with the more detrimental IM compounds is always a consequence of terminal solid solutions necessary for the interface between the weld pool and the parent metals. A similar surface melting distribution between the two parent metals should be avoided due to Ni₃Ti formation on the bulk of the weld pool, leading to higher levels of brittleness. For sample F it was not possible to identify any interface layer between it and the Ni interlayer, due to the low concentration of Ti at this interface.

4.2.4 Conclusions

It was not possible to join stainless steel to Ti by direct overlap keyhole laser welding. As expected the Fe-Ti IMC formation and its associated high hardness create very brittle weld pools that show longitudinal cracking throughout the length of the weld bead. Despite all the different weld pool compositions obtained all the welds had low mechanical properties that prevented them from being tested. The necessity of using different metals to surpass the IMC formation and low mechanical properties was evident.

With the use of a thick Ni interlayer, it was possible to obtain a reliable joint with Fe without any crack formation. This was related to the high metallurgical compatibility between stainless steel and Ni. However the Ni-Ti interface was not as successful with IMC formation and again a longitudinal crack formed along the weld bead.

Therefore the Ni-Ti interface was studied in greater detail and the IM compounds observed in the weld pool were Ni-Ti IM compounds. This study revealed that a laser beam distribution of close to 50% between the two metals should be avoided due to the higher hardness achieved in the weld pool by the formation of TiNi₃ IMC.

The use of a thick Ni interlayer in combination with keyhole laser welding changes the IMC formation. It avoids the Fe-Ti IM compounds but the IM formation is not avoided, and the IM compounds were only changed towards relatively softer Ni-Ti IM compounds.

4.3 CMT Cu deposition

4.3.1 Introduction

In the previous chapter it was verified that Ni could be used in different compositions gradients to improve on the high hardness values produced by direct joining of stainless steel and titanium. However it was not possible to create any reliable weld between Ni and Ti. In this chapter a different metal with different characteristics than Ni was selected for investigation.

To select the next metal used, several characteristics were taken into account, the most important was the high metallurgical affinity between the selected metal and at least one of the parent metals used (Fe or Ti). The second characteristic was the physical compatibility with Fe and Ti. These are translated with low melting point to avoid diffusion and reaction between the parent metals, by having the interlayer molten and the parent metals in still solid form. Also low hardness and high ductility are needed to accommodate the different expansion coefficients from the parent metals, avoiding any possible solidification cracking.

After analysing several possible candidates and comparing with metals already used from other researchers, Cu was selected as a viable candidate. The metallurgical compatibility with the parent metals can be seen by the affinity with Fe and that is expressed by the absence of intermediate phases at the Cu-Fe phase diagram (Figure 82) (ASM - International, 1992).

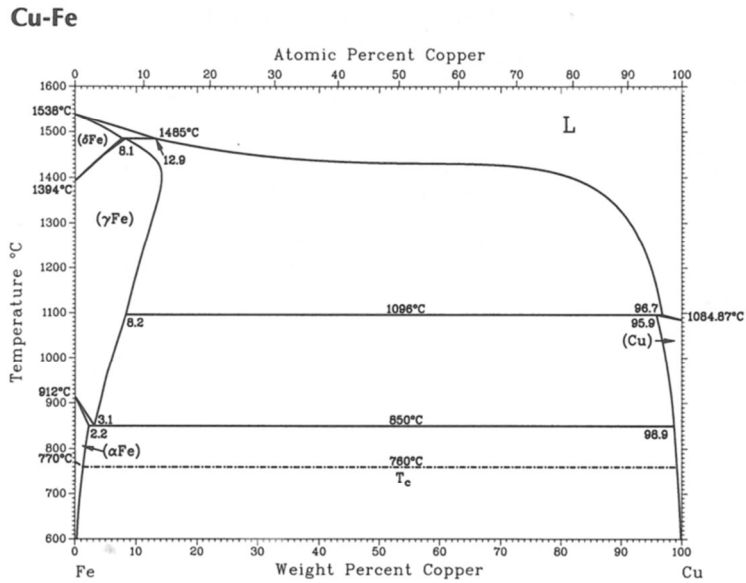


Figure 82 – Cu-Fe binary phase diagram (ASM - International, 1992).

The physical compatibility is expressed in Table 31 (Gale and Totemeier, 2003) where the low melting point and low hardness of Cu is compared with the parent metals and Ni.

Table 31 – Melting point and Vickers hardness values for Cu, Fe, Ni and Ti

Property	Cu	Ni	Fe	Ti
Melting Point (°C)	1084.62	1455	1538	1668
Hardness (HV)	37.6	65.1	62.0	98.9

The low melting point of Cu can be used to greater extent than Ni due to the greater difference against Fe and Ti. Cu can be used as a brazing agent and braze the parent metals and avoid the excessive dilution of the parent metals and possibly avoiding the brittle Fe-Ti IMC phases. To accomplish this it is necessary to melt the Cu and limit, to a greater extent, the melting of the parent metals.

A focused laser beam could be used on the Cu to take it above the melting point. This is not possible due to the Cu high reflectance (0.97) of solid Cu to the wavelength (1064 nm) used by the continuous high power laser used in the previous experiments. Cu high thermal conductivity also decreases the

possibility of the absorbed energy to be capable of increasing the temperature until the melting temperature.

It was necessary to introduce a new low heat input welding process to deposit the Cu wire and reduce the melting of the two parent alloys. The selected welding process considered was a variant form the GMAW designated CMT (Cold Metal Transfer). CMT was also selected due to its high flexibility, high gap bridge ability and high industrial application and acceptance.

Instead of pure Cu, a Cu alloy was researched for these experiments. The selection requisites were the compatibility with the welding process and parent metals, low melting point and good mechanical properties. Figure 83 shows the compatibility of different Cu and Cu alloys filler wires with a particular welding process(American Welding Society, 1996).

Alloy	UNS No.	Oxyfuel Gas Welding	SMAW	GMAW	GTAW	Resistance Welding	Solid-State Welding	Brazing	Soldering	Electron Beam Welding
ETP Copper	C11000- C11900	NR	NR	F	F	NR	G	E	G	NR
Oxygen-Free Copper	C102000	F	NR	G	G	NR	E	E	E	G
Deoxidized Copper	C12000 C123000	G	NR	E	E	NR	E	E	E	G
Beryllium-Copper	C17000- C17500	NR	F	G	G	F	F	G	G	F
Cadmium/Chromium Copper	C16200 C18200	NR	NR	G	G	NR	F	G	G	F
Red Brass - 85%	C23000	F	NR	G	G	F	G	E	E	—
Low Brass - 80%	C24000	F	NR	G	G	G	G	E	E	—
Cartridge Brass - 70%	C26000	F	NR	F	F	G	G	E	E	—
Leaded Brasses	C31400- C38590	NR	NR	NR	NR	NR	NR	E	G	—
Phosphor Bronzes	C50100- C52400	F	F	G	G	G	G	E	E	—
Copper-Nickel - 30%	C71500	F	F	G	G	G	G	E	E	F
Copper-Nickel - 10% Nickel-Silvers	C70600 C75200	F G	G NR	E G	E G	G F	G G	E E	E E	G —
Aluminum Bronze	C61300 C61400	NR	G	E	E	G	G	F	NR	G
Silicon Bronzes	C65100 C65500	G	F	E	E	G	G	E	G	G

E = Excellent G = Good F = Fair NR = Not Recommended

Figure 83 – Qualitative assessment for the welding process applicability on Cu and Cu alloys

There are only four alloys with excellent compatibility with GMAW process; deoxidized Cu, Cu-Ni 10%, aluminium bronze and silicon bronze. Cu-Ni 10% alloy was rejected, due to its higher melting point when compared with Cu (1100 to 1145 °C). Al bronze alloy was also not used due to the lack of solid solubility observed between Fe and Al verified on the previous chapters. Deoxidized Cu was also not selected due to the higher melting point when compared with the CuSi₃ alloy. The higher melting point of the deoxidized Cu would increase the melting of the parent metals and their diffusion and consequently the IMC formation. Due to the main features of silicon bronze alloys, good mechanical properties and excellent corrosion resistance these alloys were selected as suitable for this set of experiments. The selected alloy was CuSi₃ welding wire and the mechanical properties of the selected wire are presented in Table 32.

Table 32 – Selected welding wire mechanical properties and melting point

Alloy	Ultimate tensile strength (MPa)	Yield strength (MPa)	Melting Point (°C)
CuSi₃	350	145	950

After the material and welding process selection, an experimental procedure was designed to investigate the CMT welding-brazing process applied to stainless steel to Ti joining.

4.3.2 Experimental procedure

Titanium AMS4911L plates of dimensions 150 x 100 x1.7 mm (LxWxT) were joined with 316L stainless steel of identical length and width but with 2mm in thickness. The chemical composition of the metals used is given on Table 33.

Table 33 – Parent materials atomic composition (%wt)

Material	C	Si	Mn	P	S	Cr	Ni	Mo	N	Fe	Pb	Al	Cu	V	O
Stainless steel 316L	0.020	0.45	1.73	0.032	0.01	17.2	10.0	2.07	0.054	Bal	-	-	-	-	-
AMS 4911L	0.08	-	-	-	-	-	-	-	0.5	0.3	-	5.5 - 6.75	-	3.5 - 4.5	0.2
CuSi ₃	-	3.0	1.1	-	-	-	-	-	-	0.1	0.01	0.03	Bal	-	-

Each plate was manually ground and finished prior to the welding-brazing process with particular attention to the vertical faces that are brazed by the Cu. Immediately before welding each sample was cleaned and degreased with acetone. The plates were joined in a butt configuration with 1.7mm gap on which a 1mm CuSi₃ welding wire was deposited using CMT welding process (Figure 84). The selected manipulator was the VPPA 2 that is a linear three axis (X, Y and Z) manipulator.

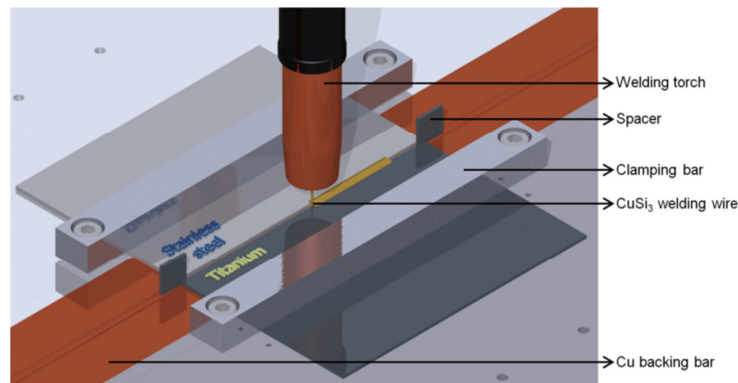


Figure 84 – Schematics from the welding-brazing technique

Besides the local shielding provided by the CMT welding torch a trailing shield was also used to protect the oxidation of the intervening metals. This was needed to protect Ti and stainless steel from oxidation during the cooling phase of the welding process. Ti is a reactive metal and needs to be protected not only at melting point but also on the cooling phase to avoid the embrittlement due to interstitial dissolution of oxygen, nitrogen and hydrogen (Donachie, 2000). Figure 85 shows the experimental setup used for the Cu deposition trials.

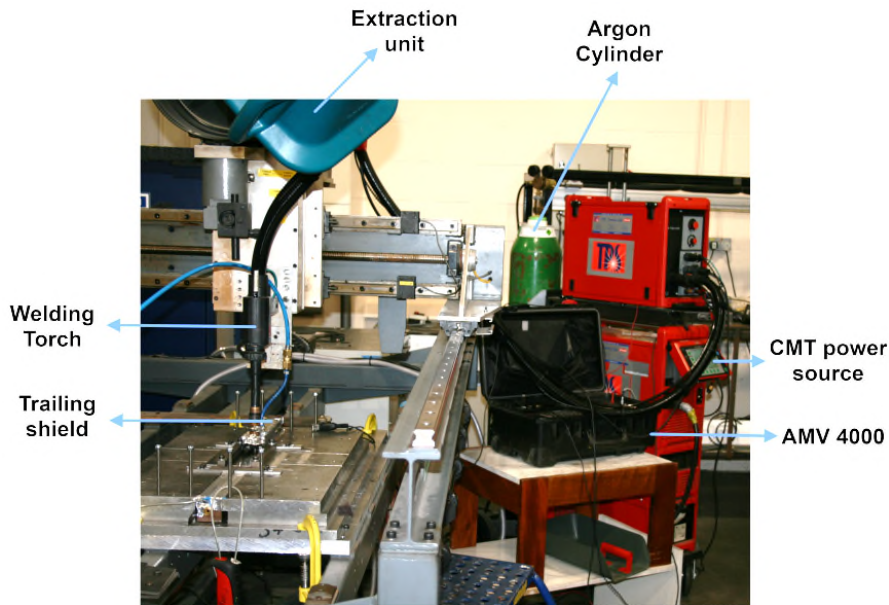


Figure 85 – CMT Cu deposition experimental setup.

After the welding process three different specimens were produced as shown in Figure 86, one for mechanical tests and two for metallographic analysis.

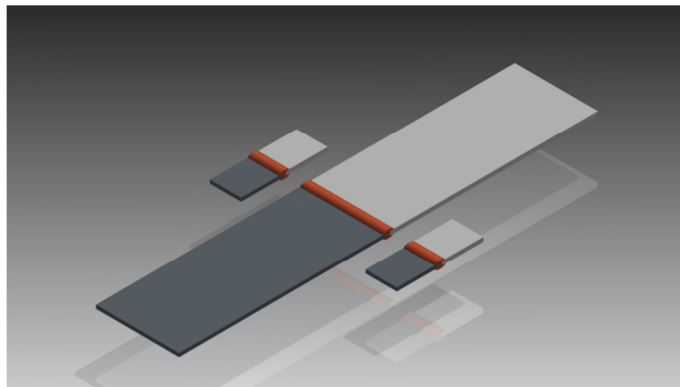


Figure 86 – Samples preparation for metallographic analysis (two) and the sample for mechanical tests.

Metallographic specimens were prepared by mounting them on conductive resin for electron microscopy, ground using silicon carbide paper and polished using diamond paste and colloidal silicon suspension mixed with oxalic acid. They were analysed by optical microscopy and by scanning electron microscopy and energy dispersive spectroscopy (SEM/EDS). Hardness mapping of the specimen was carried out by an Zwick micro hardness machine using the BS

EN ISO 6507 -1 2005, with the following parameters HV 0.1 / 10 (BS EN ISO 6507 - 1, 2005). Each sample extracted to mechanical tests was tested using the 100kN INSTRON 5500R tensile test machine. The tensile test was performed at a constant speed of 1 mm/min; the load and displacement were acquired by a National instruments system attached to a laser extensometer (Figure 87). The gauge length used during the experiments was 50 mm.



Figure 87 – Tensile test setup used for CMT Cu welded samples.

The experiments were carried out using constant welding parameters (travel speed, contact tip to work piece distance), with the exception of the wire feed speed and torch positioning in relation to centre of the gap between stainless steel and Ti plates. As CMT is a synergic process changing the wire feed speed, would change the current and voltage, translating to a heat input variation that is shown by the following expression.

$$HI = \eta \cdot \frac{60 \cdot V \cdot I}{1000 \cdot TS} \quad (5)$$

Where:

HI - heat input [J/mm]

V - voltage [V]

I - current [A]

TS - travel speed [m/min]

η - the welding process efficiency that for a MIG process has CMT is stipulated as 0.85 (Pépe et al., 2011).

Figure 88 depicts the experimental setup and the different positioning of the welding wire in relation to the central line of the gap between the parent metals.

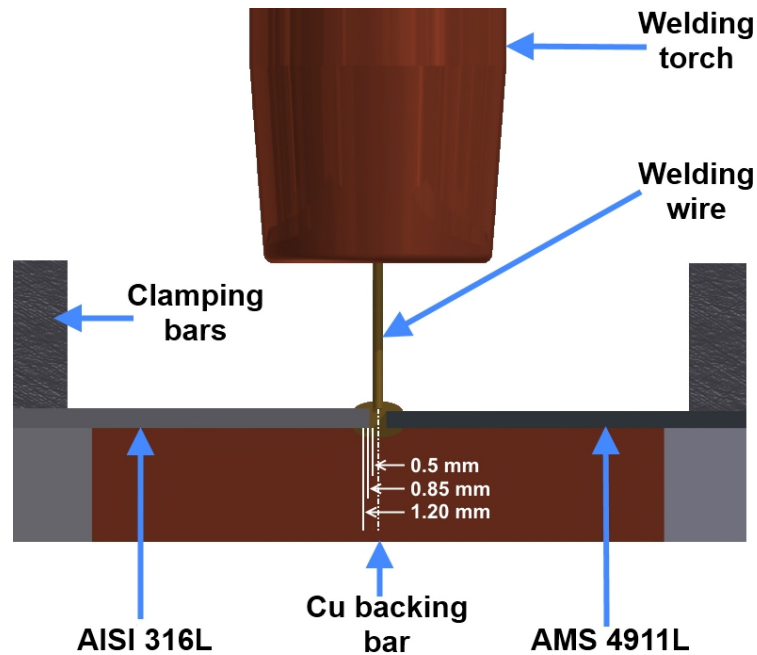


Figure 88 – Welding wire positioning during the welding-brazing experiments

Table 34 contains the experimental points used during these experimental trials.

The parameters which were not altered during the experiments are given below.

- Welding wire CuSi_3
- CMT mode 1183
- Travel speed 0.5 m/min
- CTWD (Contact Tip to Work Distance) – 13 mm
- Shielding gas flows
 - CMT torch – 22 l/min
 - Back shielding 2 l/min
 - Trailing shield 62.5 l/min

- Torch angle 0° perpendicular to the parent metals

Table 34 – CMT welding-brazing parameters for the welding-brazing experiments

Sample	Offset (mm)	Wire feed speed (m/min)	Heat Input (J/mm)	Fracture location
CMT 1	0.50	5.00	110.76	Stainless
CMT 2		6.00	118.40	Stainless
CMT 3		7.00	140.75	Stainless
CMT 4		8.00	157.67	Stainless
CMT 5		9.00	154.99	Ti
CMT 6	0.85	5.00	101.83	Stainless
CMT 7		6.00	116.51	Stainless
CMT 8		7.00	135.01	Stainless
CMT 9		8.00	149.91	Stainless
CMT 10		9.00	171.44	Ti
CMT 11	1.20	5.00	115.47	Stainless
CMT 12		6.00	108.89	Stainless
CMT 13		7.00	138.44	Stainless
CMT 14		8.00	152.99	Cu bead
CMT 15		9.00	152.59	Ti

4.3.3 Results and discussion

To evaluate the success of using Cu as a transition metal between Ti and stainless steel, mechanical tests and metallographic analysis was pursued.

The mechanical tests were performed as explained in the previous section; the ultimate tensile strength of each sample is shown in Figure 89.

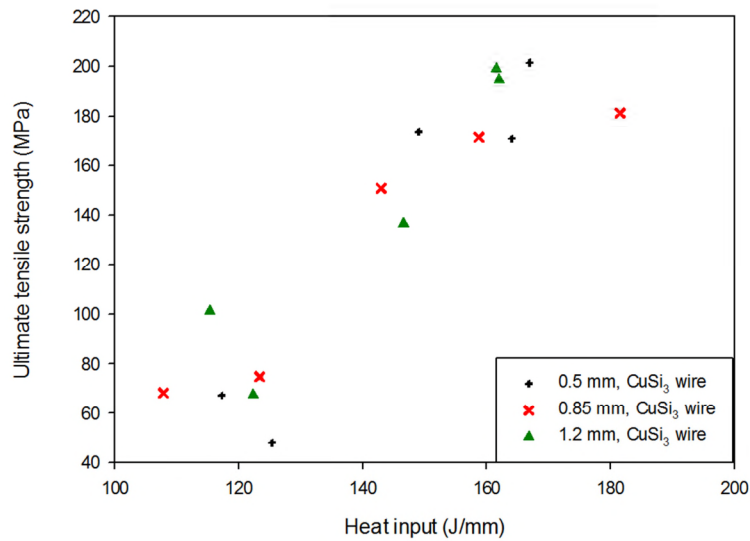


Figure 89 – Ultimate tensile strength vs heat input of welded samples with different welding wire distances to the stainless steel plate.

The ultimate tensile strength of each sample was calculated using the maximum value of the cross sectional area of each welded sample. For the calculation of the thickness of the sample the reinforcement and root values protruding from the substrates were also added to obtain a higher value of thickness. This way, a conservative calculation of the tensile load for each sample is achieved. The welded samples show an increase of tensile strength with the increase of the heat input. However the welding wire positioning does not seem to be a controlling parameter of this welding process. The tensile strength trend is independent of the welding wire positioning. This characteristic denotes that the welding process is tolerant to the positioning of the wire in relation to the parent metals. This will facilitate the alignment of the welding process making the welding technique more relevant to industry application. The maximum tensile strength obtained was 200 MPa that is 21% of the tensile strength of the Ti-6Al-4V and 44 % of the UTS of stainless steel. The lower tensile strength of the sample when compared with the parent metals and the CuSi₃ welding wire used is another example of the degradation of the mechanical properties due to IMC formation.

From these results three samples were extracted from each distance and presented in greater detail, to better understand how the mechanical properties of the samples are influenced by the presence of IMC (Figure 90).

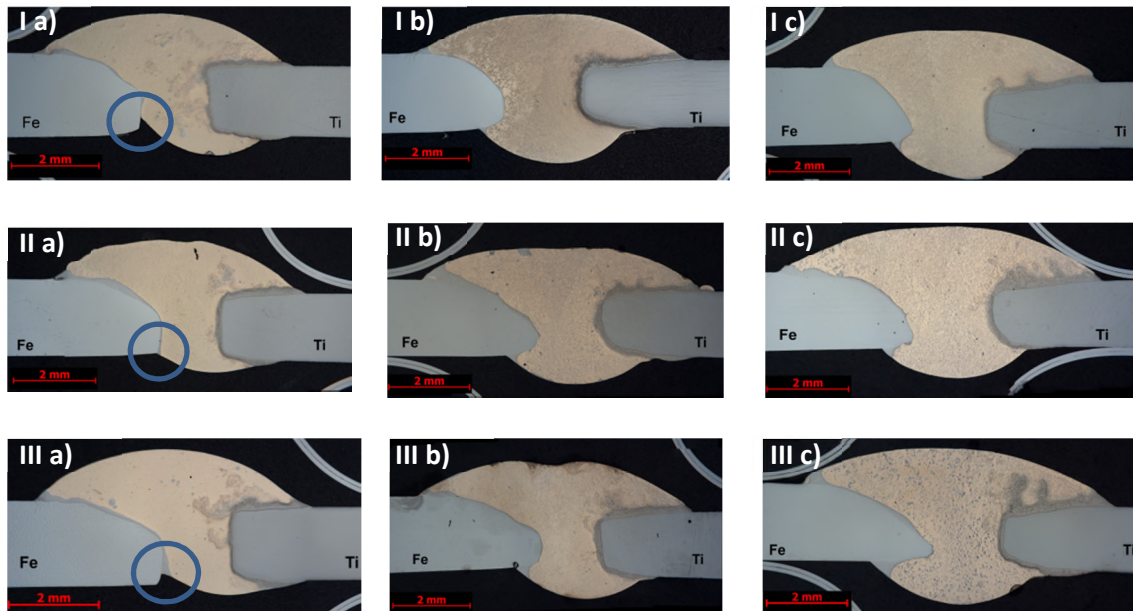


Figure 90 – Selected sample macrographs I – 0.5 mm, II – 0.85 mm III – 1.20 mm, a, b, and c increasing heat input.

The weld bead geometry shows that it is independent of the welding torch positioning, indicating once again that this is not one fundamental parameter to describe this particular welding process.

Samples with low heat input and low wire feed speed, samples I, II and III a) shown in Figure 90 do not wet correctly the stainless steel plate. The low mechanical properties of these samples can be related with low wetting of the base metals rather than the IMC formation (blue encircled regions of Figure 90). This can be seen on Figure 91 where the strain and stress curves for each selected sample are plotted. Samples a) have an inconsistent curve, related with the poor stainless steel wetting with more than one rupture load. Samples b) and c) present a better wetting of the stainless steel plate, but the contribution of the parent metals for the Cu bead is more noticeable (higher

melting of parent metals). With the increase of melting of the parent metals enables the increase of the reaction layer close to the Cu-Ti interface, being greater for the samples designated by c), with higher heat input. All samples with the exception of sample III c) broke from the stainless steel side. Sample III c) broke close to the Cu-Ti interface, denoting a higher impact of the Cu-Ti IMC compounds for the samples with higher values of heat input.

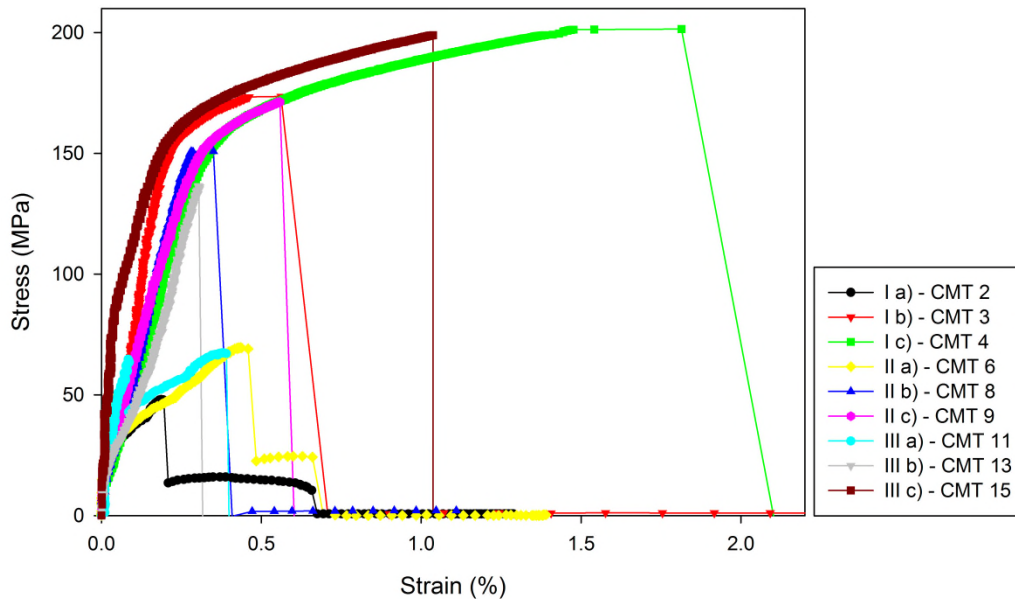


Figure 91 – Stress strain curves for the selected samples

The samples with higher tensile load also showed maximum plastic strain/ deformation with the maximum present on the sample CMT 4 with a strain close to 2%. The mechanical test results show a clear increase not only on tensile strength but also in ductility of these specimens, with the heat input e.g. samples CMT2 vs CMT4.

The specimen’s hardness was also evaluated to try to relate the hardness profiles and the mechanical properties results.

Three samples were selected for these tests, CMT 2 4 and 5. The three samples selected were made at the same welding wire positioning and have increasing heat inputs. CMT 2 and 4 have failed at the Fe-Cu interface whilst sample CMT 5 has failed at the Cu-Ti interface.

Figure 92 shows the hardness mapping results for the three selected samples.

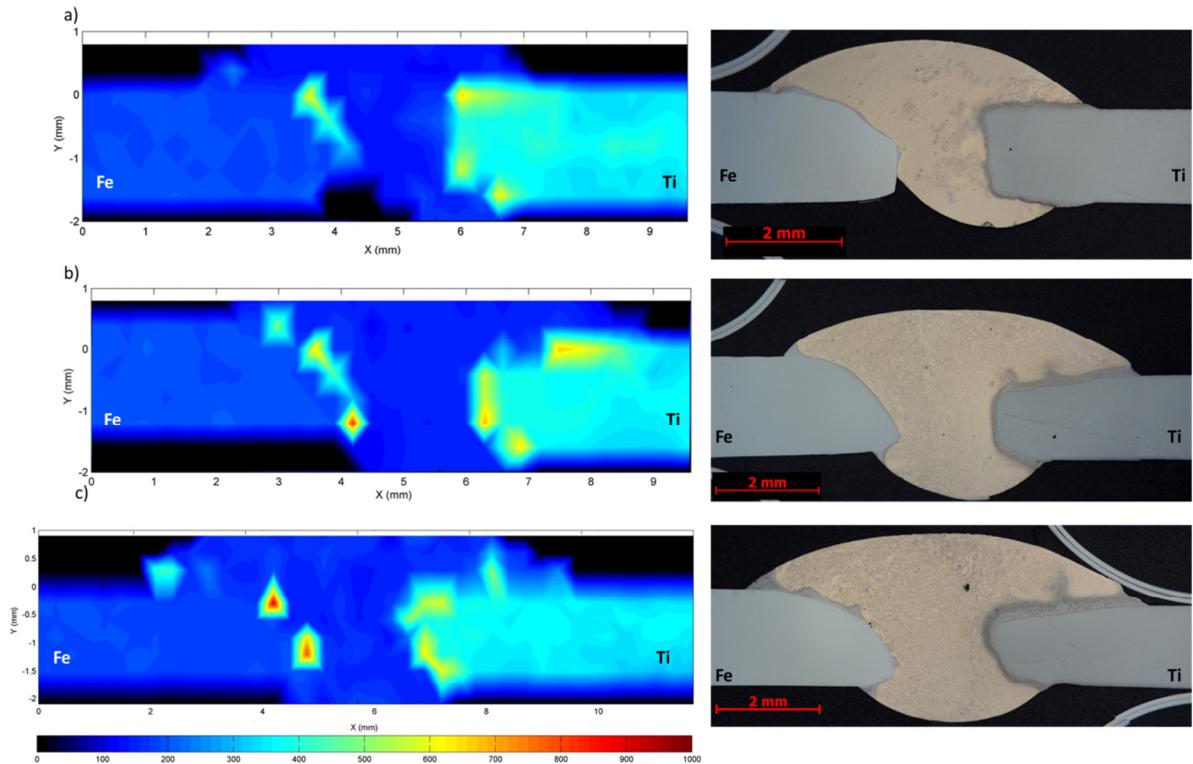


Figure 92 – Hardness mapping and corresponding optical macrographs for samples: CMT 2 a), CMT 4 b) and CMT 5 c).

All of the specimens tested show a similar welding profile with the bulk of the Cu deposited bead being the softer part of the joint and as expected; the higher hardness values are concentrated at the interfaces between the Cu bead and the stainless steel and Ti plates, at the IMC layers.

The hardness present on sample CMT2 IMC layers is lowest of the three samples. This was expected due to the lower heat input used in this weld that prevents the atomic migration, by reducing the temperature and time where the diffusion can occur. However the low mechanical properties present can be related with low wetting between the Cu bead and the stainless steel plate.

On the contrary samples CMT 4 and 5 have higher hardness values detected at the IMC layers. This can be justified by the higher heat input and consequently the increase in the melting of the parent metals that will originate higher

interdiffusion. The highest hardness values for both these samples are located at the Cu-Fe interface with values close to 1000 HV, however the fracture location of both of these samples is located in different parts of the sample. For CMT 4, the fracture location is at the Fe-Cu interface that coincides with the location of the hardest IMC phases whilst for sample CMT 5 the location is at the Ti-Cu interface. This indicates that not only the IMC hardness is the major contributing factor for the failure of this joint, but also that the IMC volume plays a role in failure location. The IMC layer volume in sample CMT 5 is higher than in CMT 4, increasing the probability of the failure being located at the Ti-Cu interface.

The tensile test results can be compared with studies done in infrared brazing of Ti and stainless steel using Cu as an interlayer (Kundu et al., 2005) and the study presented at the literature review using electron beam welding to join the same parent metals using Cu as an interlayer (Wang et al., 2010). The mechanical properties reported by this study are a maximum tensile strength of 318 MPa with a ductility of 8.5% and 234 MPa with a 3.6% elongation respectively. These results exceed mechanical strength of the results presented in this thesis, but the added flexibility of this welding process can result in easier and cost effective application for industry.

Verifying the copper bead micrographs from Figure 92, the bead morphology is quite similar between all samples, with a Cu bead with scattered IMC phases and two distinct IMC layers on the stainless steel-Cu and the Cu-Ti interfaces. SEM and EDS mapping were used to verify the presence of IM compounds on these specimens (Figure 94).

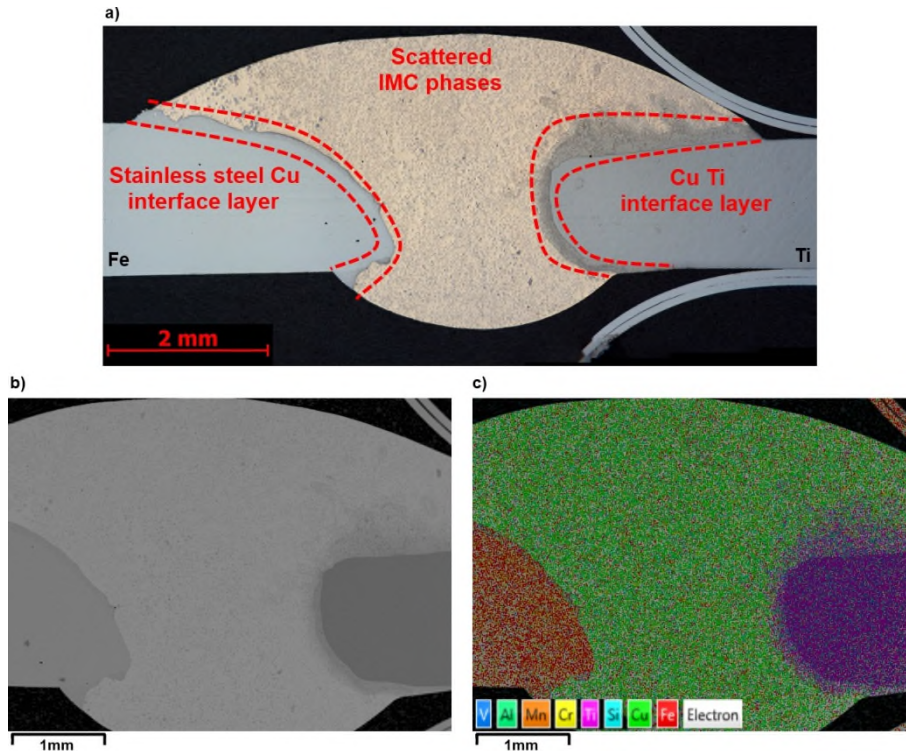


Figure 93 – Cu deposited weld bead macrograph and distinctive areas a). Backscattered SEM image b). EDS mapping showing the main elements present on the sample c).

Each of the three defined areas was examined by SEM/EDS analysis.

The first layer to be analysed was the stainless steel – Cu interlayer. This layer is discontinuous in nature and naturally it results from the reaction between the stainless steel and the deposited Cu bead. To better understand its nature an EDS mapping was made (Figure 94).

This analysis reveals the discontinuous nature of this layer. It also reveals the main elements present in this layer are Cr, Fe and Ti, whilst Cu is mainly present at the weld bead and at the discontinuities of the referred layer (Figure 94 c)

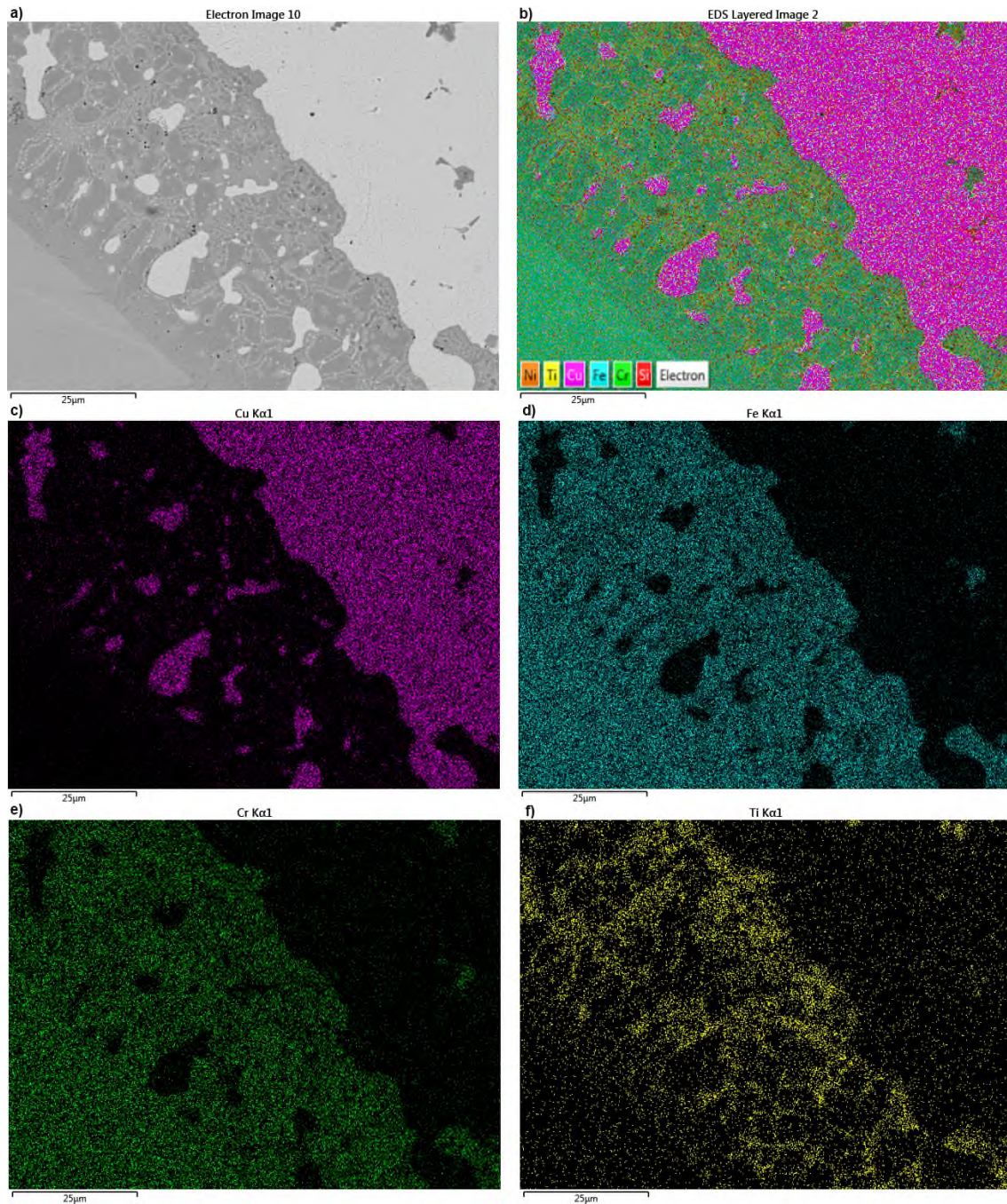


Figure 94 – SEM and EDS mapping for the stainless steel Cu interface layer. SEM image a), Composite EDS mapping b), Cu c), Fe d), Cr e) and Ti f) EDS mapping.

The presence of Ti at this layer means that even with brazing CuSi₃ with a lower melting point on a 1.7mm gap to restrict the melting of Ti it is not enough to prevent the contact between Fe and Ti. Ti diffuses through the deposited CuSi₃ weld bead and interacts with Fe at the SS-Cu interface. To understand

the amount of Ti that diffuses inside the stainless steel Cu interface layer, a semi - quantitative EDS analysis was carried. (Figure 95)

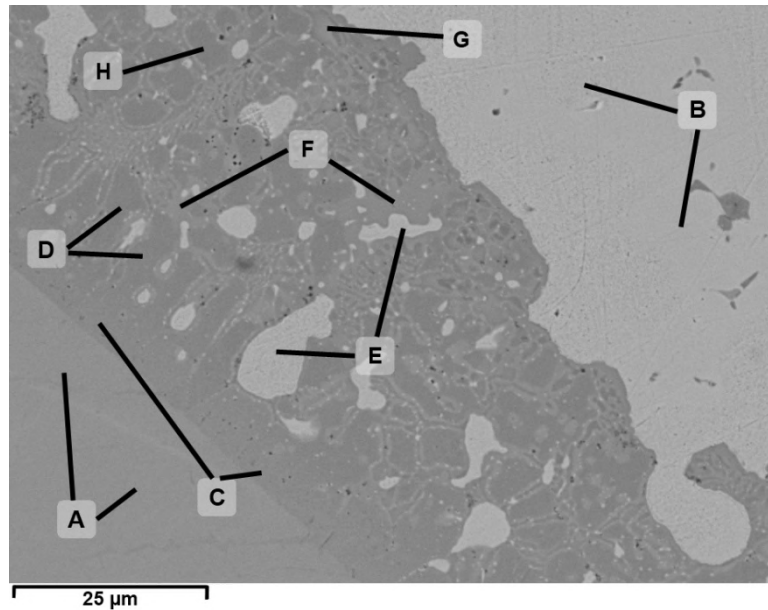


Figure 95 – Stainless steel Cu SEM backscattered image and phases investigated.

Figure 95 shows the stainless steel Cu interface layer in greater detail and the places where the spectrums were collected (phases A-H). Inside the reaction layer there are three distinguishable areas. These areas are identified by the following phases: phase E that has the lighter shade, phases F and G that have an intermediate shade and phase C D and H who have a darker shade.

This figure was acquired using the SEM back scattered electron detector that can distinguish heavier elements from lighter elements. Heavier elements backscatter electrons more strongly than lighter elements appearing on a lighter shade on the figures.

In Table 35 the elemental composition in weight percentage are shown for the different phases indicated on Figure 95.

Table 35 – Elemental composition in weight percentage from the phases identified on the stainless steel Cu interface layer.

	A	B	C	D	E	F	G	H
Si	0.4	1.5	4.0	5.6	0.9	8.9	10.1	5.7
Ti	-	-	0.8	0.6	0.1	6.3	14.5	0.7
V	-	-	-	-	-	-	-	0.4
Cr	18.0	0.3	18.1	16.9	0.9	14.2	10.6	17.1
Mn	-	1.2	-	-	1.1	0.0	0.0	0.0
Fe	70.4	1.9	66.4	67.4	5.1	54.2	46.6	67.1
Ni	9.4	-	5.8	4.6	-	6.3	3.8	3.8
Cu	-	95.1	3.9	4.5	92.0	8.0	3.2	4.2
Mo	1.9	-	1.0	0.4	-	2.1	11.2	1.1
Phase/ IMC	AISI 316 L	Cu	SS	SS	Cu	-	-	SS

As expected phase A is stainless steel with a chemical composition very similar to the AISI 316L. Phase B is the Cu from the welding wire, but it is depleted from some of the silicon content expected (3% wt), this can be explained by the higher levels of Si present on the interface layer, the Si has diffused to the stainless steel-Cu layer. Phases indicated by C and D and H have a composition similar to the AISI 316L. These phases show an increase of silicon content, Cu and also a small increase on Ti content when compared with AISI 316L, but can still be classified as stainless steel. The lighter phases present in the internal part of the layer represented by the phase E are mainly constituted by Cu with some Fe and Ti, and can be considered as Cu that was segregated during the formation of the reaction layer. The phases within the interface layer with higher content of Ti are the phases represented by F and G. This was expected, due to these areas being coincident with the areas highlighted in the Ti mapping (Figure 94). Besides Ti these phases have also an increase in Si and Mo content. But the main elements on these phases are Fe and Cr. The amount of Ti in these phases increases with the distance from the stainless steel parent metal and these phases are not identifiable close to the parent

stainless steel. The Ti was segregated to the phases similar to F and G and is almost not present on the remainder phases in the stainless steel Cu interface layer. This may have happened due to the non-equilibrium nature of the welding, generating a concentration gradient of the Ti through the stainless steel Cu interlayer, that could be harmonized if the time temperature cycles were longer. This layer acts as a prevention of the Fe Ti IMC by segregating the main levels of Ti close to Cu side of the layer.

The second layer to be investigated is at the Cu-Ti interface. This was expected to be the main interface reaction layer due to the IMC formation between Cu and Ti. In Figure 96 the EDS mapping of this layer and the distribution of the main elements individually. This region of the sample shows high hardness in the contour plots shown in Figure 92, characterized by a yellow area in the contour plots.

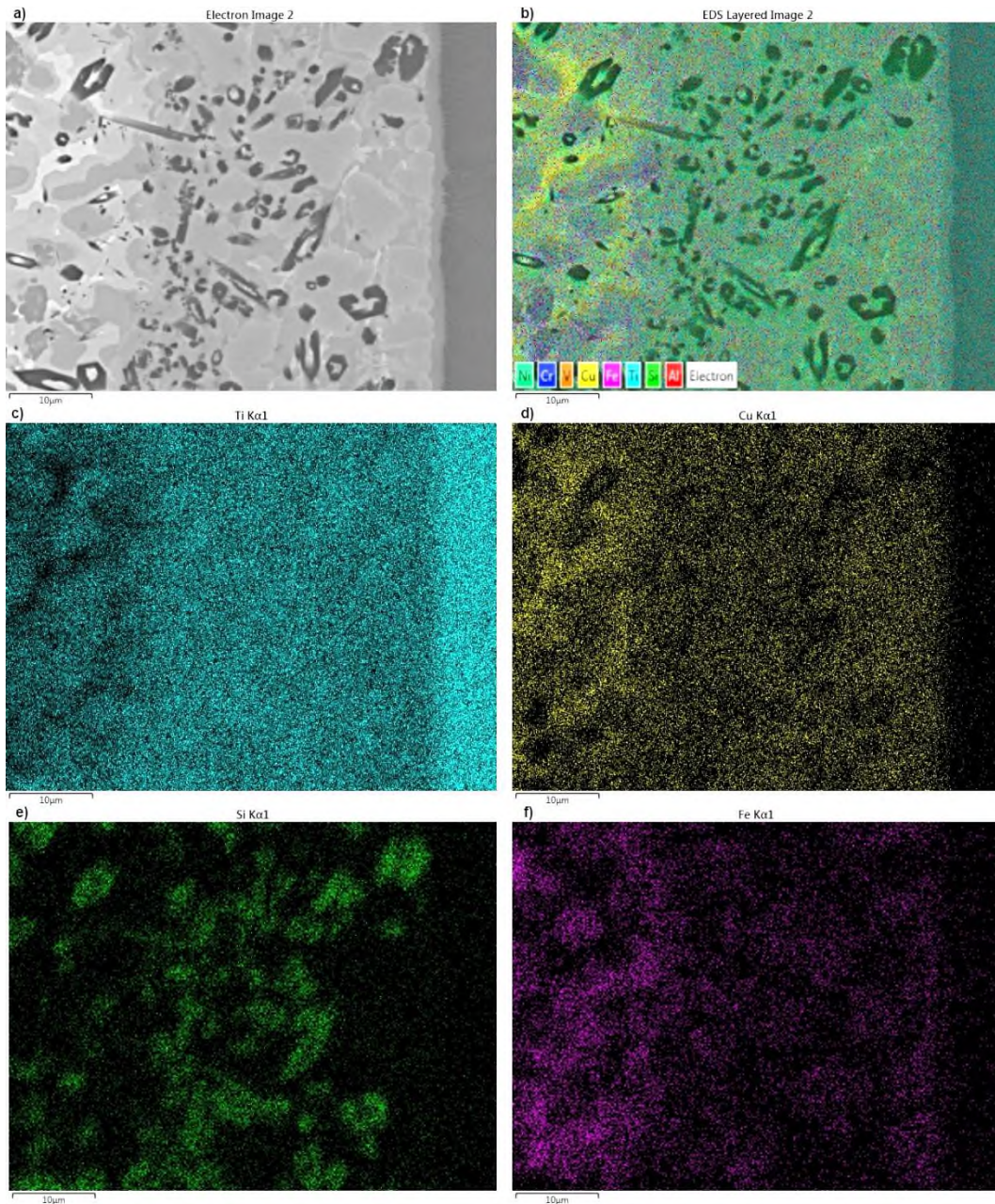


Figure 96 – SEM and EDS mapping for the Cu Ti interface layer. SEM image a), Composite EDS mapping b), Ti c), Cu d), Si e) and Fe f) EDS mapping.

From The EDS mapping and SEM backscattered image it is possible to confirm what was verified beforehand, this interlayers are mainly formed from the reactions between Cu and Ti. The darker phases present in Figure 96 a) are Si rich phases. Fe is also detected inside this IMC layer, but its concentration decreases towards the Ti parent metal. To further identify the possible IMC

phases present in this interlayer a quantitative analysis each of the phases the phases identifiable by the reaction layer's backscattered image (Figure 97).

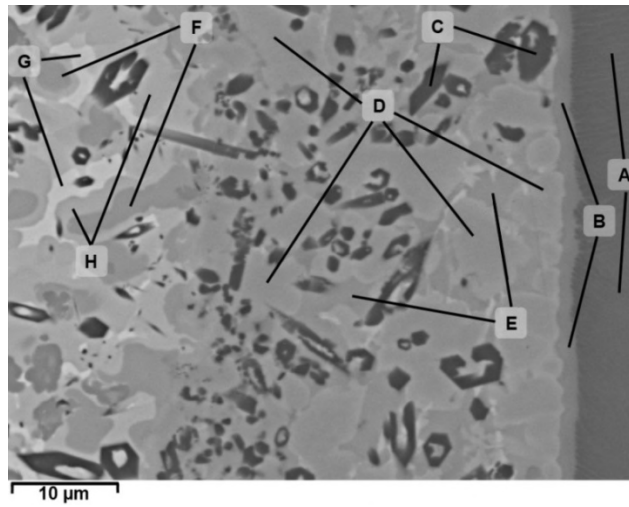


Figure 97 – Cu Ti interface layer SEM backscattered image and phases investigated.

Each of the phases was identified by a letter and multiple spectrums were analysed for each sample. The spectrum locations were identified by the lines shown in Figure 97.

Table 36 – Elemental composition in weight percentage from the phases identified on the Cu Ti interface layer.

	A	B	C	D	E	F	G	H
Al	5.83	4.97	0.26	3.54	2.68	1.35	1.35	0.86
Si	-	0.40	19.79	0.76	0.61	1.14	-	0.11
S	-	-	-	-	-	0.09	-	-
Ti	90.07	67.90	66.62	49.43	56.92	41.43	8.21	31.93
V	4.10	5.39	5.37	3.70	-	-	-	-
Cr	-	-	1.22	1.41	-	1.64	-	1.28
Mn	-	-	-	0.10	-	-	0.71	0.32
Fe	-	2.69	0.87	6.52	-	15.47	0.91	8.59
Ni	-	0.22	-	0.41	-	1.85	-	1.70
Cu	-	18.43	5.88	34.13	39.80	37.05	88.83	55.24
Possible phase	Ti-6Al-4V	CuTi ₂ +αTi	Ti ₅ Si ₃	FeTi+Ti ₂ Cu	Ti ₂ Cu	FeTi+Ti ₂ Cu	T ₂ +TiCu ₄	T ₂ +T ₄

Phase A is the Ti base plate with the same distribution of Ti, Al and V as the parent material (Ti-6Al-4V).

Phase B is mainly composed of Ti (67.90 %) and Cu (18.43%). Phase B is a continuous layer between the base metal (Ti) and the main Ti-Cu reaction layer. The identification of this layer can be done using the Cu-Ti phase diagram due to the low values of Si, Fe and Cr present. This IMC is a dual phased IMC composed of CuTi_2 and α Ti (Figure 98).

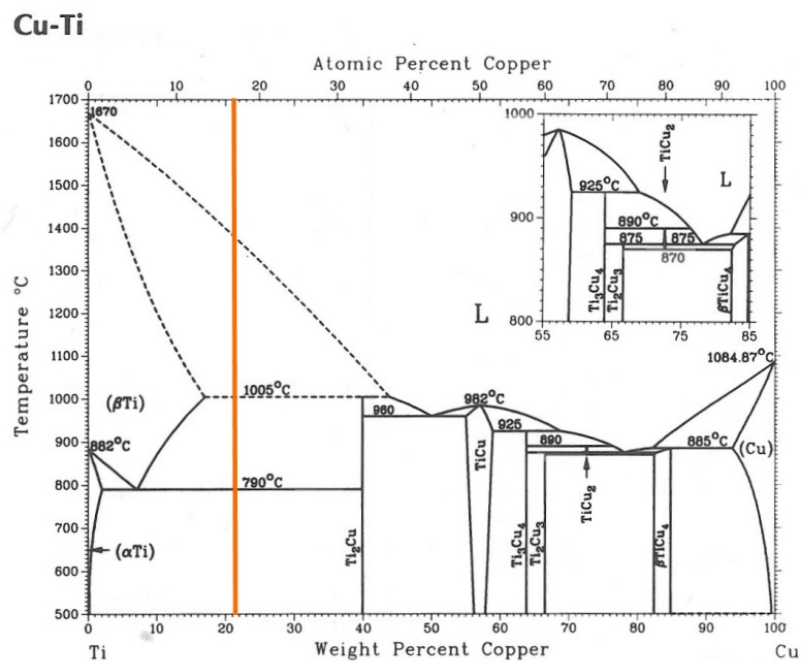


Figure 98 – Cu-Ti phase diagram with the corresponding IMC phases indicated by an orange line.

Phase C that appears in black on the SEM backscattered image is mainly composed of Si and Ti and the ratio between these elements is very close to Ti_5Si_3 phase on the Ti-Si (Figure 99) phase diagram. It was noticed that Si was segregated to produce phases that have a much higher Si content than the parent metals used.

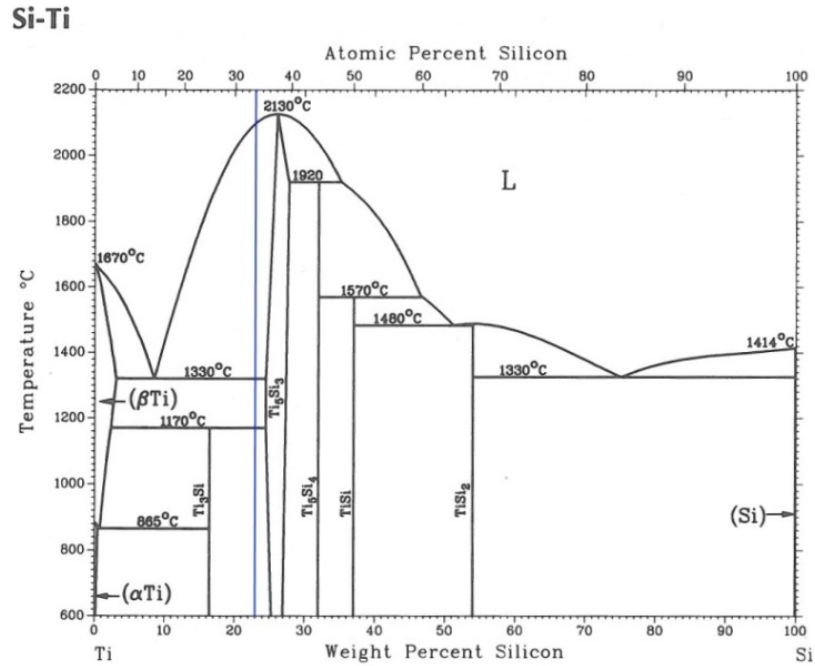


Figure 99 – Si-Ti phase diagram and the representation of phase C (ASM - International, 1992).

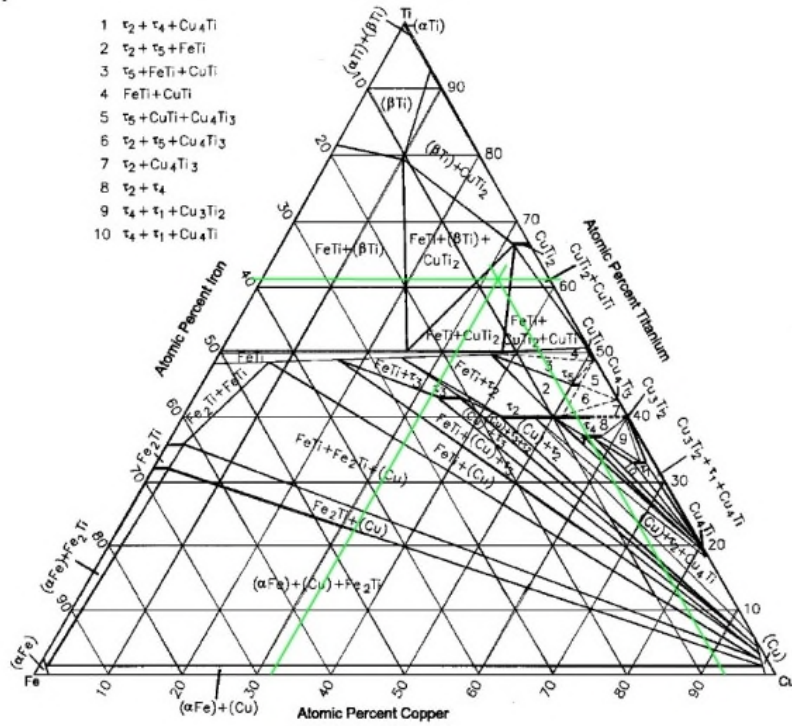
Phases D and E compose almost all of the Cu-Ti interface layer. Phase D has a cellular structure and phase E have an intracellular space structure. These two phases are similar, but the Fe content on phase D is higher, making phase e an IMC composed of three different elements and phase E a binary IMC. Evaluating phase D on the ternary Cu-Fe-Ti (Raghavan, 2002) phase diagram and phase E on the Fe-Cu phase diagram should show the IMC composition of these two phases.

Phase D points to a binary phase compound of FeTi and Ti₂Cu and phase D has a ratio between Ti and Cu very close to Ti₂Cu.

F G and H can be considered external to the Cu-Ti reaction layer due to the higher discontinuity of these phases and the lower values of Ti when compared with the previous phases.

Phases F and H are mainly composed of Cu, Ti and Fe, whilst phase G is only composed of Cu and Ti. These phases were also evaluated using the Cu-Fe-Ti.

a)



b)

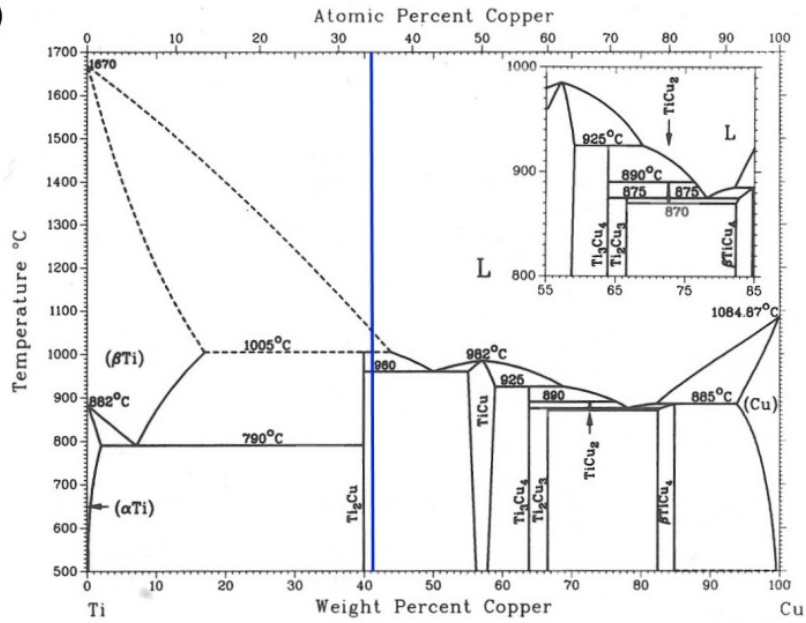


Figure 100 – Cu-Fe-Ti phase diagram isothermal section at 849 °C with phase D plotted a) (Raghavan, 2002) and Cu-Ti phase diagram with phase E plotted b) (ASM - International, 1992).

After the Cu-Ti interface layer and towards the Cu bead another phase was observed at the backscattered EDS imaging. This phase is represented by the letter I in Figure 102.

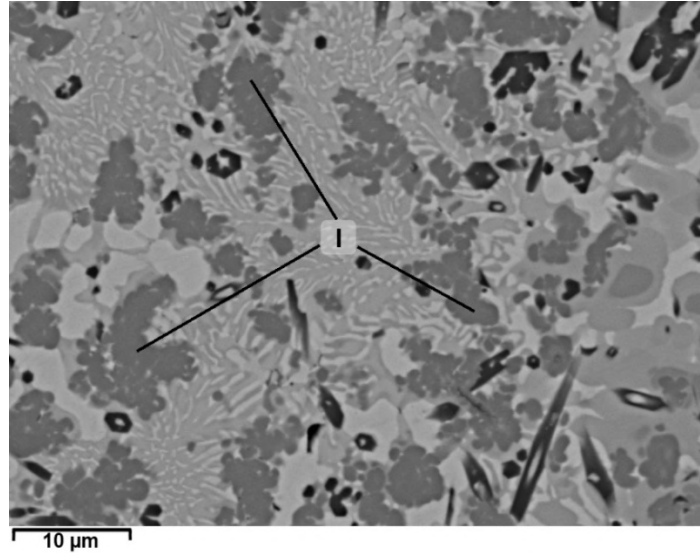


Figure 102 – Cu Ti interface layer vicinity SEM backscattered image and phase investigated.

The main elements composing this phase are Ti, Fe, Cu, Si, Cr and their distribution is shown in Table 37.

Table 37 – Elemental composition in weight percentage from the phase identified on the Cu Ti interface layer vicinity.

	Al	Si	Ti	V	Cr	Mn	Fe	Ni	Cu
I	0.12	8.97	33.01	2.97	7.16	1.25	29.86	2.11	14.54

This phase is mainly composed of five components and so it was impossible to identify to reference it against a dual or ternary phase diagram.

Inside the Cu bead scattered phases were verified using optical microscopy. Two different areas inside the Cu bead were analysed. One was closer to the stainless steel and other close to the Ti parent metals. These two different areas were analysed to verify if the proximity to the different parent metals has an influence on the IMC formation and composition. The first analysis was a

qualitative one, using EDS mapping to understand the elemental distribution (Figure 103) on the scattered phases close to the stainless steel parent metals.

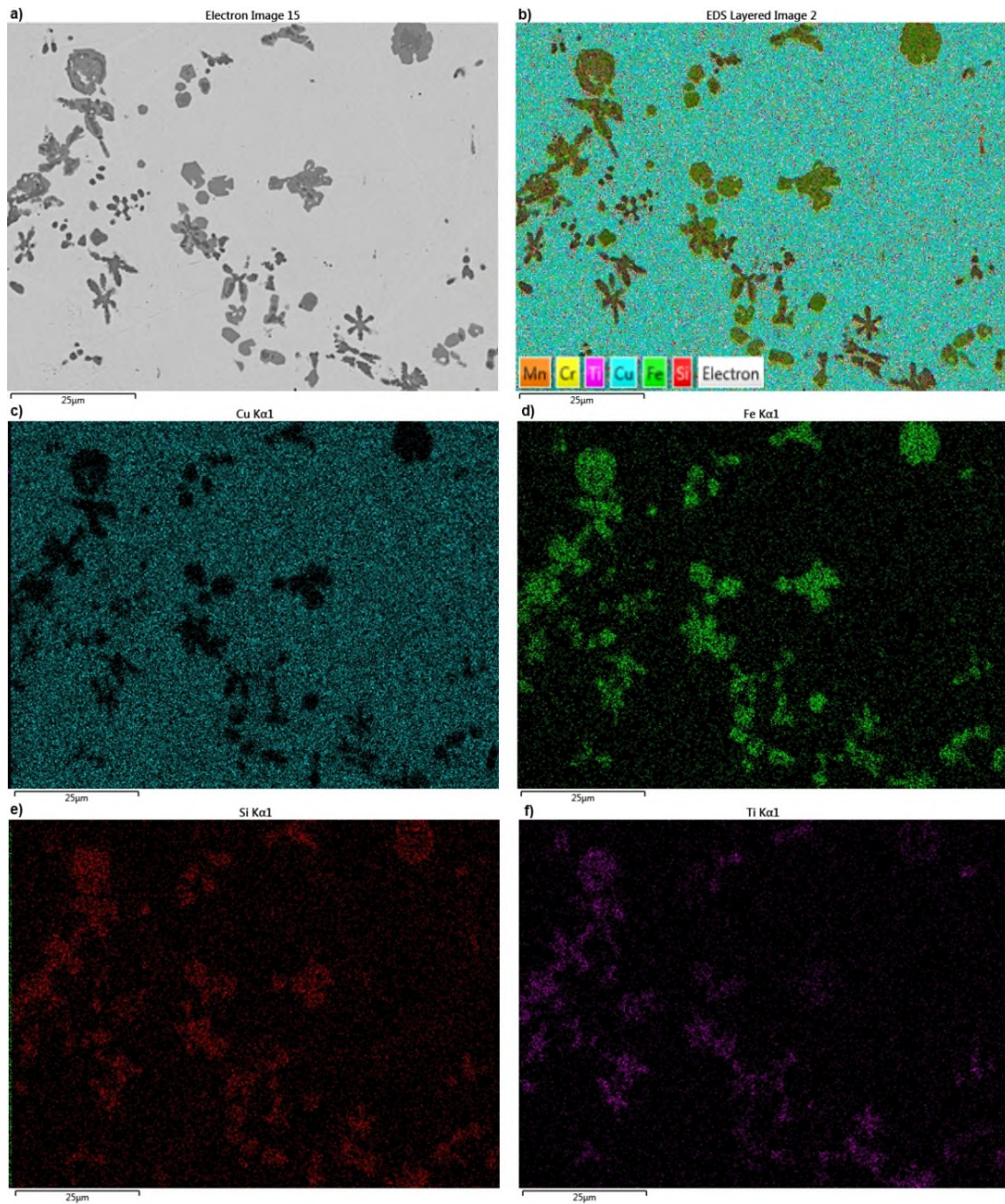


Figure 103 – SEM and EDS mapping for the scattered IM compounds close to stainless steel. a) SEM image, b) Composite EDS mapping, c) Cu, d) Fe, e) Si and f) Ti EDS mapping.

The EDS mapping shows a close to pure Cu bead and the other elements concentrated in the IMC phases. All the IMC phases contain Fe and Si, but the Ti levels are more pronounced on the darker IMC phases. This was verified by the quantitative analysis made at the phases presented on Figure 104.

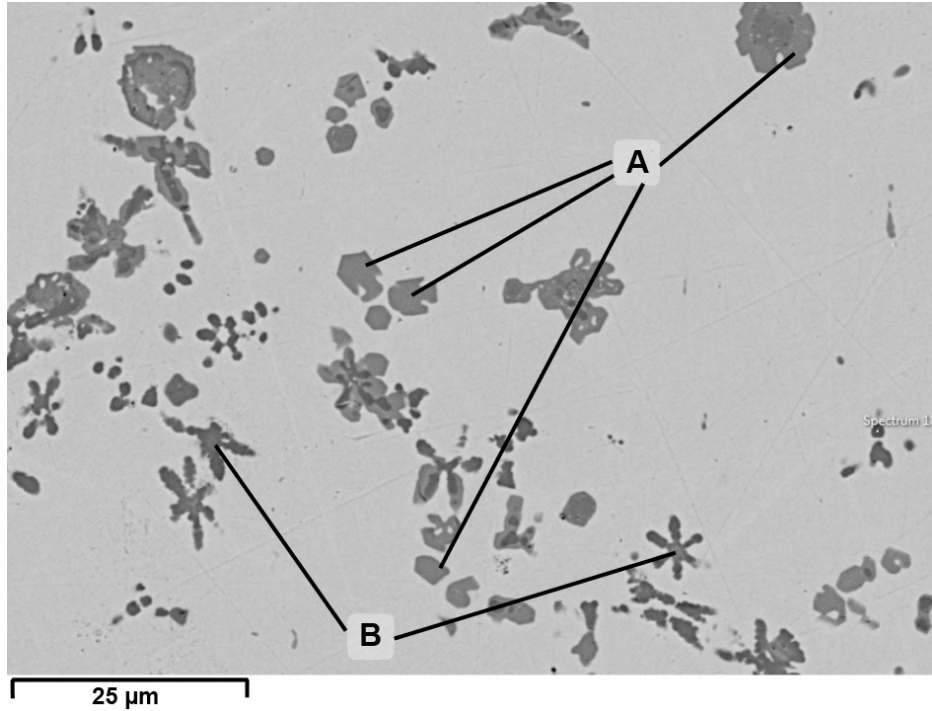


Figure 104 – Scattered IMC’s close to stainless steel SEM backscattered image and phases investigated.

The correspondent elemental distribution in weight percent is shown in Table 38.

Table 38 – Elemental composition in weight percentage from the phases identified in Figure 104.

	Si	Ti	V	Cr	Fe	Ni	Cu	Mo
A	10.34	6.48	0.00	17.19	56.03	3.56	6.42	0.00
B	11.27	16.54	1.19	8.87	43.91	2.70	9.87	5.65

The IMC’s identified are mainly composed of Fe, Cr, Si, Ti and Cu. The correct identification of the correspondent IMC phases was not possible, due to the multiplicity of important elements present on these phases.

Due to the high cooling rate it is possible to observe coring on the IMC formed and the presence of different elemental concentration values in the same intermetallic phase. This reveals the non-equilibrium conditions experienced during the welding process.

As expected the SEM/EDS analysis of the second area closer to the Ti parent metals also revealed a Cu bead with scattered IMC phases composed of Cu Si Fe and Ti.

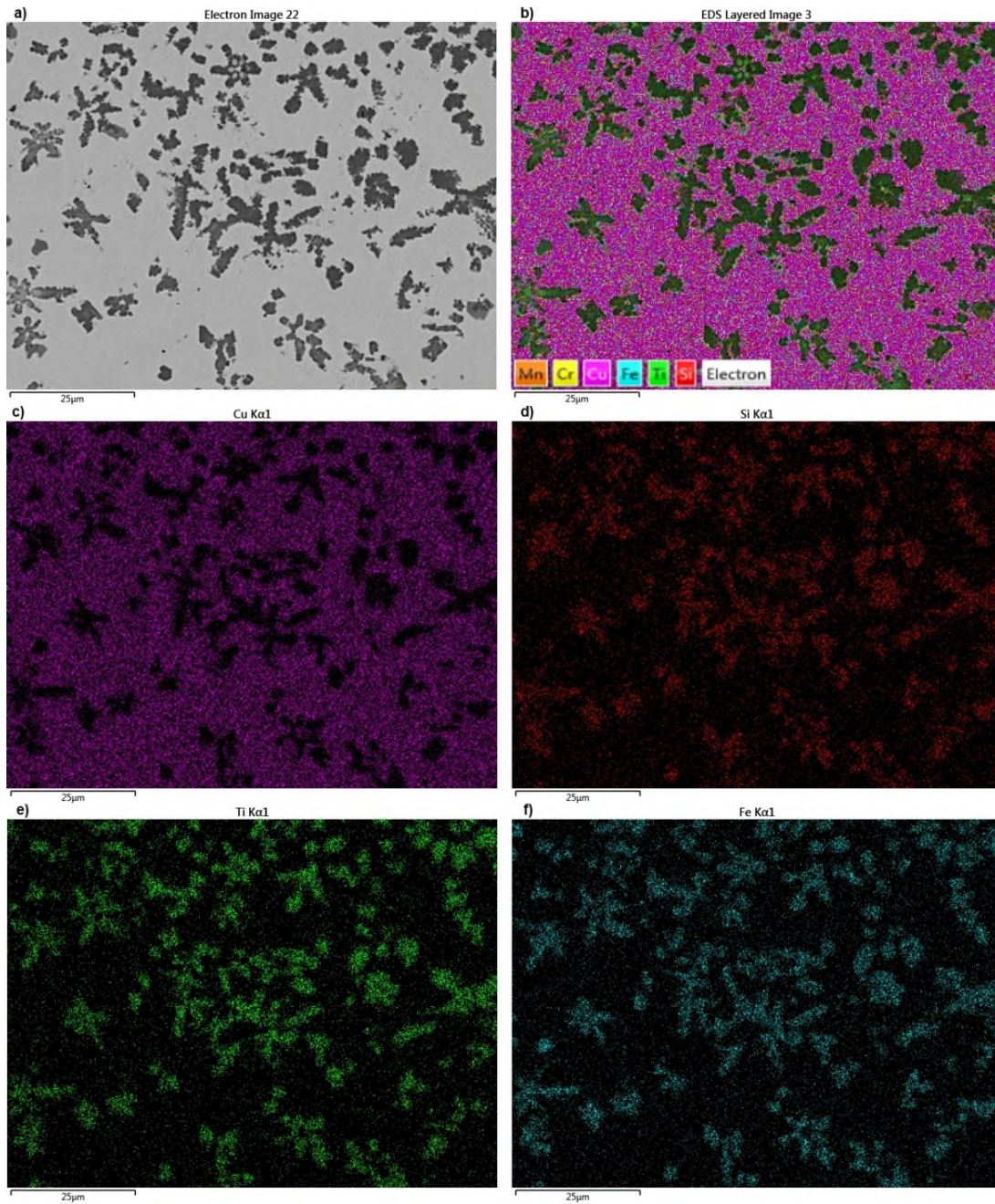


**Figure 105 – SEM and EDS mapping for the scattered IM compounds close to Ti.
a) SEM image, b) Composite EDS mapping, c) Cu, d) Si, e) Ti and f) Fe EDS mapping.**

From the qualitative analysis presented by the EDS mapping it is noticeable that the presence of Si is once again concentrated on the IM compounds and not on the Cu bead. The presence of other elements as Ti, Fe and Si is concentrated on the IMC phases and the Cu bead is composed almost exclusively of Cu

(Figure 105 c). The morphology of the IMC phases is also different with the phases closer to Ti being more angular in shape (Figure 106) while the phases closer to the stainless steel are more circular or spherical (Figure 104). For a better understanding of the stoichiometry of these phases an EDS quantitative elemental analysis was carried out.

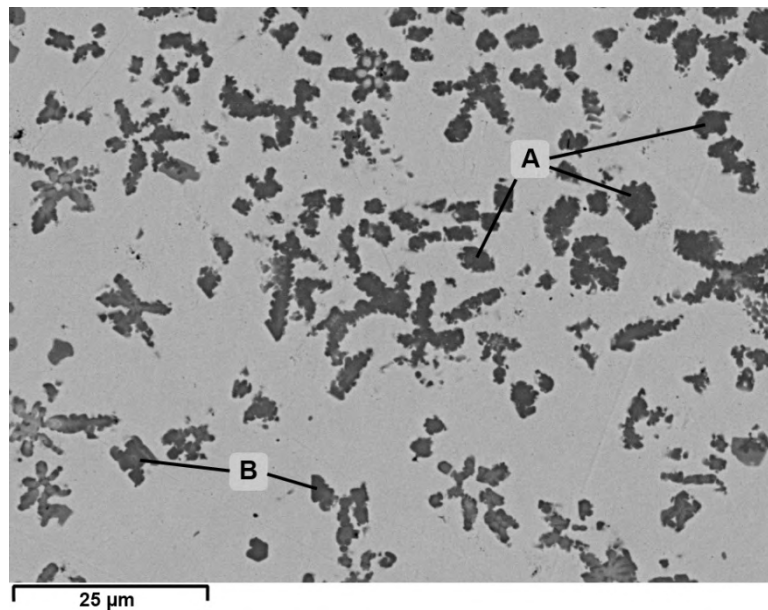


Figure 106 – Scattered IMC’s close to Ti SEM backscattered image and phases investigated.

From the EDS backscattered image (Figure 106) two phases were analysed.

Table 39 – Elemental composition in weight percentage from the phases identified in Figure 106.

	Si	Ti	V	Cr	Fe	Ni	Cu	Mo
A	11.85	27.95	1.43	7.04	39.56	3.49	8.24	0.44
B	11.50	21.04	0.55	8.92	46.86	3.09	6.89	1.17

These two IMC phases are very similar compositionally, the main elements present are Fe, Ti, Si, Cu and Cr. The main differences are the quantity of Fe and Ti. Due to the high levels of several elements present on these IMC phases, it is impossible to have an accurate estimate of their nature.

These IMC phases have higher levels of Ti when compared with the IMC's close to the stainless steel, showing that the IMC composition changes with the distance to the parent metals. This also shows a gradient of Ti and stainless steel present inside the Cu bead.

4.3.4 Conclusions

It was possible to braze stainless steel and Ti using CuSi_3 welding wire. The heat input was revealed to be the dominant parameter during the study developed. The maximum tensile properties were obtained for the samples brazed with a higher heat input. On the contrary, the wire positioning in relation to the parent metals was not a dominant parameter. This parameter did not influence the mechanical properties of the joints.

Despite the low heat input characteristic of the CMT welding process it was not possible to avoid the melting of the parent metals and IM compound formation. In particular formation Fe-Ti IM compounds, demonstrated the high mobility of these atoms (Fe and Ti) through the brazed Cu.

The IMC phases identified are mainly located at the interfaces between the parent metals and the Cu. However, scattered IMC phases are present at the Cu bead. The phases identified had a maximum hardness close to 1000HV. However the ductile nature of Cu was a great advantage to maximize the mechanical properties of the joint and avoid the crack formation due to the different expansion coefficients of the parent metals. In summary, the Cu brazed metal acted as a buffer to the dissimilar physical and chemical properties of the parent metals.

4.4 Chapter conclusions

It was not possible to perform direct joining of Ti to stainless steel using the traditional welding fusion techniques. The formation of IM compounds is always too high due to the high levels of diffusion between the parent metals in the liquid state, generating brittle weld pools and consequent failure of the joints.

To prevent the high mixture of both parent metals (Fe and Ti) and the IMC generation a single thick Ni interlayer was used. The thick Ni interlayer was successfully welded to the stainless steel, however the cracking formation could not be avoided between the Ni and the Ti. This evidenced the metallurgical compatibility between Ni and stainless steel, but showed the incompatibility between Ni and Ti. This was observed through the formation of several Ni-Ti IMC phases and high Vickers hardness associated with them. This technique did not produced strong enough joints to be mechanically tested.

Joining by a Cu deposition route using CMT was more successful when compared with the use of a thick layer of Ni and laser welding because the joints obtained could be mechanically tested. Their tensile strength was close to 20% of the Ti-6Al-4V and 44% of the 316L stainless steel used for these welding experiments. Furthermore the CMT brazing technique used to obtain the Cu brazed joints is a flexible and accepted joining process that could be easily accepted and implemented on an industrial scale.

5 Compatible metal selection and additive manufacturing

5.1 Introduction

After using two different metals compatible with Fe it was necessary to investigate if there is any metal that could be compatible with Ti or compatible with both metals (Fe and Ti). It is also necessary to introduce quantitative physical metrics to decide which metals to use. The metrics used were melting point and mechanical properties:

1. Melting point: The metal to be used needs to have a melting point at least half of the lowest parent metal (AISI 316L - 1398.89 °C).
2. Mechanical properties: The metal to be used needed to have at least half of the tensile strength of the lowest parent metal (AISI 316L – 515 MPa).

These metrics were decided to prevent the excessive deterioration of the two parent metal properties:

- Metric 1 = T. Melt \geq 699.45 °C
- Metric 2 = UTS \geq 257.5 MPa.

To verify the existence of such metal it is necessary to verify if there is any metal that can mix with Fe and Ti without creating any IMC phases. This can be verified by examination of phase diagrams or by verifying the diagram by (Ferro and Saccone, 2007) Figure 107.

This map is a collection of information extracted from several phase diagrams and it states the presence of no IMC, one IMC or several IMC for several metallic combinations.

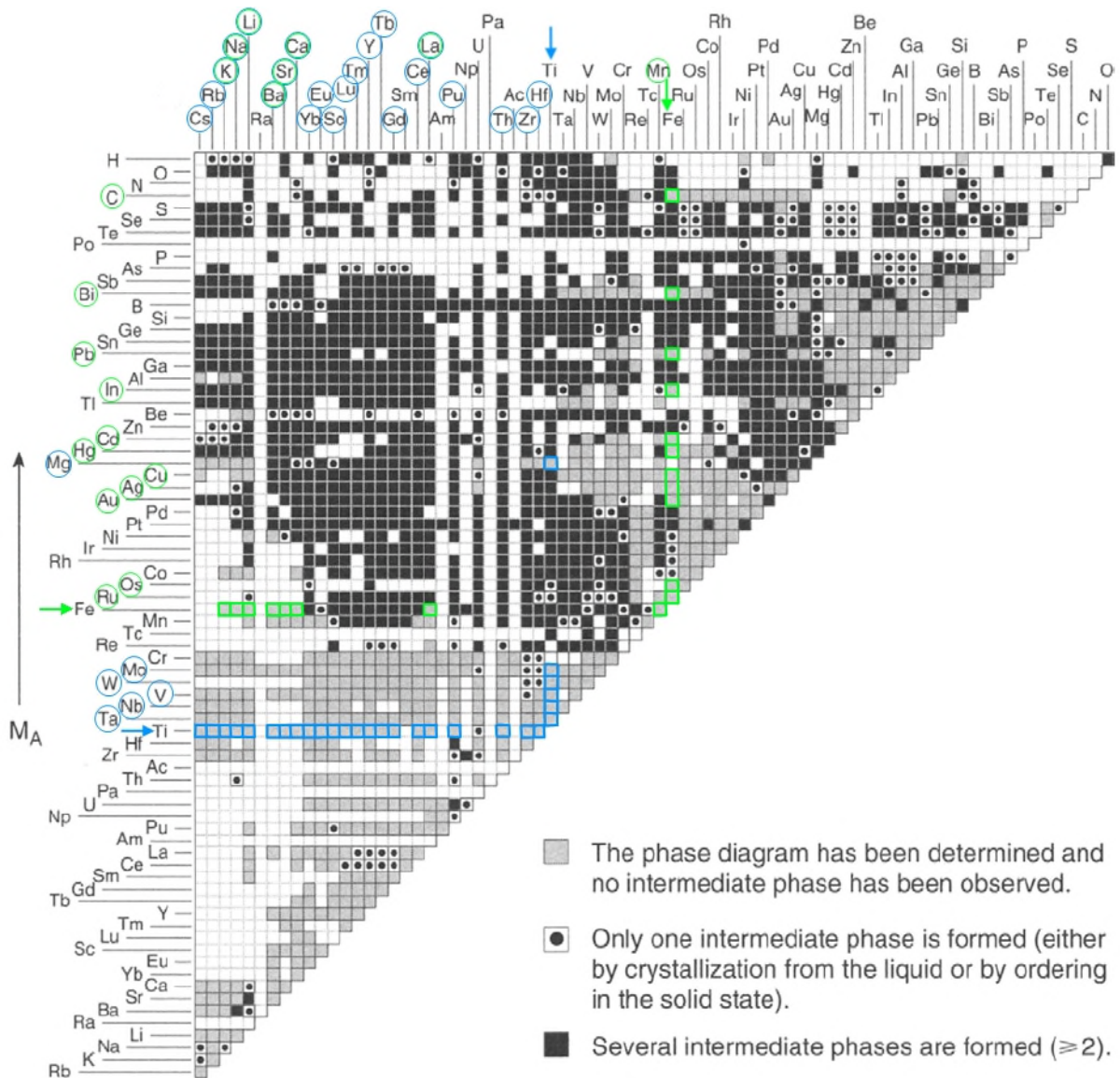


Figure 107 – IM phase formation for different elements (Fe – green, Ti – blue)
(Ferro and Saccone, 2007).

After analysing the diagram, the metals with green circles represented the metals that do not form any IM compounds with Fe and in blue are represent all the elements that do not make any IM compounds with Ti. From Figure 107 the common elements without IM compounds between Fe and Ti are K (potassium), Na (Sodium), Li (Lithium), Ba (Barium), Sr (Strontium), Ca (Calcium) and La (Lanthanum). Table 40 presents the melting point of the

possible candidates to be used as compatible metals on welds between stainless steel and Ti.

Table 40 – Melting temperature the selected compatible metals (Gale and Totemeier, 2003).

Metal	Melting temperature (°C)
K (Potassium)	63.38
Na (Sodium)	97.72
Li (Lithium)	180.5
Ba (Barium)	727
Sr (Strontium)	777
Ca (Calcium)	842
La (Lanthanum)	918

K, Na and Li have lower melting point than metric one and Ba, Sr and Ca oxidize heavily in contact with oxygen and are not suitable as well. The only metal that can be considered to use as transition metal on a joint between stainless steel and Ti is La. Due to its low mechanical properties (131 MPa) which are lower than metric two and its high cost it is not a suitable metal to be used.

As none of the metals present on the list are suitable it is necessary to verify if it is possible to find two metals that are compatible between themselves and compatible with either of the parent metals. This will make possible to use a hybrid interlayer composed of two or more metals.

Once again it is necessary to analyse all of the metals compatible with Fe and compatible with Ti. In Table 41 are presented all of the metals that are compatible either with Fe or Ti and in red are presented the metals that do not comply with metric one (Melting point < 699.45 °C).

In Figure 108 the green squares are a representation of the metals that are compatible with Fe and do not make any IM compounds with a given element.

Table 41 – Melting temperature for no IMC selected metals.

No IMC's with Ti		No IMC's with Fe	
Metal	Melting Temperature (°C)	Metal	Melting Temperature (°C)
Cs (Caesium)	28.44	Mn (Manganese)	1246
Rb (Rubidium)	39.30	C (Carbon)	-----
Yb (Ytterbium)	819	Bi (Bismuth)	271.4
Eu (Europium)	826	Pb (Lead)	327.462
Sc (Scandium)	1541	In (Indium)	150.6
Lu (Lutetium)	1663	Cd (Cadmium)	321.07
Tm (Thulium)	1545	Cu (Copper)	1084.62
Y (Yttrium)	1552	Ag (Silver)	961.78
Tb (Terbium)	1356	Au (Gold)	1064.18
Gd (Gadolinium)	1313	Os (Osmium)	3033
Ce (Cerium)	798	Ru (Ruthenium)	2334
Pu (Plutonium)	640		
Th (Thorium)	1750		
Zr (Zirconium)	1855		
Hf (Hafnium)	2233		
Mg (Magnesium)	650		
Mo (Molybdenum)	2623		
W (Tungsten)	3422		
V (Vanadium)	1910		
Nb (Niobium)	2477		
Ta (Tantalum)	3017		

On blue circles are represented the metals that do not make IM compounds with Ti. By intersecting the blue circles with the green squares it is possible to find the metals that are compatible with Fe or Ti and are compatible between them.

Table 42 – Physical and mechanical properties and prices of selected metals

(Gale and Totemeier, 2003)

Metal	Melting Point (°C)	Boiling Point (°C)	Thermal conductivity (W/(mk))	Thermal expansion (25°C) (µm/(mK))	Tensile strength (MPa)	Price (£/cm³)¹
Ti	1668	3287	11.4	8.6	460	0.91
Fe	1538	2861	80.4	11.8	210	0.53
Cu	1084.62	2562	398	16.5	314	0.56
Ag	961.78	2162	428	18.9	330	3.02
Au	1064.18	2856	317.9	14.2	220	N.A.
Ta	3017	5458	54.4	6.3	760	3.93
Nb	2477	4744	52.3	7.3	550	2.16
V	1910	3407	31	8.4	730	6.16
W	3422	5555	160	4.5	1920	2.42
Mo	2623	4639	142	4.8	690	1.3

After analyzing the table, several metal combinations can be used. Cu can be selected for the Fe compatible metal (as it is compatible with a greater range of metals), it has been used with relative success in several studies (Elrefaey and Tillmann, 2009; Tomashchuk et al., 2011; Wang et al., 2010) and also in the previous chapter of this thesis.

The metals compatible with Ti it is necessary to divide the into two groups, one that have melting point higher than Cu boiling point (2562 °C), (Ta, W, Mo) and the rest with melting point lower that Cu boiling point (V, Nb). To minimize the thermal difference between the metals the only two metals considered for this study were V and Nb, however V was the most expensive metal, and so Nb was the selected metal to be used.

¹ Price value was calculated using data form Goodfellow supplier; prices can vary with different suppliers.

The final metal combination selected for the joint was:

Ti-6Al-4V – Niobium – Copper – AISI 316L

After accessing the possibility of using compatible metals to avoid the formation of IMC, it was necessary to identify the best joining process to join the selected metals.

5.1.1 Joining process selection

Laser could not be used due to its high reflectivity with Cu and CMT or GMAW are not efficient in the Ti deposition, due to arc wandering during deposition. GMAW process has a very unstable Ti deposition due to spatter formation and a non-uniform deposited bead (Eickhoff and Eagar, 1990; Shinn et al., 2005). Also the low diversity of forms that pure Nb is available forced the selection of GTAW welding using additive manufacturing (AM) as the joining process chosen for the application.

GTAW and plasma were already used to deposit Ti for AM applications. This process is named WAAM (Wire Plus Arc Additive Manufacturing) and can be used to build components with several different shapes. WAAM (Martina et al., 2012; Wang et al., 2011) is a process in which a weld bead is deposited on a substrate using an arc welding process (GMAW, GTAW etc) and subsequently other weld beads are deposited on top generating a 3D component built in layers.

The mode selected for the AM building was DC current with direct mode, as explained in chapter 1.6.3, to concentrate the energy on the substrate and increase the life of the tungsten electrode. With GTAW welding it is also possible to control the wire feeding independently from the welding parameters increasing the flexibility of the welding process.

In this case it is necessary to make dissimilar structures by using different metals. It is possible to make these transitions because when depositing a subsequent layer, the previous ones are not completely molten, making

possible to introduce a new layer with just a partial dilution of the previous. If enough layers are deposited it is possible to reduce the amount of the previous metal on the new metal to 0% (Figure 109).

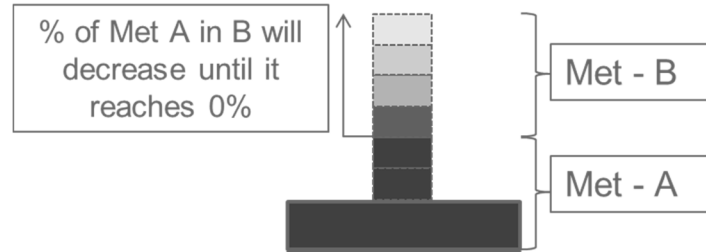


Figure 109 – Schematic representation for the dilution of metal B into metal A.

In Figure 109 there are two metals used, the first one (Met A) is the same as the substrate and two layers were deposited. The second metal was deposited subsequently (Met B) in four layer, the first layer has some dilution of metal A, but the following layers start to have lower levels of Met A. Using this principle it is possible to transfer from a second metal to a third without the interference of the first one (Nb to Cu without Ti), and so enabling the formation of transition components with several dissimilar metals. As the compatibility of our metals was verified beforehand it is possible to build a component from Ti-6Al-4V to AISI 316L without the formation of IM compounds.

The added flexibility provided by the GTAW welding process (independent control of wire feeding and current) is especially useful for the different mixing ratios and thermal properties found during the build of the components.

5.2 Experimental procedure

Plates of 200x200x6 mm (WxLxT) of Ti-6Al-4V were used as substrate. The substrate plates were cleaned previously with a handheld grinder to remove the oxidation and surface contaminants.

Five different welding wires were used during the experiments, the chemical composition for all of the metals previously referred are in Table 43:

Table 43 – AM used alloys chemical composition in weight percentage.

	Al	V	Fe	C	N	O	Ti	Cr	Mn	Mo	Ni	Si	Sn	Ta	Ag	Pb	Other
Ti-6Al-4V	6.43	3.91	0.15	0.04	0.02	0.149	Bal.	-	-	-	-	-	-	-	-	-	-
Nb (ppm)	<10	-	<10	25	35	230	20	<10	<10	<10	<10	<10	<10	255	-	-	-
Cu (ppm)	-	-	-	-	-	400	-	-	-	-	-	-	-	-	500	<40	<300
CuSi₃	0.01	-	-	-	-	-	-	-	0.38	-	-	0.41	0.91	-	-	0.01	-
AISI 316L	-	-	-	0.02	0.054	-	-	17.2	1.73	2.07	10.0	0.45	-	-	-	-	-

WAAM experiments were made inside low oxygen flexible enclosure filled with argon. This enclosure is fitted with a three axis motion system controlled via software. The oxygen content was controlled using an oxygen monitor (Figure 110).

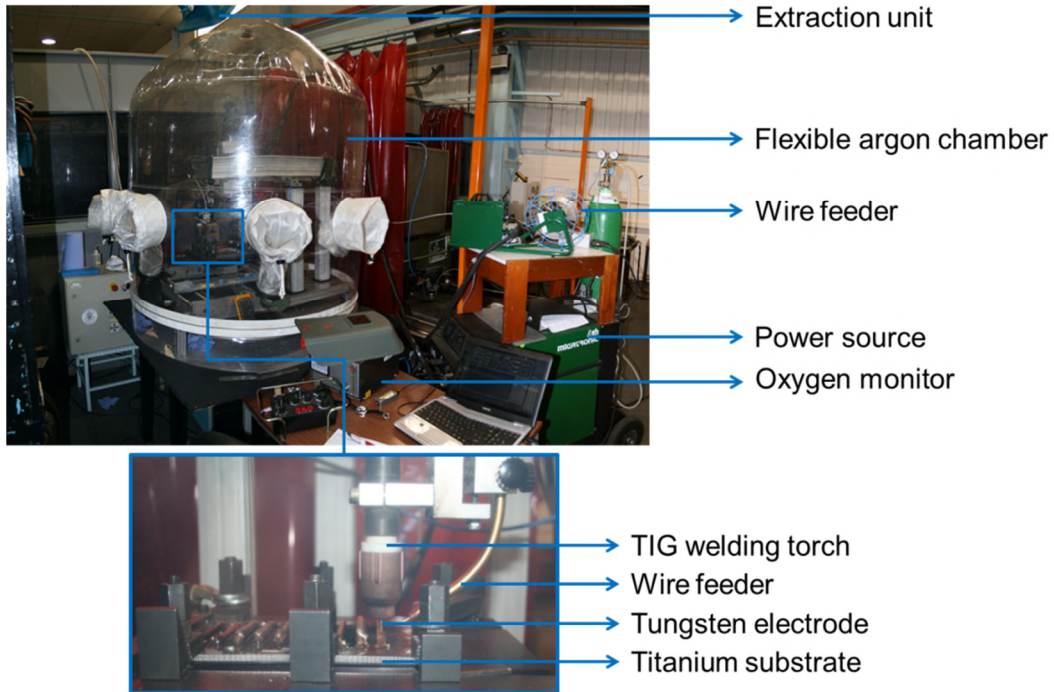


Figure 110 – AM experimental setup.

MIGATRONIC GTAW power source was used on DC mode and the MIGATRONIC KT4 wire feeder was connected to it. The maximum feeding speed for this wire feeder is 4 m/min.

The substrates were mechanically clamped in the edges (four corner and at the centre of longer edges) to avoid buckling due to the residual stresses accumulation during the build-up of the walls. The substrates were cleaned with acetone before welding. The wires were fed in the transversal direction to the welding direction (Figure 111 a) and with an angle of 20° with the substrate (Figure 111 b).

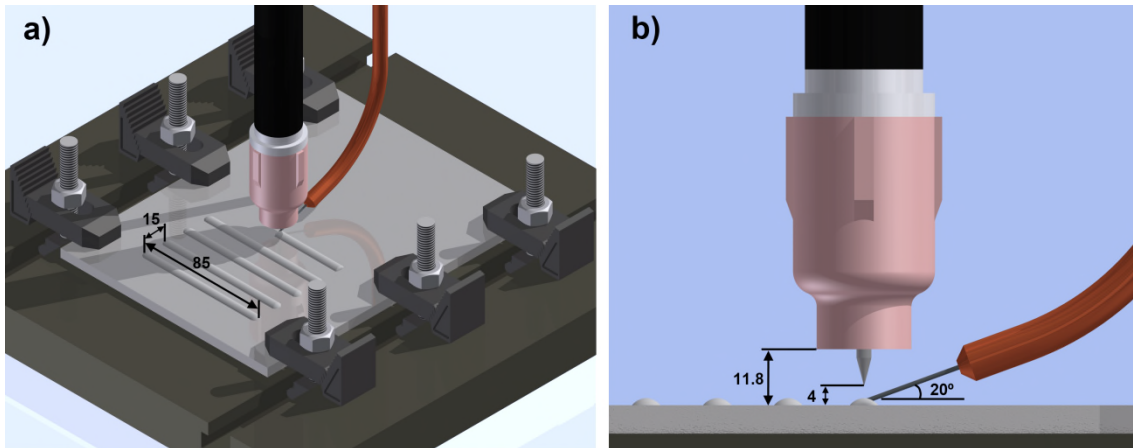


Figure 111 – Metal deposition strategy a) distance and angles used when feeding the wires b).

A Multi strike tungsten electrode with 3.2 mm of diameter from Huntingdon Fusion Techniques was used. The tip of the tungsten electrode was ground to an angle of 30°. The distance from the tip of the electrode to the substrate or to the top of the previous weld bead was 4 mm and from the shroud to the substrate 11.8 mm this translates to a tungsten stick out of 7.8 mm. The current mode used was straight DC and the travel speed was maintained constant.

The deposition strategy was the production of walls with 85 mm length and 15mm apart. Each metal was deposited separately; the first layer of the first metal was deposited in every wall. This strategy was selected to enable the cooling of the deposited layer and reduce changes of wire.

The deposition direction for each layer of each wall was inverted, so that the position X and Y position of the start of the previous layer is the position where the next layer ends. As the start of a weld bead has higher layer height and the end has a depression, lower layer height, this deposition strategy was selected to avoid the bead start and end transitions to accumulate during the wall build up, generating a constant layer height and consequently a constant wall height.

From the walls built during this set of experiments a selected group was examined in greater detail. The variable deposition parameters are presented in Table 48, Table 49 and Table 50 that are shown in appendix A.

After the walls were built the substrate was extracted from the chamber and the walls were separated. Each wall was sectioned using the Struers discotom 60 cut-off saw in two different specimens for metallographic analysis. Each specimen was identified and mounted on conductive resin. The specimens were ground using an automated polisher and several stages of silicon carbide papers of higher granulometry level. The two next grinding steps were using a cloth with 3 μm diamond suspension and lubricant followed by a 1 μm diamond paste and lubricant. The final polishing step was done with Struers OP-S colloidal silica suspension with oxalic acid as lubricant.

After polishing the specimens, they were observed under the optical microscope to evaluate the wall features and afterwards under scanning electrode microscope to evaluate the IMC formation. The last experimental setup was the hardness evaluation following the standard (BS EN ISO 6507 - 1, 2005) using an automatic Zwick micro hardness machine, to corroborate the IMC formation with the hardness profiles.

5.3 Results and discussion

This set of experiments can be separated in three different phases. The first was an initial feasibility verification of the different metal deposition (samples AM1 and AM2). The second was an understanding on the Titanium diffusion through the niobium layers (samples AM3 and AM4). The final stage was the build of AM parts from titanium to stainless steel without the formation of brittle IMC's (samples AM5 and AM6).

In all the specimens produced the first three layers deposited were the same metal as the substrate. This step was taken to have the Ti deposited layers present, enabling the detachment of the specimens from the substrate without losing the Ti at the end of the transition. This will enable the possibility of attaching these inserts without the necessity of generating any dissimilar welds. Figure 112 describes the possible implementation process for this technique.

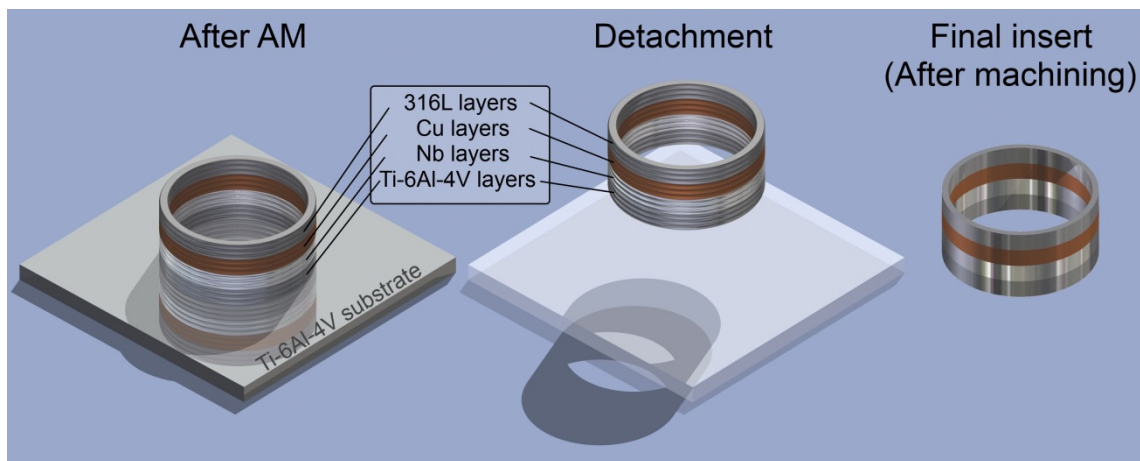


Figure 112 – Schematic representation for final steps on the inserts manufacturing process.

Samples AM1 and AM2 were made to verify the possibility and the range of deposition parameters that could be used to produce components with these four different metals. Figure 113 shows that the Cu deposition is the critical metal to deposit due to its high fluidity making its deposition very difficult and not straight.

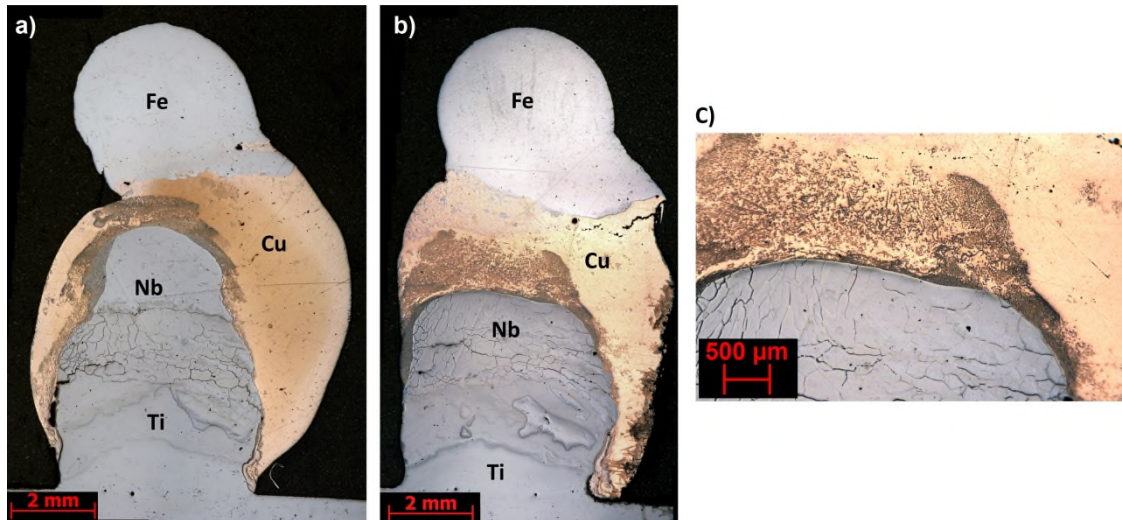


Figure 113 – Composite macro from sample AM1 a), AM2 b) and detailed macrostructure of sample AM2 interface between Nb and Cu c).

During the experimental work it was observed that Cu tends to form very large droplets of liquid metal at the tip of the wire. These droplets take very long time to detach and when they detach they tend to make the weld bead unstable and tend to wet previously deposited metals enhancing the possibility for the formation of IMC compounds.

In the optical micrographs of both samples (Figure 113) different phases or components can be identified dispersed on the Nb-Cu and Cu-Fe interfaces. There is also the presence of cracks on the Nb deposited layers and as the Cu wetted Nb layers close to Ti and Ti there is the possibility of IMC formation at these points. Subsequently SEM/EDS analysis was carried out to further investigate the presence and nature of the IMC formation at this interface. A general assessment of the elemental dispersion through the total dimension of the sample was made and the graph for the correspondent spectrums is plotted in Figure 114.

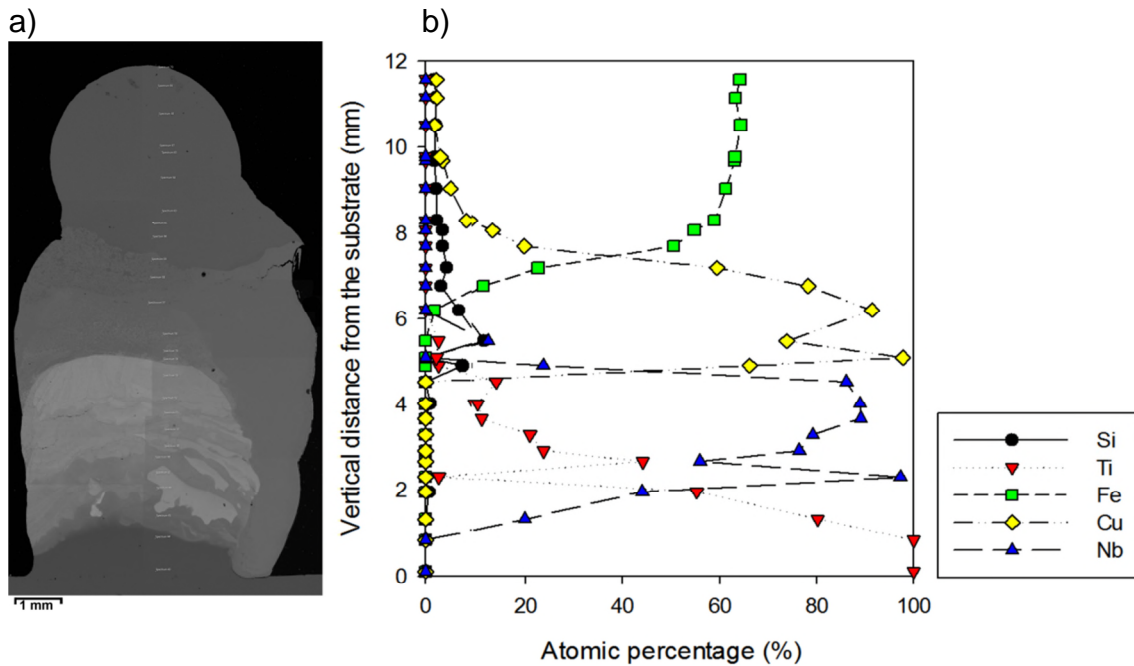


Figure 114 - Composite macrograph from specimen AM2 SEM/EDS analysis a) and graphic with elemental atomic composition across AM4 specimen b).

Observing Figure 114 it is possible to identify the elemental distribution across the vertical distance of the deposited wall. From the bottom of the sample the deposited titanium remains there and during the Nb deposition the titanium content decreases with the height of the sample. The titanium distribution across the Niobium layers is not uniform, with areas having higher concentration of Ti (darker areas) and other areas with lower Ti levels. However the trend is of decreasing concentrations of Ti when the Nb deposition is further away from the Ti interface. At the Nb-Cu interface the presence of Ti is still noticeable; despite its low concentrations (2 to 3% at.). To prevent IMC formation Ti needs to be close to 0% when the deposition of Cu is initiated due to the low solid solubility of Cu in Ti and the possible formation of IMC compounds. At the Cu area of the samples it is possible to detect the presence of Nb and Fe, once again there is the necessity of avoiding the interaction of Nb and Fe, due to the possibility of IMC formation between these two metals. At the Fe deposition phase a migration of Cu inside Fe is observed, however Cu is compatible with Fe. The previously deposited Nb is at 0% when the stainless steel is deposited. From these results it was possible to identify a critical area

that needed to be addressed during the next set of experiments, the diffusion between two subsequent metals. The critical metal identified was Ti, because it migrated across the Nb deposition and was still present when the Cu was deposited. So, to better understand the migration of Ti through the Nb and to understand the different deposition parameters to be used on the Nb layer, the next experiments were made by depositing 10 layers of Nb on top of the three previously deposited layers of Ti. Comparing the macros on Figure 115 and the welding parameters the necessity of changing the parameters during the build of walls is evident.

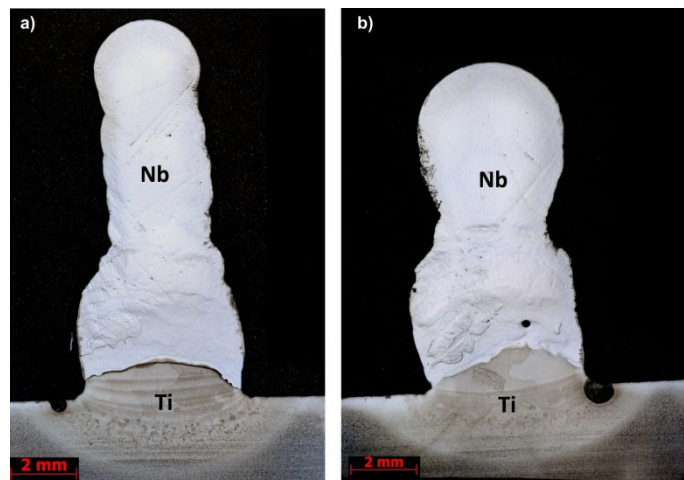


Figure 115 – Composite macro from samples AM3 a) and AM4 b).

On sample AM3 the deposition parameters were constant and it was possible to verify a narrowing of the sample after the Ti to Nb transition finishes. This happens due to the formation of a gradient of Ti mixing in the Nb deposited metal from the Nb-Ti interface to the top of the Nb layers. This mixing gradient introduces continuous changes on the metal thermal properties, due to the dissimilar properties (Table 44) from the two metals used (lower thermal conductivity for high dispersions of Ti in Nb and higher thermal conductivity for lower dispersion of Ti in Nb).

Table 44 – Ti and Nb thermal properties (Gale and Totemeier, 2003).

Metal	Melting Point (°C)	Thermal conductivity (W/mK)
Ti	1668	11.4
Nb	2477	52.3

With lower thermal conductivity of the substrate and with a lower melting point due to the Ti alloying effect, the molten alloy stays molten for longer. This enables a better wetting of the previous layer. On the contrary, when the Ti is reduced or eliminated, the higher thermal conductivity and melting temperature of Nb, decrease the melting time and consequently the deposit width.

On sample AM4 the deposition parameters were changed to avoid the narrowing of the wall during the build. There was an increase in the welding current and consequently an increase on the heat input, which counteracted the higher thermal conductivity originated by the Nb layers. The wall width from sample AM4 is closer to the wall width originated from the Ti deposition. The height of the wall is lower because the amount of wire deposited is the same on the two samples (same wire feed speed).

After a global SEM/EDS analysis it is possible to identify the mixing and dispersion of Ti on the Nb layers. Figure 116 presents the SEM/EDS spectrums and their correspondent compositions. The last element to disperse from the Ti alloy is (5 mm to 6 mm), while Al and V decrease to zero before (4mm), after the Nb deposition is initiated.

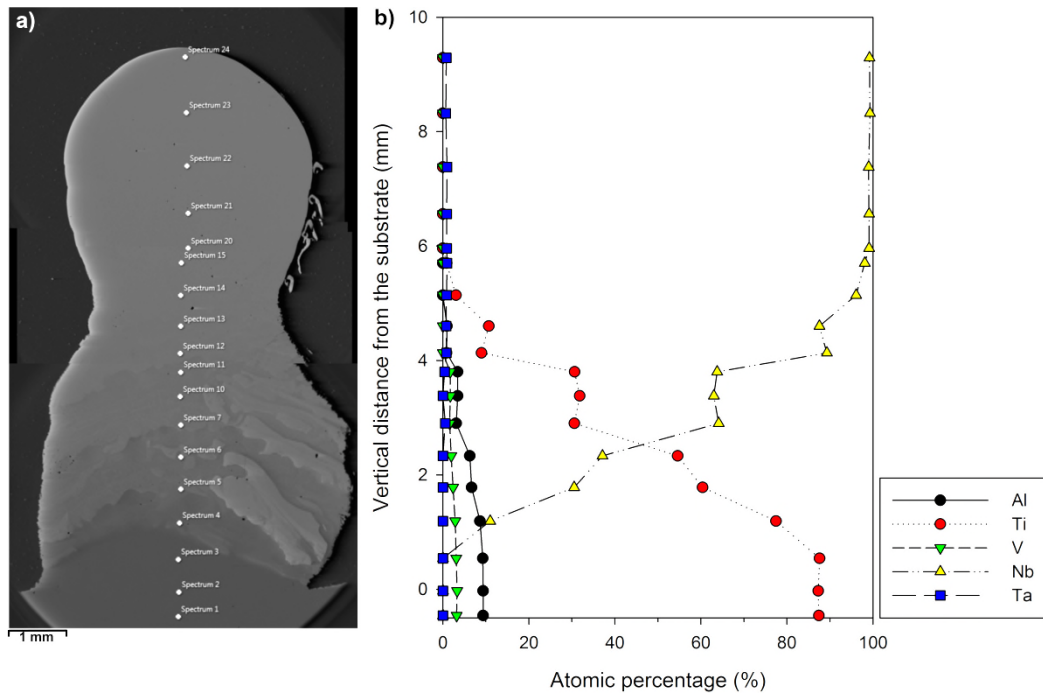


Figure 116 – Composite macrograph from AM4 SEM/EDS analysis a) and graphic with elemental atomic composition across AM4 specimen b).

This shows that with these deposition parameters when the wall was 6 mm of height the wall is free of Ti, Al and V that comes from the previously deposited Ti-6Al-4V alloy. After this point, the next Nb deposited layers act as a buffer for the subsequent Cu deposition.

This shows that with ten layers of Nb it was possible to block the diffusion of Ti on the Nb layer and prevent the formation of Cu-Ti IM compounds when the copper deposition is initiated. These results were extrapolated for the next set of experiments where 10 layers of Cu were also deposited to prevent any interaction between Nb and stainless steel.

On the final set of experiments the number of Nb deposited layers was increased from five to ten. The CuSi₃ welding wire was substituted by a pure Cu wire (to remove the Si present on the Cu deposited layers) due to the possible formation of IMC formation between Si and Fe.

Figure 117 shows the macrographs from samples AM5 and AM6.

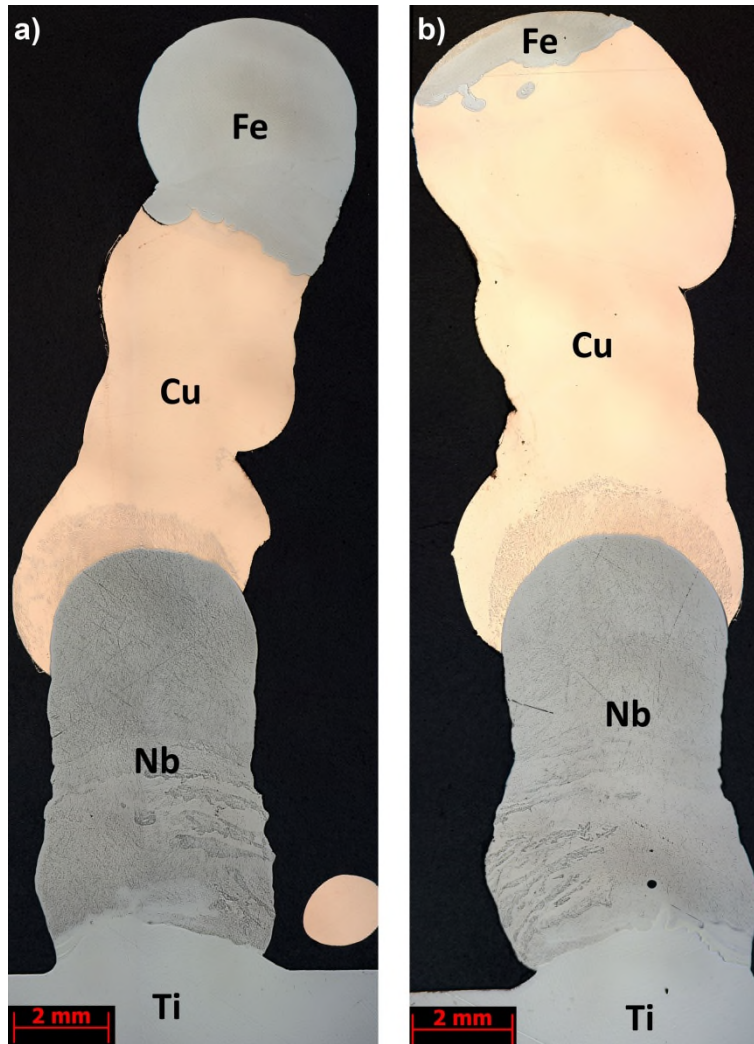


Figure 117– Composite macro from sample AM5 a) and AM6 b).

As the number of layers for each metal deposited is higher, each metal is deposited at higher distance from each other. Cu was deposited in a more controlled way, avoiding the contact with the side of the Nb deposited layers. The diffusion of Nb in Cu is localized close to the Nb-Cu interfaces and the Nb cracking present on the Nb layers from samples AM1 and AM2 is absent. A general SEM/EDS analysis along the deposited metal was carried out and the results presented on Figure 118.

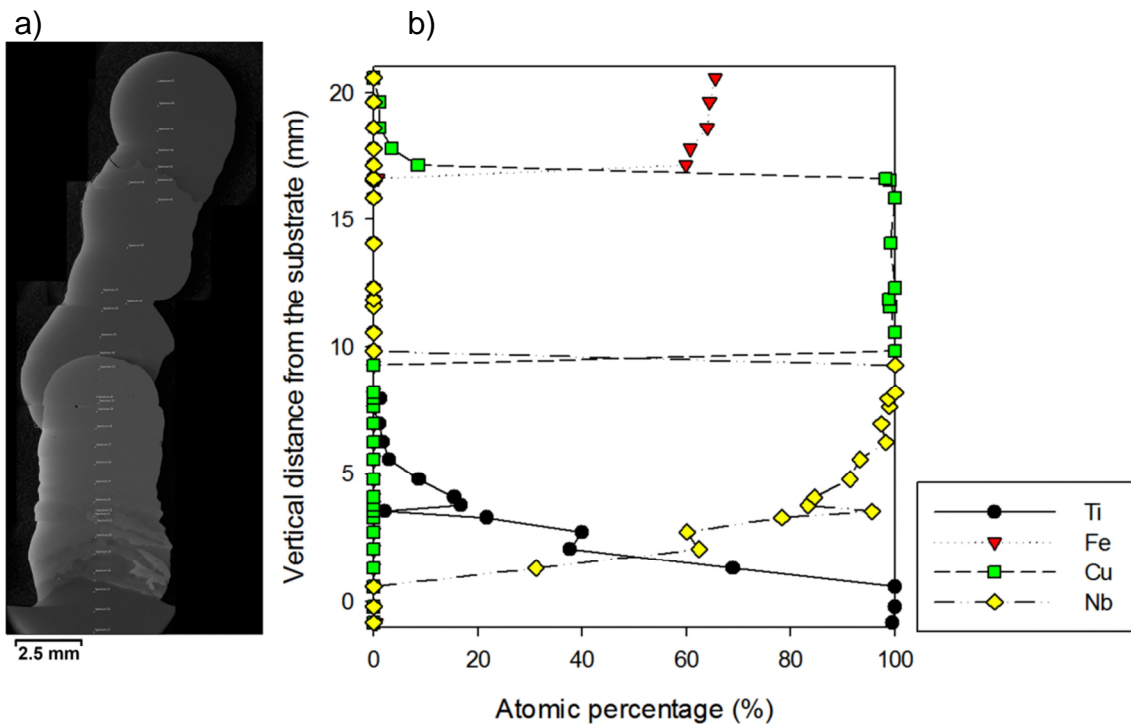


Figure 118 - Composite macrograph from sample AM5 SEM/EDS analysis a) and graphic with elemental atomic composition across AM5 specimen b).

The Titanium layers are well defined, right next to it there is the Nb deposited layers. On the Nb layers, the Ti content decreases until it reaches zero, at 8 mm from the substrate, so the ten deposited layers of Nb were enough to prevent the contact between Ti and Cu. There is a low diffusion of Nb in the Cu, this can be related to the low heat input necessary to melt the copper wire in comparison with the Nb wire. The remelting of Nb is lower at the first layer and consequently lower levels of Nb are carried to the subsequent deposited Cu layers. Once again the transition from Cu to stainless steel is very fast, with the content of Cu decreasing to zero in a 3 mm distance from the Cu-Fe interface. To further investigate the presence of IMC higher magnification SEM analysis were carried out close to the Nb-Cu and Cu-Fe interfaces (Figure 119 and Figure 121).

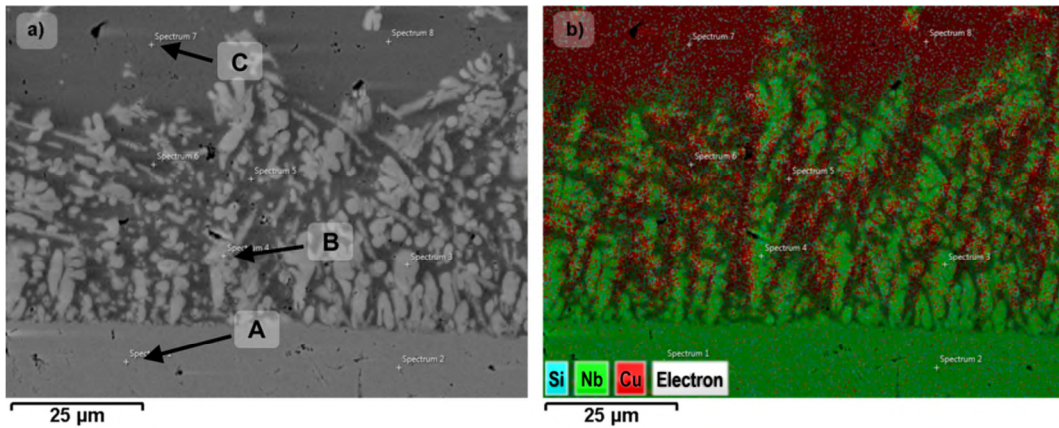


Figure 119 – Nb-Cu interface SEM micrograph a) and corresponding EDS mapping b).

From the EDS mapping it is possible to verify that Nb and Cu are at different places at the interface. The mixing is not very evident and the formation of new phases is difficult due to the good affinity between these two elements (Figure 120).

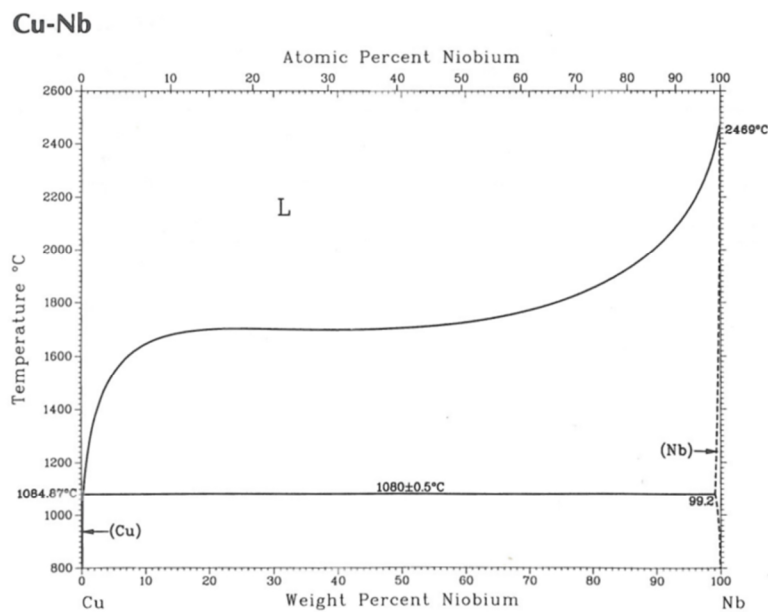


Figure 120 – Cu-Nb phase diagram (ASM - International, 1992).

The different phases present on the SEM micrograph were analysed and the correspondent spectrums are presented in Table 45.

Table 45 – EDS quantitative analysis from phases identified on Figure 119 a).

Elements	A	B	C
Si	-	-	2.7
Ti	0.66	-	-
Mn	-	-	0.4
Cu	-	0.81	80.34
Nb	98.55	98.29	16.27
Sn	0	0	0.29
Ta	0.79	0.9	-

Phase A has been identified as Nb with a small amount of Ti dispersed (0.66 %at), once again showing that the levels of Ti at the interface are reduced to almost 0%. Phases B and C were identified as solid solutions between Cu and Nb. No IM compounds were identified at the Nb-Cu interface. The same approach was taken to evaluate the possible IM compounds formed at the Cu-Fe interface.

Higher magnification SEM micrograph and EDS mapping were taken at the Cu-Fe interface (Figure 121 and Figure 122).

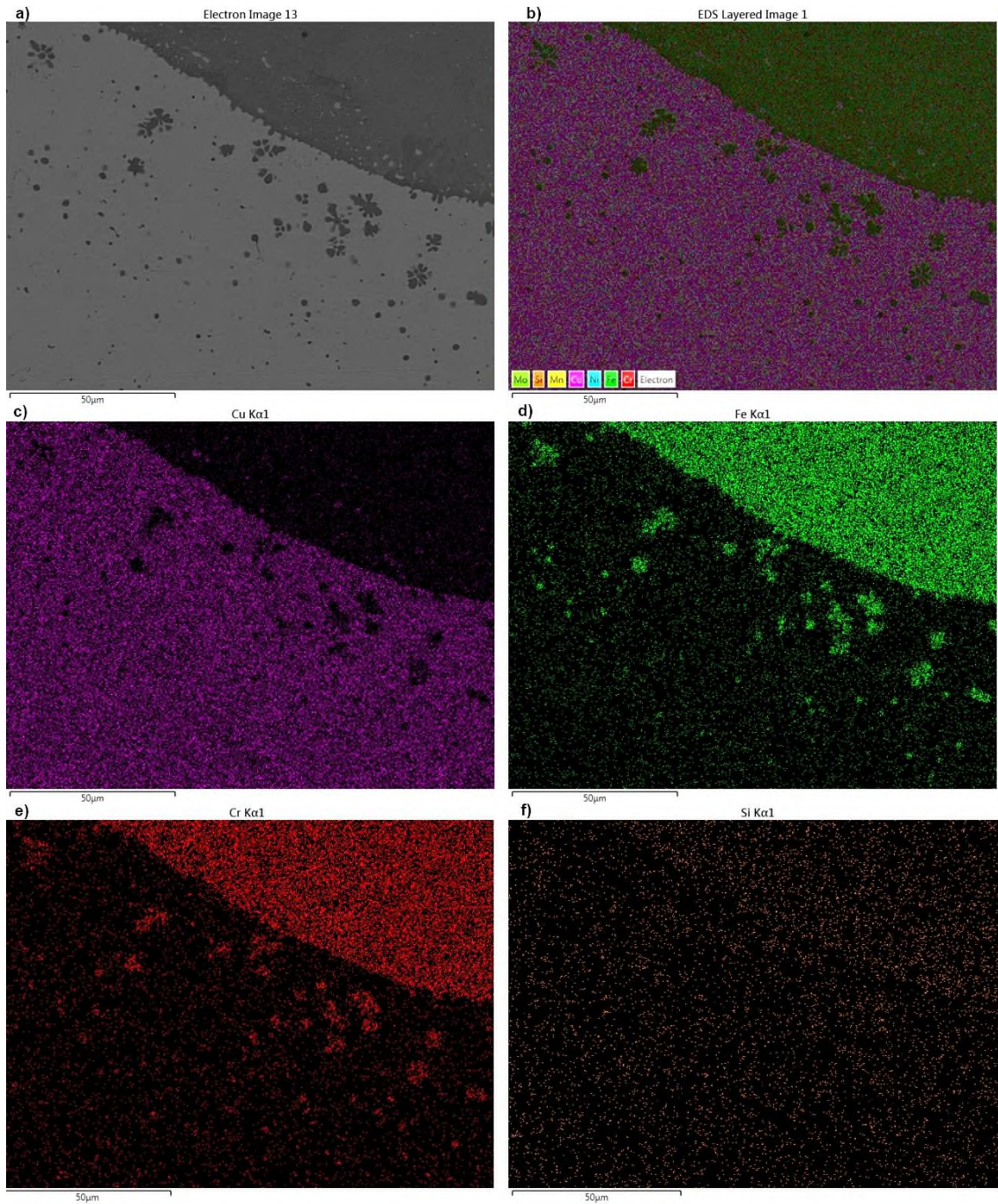


Figure 121 –SEM and EDS mapping for the Cu-Fe interface. a) SEM image, b) Composite EDS mapping, c) Cu, d) Fe, e) Cr and f) Si EDS mapping.

During the EDS mapping, it was not possible to detect the presence of either Ti or Nb, this indicates once again that the deposition of Cu was enough to prevent any interaction between Fe and Ti or Fe and Nb. The Cu and Fe EDS

mapping shows low to none interaction between Fe and Cu, this means the metals diffused without interacting and creating new intermediate phases.

Semi-quantitative EDS analysis was carried out to verify if the qualitative EDS mapping results are accurate (Figure 122 and

Table 46).

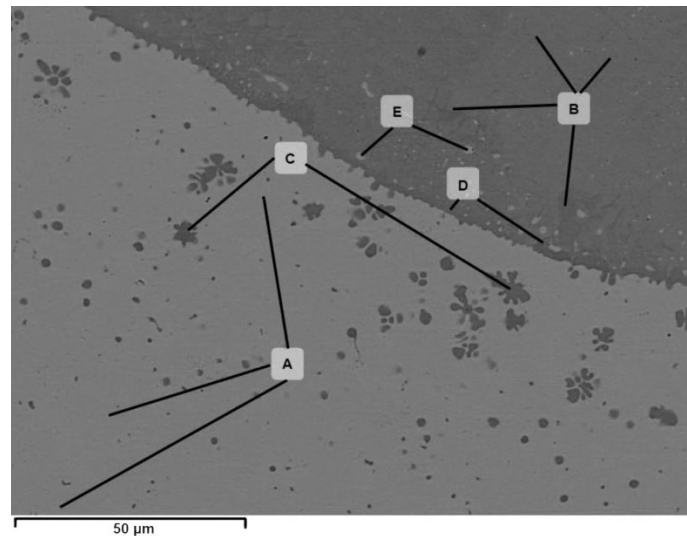


Figure 122 – Cu-Fe interface SEM micrograph and corresponding identifiable phases.

Several different phases were identified at Figure 122, A and B away from the Cu Fe interfaces C and E as different segregated phases on the Fe and Cu deposited metals and D close to the interface between the two metals. The correspondent composition of each phase selected is shown in

Table 46.

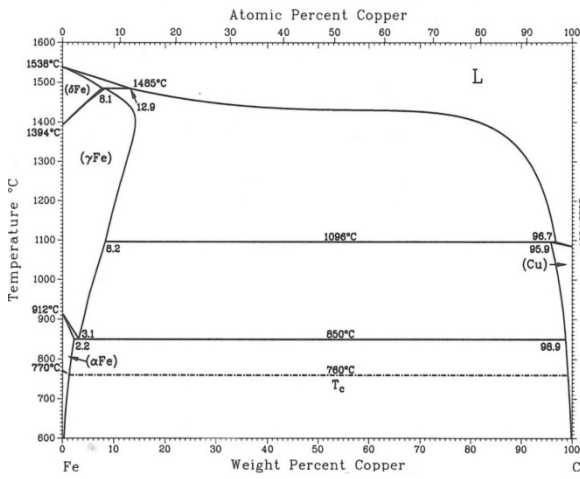
Phases A and B are similar to the parent metals, with some dissolution from Fe on Cu (2.27%) and Cu on stainless steel (8.11%). Phase C is similar to the parent metal stainless steel composition higher silicon and lower Ni. Phase E is similar to Cu parent metal with higher Fe Cr and Ni contents due to being Cu phases segregated in a stainless steel matrix. Phase D has a very similar composition to phase B with the exception of a decrease Ni.

Table 46 – EDS semi-quantitative analysis (Wt%) from phases identified on Figure 122.

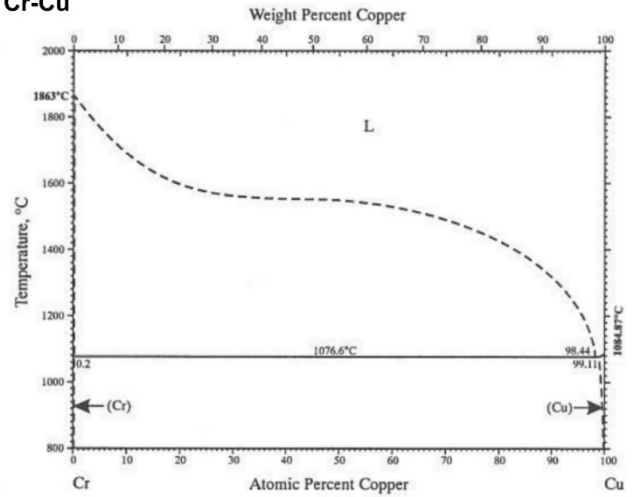
	A	B	C	D	E
Si	0.15	1.05	3.69	2.32	0.14
Cr	0.47	18.39	18.8	18.9	2.62
Mn	0.66	0.4	0	0	1.56
Fe	2.27	59.88	64.33	61.89	9.02
Ni	1.00	10.00	5.67	6.02	2.72
Cu	95.44	8.11	7.52	8.04	83.95
Mo	0	2.18	0	2.82	0

With the high compatibility between Cu-Fe, Cr-Cu and Cu-Ni shown by their phase diagrams (Figure 123) and the low reaction between these deposited metals the Cu stainless steel interface can be considered IMC free.

Cu-Fe



Cr-Cu



Cu-Ni

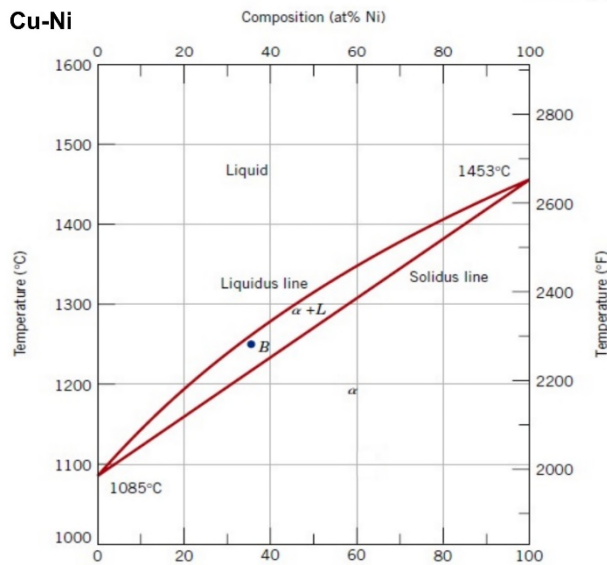


Figure 123 – Fe-Cu Cu-Cr and Cu-Ni phase diagrams

To further investigate the possibility of IMC formation during the build of this final component, the hardness of the sample was also considered. As the IMC phases have considerable high hardness values when compared to the hardness of the base metals if an IMC phase is present in the sample it can be detected by a rise in the hardness at that particular point. Table 47 shows the Vickers hardness from the participating metals/alloys.

Table 47 – Hardness values for the alloys used at samples AM5 and AM6.

Metal/alloy	Ti-6Al-4V	Nb	Cu	AISI 316L
Vickers hardness	349.0	134.6	37.63	152

Vickers micro-hardness tests with a load of 200 g, 1mm spacing (wall), 0.5 mm spacing (substrate) and waiting time of 10s were carried out on sample AM5. From this data was possible to make a surface hardness profile (Figure 124) and evaluate the sample hardness against the parent metals hardness.

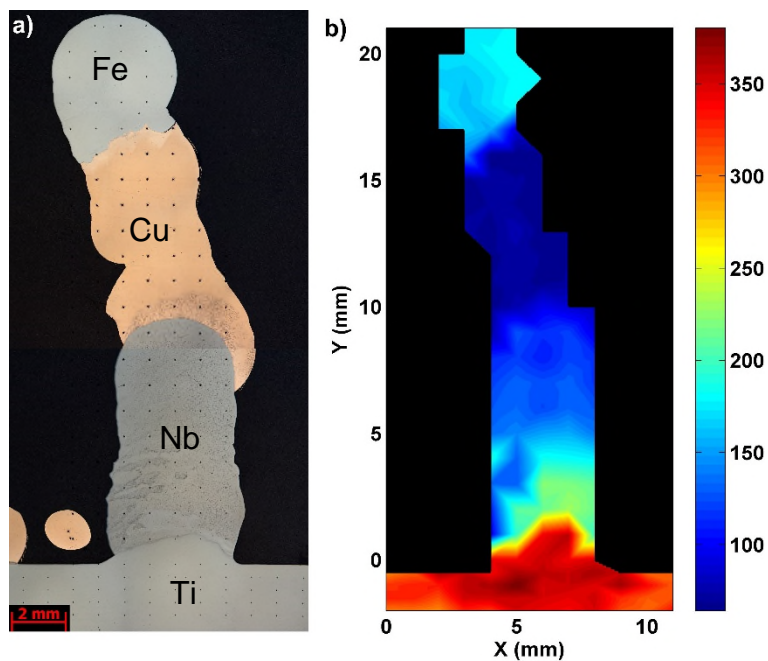


Figure 124 – Sample AM5 hardness mapping indents a) and corresponding hardness map b).

The highest hardness values are at the substrate and the deposited Ti layers, with values around 390 HV. These values are in agreement with the regular hardness for Ti-6Al-4V that is around 350 HV (Table 47). The remainder deposited metals also correspond to their typical hardness values with a softer area corresponding to the Cu layers and intermediate values of hardness verified for the Nb and stainless steel layers. As the high hardness values are found on the substrate and on the Ti deposited layers and not at the diffusion

zones of the metals it is possible to state that the formation of IM Compounds was also not detected by the hardness profile of the sample.

5.4 Chapter conclusions

A new technique to select the best metallic interlayers to use for any particular dissimilar combination was successfully applied to generate an IMC free structure between Fe and Ti. This technique uses a systematic examination of phase diagrams to determine a metallic selection of compatible metals between the parent metals and between themselves.

The hypothesis postulated at the introduction of this chapter that it was possible to control the diffusion between the four compatible metals Ti, Nb, Cu and Fe, to avoid the IMC formation was confirmed using the SEM/EDS analysis and the hardness profiling of the specimens.

To obtain this IMC free structure it was necessary to use an arc based 3D printing technology, designated WAAM, that deposits the metal in successive layers. This 3D printing technology enabled the achievement of different controlled diffusions between the metals. Before the transition from metal A to B, the percentage of metal A was decreased to zero, preventing the formation of IMC with the next metal that needed to be deposited.

This showed that to fully prevent the IMC formation for fusion based processes it is necessary to apply the correct weld metal engineering, and select the correct metals to be used as interlayers between the dissimilar parent metals.

6 Conclusions

Fe-Al:

This work showed that it is possible to use the different physical properties of Fe and Al, melting point and thermal conductivity, to obtain a joint. Laser dissimilar spot joining in conduction mode achieved controlled selective melting of Al without melting Fe. This enabled the control of the diffusion between the two parent metals and consequently a control of the IMC layer thickness. However although control of the IMC thickness was achieved, the mechanical properties of the joints were always compromised and an interfacial failure of the joints was always verified .

The Zn layer present at the galvanized steel did not reduce the IMC layer formation, generating an increase in its thickness and an increase mixing in the weld pool. This could be related to a higher turbulence and mixing generated at the weld pool by the vaporization of Zn. In spite of the higher levels of IMC the mechanical properties of the joints were very similar to the uncoated steel to Al spot welds.

Besides the IMC formation, the joining parameters range obtained by this joining technique is also very limited with a final interaction time of 3s that can be too long for application by the automotive industry.

Ti-stainless steel:

The physical properties of these alloys are not so different as Fe and Al, and so the control of the welding parameters is not enough to obtain a selective melting of one of the parent metals. The autogenous keyhole laser welds showed that even obtaining different Fe-Ti melt pool compositions, these weld pools are too brittle to form a joint and so weld metal engineering is always needed to obtain a fusion based joint between Fe and Ti.

The use of interlayers is necessary to achieve better mechanical properties and avoid the diffusion of Fe into the Ti. The use of Ni as a thick interlayer showed

that it is possible to obtain a sound joint between Ni and stainless steel; however it was impossible to obtain a crack free weld bead at the Ti-Ni interface.

The use of Cu as a transition metal generated a melt pool with IMC layers at the Ti and stainless steel interfaces with dispersed IMC phases in the Cu weld bead. However due to its high ductility, the welds were mechanically sound with a maximum strength of 200 MPa, that is 20% of the UTS of the Ti-6Al-4V. The study of two possible single metals as interlayers (Ni and Cu) to prevent the IMC formation revealed that it was not possible to use a single interlayer to fully avoid the IMC formation. It was necessary to study the possibility of using a hybrid interlayer to achieve an IMC free joint.

To obtain the ideal hybrid interlayer combination an innovative systematic selection approach was taken. This approach used a diagram with all the possible combinations of phase diagrams and selected the candidate interlayer metals that did not have any IMC with the parent metals and between themselves. This new systematic selection of possible interlayers revealed that the hybrid interlayer to be used was composed of Cu and Nb. To generate this interlayer, WAAM, a 3D printing technology that deposits several layers of the selected metals was selected. The layered component generated was IMC free and could bridge the dissimilarity between Ti and stainless steel.

This innovative systematic selection of metals to be used as interlayers could be applied towards several other type 2 dissimilar combinations and possibly solve several other unweldable dissimilar metallic combinations.

7 Future work

7.1 Fe-Al spot welding

Fe-Al spot welding in conduction mode can be used to join Fe and Al, however, the joining parameters that can be used are still very restricted and so the future work should address this point.

This can be done by modelling the process to understand the time-temperature cycle and relate them with the fundamental material interaction parameters and also with the IMC formation.

As the steel interface is not melted during the joining process, it can be laser textured to increase the wetting area of Al onto steel. The use of thin interlayers or different coatings that are compatible with one of the parent metals should also be investigated.

7.2 Ti to stainless steel

This work also shows that by selecting the appropriate metals it is possible to form IMC free joints between stainless steel and Ti. And so the future work in this field should be centred in improving the material selection for this type of joints and investigating if this approach can be used for different dissimilar combinations.

Future improvements in the Ti stainless steel dissimilar joining.

To further control the diffusion between Ti and Cu, V should be used as a substitute for Nb due to its lower melting point.

The deposition of Cu can also be improved by using reusable graphite tooling.

The investigation of laser welding as a manner of joining these different metals should also be investigated to reduce the complexity of the build-up strategies. Each of the different metals could be deposited individually and the final component could be assembled by laser welding of the individual components.

Future research in general dissimilar welding

This work presents a theory of material selection that can be applied to a multitude of dissimilar metallic combinations. This opens the possibility of using this theory to solve major part of the dissimilar metallic combination issues, and so this theory should be investigated for different dissimilar joints, e.g. Al-Ti and Ti-Cu.

REFERENCES

- Agudo, L., Eyidi, D., Schmaranzer, C.H., Arenholz, E., Jank, N., Bruckner, J., Pyzalla, A.R., 2007. Intermetallic Fe x Al y -phases in a steel/Al-alloy fusion weld. *J. Mater. Sci.* 42, 4205–4214. doi:10.1007/s10853-006-0644-0
- Alu matter, 2014. RSW in the Automotive Industry [WWW Document]. URL <http://aluminium.matter.org.uk/content/html/eng/default.asp?catid=204&pageid=2144416851> (accessed 2.19.14).
- American Welding Society, 1996. *Welding Handbook, Materials and Applications - Vol 3 Part 1*, 8th editio. ed. American Welding Society, Miami.
- American Welding Society, 1991. *Welding Handbook: Welding Processes, Vol. 2 (American Welding Society/Welding Handbook)*, 8th Editio. ed. American Welding Society, Miami.
- Ashfaq, M., Rao, K.P., Rafi, H.K., Murty, B.S., Dey, H.C., Bhadurp, A.K., 2011. Friction Welding of Titanium to 304L Stainless Steel Using Interlayers. *Pract. Metallogr.* 48, 188–207.
- ASM - International, 2012. *Phase Diagrams: Understanding the Basics*. ASM International.
- ASM - International, 1992. *ASM Handbook: Alloy Phase Diagrams v. 3*. ASM International.
- Assuncao, E., Williams, S., 2013. Comparison of continuous wave and pulsed wave laser welding effects. *Opt. Lasers Eng.* 51, 674–680. doi:10.1016/j.optlaseng.2013.01.007
- Assuncao, E., Williams, S., Yapp, D., 2012. Interaction time and beam diameter effects on the conduction mode limit. *Opt. Lasers Eng.* 50, 823–828. doi:10.1016/j.optlaseng.2012.02.001
- Bouche, K., Barbier, F., Coulet A., 1998. Intermetallic compound layer growth between solid iron and molten aluminium. *Mater. Sci. Eng. A* 249, 167–175.

BS EN ISO 14273, 2001. Specimen dimensions and procedure for shear testing resistance spot , seam and embossed projection welds. Br. Stand.

BS EN ISO 6507 - 1, 2005. Metallic materials — Vickers hardness test — Part 1: Test method. Br. Stand. 20.

Buchfink, G., 2007. THE LASER AS A TOOL - A light beam conquers industrial production, 1st editio. ed. Vogel Buchverlag, Wuzburg.

Cao, R., Yu, G., Chen, J.H., Wang, P., 2013. Journal of Materials Processing Technology Cold metal transfer joining aluminum alloys-to-galvanized mild steel 213, 1753–1763.

Chatterjee, S., Abinandanan, T. a., Chattopadhyay, K., 2006. Microstructure development during dissimilar welding: Case of laser welding of Ti with Ni involving intermetallic phase formation. J. Mater. Sci. 41, 643–652. doi:10.1007/s10853-006-6480-4

Chen, Y.C., Gholinia, a., Prangnell, P.B., 2012. Interface structure and bonding in abrasion circle friction stir spot welding: A novel approach for rapid welding aluminium alloy to steel automotive sheet. Mater. Chem. Phys. 134, 459–463. doi:10.1016/j.matchemphys.2012.03.017

Dey, H.C., Ashfaq, M., Bhaduri, A.K., Rao, K.P., 2009. Joining of titanium to 304L stainless steel by friction welding. J. Mater. Process. Technol. 209, 5862–5870. doi:10.1016/j.jmatprotec.2009.06.018

Donachie, M.J., 2000. Titanium: A Technical Guide. ASM International.

Dong, H., Hu, W., Duan, Y., Wang, X., Dong, C., 2012. Dissimilar metal joining of aluminum alloy to galvanized steel with Al–Si, Al–Cu, Al–Si–Cu and Zn–Al filler wires. J. Mater. Process. Technol. 212, 458–464. doi:10.1016/j.jmatprotec.2011.10.009

Eickhoff, S.T., Eagar, T.W., 1990. Characterization of Spatter in Low-Current GMAW of Titanium Alloy Plate. Weld. J.

Elrefaey, a., Tillmann, W., 2009. Solid state diffusion bonding of titanium to steel using a copper base alloy as interlayer. *J. Mater. Process. Technol.* 209, 2746–2752. doi:10.1016/j.jmatprotec.2008.06.014

Fazel-Najafabadi, M., Kashani-Bozorg, S.F., Zarei-Hanzaki, a., 2011. Dissimilar lap joining of 304 stainless steel to CP-Ti employing friction stir welding. *Mater. Des.* 32, 1824–1832. doi:10.1016/j.matdes.2010.12.026

Ferro, R., Saccone, A., 2007. *Intermetallic Chemistry* (Pergamon Materials Series). Pergamon Press, Amsterdam.

Forward Precision Equipment Ltd, 2011. Processes | FPE Gatwick | Friction Welding, Friction Stir Welding (FSW), Electrical Upsetting and Resistance Welding machinery [WWW Document]. URL <http://www.fpe.co.uk/processes/friction-welding> (accessed 3.7.11).

Gale, W.F., Totemeier, T.C., 2003. *Smithells Metals Reference Book*. Butterworth-Heinemann.

Gao, M., Mei, S.W., Wang, Z.M., Li, X.Y., Zeng, X.Y., 2012. Characterisation of laser welded dissimilar Ti/steel joint using Mg interlayer. *Sci. Technol. Weld. Join.* 17, 269–276. doi:10.1179/1362171812Y.0000000002

H.M. Government, 2009. The UK Low Carbon Five point plan.

Hayden corp., 2014. GMAW welding [WWW Document]. URL http://www.haydencorp.com/content.php?p=manual_welding

He, P., Zhang, J., Zhou, R., Li, X., 1999. Diffusion Bonding Technology of a Titanium Alloy to a Stainless Steel Web With an Ni Interlayer. *Mater. Charact.* 43, 287–292. doi:10.1016/S1044-5803(99)00008-X

Jácome, L.A., Weber, S., Leitner, A., Arenholz, E., Bruckner, J., Hackl, H., Pyzalla, A.R., 2009. Influence of Filler Composition on the Microstructure and Mechanical Properties of Steel-Aluminum Joints Produced by Metal Arc Joining. *Adv. Eng. Mater.* 11, 350–358. doi:10.1002/adem.200800319

- Kahraman, N., Gulenc, B., Findik, F., 2005. Joining of titanium/stainless steel by explosive welding and effect on interface. *J. Mater. Process. Technol.* 169, 127–133. doi:10.1016/j.jmatprotec.2005.06.045
- Kazanas, P., Deherkar, P., Almeida, P., Lockett, H., Williams, S., 2012. Fabrication of geometrical features using wire and arc additive manufacture. *Proc. Inst. Mech. Eng. Part B J. Eng. Manuf.* 226, 1042–1051. doi:10.1177/0954405412437126
- Kobayashi, S., Yakou, T., 2002. Control of intermetallic compound layers at interface between steel and aluminum by diffusion-treatment. *Mater. Sci. Eng. A* 338, 44–53. doi:10.1016/S0921-5093(02)00053-9
- Kundu, S., Chatterjee, S., 2008a. Diffusion bonding between commercially pure titanium and micro-duplex stainless steel. *Mater. Sci. Eng. A* 480, 316–322. doi:10.1016/j.msea.2007.07.033
- Kundu, S., Chatterjee, S., 2008b. Characterization of diffusion bonded joint between titanium and 304 stainless steel using a Ni interlayer. *Mater. Charact.* 59, 631–637. doi:10.1016/j.matchar.2007.05.015
- Kundu, S., Ghosh, M., Laik, a, Bhanumurthy, K., Kale, G., Chatterjee, S., 2005. Diffusion bonding of commercially pure titanium to 304 stainless steel using copper interlayer. *Mater. Sci. Eng. A* 407, 154–160. doi:10.1016/j.msea.2005.07.010
- Lee, K.-J., Kumai, S., Arai, T., Aizawa, T., 2007. Interfacial microstructure and strength of steel/aluminum alloy lap joint fabricated by magnetic pressure seam welding. *Mater. Sci. Eng. A* 471, 95–101. doi:10.1016/j.msea.2007.04.033
- Lee, M.K., Lee, J.G., Choi, Y.H., Kim, D.W., Rhee, C.K., Lee, Y.B., Hong, S.J., 2010. Interlayer engineering for dissimilar bonding of titanium to stainless steel. *Mater. Lett.* 64, 1105–1108. doi:10.1016/j.matlet.2010.02.024

Liao, J., Yamamoto, N., Liu, H., Nakata, K., 2010. Microstructure at friction stir lap joint interface of pure titanium and steel. *Mater. Lett.* 64, 2317–2320. doi:10.1016/j.matlet.2010.07.049

Linnert, G.E., 1995. *Welding Metallurgy: Volume I, Fundamentals*. American Welding Society.

Liyanage, T., Kilbourne, J., Gerlich, a. P., North, T.H., 2009. Joint formation in dissimilar Al alloy/steel and Mg alloy/steel friction stir spot welds. *Sci. Technol. Weld. Join.* 14, 500–508. doi:10.1179/136217109X456960

Marder, A.R., 2000. The metallurgy of zinc-coated steel. *Prog. Mater. Sci.* 45, 191–271. doi:10.1016/S0079-6425(98)00006-1

Martina, F., Mehnen, J., Williams, S.W., Colegrove, P., Wang, F., 2012. Investigation of the benefits of plasma deposition for the additive layer manufacture of Ti–6Al–4V. *J. Mater. Process. Technol.* 212, 1377–1386. doi:10.1016/j.jmatprotec.2012.02.002

Mathieu, A., Shabadi, R., Deschamps, A., Suery, M., Mattei, S., Grevey, D., Cicala, E., 2007. Dissimilar material joining using laser (aluminum to steel using zinc-based filler wire). *Opt. Laser Technol.* 39, 652–661. doi:10.1016/j.optlastec.2005.08.014

Meshram, S., Mohandas, T., Reddy, G., 2007. Friction welding of dissimilar pure metals. *J. Mater. Process. Technol.* 184, 330–337. doi:10.1016/j.jmatprotec.2006.11.123

Mitschang, P., Velthuis, R., Didi, M., 2013. Induction Spot Welding of Metal/CFRPC Hybrid Joints. *Adv. Eng. Mater.* 15, 804–813. doi:10.1002/adem.201200273

Möller, F., Thomy, C., Vollertsen, F., Schiebel, P., Hoffmeister, C., Herrmann, A.S., 2010. Novel method for joining CFRP to aluminium. *Phys. Procedia* 5, 37–45. doi:10.1016/j.phpro.2010.08.027

Murakami, T., Nakata, K., Tong, H., Ushio, M., 2003. Dissimilar Metal Joining of Aluminum to Steel by MIG Arc Brazing Using Flux Cored Wire. *ISIJ Int.* 43, 1596–1602. doi:10.2355/isijinternational.43.1596

Murr, L.E., 2010. A review of FSW research on dissimilar metal and alloy systems. *J. Mater. Eng. Perform.* 19, 1071–1089. doi:10.1007/s11665-010-9598-0

Oikawa, H., Ohmiya, S., Yoshimura, T., Saitoh, T., 1999. Resistance spot welding of steel and aluminium sheet using insert metal sheet. *Sci. Technol. Weld. Join.* 4, 80–88. doi:10.1179/136217199101537608

Okamoto, H., 2010. *Desk Handbook: Phase Diagrams for Binary Alloys*. ASM International.

Otsuka, K., Ren, X., 2005. Physical metallurgy of Ti–Ni-based shape memory alloys. *Prog. Mater. Sci.* 50, 511–678. doi:10.1016/j.pmatsci.2004.10.001

Paul, C.P., Kumar, A., Bhargava, P., Kukreja, L.M., 2013. *Nontraditional Machining Processes*. Springer London, London. doi:10.1007/978-1-4471-5179-1

Pépe, N., Egerland, S., Colegrove, P. a, Yapp, D., Leonhartsberger, a, Scotti, a, 2011. Measuring the process efficiency of controlled gas metal arc welding processes. *Sci. Technol. Weld. Join.* 16, 412–417. doi:10.1179/1362171810Y.0000000029

Poddar, D., 2009. Solid-State Diffusion Bonding of Commercially pure Titanium and Precipitation Hardening Stainless steel. *Int. J. Recent Trends Eng.* 1, 93–99.

Qiu, R., Iwamoto, C., Satonaka, S., 2009. Interfacial microstructure and strength of steel/aluminum alloy joints welded by resistance spot welding with cover plate. *J. Mater. Process. Technol.* 209, 4186–4193. doi:10.1016/j.jmatprotec.2008.11.003

- Raghavan, V., 2002. Cu-Fe-Ti (Copper-Iron-Titanium). *J. Phase Equilibria* 23, 172–174. doi:10.1361/1054971023604152
- Raynor, G.V., Rivlin, V.G., 1988. *Phase Equilibria in Iron Ternary Alloy*. London.
- Reardon, A.C., 2011. *Metallurgy for the Non-Metallurgist (2nd Edition)*. ASM International.
- Santos, J.F.O., Quintino, L., 1997. *Processos de soldadura - Volume I, 1st editio. ed. Edicoes Tecnicas do Instituto de Soldadura e Qualidade, Lisboa.*
- Sasabe, S., Iwase, T., Matsumoto, T., Hattori, Y., Miono, T., 2009. Dissimilar Metal Joining of Aluminum Alloys to Steel in MIG Braze Welding by using the advanced Hot-dip Aluminized Steel Sheet. *Q. J. Japan Weld. Soc.* 27, 55s–59s. doi:10.2207/qjws.27.55s
- Sepld, G., Kreimeyer, M., 2003. Joining of Dissimilar Materials. *SPIE - Int. Symp. High-Power Laser* 4831, 526–533.
- Shinn, B.W., Farson, D.F., Denney, P.E., 2005. Laser stabilisation of arc cathode spots in titanium welding. *Sci. Technol. Weld. Join.* 10, 475–481. doi:10.1179/174329305X46673
- SLC Consortium, 2008. *Multi-material Lightweight Vehicle Structure - SuperLightCar [WWW Document]. URL http://www.superlightcar.com/public/docs/20080710_SLC_Final_Concept_PUBLISHABLE.pdf*
- Steen, W.M., Mazumder, J., 2010. *Laser Material Processing, 4th editio. ed. Spinger.*
- Tamrin, K.F., Nukman, Y., Zakariyah, S.S., 2013. Laser Lap Joining of Dissimilar Materials – A Review of Factors Affecting Joint Strength. *Mater. Manuf. Process.* 6914, 130715070734009. doi:10.1080/10426914.2013.792413

Tanaka, T., Morishige, T., Hirata, T., 2009. Comprehensive analysis of joint strength for dissimilar friction stir welds of mild steel to aluminum alloys. *Scr. Mater.* 61, 756–759. doi:10.1016/j.scriptamat.2009.06.022

Thoma, M., 1986. Patent Number: 4,588,480 - Method of producing wear-protection layers on surfaces of structural parts of titanium or titanium-base alloys.

Thomy, F., Moller, C., 2013. Laser welding and brazing of dissimilar materials - Chap 9, in: *Handbook of Laser Welding Technologies*. pp. 255–279.

Threadgill, P., 2008. Linear friction welding (Knowledge Summary) [WWW Document]. URL <http://www.twi.co.uk/content/ksplt001.html> (accessed 3.7.11).

Tomashchuk, I., Sallamand, P., Andrzejewski, H., Grevey, D., 2011. The formation of intermetallics in dissimilar Ti6Al4V/copper/AISI 316 L electron beam and Nd:YAG laser joints. *Intermetallics* 19, 1466–1473. doi:10.1016/j.intermet.2011.05.016

Uematsu, Y., Tokaji, K., Tozaki, Y., Nakashima, Y., Shimizu, T., 2011. Fatigue behaviour of dissimilar friction stir spot welds between A6061-T6 and low carbon steel sheets welded by a scroll grooved tool without probe. *Fatigue Fract. Eng. Mater. Struct.* 34, 581–591. doi:10.1111/j.1460-2695.2010.01549.x

Vacuum Furnace Engineering Limited, 2011. TAV - Special Systems [WWW Document]. URL [http://www.vfe.co.uk/Products/Vacuum Furnaces/TAV Range/tav-spsystems.html](http://www.vfe.co.uk/Products/Vacuum_Furnaces/TAV_Range/tav-spsystems.html) (accessed 3.7.11).

Wagner, G., Balle, F., Eifler, D., 2013. Ultrasonic Welding of Aluminum Alloys to Fiber Reinforced Polymers. *Adv. Eng. Mater.* 15, 792–803. doi:10.1002/adem.201300043

Wang, F., Williams, S., Rush, M., 2011. Morphology investigation on direct current pulsed gas tungsten arc welded additive layer manufactured Ti6Al4V alloy. *Int. J. Adv. Manuf. Technol.* 57, 597–603. doi:10.1007/s00170-011-3299-1

Wang, T., Zhang, B., Chen, G., Feng, J., 2013. High strength electron beam welded titanium–stainless steel joint with V/Cu based composite filler metals. *Vacuum* 94, 41–47. doi:10.1016/j.vacuum.2013.01.015

Wang, T., Zhang, B., Chen, G., Feng, J., Tang, Q., 2010. Electron beam welding of Ti-15-3 titanium alloy to 304 stainless steel with copper interlayer sheet. *Trans. Nonferrous Met. Soc. China* 20, 1829–1834. doi:10.1016/S1003-6326(09)60381-2

Wang, T., Zhang, B., Feng, J., Tang, Q., 2012. Effect of a copper filler metal on the microstructure and mechanical properties of electron beam welded titanium–stainless steel joint. *Mater. Charact.* 73, 104–113. doi:10.1016/j.matchar.2012.08.004

Wiki, 2014. wikiwand [WWW Document]. URL http://www.wikiwand.com/en/Friction_stir_welding (accessed 5.17.14).

Yao, C., Xu, B., Zhang, X., Huang, J., Fu, J., Wu, Y., 2009. Interface microstructure and mechanical properties of laser welding copper–steel dissimilar joint. *Opt. Lasers Eng.* 47, 807–814. doi:10.1016/j.optlaseng.2009.02.004

APPENDICES

Appendix A – Experimental tables from chapter 5

Table 48 – AM feasibility experiments deposition parameters.

Specimen	AM 1			AM 2		
Parameters	Metal	Wire feed speed (m/min)	Current (A)	Metal	Wire feed speed (m/min)	Current (A)
18 th Layer	316 L	1.54	120	316 L	1.54	120
17 th Layer	316 L	1.54	120	316 L	1.54	120
16 th Layer	316 L	1.54	120	316 L	1.54	120
15 th Layer	316 L	1.54	120	316 L	1.54	120
14 th Layer	316 L	1.54	120	316 L	1.54	120
13 th Layer	CuSi ₃	1.54	115	CuSi ₃	1.54	115
12 th Layer	CuSi ₃	1.54	115	CuSi ₃	1.54	115
11 th Layer	CuSi ₃	1.54	115	CuSi ₃	1.54	115
10 th Layer	CuSi ₃	1.54	115	CuSi ₃	1.54	115
9 th Layer	CuSi ₃	1.54	115	CuSi ₃	1.54	115
8 th Layer	Nb	1.30	125	Nb	1.30	135
7 th Layer	Nb	1.30	125	Nb	1.30	135
6 th Layer	Nb	1.30	125	Nb	1.30	135
5 th Layer	Nb	1.30	125	Nb	1.30	130
4 th Layer	Nb	1.30	125	Nb	1.30	125
3 rd Layer	Ti-6Al-4V	1.54	120	Ti-6Al-4V	1.54	120
2 nd Layer	Ti-6Al-4V	1.54	120	Ti-6Al-4V	1.54	120
1 st Layer	Ti-6Al-4V	1.54	120	Ti-6Al-4V	1.54	120
Substrate	Ti-6Al-4V			Ti-6Al-4V		

Table 49 – AM Ti diffusion experiments deposition parameters.

Specimen	AM 3			AM 4		
Parameters	Metal	Wire feed speed (m/min)	Current (A)	Metal	Wire feed speed (m/min)	Current (A)
13 th Layer	Nb	1.75	130	Nb	1.75	170
12 th Layer	Nb	1.30	130	Nb	1.30	170
11 th Layer	Nb	1.30	130	Nb	1.30	165
10 th Layer	Nb	1.30	130	Nb	1.30	155
9 th Layer	Nb	1.30	130	Nb	1.30	140
8 th Layer	Nb	1.30	130	Nb	1.30	135
7 th Layer	Nb	1.30	130	Nb	1.30	135
6 th Layer	Nb	1.30	130	Nb	1.30	130
5 th Layer	Nb	1.30	130	Nb	1.30	130
4 th Layer	Nb	1.30	130	Nb	1.30	130
3 rd Layer	Ti-6Al-4V	1.54	120	Ti-6Al-4V	1.54	120
2 nd Layer	Ti-6Al-4V	1.54	120	Ti-6Al-4V	1.54	120
1 st Layer	Ti-6Al-4V	1.54	120	Ti-6Al-4V	1.54	120
Substrate	Ti-6Al-4V			Ti-6Al-4V		

Table 50 – AM final experiments deposition parameters.

Specimen	AM 5			AM 6		
Parameters	Metal	Wire feed speed (m/min)	Current (A)	Metal	Wire feed speed (m/min)	Current (A)
30 th Layer	316L	1.54	120	316L		
29 th Layer	316L	1.54	120	316L		
28 th Layer	316L	1.54	120	316L		
27 th Layer	316L	1.54	120	316L		
26 th Layer	316L	1.54	120	316L		

Specimen	AM 5			AM 6		
Parameters	Metal	Wire feed speed (m/min)	Current (A)	Metal	Wire feed speed (m/min)	Current (A)
25 th Layer	316L	1.54	120	316L		
24 th Layer	Cu	2.18	120	Cu		
23 rd Layer	Cu	1.94	120	Cu		
22 nd Layer	Cu	1.54	120	Cu		
21 st Layer	Cu	1.54	120	Cu	2.40	120
20 th Layer	Cu	1.30	100	Cu	2.40	120
19 th Layer	Cu	1.30	120	Cu	2.40	120
18 th Layer	Cu	1.10	120	Cu	2.40	120
17 th Layer	Cu	1.10	135	Cu	2.40	130
16 th Layer	Cu	1.10	110	Cu	2.18	135
15 th Layer	Cu	1.10	100	Cu	2.18	120
14 th Layer	Cu	1.10	100	Cu	2.18	120
13 th Layer	Nb	1.30	180	Nb	1.30	180
12 th Layer	Nb	1.30	170	Nb	1.30	175
11 th Layer	Nb	1.30	180	Nb	1.30	170
10 th Layer	Nb	1.30	165	Nb	1.30	165
9 th Layer	Nb	1.30	160	Nb	1.30	155
8 th Layer	Nb	1.30	145	Nb	1.30	150
7 th Layer	Nb	1.30	140	Nb	1.30	140
6 th Layer	Nb	1.30	140	Nb	1.30	140
5 th Layer	Nb	1.30	130	Nb	1.30	130
4 th Layer	Nb	1.30	130	Nb	1.30	130
3 rd Layer	Ti-6Al-4V	1.54	120	Ti-6Al-4V	1.54	120
2 nd Layer	Ti-6Al-4V	1.54	120	Ti-6Al-4V	1.54	120
1 st Layer	Ti-6Al-4V	1.54	120	Ti-6Al-4V	1.54	120
Substrate	Ti-6Al-4V			Ti-6Al-4V		

Appendix B – Research papers generated during the period of this research

B.1 Dissimilar metal laser spot joining of steel to aluminium in conduction mode

Dissimilar metal laser spot joining of steel to aluminium in conduction mode

G. Pardal^a, S. Mecco^a, S. Ganguly^a, S. Williams^a, P. Prangnell^b

^aWelding Engineering and Laser Processing Centre (WELPC), Cranfield University, Bedford MK43 0AL United Kingdom

^bMaterials Science Centre, The University of Manchester, Manchester M13 9PL

Email: g.n.rodriquespardal@cranfield.ac.uk, tel: +44 (0)1234 750111 ext-5055

Abstract:

Dissimilar joining of thin (~1mm) 6111-T4 aluminium alloy and DC04 uncoated low carbon steel used in automobile structures was carried out using laser spot joining in conduction mode. Two sets of experiments were carried out, using copper and aluminium backing bars respectively. The welds were produced in overlap configuration with steel on the top. The steel surface was irradiated by the laser and the heat was conducted through the steel into the aluminium. Temperature at the interface was controlled using the fundamental laser energy parameters so that aluminium melts and wets the steel surface. Reaction between the two metallic alloys resulted in the formation of intermetallic compounds (IMC). The formation pattern of IMC was dependent on the temperature profile and the distribution across the interface and was thicker in the centre of the weld and thinner near the edges. The stoichiometry of the IMC formed was varied across the layer and was principally composed of two different layers of Fe_2Al_5 and FeAl_3 . Micro hardness tests were carried out to characterise the IMC layer. Mechanical shear tensile tests showed a maximum joint shear strength of up to 68% of the shear strength of the aluminium alloy.

Keywords: dissimilar joining; laser welding; conduction mode; intermetallic compound

1. Introduction:

The development of new techniques for welding dissimilar metals has been intensively researched in the automotive sector. According to a recent white paper [1] the carbon emission target for UK's domestic transportation sector is 130 g/km by 2012 and is likely to be further restricted to 95 g/km by 2020. The automotive manufacturers want to incorporate metallic alloys with higher specific modulus to reduce mass of a vehicle. Aluminium has been—used by several automotive manufacturers over the past years due to its greater strength to weight ratio when compared with steel. Therefore, in recent years a lot of research focus has been given towards welding steel to aluminium for application by the automotive industry.

However Al and Fe are incompatible and in equilibrium conditions while Al has some solubility in Fe (12% in wt%) however Fe has virtually no solubility on Aluminium (figure 1).

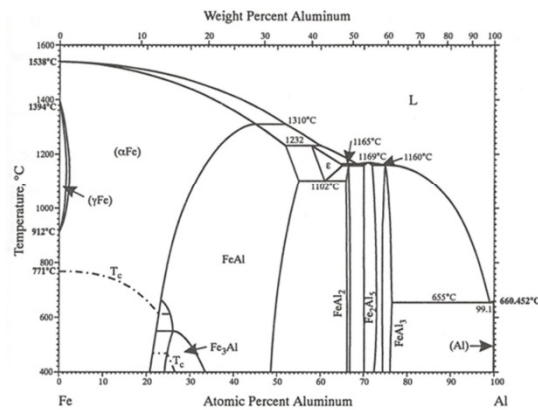


Fig. 1 – Fe – Al phase diagram [2]

This translates on the possible formation of several intermetallic (IMC) phases (FeAl₂, Fe₂Al₅ and FeAl₃) during welding. Laser welding is not an equilibrium process

due to its fast heating and cooling cycle, but the phase diagram can be used as a guideline for the stoichiometry of IMC that are formed between these two metallic materials. Due to the formation of IMC at the interface, welds between Fe and Al suffer from poor mechanical properties. In order to avoid these issues several continuous joining processes have been researched, explosive welding [3], magnetic pressure welding [4], friction stir welding [5], [6], tungsten inert gas welding [7], [8], gas metal arc brazing [9]–[11] and laser welding [12]–[15]. Gas metal arc brazing process is now at an advanced stage of development and application. T. Murakami et al. explored the application of Al-Si fluxed cored wire, with a resulting IMC layer of 2.5 μm and 80 MPa of strength. L.A. Jacome et al. reported the application of different filler wires to join Al and Fe on a voestalpine welding geometry. This study resulted in an IMC layer with thickness lower than 5 μm and a plastic strain of at least 9%. The best mechanical properties were found for AlSi3Mn1 welding wire. S. Sasabe et al. used a steel coated with Al-Si (Al - 9.2 % mass Si) to join the two metals with resulting better mechanical properties than direct joining. This is explained by the localized free IMC region obtained in contrast to the more constant IMC interface obtained with regular steel to Al joining. However the development of a successful joining process using laser would give the additional benefits of cost and weight saving from the formation of autogenous welds. Needless to say the operational and logistical simplicities through the use of no filler wire. In the automotive industry, resistance spot welding is probably the most widely used joining mechanism. RSW is used to reduce the mass of the vehicles during the joining processes, because it does not use welding wires, it has a fast welding cycle and can be performed simultaneously by several manipulators. Dissimilar resistance spot welding (RSW) of Al to Fe have been analysed with and without insert metal sheets. In this work it has been found that aluminium to steel RSW without an insert resulted into formation of Fe_2Al_5 type of intermetallic compound about 2 μm thick which undermines the mechanical properties of the joints. It has been reported that RSW with insert sheets of steel clad aluminium produced welds with better mechanical properties despite the formation of thicker ($\sim 5\mu\text{m}$) layer of IMC on the clad material interface[16]. Dissimilar RSW has been also investigated by other researchers and it was discussed that an IMC layer with more than 1.5 μm thickness may result into significant deterioration of the joint mechanical strength [17], [18]. Friction spot welding[19] has also been studied with a thinner IMC layer reported or

in some cases with no observable IMC layer at the joint. In this paper a novel approach was presented whereby laser welding was applied in conduction mode on the steel surface for spot welding of thin Fe to Al sheets as used in automotive structures. Conduction mode laser spot welding was used, due to its lower power densities, higher molten area and lower penetration depth to width ratio to increase the welded area between the two metals. Laser was also extremely useful for its ability to apply a controlled power density over an area with high spatial resolution. This allows the necessary energy distribution required to melt the aluminium in the interface while keeping the steel in solid state. In non-consumable arc process to melt the Al without melting the bulk of the steel within such thin sheet would be quite difficult and unsustainable due to instability. However plasma arc process could be explored as it can be operated at different current levels.

2. Experimental:

2.1. Conduction mode laser spot welding.

In the presented study, uncoated steel (DC04) was welded to an Al alloy (6111 Al alloy) in an overlapping configuration with steel on the top. Two different backing bars were used (copper and aluminium) to vary the heat extraction coefficient and thermal profiles during welding.

The power density of the laser spot was controlled so that the impinged energy was transferred through the steel plate to the aluminium resulting in melting of Al and wetting of the steel surface (which remains on solid state). The melting of aluminium and wetting of steel surface enables the joint formation (figure 2). This is possible due to the dissimilar melting points, 652°C and 1535°C of the metals used, Al and Fe respectively.

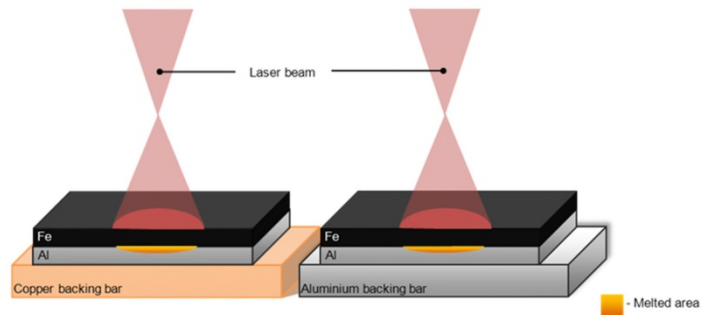


Fig. 2 – Schematic representation of conduction mode laser spot welding for each set of experiments

To achieve the required melting of Al at the interface, special care needs to be taken to ensure proper interfacial contact. A clamping system with a metallic ring around the spot weld was developed with two clamps exerting pressure to avoid any gap between the plates (Fig 3). This was developed to ensure consistent contact between the plates necessary for repeatability and reproducibility of the process.

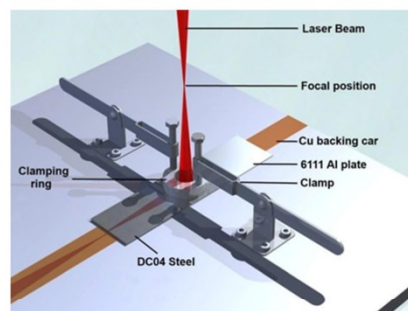


Fig. 3 – Clamping system with laser beam schematic representation.

A gap between the two plates would prevent the heat to conduct from the steel to the aluminium and would result on a rise of temperature in the steel plate and consequently the melting of this plate. In thin sheet dissimilar welding, the formation of a keyhole is undesirable as it would result in melting of the steel substrate material and result in uncontrolled mixing and consequent reaction of Fe and Al. To achieve the conduction mode the laser beam was defocused to have a lower power density (Fig 3). This laser welding process differs from regular laser welding due to the solid-

liquid interface generated by the melting of the Al substrate whilst the steel remained in solid state.

2.2. Material

The material used was 1 mm thick DC04 steel and 1 mm thick 6111-T4 aluminium alloy. Chemical compositions and mechanical properties of the two alloys are given in table 1 and 2 respectively.

Table 1 – Chemical composition (%wt) for DC04 steel and 6111-T4 aluminium alloy

Material	C	Mn	P	S	Al	Fe	Mg	Si	Cu
DC04	0.08	0.4	0.03	0.03	-	Bal.	-	-	-
6111-T4	-	-	-	-	Bal.	0.25	0.8	0.7	0.7

Table 2 – Mechanical properties of the weld members

Material	Yield strength [MPa]	Tensile Strength [Mpa]	Elongation [%]
DC04	210	270 – 350	----
6111-T4	165	295	26

2.3. Experimental setup and equipment

Plates cut into 105 x 45 mm rectangular section were used in the experiments. Both the steel and aluminium plates were 1 mm thick. The aluminium plates were finished immediately before welding, time from finishing to welding was restricted to below 10 min to avoid reoxidation and both plates were cleaned with acetone. In order to make specimens for mechanical testing the plates were positioned with an overlap of 35 mm to comply with the EN ISO142743:2001 standard (figure 4).

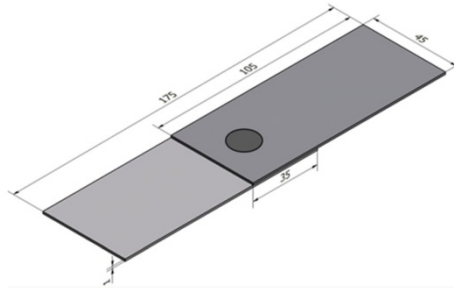


Fig. 4 – Welding configuration

The welds were made using an 8 kW fibre laser (IPG YLR 8000) with an optical lens of 500 mm focal length. Two different, copper and aluminium, backing bars were used in these experiments. The aluminium backing bar was water cooled to facilitate the heat extraction. To produce the spot welds, the laser beam was irradiated on the steel surface without any movement (the laser is stationary in relation to the substrate). Metallographic examination of the welds were carried out by cutting and mounting the weld cross section and then an appropriate polishing and grinding technique was used to reveal the metallographic details near the weld centre. After polishing the samples were etched with 2% Nital (steel) and Keller's reagent (Al). The samples were observed under an optical microscope for microstructural and weld profile analysis and then analysed by energy dispersive spectroscopy (EDS) in a FEG-SEM (Field Emission Gun – Scanning Electron Microscopy) to determine the stoichiometry of the IMC formed. Finally shear strength of the joints were determined by tensile shear tests using an INSTRON universal tensile testing machine.

2.4. System and fundamental energy parameters

The system parameters used during the experiments are presented in table 3.

Table 3 – System parameters used for conduction mode laser spot welding

Spot size [mm]	Irradiation time [s]	Power [kW]
13	3	3.00
13	3	3.35
13	3	3.50
13	3	3.65

Spot size [mm]	Irradiation time [s]	Power [kW]
13	3	3.80

In order to understand the laser-metal interaction, three fundamental energy parameters were studied, power density (PD), interaction time (IT) and specific point energy (Esp) [20]. In spot welding the definition of interaction time is the time that substrate surface is irradiated by the laser beam [21].

Interaction time (IT):

$$\text{Interaction time} = \text{irradiation time}$$

Derivation of the other two interaction parameters, power density and specific point energy, are as given bellow.

Power density (PD):

$$\text{Power density} = \frac{\text{Power}}{\text{Beam area}}$$

Specific point energy is the energy that a volume of material experiences during the welding process.

Specific point energy

$$\text{Specific Point Energy} = \text{Power density} \cdot \text{Interaction time} \cdot \text{Beam area}$$

The values for the fundamental energy parameters used during the experiments were calculated from the system parameters and are presented in table 4.

Table 4 – Fundamental energy parameters used for conduction mode laser spot welding

Power density [MW/cm ²]	Interaction time [s]	Specific point energy [kJ]
2.26 E-3	3.0	9.00
2.52 E-3	3.0	10.05
2.64 E-3	3.0	10.50

2.75 E-3	3.0	10.95
2.86 E-3	3.0	11.40

The Interaction time was kept constant and to a maximum of 3 s to maintain the process economically viable, large interaction times are not recommended for spot welding operations.

3. Results

3.1. Macrostructure

The macrostructures of the welds revealed that an appropriate thermal gradient could be established which allowed melting of the Al along the joint interface. There was some evidence of steel melting at the top surface, under the area which is directly irradiated by the laser. It is clear from the macrograph (figure 5) that the two different alloys were not mixed in the molten state. The heat from the top surface was, therefore, conducted to the interface which resulted in a thermal field that allowed the aluminium to melt and wet the steel surface, while the steel itself remained in the solid state.



Fig. 5 – Conduction mode laser spot welding macro section

3.2. Formation of Intermetallic compounds

To have an accurate measurement of the IMC layer thickness formed by the Fe-Al reaction five micrographs were taken along the IMC layer (Fig 6 a). In each micrograph 20 IML thickness measurements were taken where each measurement was separated by 10 μm . The mean of the measurements for each micrograph was calculated and the maximum value for the five inspected micrographs was considered as the maximum of the IMC layer thickness and reported (Figure 6).

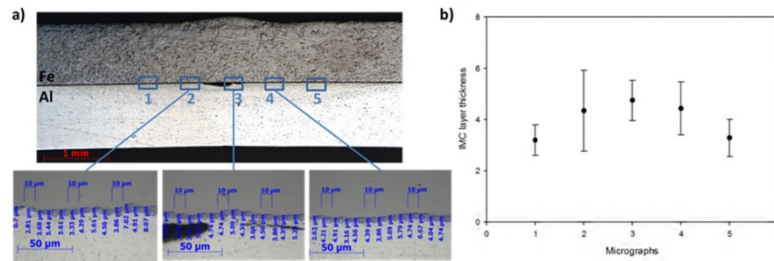


Fig. 6– Intermetallic measurement example (a) and plot of the IMC layer thickness for each of the five micrographs done across the weld interface and the IMC layer standard deviation (b)

Micrograph 3 was selected as the maximum for the IMC layer thickness for this particular sample. Table 5 show the IMC layer maximum thickness for each sample and the associated standard deviation.

Table 5 – IMC layer thickness and corresponding standard deviation.

Sample	Backing bar	Power density [MW/cm ²]	Interaction time [s]	Specific point energy [kJ]	IMC layer thickness (µm)	Standard deviation (µm)
1	Cu	2.52 E-3	3.0	10.05	4.64	1.06
2	Cu	2.64 E-3	3.0	10.50	4.75	0.79
3	Cu	2.75 E-3	3.0	10.95	7.59	1.26
4	Cu	2.86 E-3	3.0	11.40	20.21	3.79
5	Al	2.26 E-3	3.0	9.00	32.36	2.66
6	Al	2.52 E-3	3.0	10.05	35.16	1.21

The formation of IMC's is a diffusion controlled process and therefore dependent on the time and temperature of the weld pool or in other words the thermal profile of the spot.

As discussed the spot welds were made in laser conduction mode where the energy within the laser spot was controlled by holding the specimens in a defocused position. In the defocused condition the energy shows a Gaussian distribution, whilst on the focal position the beam has a top hat energy distribution. Figure 7 [21] shows the energy distribution (Gaussian distribution) of a laser beam with a power distribution of 1000 W for a focal lens of 250 mm in defocus position.

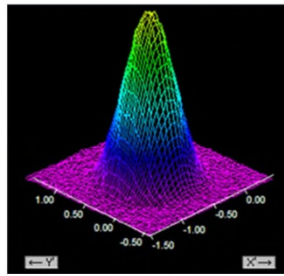


Fig. 7 – IPG YLR 8000 laser energy distribution for a defocused position.

This translates in a temperature distribution which has a maximum near the centre while substantially less towards the edge of the spot. This will also result into a faster cooling rate near the edge of the weld pool as compared to the centre of the weld. The pattern of intermetallic compound formation followed the weld thermal profile across the melt pool. On the extreme edges of the spot, the intermetallic layer had a lower thickness and it was fragmented in appearance (due to the lower intensities on the extremities of the spot, Gaussian profile, and the non-constant cooling conditions from the edge of the spot into the parent metals). On the central part of the spot, where the temperature was higher, the intermetallic layer was thicker and continuous in nature.

In figure 8 the maximum IMC layer thickness as function of specific point energy was plotted for both the Cu and Al backing bars. The corresponding micrographs for the welds made with a copper backing bar, along with the specific point energy were shown in fig 8 b.

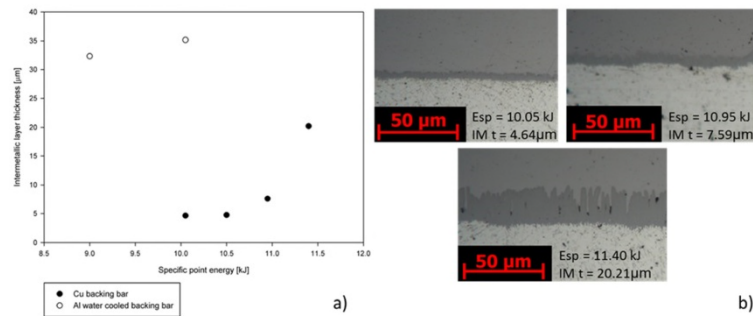


Fig. 8– Evolution of the IMC layer thickness with the specific point energy (a) and selected Cu backing bar micrographs (b)

Irrespective of the backing bar, IMC layer thickness increased, as the laser specific point energy was increased. However, it can be observed that as the aluminium backing bar had a lower thermal conductivity the heat extraction was slower which resulted in a lower cooling rate. The resulting thermal profile of the spot welds from the aluminium backing bar caused the formation of a thicker intermetallic layer even at a lower energy level when compared to the copper backing bar at a higher energy level as shown in figure 8a for example. At a comparable value of Esp, 10.05 kJ, the IMC layer thickness of the sample welded with an aluminium backing bar was 35μm whilst the sample welded with a Cu bar is 5μm (figure 8a)

The IMC layer thickness for the copper backing bar exhibited an exponential growth with increase in Esp, revealing that this parameter has an important role on the formation and growth of the IMC layer.

3.3. Metallography

On the optical micrograph after etching two different intermetallic layers can be observed, as shown in figure 9. A thinner layer (represented by IMC-1) was present closer to the aluminium side and a thicker layer (represented by IMC-2) was present closer to the steel side. The contrast in their appearance in optical microscopy can be attributed to the difference in stoichiometry between the two layers.

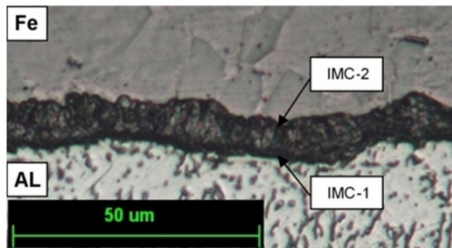


Fig. 9 – Optical micro section of IMC layer

From EDS analysis it is possible to determine the atomic proportion of Fe and Al in the IMC layers. It was found that the intermetallic compound was principally formed by Fe and Al. By the element map distribution it is possible to identify three different areas near the fusion zone of the weld. Area A (green) and C (red) are the two parent materials Fe and Al correspondently whilst area B is the IMC layer that is originated from the diffusion between Fe and Al.

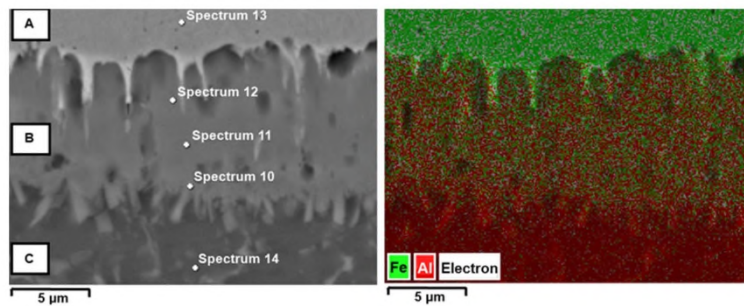


Fig. 10 – SEM of the intermetallic layer (left), Element mapping distribution (right)

The EDS analysis (table 6) indicated that the stoichiometry of the thinner layer IMC-1 (Figure 9) as FeAl_3 and IMC-2 as Fe_2Al_5 .

Table 6 – EDS quantitative analysis results

Spectrum	Fe [%wt]	Al [%wt]	IMC
10	39.66	60.34	FeAl_3
11	45.57	54.43	Fe_2Al_5
12	46.47	53.53	Fe_2Al_5
13	100	0	Fe
14	4.19	95.81	Al

These observations are in agreement with previous research by Qiu et al [22] and in accordance with the diffusion mechanisms that rule the IMC formation; in that the Al richer phase (FeAl_3) is closer to the Al side whilst the phase richer in Fe (Fe_2Al_5) is closer to the Fe side of the weld.

3.4. Hardness evaluation

To evaluate the hardness of the samples and in particular the hardness of the IMC layer, a micro hardness testing was carried out. A vertical line of indentations was made across the centre of the weld with the spacing between indentations of 0.1 mm, as shown on figure 11. The indentations load used was 25 g with load application duration of 10 s.

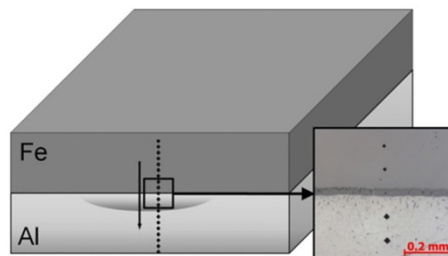


Fig. 11 – Micro hardness pattern representation

A low value of hardness was observed on Fe and Al, when compared with the maximum hardness value of 968 HV on the centre of the IMC layer. The hardness of the IMC layer was 4.5 times the hardness of the welded steel, and around 14.5 times the hardness of the aluminium therefore, it is more brittle when compared to the matrix structure (figure 12). Al-Fe IMC are also known to be inherently brittle [23].

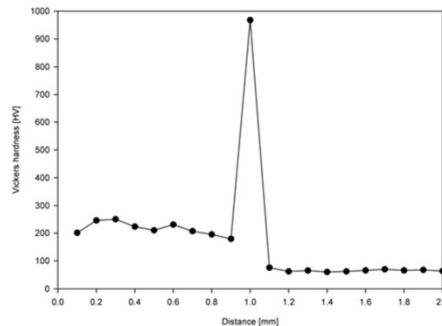


Fig. 12 – Hardness values in a vertical traverse across the weld interface (sample 5)

3.5. Mechanical properties

For the welds made using an aluminium backing bar the lap shear strength decreased as the Esp increased (figure 13a). The level of IMC formation was also higher for welds made using the aluminium backing bar when compared to welds produced with the copper backing bar (figure 13 b), even when the energy levels were lower. This can be related to the different thermal cycle experienced by the two sets of welds. As the aluminium backing bar has a lower thermal conductivity, the energy was kept in the weld for longer and consequently the temperature at the interface was higher for a longer time, resulting in a thicker IMC layer that negatively affects the joint mechanical behaviour.

As the copper backing bar has a higher thermal conductivity, the energy was dissipated more quickly and therefore, the thermal cycle was shorter, reducing the overall growth of the IMC layer, even for welds with higher energy levels. From figure 13a it can be seen that there is an increase in mechanical properties with an increase of the applied energy, but after 11kJ the trend reversed. The maximum shear stress value of around 130MPa was observed when the IMC layer thickness was close to 10 μm (fig 13 b) which has been reported as an important value for the mechanical properties of a dissimilar weld between aluminium and steel [24]. This condition seems to produce the best combination of diffusion and bonding strength relative to the interface brittleness introduced by the IMC layer. The two IMC layer thicknesses for the samples with 10 and 10.5 kJ are very similar, as shown in figure 8, this is due the applied energy being used to melt more aluminium and increase

the wetting/bonding area. For lower energy levels, the energy is enough to create a bonding and increase the melting of the Al, but there is not enough energy to increase the IMC thickness. This can be substantiated from the increase in shear strength for the sample made with 10.5 kJ of applied energy without a big increase of the IMC layer thickness.

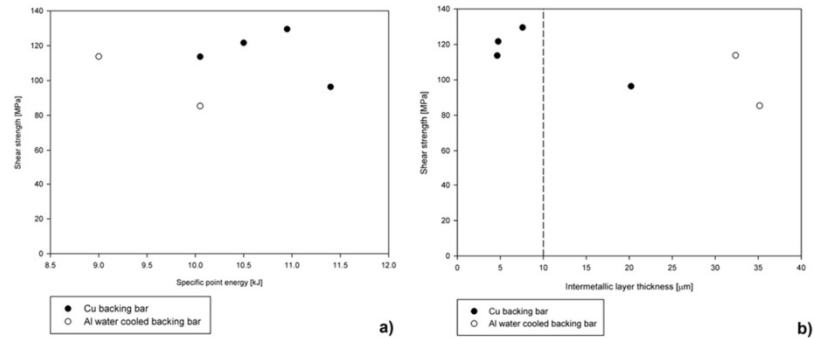


Fig. 13 – Lap Shear strength behaviour vs. specific point energy (a), shear strength vs. IMC layer thickness (b)

In figure 14 shear strength is plotted against sample displacement, this also shows evidence of plastic deformation until fracture, which can be important for engineering. For specimens with IMC layer thicknesses greater than 10 μm not only was the shear strength lowered, but also the plastic deformation was reduced (figure 14). The effect of the thicker IMC is not only to lower the shear strength of the weld, but also to lower its deformability. This can be correlated to the high hardness and brittle nature of the IMC compounds which facilitates crack propagation, resulting in lowering the failure energy (toughness) of the welded joint.

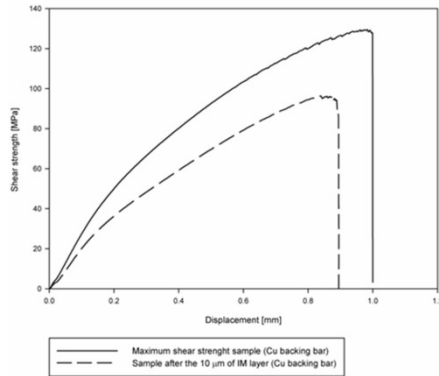


Fig. 14 - Shear strength – displacement graph

To obtain the best mechanical properties it is necessary to balance the energy input with the formation of the IMC layer. With lower energy levels a thinner IMC layer formed, but there isn't enough energy to make an effective bond between the two materials over a large weld area. In contrast, when the energy level is significantly higher diffusion of aluminium into iron is much faster and the IMC layer is thick, resulting in a lowering of the mechanical properties of the joint. Thus in the presented work a higher energy level with a very fast heat extraction resulted in an improved joint strength.

4. Conclusions

- This work has shown that it is possible to laser spot weld DC04 to 611-T4 aluminium in conduction mode using a defocused laser beam. It was possible to melt the aluminium and avoid the bulk melting of the steel. This enabled a liquid-solid interface region and reduced the inter-diffusion of both materials and subsequently the thickness of the IMC layer.
- Despite exploring a range of conditions an IMC reaction layer was always found in the weld, which was determined to be composed mainly of Fe_2Al_5 and FeAl_3 IMC.
- With the same backing bar, the IMC layer thickness could be controlled by controlling the fundamental energy parameters. Due to the high level of hardness of the IMC layer (968 HV), failure of the joints always tended to be

located in the interfacial region. The best tensile shear strength of 130 MPa, was observed for an IMC layer thickness close to 10 μm , when welded using copper backing bar.

- Application of different, Al and Cu, as backing bars revealed that IMC formation and growth is a function of the transient thermal cycle. Samples produced with identical energy level of 10.01 kJ showed 757% increase in IMC layer thickness. This also adversely affected the mechanical strength of the samples produced using the Al backing bar.

Acknowledgments:

The authors acknowledge the support received through LATEST 2 platform grant. Supriyo Ganguly also acknowledge the support received vide EPSRC (Engineering and Physical Sciences Research Council) project no. EP/J017086/1

References:

1. H.M. Government (2009) The UK Low Carbon Five point plan. 220.
2. Okamoto H (2010) Desk Handbook: Phase Diagrams for Binary Alloys. 855.
3. Acarer M, Demir B (2008) An investigation of mechanical and metallurgical properties of explosive welded aluminum–dual phase steel. *Mater Lett* 62:4158–4160. doi: 10.1016/j.matlet.2008.05.060
4. Lee K-J, Kumai S, Arai T, Aizawa T (2007) Interfacial microstructure and strength of steel/aluminum alloy lap joint fabricated by magnetic pressure seam welding. *Mater Sci Eng A* 471:95–101. doi: 10.1016/j.msea.2007.04.033
5. Tanaka T, Morishige T, Hirata T (2009) Comprehensive analysis of joint strength for dissimilar friction stir welds of mild steel to aluminum alloys. *Scr Mater* 61:756–759. doi: 10.1016/j.scriptamat.2009.06.022
6. Uzun H, Dalle Donne C, Argagnotto A, et al. (2005) Friction stir welding of dissimilar Al 6013-T4 To X5CrNi18-10 stainless steel. *Mater Des* 26:41–46. doi: 10.1016/j.matdes.2004.04.002
7. Song JL, Lin SB, Yang CL, Fan CL (2009) Effects of Si additions on intermetallic compound layer of aluminum–steel TIG welding–brazing joint. *J Alloys Compd* 488:217–222. doi: 10.1016/j.jallcom.2009.08.084

8. Lin SB, Song JL, Yang CL, Ma GC (2009) Metallurgical and mechanical investigations of aluminium-steel butt joint made by tungsten inert gas welding–brazing. *Sci Technol Weld Join* 14:636–639. doi: 10.1179/136217109X12464549883493
9. Jácome LA, Weber S, Leitner A, et al. (2009) Influence of Filler Composition on the Microstructure and Mechanical Properties of Steel-Aluminum Joints Produced by Metal Arc Joining. *Adv Eng Mater* 11:350–358. doi: 10.1002/adem.200800319
10. Murakami T, Nakata K, Tong H, Ushio M (2003) Dissimilar Metal Joining of Aluminum to Steel by MIG Arc Brazing Using Flux Cored Wire. *ISIJ Int* 43:1596–1602. doi: 10.2355/isijinternational.43.1596
11. Sasabe S, Iwase T, Matsumoto T, et al. (2009) Dissimilar Metal Joining of Aluminum Alloys to Steel in MIG Braze Welding by using the advanced Hot-dip Aluminized Steel Sheet. *Q J Japan Weld Soc* 27:55s–59s. doi: 10.2207/qjwjs.27.55s
12. Mathieu A, Shabadi R, Deschamps A, et al. (2007) Dissimilar material joining using laser (aluminum to steel using zinc-based filler wire). *Opt Laser Technol* 39:652–661. doi: 10.1016/j.optlastec.2005.08.014
13. Laukant H, Wallmann C, Müller M, et al. (2005) Fluxless laser beam joining of aluminium with zinc coated steel. *Sci Technol Weld Join* 10:219–226. doi: 10.1179/174329305X37051
14. Yan S, Hong Z, Watanabe T, Jingguo T (2010) CW/PW dual-beam YAG laser welding of steel/aluminum alloy sheets. *Opt Lasers Eng* 48:732–736. doi: 10.1016/j.optlaseng.2010.03.015
15. Takemoto T, Kimura S, Kawahito Y, et al. (2009) Fluxless joining of aluminium alloy to steel by laser irradiation method. *Weld Int* 23:316–322. doi: 10.1080/09507110802542643
16. Oikawa H, Ohmiya S, Yoshimura T, Saitoh T (1999) Resistance spot welding of steel and aluminium sheet using insert metal sheet. *Sci Technol Weld Join* 4:80–88. doi: 10.1179/136217199101537608
17. Qiu R, Iwamoto C, Satonaka S (2009) The influence of reaction layer on the strength of aluminum/steel joint welded by resistance spot welding. *Mater Charact* 60:156–159. doi: 10.1016/j.matchar.2008.07.005
18. Qiu R, Satonaka S, Iwamoto C (2009) Effect of interfacial reaction layer continuity on the tensile strength of resistance spot welded joints between aluminum alloy and steels. *Mater Des* 30:3686–3689. doi: 10.1016/j.matdes.2009.02.012
19. Liyanage T, Kilbourne J, Gerlich a. P, North TH (2009) Joint formation in dissimilar Al alloy/steel and Mg alloy/steel friction stir spot welds. *Sci Technol Weld Join* 14:500–508. doi: 10.1179/136217109X456960
20. Assuncao E, Williams S, Yapp D (2012) Interaction time and beam diameter effects on the conduction mode limit. *Opt Lasers Eng* 50:823–828. doi: 10.1016/j.optlaseng.2012.02.001
21. Assuncao E, Williams S (2013) Comparison of continuous wave and pulsed wave laser welding effects. *Opt Lasers Eng* 51:674–680. doi: 10.1016/j.optlaseng.2013.01.007

22. Qiu R, Iwamoto C, Satonaka S (2009) Interfacial microstructure and strength of steel/aluminum alloy joints welded by resistance spot welding with cover plate. *J Mater Process Technol* 209:4186–4193. doi: 10.1016/j.jmatprotec.2008.11.003
23. Kobayashi S, Yakou T (2002) Control of intermetallic compound layers at interface between steel and aluminum by diffusion-treatment. *Mater Sci Eng A* 338:44–53. doi: 10.1016/S0921-5093(02)00053-9
24. Sepld G, Kreimeyer M (2003) Joining of Dissimilar Materials. *SPIE - Int Symp High-Power Laser* 4831:526–533.

B.2 Dissimilar metal joining of stainless steel and titanium using Cu as a transition metal

Int J Adv Manuf Technol
DOI 10.1007/s00170-015-8110-2



ORIGINAL ARTICLE

Dissimilar metal joining of stainless steel and titanium using copper as transition metal

Gonalo Parda¹ & Supriyo Ganguly¹ & Stewart Williams¹ & Jay Vaja²

Received: 27 September 2015 / Accepted: 12 November 2015
The Author(s) 2016. This article is published with open access at Springerlink.com

Abstract Joining of stainless steel and titanium dissimilar metal combination has a specific interest in the nuclear industry. Due to the metallurgical incompatibility, it has been very difficult to produce reliable joints between these metals due to the formation of FeTi and Fe₂Ti types of intermetallic compounds. The metallurgical incompatibility between both materials is enhanced by the time–temperature profile of the welding process used. Brittle intermetallics (IMCs) are formed during Fe–Ti welding (FeTi and Fe₂Ti). The present study uses the low thermal heat input process cold metal transfer (CMT), when compared with conventional GMAW, to deposit a copper (Cu) bead between Ti and stainless steel. Cu is compatible with Fe, and it has a lower melting point than the two base materials. The welds were produced between AMS 4911L (Ti-6Al-4V) and AISI 316L stainless steel using a CuSi-3 welding wire. The joints produced revealed two IM layers located near the parent metals/weld interfaces. The hardness of these layers is higher than the remainder of the weld bead. Tensile tests were carried out with a maximum strength of 200 MPa, but the interfacial failure could not be avoided. Ti atomic migration was observed during experimental trials; however, the IMC formed are less brittle than FeTi, inducing higher mechanical properties.

Keywords Titanium · Stainless steel · Intermetallic · Dissimilar welding

1 Introduction

The main challenge when joining dissimilar metals is the metallurgical incompatibility of the metals used. This is applicable to the dissimilar joint of titanium (Ti) and stainless steel (Fe). This incompatibility is reflected by the formation of intermetallic (IMC) phases formed during the welding of these materials. Binary phase diagrams show the different IMC phases formed during equilibrium conditions for a particular combination of materials. In Fig. 1, the phase diagram between Fe and Ti [1] is shown.

The Fe–Ti binary phase diagram depicts also the absence of solid solubility between Fe and Ti.

IMC formation is also dependent on the time–temperature profile that both metals are subjected. As the IMC formation is dependant of diffusion and reaction between the parent metals, an increase in the time–temperature cycles increases the mobility of the metals and, consequently, the formation of different IMC phases. To avoid the formation of brittle IMCs, there are two different routes or a combination of the two that can be followed:

- & Welding process control (low heat input).
- & Weld metal engineering (use of other metals to change the weld pool composition).

1.1 Welding process control

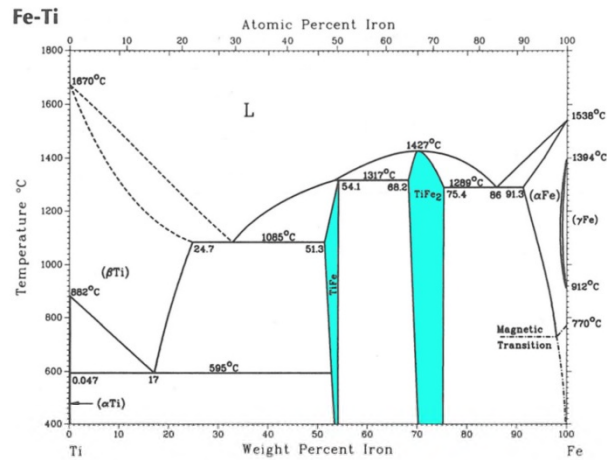
This route uses physical principles to deter the IMC formation. As the IMC formation is mainly controlled by diffusion and

* Gonalo Parda
g.n.pardalrodrigues@cranfield.ac.uk
Supriyo Ganguly
s.ganguly@cranfield.ac.uk
Stewart Williams
s.williams@cranfield.ac.uk
Jay Vaja
Jay.Vaja@awe.co.uk

¹ Cranfield University–Welding Engineering and Laser Processing Centre, Bedford MK43 0AL, UK

² AWE–Aldermaston Reading, Berkshire RG7 4PR, UK

Fig. 1 Fe-Ti binary phase diagram



reaction processes if the heat input and the interaction time are lowered, they will induce lower IMCs. Several studies were made to join stainless steel and Ti using low thermal input processes as diffusion bonding [2, 3] and friction stir welding [4]. In the first study, D. Poddar used diffusion bonding to join commercially pure (CP) titanium to precipitation hardening stainless steel. D. Poddar verified that a temperature of 950 °C with a holding time of 3600 s and with a loading of 4 to 6 E-3 MPa could achieve the best joint conditions. This joint had a reaction layer of 79.9 μm but had a tensile strength of 344.3 MPa and an elongation of 12.8 %. S. Kundu et al. also used diffusion bonding to join CP titanium and microduplex stainless steel obtaining also a reaction layer and joint properties of 306 MPa of tensile strength with ductility of 6.9 %. M. Fazel-Najafabadi et al. used friction stir welding to lap weld CP Ti with 304 stainless steel using a double shoulder tool. The presence of Ti-Fe IMC compounds was detected, but the strength of the sample was attributed to the bimetallic vortices that contributed to a mechanical interlock. The samples obtained had maximum shear strength of 119 MPa. Explosive welding was also used to joint titanium and stainless steel; these joints were defect free and no IMCs were detected at the joint interface [5], but the flexibility of explosion welding is very low when compared with the fusion

welding processes. To allow more flexibility to the welding process, laser in key-hole mode was also studied [6]; however, even with high cooling rates obtained by this process, it was not possible to make any sound joint.

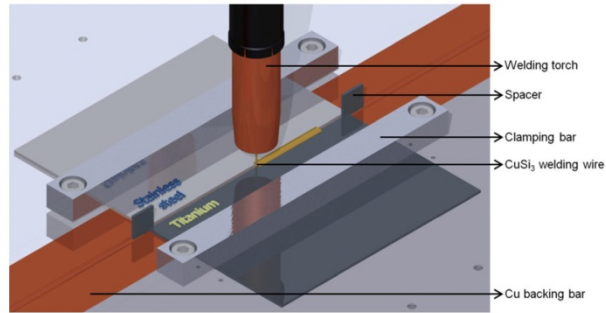
1.2 Weld metal engineering

The second route is to control the reaction between the two alloys by adding a third metal that inhibits IMC formation or that modifies the IMC composition suitably to make it tougher. Silver and silver alloys have been studied due to its low melting point and high compatibility towards Fe. In [7], J. Lee et al. used an Ag interlayer of 20 and 40 μm to braze titanium and stainless steel. The brazing material remained in the centre of the weld and prevented the formation of the brittle Fe-Ti IMCs and substitute them to AgTi IMCs which improved the joint strength considerably. Other metal researched on joining of Ti and stainless steel is Ni, the melting temperature is higher than Ag, but it is also very compatible with Fe. R Shiue et al. [8] used a commercial silver alloy (BAg-8) to braze Ti-6Al-4V to 17-4PH stainless steel coated with a 10 μm Ni barrier layer. Using the Ni Ag combination, they managed to avoid the formation of Fe-Ti IMCs. Cu

Table 1 Parent material atomic composition (%wt)

Material	C	Si	Mn	P	S	Cr	Ni	Mo	N	Fe	Pb	Al	Cu	V	Y	H	O
Stainless steel 316L	0.020	0.45	1.73	0.032	0.01	17.2	10.0	2.07	0.054	Bal	-	-	-	-	-	-	-
AMS 4911L	0.08	-	-	-	-	-	-	-	0.5	0.3	-	5.5-6.75	-	3.5-4.5	0.005	0.0125	0.2
CuSi-3	-	3.0	1.1	-	-	-	-	-	-	0.1	0.01	0.03	Bal	-	-	-	-

Fig. 2 Schematics from the welding–brazing technique



was also studied as a barrier for the IMC formation. T. Wang et al. [9] investigated electron beam welding with a thick interlayer of 1 mm, but the formation of IMC could not be avoided as dispersive distribution of $TiFe_2$ IMCs, and Ti-Cu and Ti-Cu-Fe IM compounds were observed. Electron beam welding and pulsed laser welding were investigated by I. Tomashchuck et al. [10] using a 0.5 mm pure Cu interlayer. The tensile strength of the joints was limited by the different Ti-Cu IMC present. S. Kundu et al. [11] used diffusion bonding and a 300 μm Cu interlayer obtaining a maximum tensile strength of 318 MPa and a ductility of 8.5 %

The present investigation reported a combination of these two main strategies to improve the mechanical properties of Ti to stainless steel welding. Cu was selected as a transition metal due to its lower melting temperature vs mechanical properties relationship when compared to other possible transition metals like Ag and Ni. Cu is compatible with Fe, and the IMC phases produced with Ti are tougher than the Fe-Ti IMC. It also used a low heat input cold metal transfer (CMT) welding process when compared with conventional GMAW welding. CMT relies in wire control and surface tension to detach the molten metal and deposit it. This reduces the time-

temperature cycle, decreasing diffusion and IMC formation. A copper backing bar was used to quickly extract the heat generated during the welding process. CMT was chosen not only for its low heat input, but also by its flexibility (does not need a furnace, can be used for different types of joints, can adapt to several joint designs and or paths, etc.) when compared with some of the joining processes mentioned before (infrared brazing, explosion welding, etc.)

2 Experimental procedure and materials

Titanium AMS4911L plates of dimensions 150 (L) \times 100 (W) \times 1.7 mm (T) were joined with 316L stainless steel of identical length and width but with 2 mm in thickness. The chemical composition of the alloys and the filler wires used in the experiments is given in Table 1.

Each plate was manually ground and finished prior to the welding–brazing process with particular attention to the surfaces that form the gap brazed by the CuSi-3 welding wire (vertical faces). The plates were joined in butt welding configuration with 1.7 mm gap. This gap was obtained by controlled experimentation in an attempt

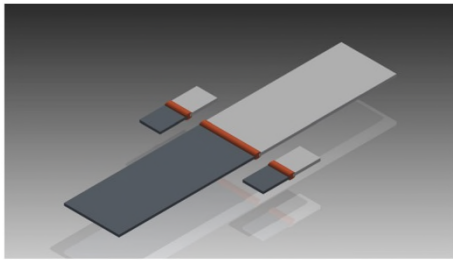


Fig. 3 Sample preparation for metallographic analysis (two) and the sample for mechanical tests



Fig. 4 Tensile test setup used for CMT Cu welded samples

to empirically optimise the welding process. A narrower gap would result in lack of fusion type defect near the root by improper wetting by the copper alloy while larger gap would cause underfilling. A 1 mm diameter CuSi-3 welding wire was deposited between the Ti and stainless steel plates using CMT welding process (Fig. 2).

After the welding process, three different specimens were produced as shown in Fig. 3, one for mechanical tests and two for metallographic analysis.

Metallographic specimens were prepared by mounting them on conductive resin for electron microscopy, ground using silicon carbide paper and polished using diamond paste and colloidal silicon suspension mixed with oxalic acid. They were analysed by optical microscopy, scanning electron microscopy and electron-dispersive spectroscopy (SEM/EDS). Hardness mapping of the specimen was carried out by a Zwick microhardness machine, with the following parameters: HV0.1/10 [12]. Each sample extracted to mechanical tests was tested using the 100 kN INSTRON 5500R tensile test machine. The tensile test was performed at a constant speed of 1 mm per second; the load and displacement were acquired by a National Instruments system attached to a laser extensometer (Fig. 4). The gauge length used during the experiments was 50 mm.

3 Welding parameters

The experiments were carried out using constant welding parameters (travel speed - 0.5 m/min, contact tip to work piece distance - 13.5 mm and CMT mode - 1183), except the wire

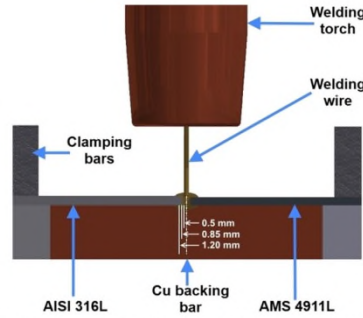


Fig. 5 Welding wire positioning during the welding-brazing experiments

feed speed that was varied as shown in Table 2. As CMT is a synergic process changing the wire feed speed, it would change the current and voltage, translating to a heat input variation that is shown by the following expression:

$$HI = \frac{V \cdot I}{TS} \cdot \eta \quad \delta \beta$$

where HI is the heat input, V is the voltage, I is the intensity, TS is the travel speed and η is the welding process efficiency that for a MIG process has CMT is stipulated as 0.85 [13].

The welding wire was positioned towards the stainless steel plate to enhance the melting of stainless steel and avoid Ti melting. This will prevent the diffusion of Ti into the weld pool and avoid the formation of Fe-Ti intermetallics. Figure 5 depicts the experimental setup and the different positioning of the welding wire in relation to the central line of the gap between the parent metals.

Table 2 CMT welding-brazing parameters for the welding-brazing experiments

Sample	Offset (mm)	Wire feed speed (m/min)	Heat input (J/mm)	Fracture location
CMT 1	0.50	5.00	110.76	Stainless
CMT 2	0.50	6.00	118.40	Stainless
CMT 3	0.50	7.00	140.75	Stainless
CMT 4	0.50	8.00	157.67	Stainless
CMT 5	0.50	9.00	154.99	Ti
CMT 6	0.85	5.00	101.83	Stainless
CMT 7	0.85	6.00	116.51	Stainless
CMT 8	0.85	7.00	135.01	Stainless
CMT 9	0.85	8.00	149.91	Stainless
CMT 10	0.85	9.00	171.44	Ti
CMT 11	1.20	5.00	115.47	Stainless
CMT 12	1.20	6.00	108.89	Stainless
CMT 13	1.20	7.00	138.44	Stainless
CMT 14	1.20	8.00	152.99	Cu bead
CMT 15	1.20	9.00	152.59	Ti

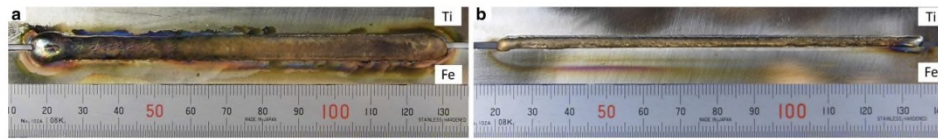


Fig. 6 Weld bead stability and oxidation from sample CMT 11: a top surface and b weld root

Table 2 contains the experimental points used during these experimental trials.

The remainder constant parameters not shown in Table 2 are as follows:

- & Contact tip to work distance (CTWD)—13 mm
- & Shielding gas flows
 - CMT torch—22 l/min
 - Back shielding—2 l/min
 - Trailing shield—62.5 l/min
- & Torch angle 0° perpendicular to the parent metals

4 Results

4.1 Weld bead geometry

Similar weld bead geometry was obtained, as shown in Fig. 6, from all the different experimental trials listed in Table 2.

The top surface (Fig. 6a) showed traces of oxidation even though a trailing shield was used; however, the weld root was successfully shielded with no apparent sign of oxidation (Fig. 6b).

After macroscopic analysis, it is possible to verify that the weld bead geometry is very similar for all of the welded samples. The welding wire positioning does not influence the weld bead geometry (Fig. 7 (I, II and III)). However, the geometry is slightly different when the heat input is increased (Fig. 7a–c).

Samples with low heat input, i.e. with lower wire feed speeds as shown in Fig. 7a (I, II and III), do not wet correctly the stainless steel plate. A clear undercut can be seen at the Fe–Cu interface; this is due to a low heat input and a fast solidification of the melt pool when in contact with the stainless steel plate. As the heat input is increased in samples in Fig. 7b, c, a better wetting of the stainless steel plate is achieved. However, the contribution of the parent metals in the Cu bead is more noticeable (higher melting of parent metals).

With the microscopic examination, it is also possible to identify three different areas in each joined sample: two different reaction layers between the parent metals

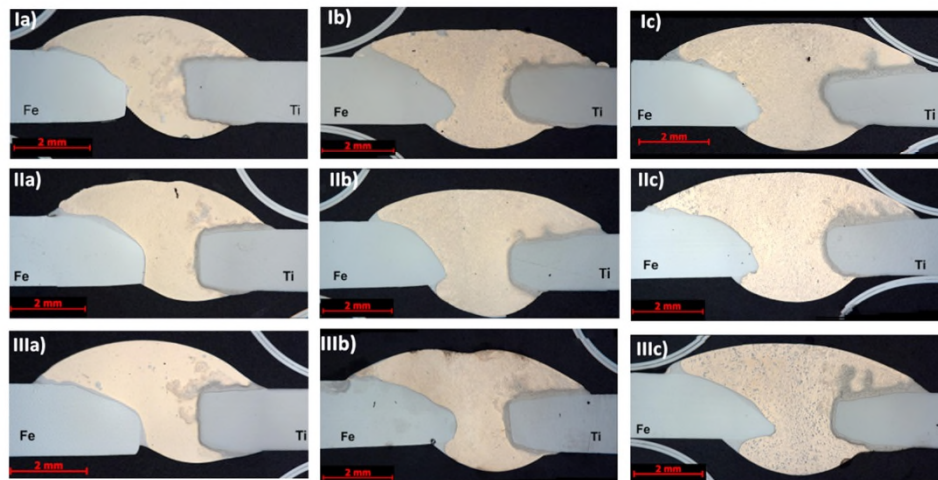


Fig. 7 Selected sample macrographs. I—0.5 mm, II—0.85 mm, III—1.20 mm, a–c increasing the wire feed speed

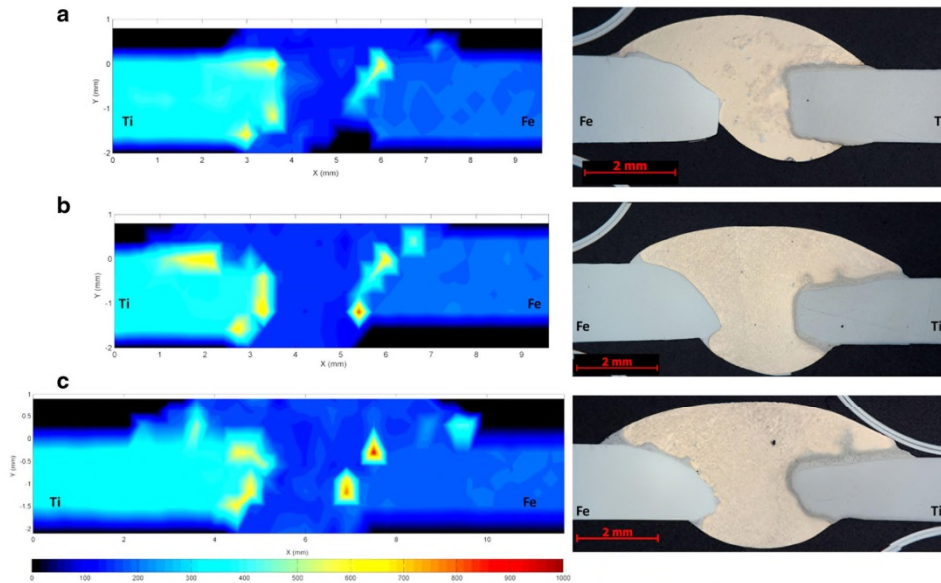


Fig. 8 Hardness mapping and corresponding optical macrographs for samples: a CMT 2, b CMT 4 and c CMT 5

and the Cu bead and also the Cu bead with several dispersed phases.

4.2 Hardness evaluation

As stated in Sect. 1, this metallic combination (Fe–Cu–Ti) can generate IMC phases, and so, to identify their location, microhardness testing was carried out.

Three samples were selected for these tests, CMT 2, 4 and 5 (Table 2). The three samples selected were made at the same welding wire positioning (0.5 mm from the centre of the gap and towards the stainless steel) and have increasing heat inputs. CMT 2 and 4 have failed at the

Fe–Cu interface whilst sample CMT 5 has failed at the Cu–Ti interface.

Figure 8 shows the hardness mapping results for the three selected samples (Fig. 7a–c (I)).

All of the specimens tested showed similar hardness profiles with the bulk of the Cu deposited bead being the softer part of the joint and as expected; the higher hardness values are concentrated at the interfaces between the Cu bead and the stainless steel and Ti plates, at previously observed reaction layers.

Sample CMT 2 has the lower average hardness due to the lower heat input used in this weld. This lower heat input induces a lower melting of the parent metals,

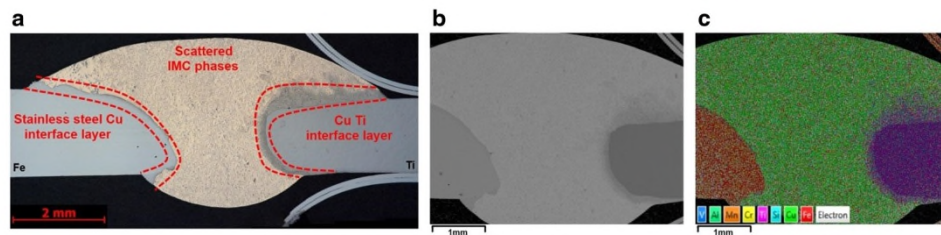


Fig. 9 a Cu deposited weld bead macrograph and distinctive areas. b Backscattered SEM image. c EDS mapping showing the main elements present on the sample

Table 3 Elemental composition in weight percentage from the phases identified on the stainless steel–Cu interface layer

	A	B	C	D	E	F	G	H
Si	0.39	1.54	3.95	5.59	0.87	8.87	10.14	5.71
Ti	–	–	0.82	0.57	0.12	6.29	14.47	0.69
V	–	–	–	–	–	–	–	0.36
Cr	17.96	0.27	18.11	16.92	0.92	14.24	10.63	17.06
Mn	–	1.21	–	–	1.07	0	0	0
Fe	70.37	1.86	66.36	67.43	5.07	54.22	46.59	67.14
Ni	9.41	–	5.82	4.61	–	6.29	3.79	3.79
Cu	–	95.14	3.92	4.48	91.97	8.04	3.16	4.18
Mo	1.89	–	1.03	0.4	–	2.08	11.22	1.07

reducing the diffusion/reaction between intervening Fe, Ti and Cu.

On the contrary, samples CMT 4 and 5 have higher average hardness particularly at the Fe–Cu and Ti–Cu interfaces. This can be justified by the higher heat input and, consequently, the increase in the melting of the parent metals that will originate higher interdiffusion. The higher hardness values for both these samples are located at the Cu–Fe interface with values close to 1000 HV. However, the fracture location of both of these samples is located in different parts of the sample. For CMT 4, the fracture location is at the Fe–Cu interface that coincides with the location of the hardest IMC phases whilst, for sample CMT 5, the location is at the Ti–Cu interface. This indicates not only that the IMC hardness is the major contributing factor for the failure of this joint, but also that the IMC volume plays a role in failure location. As the time–temperature profile increases with the increase of the heat input, the Ti–Cu IMC layer volume increases,

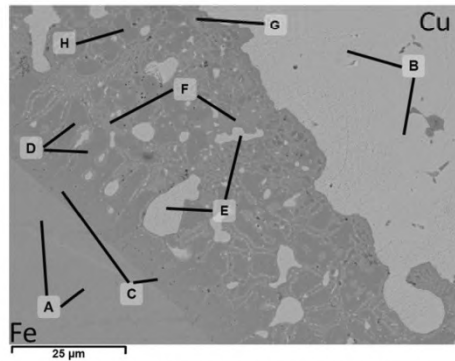


Fig. 10 Interface of stainless steel to Cu and IMC phase formation

increasing the probability of the failure being located at this interface.

4.3 SEM/EDS analysis

To identify the nature of the possible IMC phases formed at these samples, the three previously identified areas were subjected to SEM/EDS analysis (Fig. 9).

The first layer to be analysed was the stainless steel–Cu interlayer. This layer is discontinuous in nature, and naturally, it results from the reaction between the stainless steel and the deposited Cu bead.

Figure 10 shows the stainless steel–Cu interface layer in greater detail and the places where the spectrums were collected (phases A–H). Inside the reaction layer, there are three distinguishable areas. These areas are identified by the following phases: phase E that has the lighter grey shade; phases F and G that have an intermediate shade of grey; and phases C, D and H that have a darker shade.

In Table 3, the elemental composition in weight percentage is shown for the different phases indicated in Fig. 10.

As expected, phase A is stainless steel with a chemical composition very similar to the AISI 316L. Phase B is the Cu from the welding wire, but it is depleted from some of the silicon content expected (3 % wt); this can be explained by the higher levels of Si present on the interface layer, and the Si has diffused to the stainless steel–Cu layer. Phases indicated by C and D have again a composition similar to the AISI 316L, with traces of silicon, Cu and Ti. The lighter phases present in the internal part of the layer represented by the phase E are mainly constituted by Cu with some Fe and Ti and can be considered as Cu that was segregated during the formation of the reaction layer; once again, it is observable a depletion of Si at these Cu islands. The phases within the interface layer with higher content of Ti are the phases represented by F and G. Besides Ti, these phases have also an increase in Si and Mo content; however, the main elements on these phases are Fe and Cr. The amount of Ti in these phases increases with the distance from the stainless steel to the parent metal. Ti was segregated in the phases similar to F and G and is almost not present on the remainder phases in the stainless steel–Cu interface layer. This happened due to the non-equilibrium nature of the welding process, generating a concentration gradient of the Ti through the stainless steel–Cu interlayer that could be harmonised if the time–temperature cycles were longer. The Fe–Ti composition in these phases can justify the higher hardness present in the Fe–Cu interlayer, due to the higher hardness shown by the Fe–Ti intermetallics.

The presence of Ti within this layer means that even with CuSi-3 brazing wire with a lower melting point on a 1.7-mm gap to restrict the melting of Ti, it is not enough

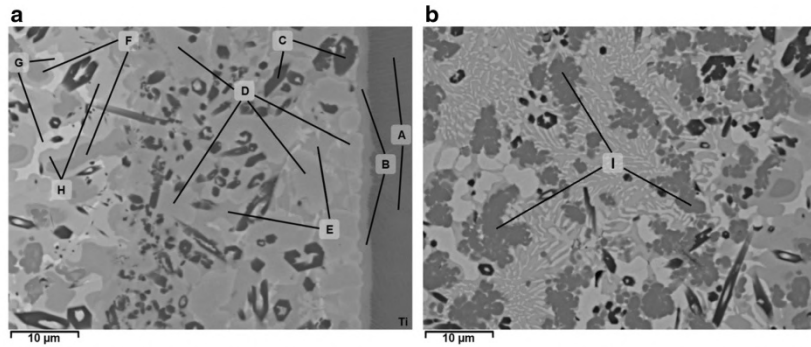


Fig. 11 Cu-Ti interface layer SEM backscattered image and phases investigated: a IMC layer close to the Ti parent metal and b transition between the IMC layer and the beginning of the Cu weld bead

to prevent Ti diffusion within the Cu weld bead. Ti diffuses across the deposited CuSi-3 weld bead and interacts with Fe at the Fe-Cu interface (the backscattered EDS images taken from the Cu-Ti interface layer are shown in Fig. 11).

Each of the phases was identified by a letter, and multiple spectrums were analysed for each sample. The spectrum locations were identified by the lines shown in Fig. 11.

Phase A is the Ti base plate with the same distribution of Ti, Al and V as the parent material (Ti-6Al-4V).

Phase B is mainly composed of Ti (67.90 %) and Cu (18.43 %). Phase B is a continuous layer between the base metal (Ti) and the main Ti-Cu reaction layer. The identification of this layer can be done using the Cu-Ti phase

diagram due to the low values of Si, Fe and Cr present. This IMC is a dual-phased IMC composed of CuTi_2 and α Ti (Fig. 12a).

Phase C that appears in black on the SEM backscattered image is mainly composed of Si and Ti, and the ratio between these elements is very close to Ti_5Si_3 phase on the Ti-Si (Fig. 12b) phase diagram. This phase has 20 % wt content while the CuSi-3 wire only has 3 %; this shows once again that the silicon content of the wire was segregated to particular areas of the joint, producing IMC phases with higher contents of silicon.

Phases D and E compose almost all of the Cu-Ti interface layer. Phase D has a cellular structure, and phase E has an intercellular space structure. These two phases are similar; however, from the Fe atomic

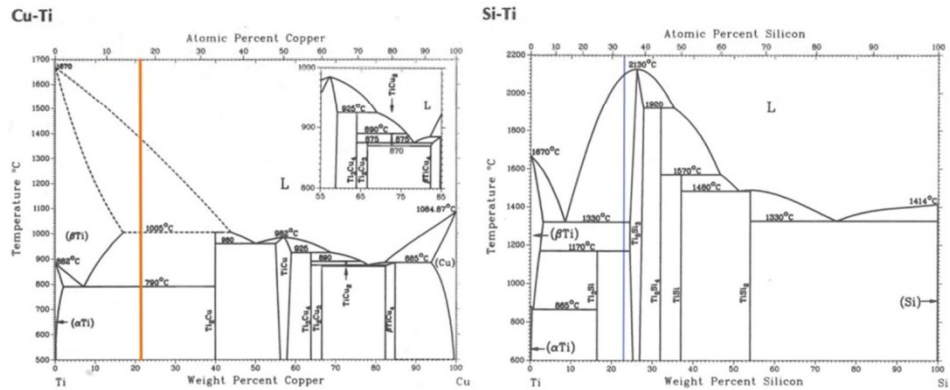


Fig. 12 Cu-Ti phase diagram with phase B indicated by an orange line: a Si-Ti phase diagram with phase C represented by a blue line [1]

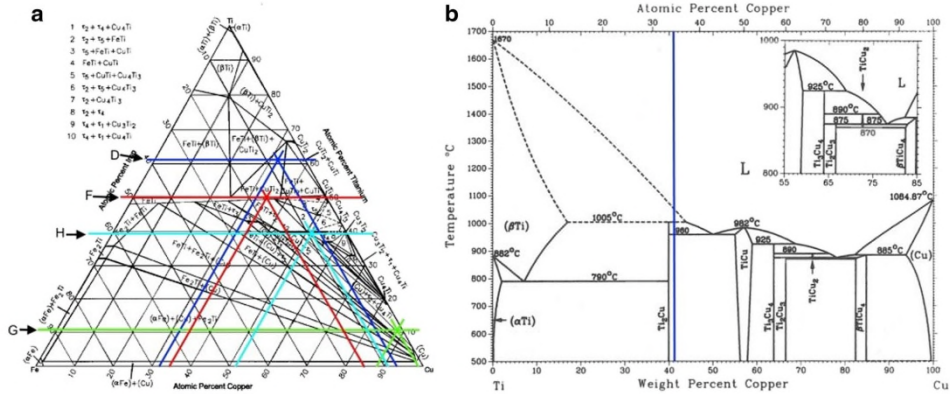


Fig. 13 Cu-Fe-Ti phase diagram isothermal section at 849 °C with phase D plotted (a) [14]. Cu-Ti phase diagram with phase E plotted (b) [1]

proportion present, phase D can be estimated to the closest stoichiometric composition being a ternary IMC compound, whilst phase E can be estimated to be a binary IMC. And so, phase D can be evaluated by a ternary Cu-Fe-Ti phase diagram [14] and phase E can be evaluated by a Fe-Cu phase diagram (Fig. 12).

Phase D points to a binary phase compound of FeTi and Ti_2Cu , and phase E has a ratio between Ti and Cu very close to Ti_2Cu . F, G and H can be considered external to the Cu-Ti reaction layer due to the higher discontinuity of these phases and the lower values of Ti when compared with the previous phases. Phases F and H are mainly composed of Cu, Ti and Fe, whilst phase G is only composed of Cu and Ti. These phases were also evaluated using the Cu-Fe-Ti. When plotted on the Cu-Fe-Ti phase diagram, phase F is a dual-phased IMC

composed of FeTi and Ti_2Cu , but much closer to FeTi composition than phase D, showing a much bigger presence of Fe, due to being out of the IMC layer and in the area with higher Fe concentrations shown in Fig. 13. Phase G points to a dual-phased τ_2 and TiCu_4 IMC phase in solid solution with Cu, and finally, phase H indicates to be also a dual-phased IMC of $\tau_2 + \tau_4$ ($\text{Ti}_{37}\text{Cu}_{67-x}\text{Fe}_x$, $x=5-7$)

After the Cu-Ti interface layer and towards the Cu bead, another phase was observed at the backscattered EDS imaging (Fig. 11b). The main elements composing phase I (Fig. 10b) are Ti, Fe, Cu, Si and Cr, and their distribution is shown in Table 4. As this phase is mainly composed of five components, it was impossible to identify it against a dual or ternary phase diagram.

The final area to be investigated was the area of dispersed IMC phases within the Cu bead. Two different areas inside the Cu bead were analysed. One was closer to the stainless steel and other close to the Ti. These two different areas were analysed to verify if the proximity to the different parent metals has an influence on the IMC formation and composition. Figure 14 shows the two different IMC areas and the corresponding phases selected.

The correspondent elemental distribution in weight percent is shown in Table 5. The IMCs identified are mainly composed of Fe, Cr, Si, Ti and Cu. The correct identification of the stoichiometric composition of the IMC phases was not possible, due to the multiplicity of important elements present within these phases.

Due to the high cooling rate, it is possible to observe coring on the IMC formed closer to the stainless steel, with the presence of different elemental concentration values in the same

Table 4 Elemental composition in weight percentage from the phases identified on the Cu-Ti interface layer

	A	B	C	D	E	F	G	H	I
Al	5.83	4.97	0.26	3.54	2.68	1.35	1.35	0.86	0.12
Si	-	0.40	19.79	0.76	0.61	1.14	-	0.11	8.97
S	-	-	-	-	-	0.09	-	-	-
Ti	90.07	67.90	66.62	49.43	56.92	41.43	8.21	31.93	33.01
V	4.10	5.39	5.37	3.70	-	-	-	-	2.97
Cr	-	-	1.22	1.41	-	1.64	-	1.28	7.16
Mn	-	-	-	0.10	-	-	0.71	0.32	1.25
Fe	-	2.69	0.87	6.52	-	15.47	0.91	8.59	29.86
Ni	-	0.22	-	0.41	-	1.85	-	1.70	2.11
Cu	-	18.43	5.88	34.13	39.80	37.05	88.83	55.24	14.54

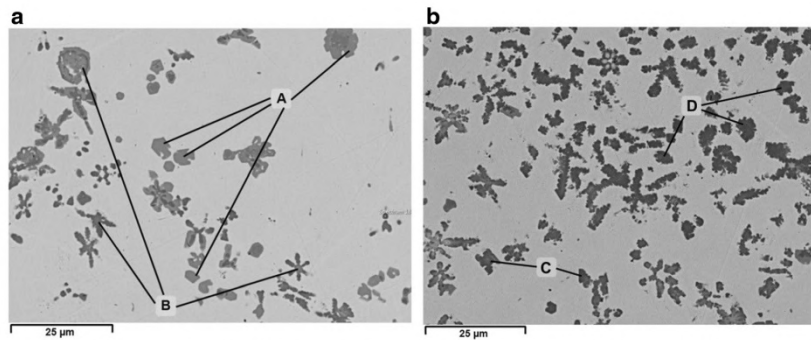


Fig. 14 Scattered IMCs close to stainless steel SEM backscattered image and phases investigated (a) and scattered IMC phases close to Ti (b)

intermetallic phase. This reveals the non-equilibrium conditions experienced during the welding process. The morphology of the IMC phases is also different with the phases closer to Ti being more angular in shape while the phases closer to the stainless steel are more circular or spherical.

Phases C and D IMC phases have higher levels of Ti when compared with the IMCs close to the stainless steel (phases A and B), showing that the IMC composition changes with the distance to the parent metals. This also reveals a gradient of Ti and stainless steel present inside the Cu bead.

4.4 Mechanical strength

To evaluate the success of using Cu as a transition metal between Ti and stainless steel, mechanical tests were also carried out and the results are shown in Fig. 15.

The ultimate tensile strength of each sample was calculated using the thickest value for the cross-sectional area of each sample and the maximum thickness of the

Table 5 Elemental composition in weight percentage from the phases identified in Fig. 14

	Si	Ti	V	Cr	Fe	Ni	Cu	Mo
A	10.34	6.48	0.00	17.19	56.03	3.56	6.42	0.00
B	11.27	16.54	1.19	8.87	43.91	2.70	9.87	5.65
C	11.85	27.95	1.43	7.04	39.56	3.49	8.24	0.44
D	11.50	21.04	0.55	8.92	46.86	3.09	6.89	1.17

The IMCs identified are mainly composed of Fe, Cr, Si, Ti and Cu. The correct identification of the stoichiometric composition of the IMC phases was not possible, due to the multiplicity of important elements present within these phases

sample; this includes the reinforcement and root penetration curves introduced by the CuSi-3 brazed metal. This way, a conservative calculation of the tensile load for each sample was achieved.

The welded samples show an increase of tensile strength with the increase of the heat input. However, the welding wire positioning does not seem to be a controlling parameter of this welding process. This characteristic denotes that the welding process is tolerant to the positioning of the wire in relation to the parent metals. This will facilitate the alignment of the welding process making the welding technique more relevant to industry application.

The samples with higher tensile load also have the maximum strain with the maximum present on the sample CMT 4 with a strain close to 2 %. The mechanical test results show a clear increase not only on tensile strength but also in ductility of these specimens, with the heat input. This indicates that this process can be further improved, by a further increase. As the IMC formation is time-temperature dependant, there is critical value where an increase in heat input and, consequently, an increase in the time-temperature cycle will have a negative effect in the tensile strength of the joint. However, this point was not achieved during this work. From that value of heat input, a further increase of energy will always result in a loss of mechanical properties of the welded joint.

The tensile test results can be compared with studies done in infrared brazing of Ti and stainless steel using Cu as an interlayer [11] and the study done using electron beam welding to join the same parent metals using Cu as an interlayer [9]. The mechanical properties reported by this study are a maximum tensile strength of 318 MPa with a ductility of 8.5 % and 234 MPa with a

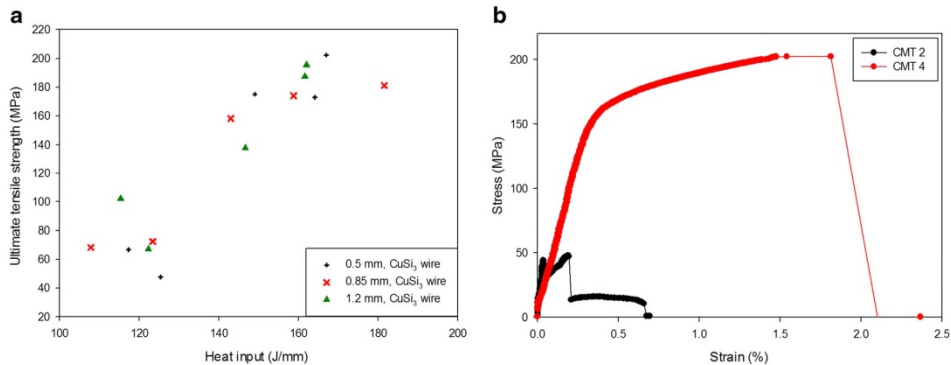


Fig. 15 Ultimate tensile strength vs heat input for all welded samples (a) and stress strain curves for samples CMT 2 and 4 (b)

3.6 % elongation, respectively. These results exceed mechanical strength of the results presented in this work; however, the added flexibility of this joining process when compared with infrared brazing and electron beam welding can result on easier and cost-effective application in industry.

5 Conclusions

It was possible to join stainless steel and Ti using CuSi-3 welding wire.

The heat input revealed to be the dominant parameter during the study developed. The maximum tensile properties were obtained for the samples brazed with higher heat input. Samples with the lowest heat input did not wet properly the parent metals, resulting in the lowest mechanical properties.

The IM phase formation was not avoided, but the IMCs formed are more ductile in nature when compared with the Fe-Ti IMCs. The phases identified are and the maximum hardness measured was of 1000 HV0.1.

The IMC phases identified are mainly located at the interfaces between the parent metals and the Cu. However, scattered IMC phases are present at the Cu bead.

Acknowledgments Supriyo Ganguly acknowledges the support received vide EPSRC (Engineering and Physical Sciences Research Council) project no. EP/J017086/1. Enquiries for access to the data referred to this article should be directed to researchdata@cranfield.ac.uk.

Open Access This article is distributed under the terms of the Creative Commons Attribution 4.0 International License (<http://creativecommons.org/licenses/by/4.0/>), which permits unrestricted use, distribution, and reproduction in any medium, provided you give

appropriate credit to the original author(s) and the source, provide a link to the Creative Commons license, and indicate if changes were made.

References

1. ASM International (1992) ASM handbook: alloy phase diagrams v. 3. ASM International
2. Poddar D (2009) Solid-state diffusion bonding of commercially pure titanium and precipitation hardening stainless steel. *Int J Recent Trends Eng* 1:93–99
3. Kundu S, Chatterjee S (2008) Diffusion bonding between commercially pure titanium and micro-duplex stainless steel. *Mater Sci Eng A* 480:316–322. doi:10.1016/j.msea.2007.07.033
4. Fazel-Najafabadi M, Kashani-Bozorg SF, Zarei-Hanzaki A (2011) Dissimilar lap joining of 304 stainless steel to CP-Ti employing friction stir welding. *Mater Des* 32:1824–1832. doi:10.1016/j.matdes.2010.12.026
5. Kahraman N, Gulenc B, Findik F (2005) Joining of titanium/stainless steel by explosive welding and effect on interface. *J Mater Process Technol* 169:127–133. doi:10.1016/j.jmatprotec.2005.06.045
6. Shanmugarajan B, Padmanabham G (2012) Fusion welding studies using laser on Ti-SS dissimilar combination. *Opt Lasers Eng* 50:1621–1627. doi:10.1016/j.optlaseng.2012.05.008
7. Lee JG, Hong SJ, Lee MK, Rhee CK (2009) High strength bonding of titanium to stainless steel using an Ag interlayer. *J Nucl Mater* 395:145–149. doi:10.1016/j.jnucmat.2009.10.045
8. Shiue RK, Wu SK, Chan CH, Huang CS (2006) Infrared brazing of Ti-6Al-4V and 17-4 PH stainless steel with a nickel barrier layer. *Metall Mater Trans A* 37:2207–2217. doi:10.1007/BF02586140
9. Wang T, Zhang B, Chen G et al (2010) Electron beam welding of Ti-15-3 titanium alloy to 304 stainless steel with copper interlayer sheet. *Trans Nonferrous Met Soc China* 20:1829–1834. doi:10.1016/S1003-6326(09)60381-2
10. Tomashchuk I, Sallamand P, Andrzejewski H, Grevey D (2011) The formation of intermetallics in dissimilar Ti6Al4V/copper/

- AISI 316 L electron beam and Nd:YAG laser joints. *Intermetallics* 19:1466–1473. doi:10.1016/j.intermet.2011.05.016
11. Kundu S, Ghosh M, Laik a et al (2005) Diffusion bonding of commercially pure titanium to 304 stainless steel using copper interlayer. *Mater Sci Eng A* 407:154–160. doi:10.1016/j.msea.2005.07.010
 12. BS EN ISO 6507-1 (2005) Metallic materials—Vickers hardness test—part 1: test method. *Br Stand* 20
 13. Pépe N, Egerland S, Colegrove P a et al (2011) Measuring the process efficiency of controlled gas metal arc welding processes. *Sci Technol Weld Join* 16:412–417. doi:10.1179/1362171810Y.0000000029
 14. Raghavan V (2002) Cu-Fe-Ti (copper-iron-titanium). *J Phase Equilibria* 23:172–174. doi:10.1361/1054971023604152